Effectiveness of Silt Screens
Final Report

MSc-thesis
Max Radermacher
1304178

Graduation Committee:
prof. dr. ir. J.C. Winterwerp (TU Delft)
prof. dr. ir. W.S.J. Uijttewaal (TU Delft)
MSc. L. de Wit (TU Delft)
MSc. F. van der Goot (Boskalis)

TU Delft Delft University of Technology

Boskalis Dredging & Marine Experts

SVASEK HYDRAULICS COASTAL, HARBOUR AND RIVER CONSULTANTS

January 2013

Preface

This thesis constitutes the final part of my Master's degree programme in Civil Engineering at Delft University of Technology. At the section of Environmental Fluid Mechanics I have made an effort to determine the effectiveness of silt screens, or the effectiveness of hanging silt screens in cross flow to be more precise. This topic was put forward by dredging company Boskalis, as they question the effectiveness of silt screens after extensive experiences with this environmental mitigation measure at dredging projects all over the world. Boskalis' intention to apply both laboratory experiments and numerical model simulations to this research made it highly appealing to me. Following the positive experience during my internship at Svašek Hydraulics, I regarded Svašek an ideal second party to be involved in the numerical share of this research. As Boskalis agreed on this, I was able to work with the interesting combination of a dredging contractor and a consultant.

Virtually no fundamental investigations into the effectiveness of hanging silt screen in cross flow had been conducted before, which gave me a high degree of freedom in determining the focus of this thesis. Nevertheless I have tried to deliver all the missing pieces for Boskalis to complete their silt screen puzzle. Hopefully the results of my research can be implemented in everyday dredging practice, so that protection of the marine environment can make another step forward.

At the half way mark of this research, after having completed the laboratory experiments, Boskalis offered me the unique opportunity to assist at a dredging and reclamation project in Genoa, Italy for one month. During this short but very diverse assignment, I was involved in the design, placement, and testing of an air bubble screen. The obvious link between air bubble screens and silt screens as a mitigation measure to prevent free spreading of turbidity made it possible to experience the decision making process and implementation of such measures in dredging practice. It was also very instructive and at times amusing to work in an international environment bearing considerable responsibilities ('You are the bubble screen expert, you should know this!'). Besides these benefits from a professional and educational point of view, I had a very pleasant time with my temporary colleagues in the Mediterranean September sun.

I can not finalise this preface without expressing my gratitude to a whole group of people who have facilitated this research with their highly appreciated contributions. First of all, I have to thank Lynyrd de Wit and Fokko van der Goot for their frequent and adequate supervision. Through his personal expertise, Lynyrd has been able to provide me with numerous fruitful advices and tips for further reading in the field of fluid mechanics. Furthermore, he kick-started the numerical model study by repeatedly adapting his Dflow3D code to my needs. Fokko has introduced me to the world of marine biology, which forms an indispensable part of this thesis. His comments on my English writing have helped me to improve readability of the report. I am grateful to Fokko and Boskalis for suggesting and facilitating my contribution to the Genoa air bubble screen project.

I thank professor Winterwerp for his critical and striking remarks during the meetings with the graduation committee, which were of great help in staying on track and keeping the right

focus. Professor Uijttewaal has made valuable contributions to the scientific justification and interpretation of the model outcomes. After he had been involved with my Bachelor's thesis, my internship and my part time job as a student assistant, having him in my graduation committee has been a worthy conclusion.

The 'Hydronamici' and 'Svasekkers' have provided me with pleasant days at the office, useful discussions and moral support. In particular Stefan Aarninkhof, Bram Bliek, Harmen Talstra and Gerard Hoogewerff are thanked for their involvement in this study. Sander de Vree and Jaap van Duin have helped me with setting up and conducting the laboratory experiments, which always bring along more trouble than expected. Without their expertise, physical modelling would not be possible at university's the fluid mechanics laboratory.

Finally, I thank my friends, my brother and my girlfriend Rosaura for their support and patience and especially my parents for their unconditional trust in my activities in Delft, which did not always serve a directly educational purpose.

Enjoy reading this thesis!

Max Radermacher
Delft, January 2013

Abstract

Dredging and reclamation works are known to generate significant amounts of turbidity. During the cycle of dislodging, transporting and placing sediment, multiple activities may cause spillage of dredged material. Especially fine sediment fractions are able to stay suspended for long periods of time. In most coastal zones around the world, the resulting clouds of turbidity bring along environmental risks. Incoming daylight is scattered by the sediment particles and substantial amounts of deposition may occur up to many kilometres away from the dredging site. The former effect, which is often referred to as shading, hampers the activities and growth of benthic flora and fauna. The latter effect can cover especially benthic flora with a layer of sediment and is therefore often called burial. Both shading and burial may lead to irreversible impact on the environment.

Dredging contractors are aware of these risks. Hence they take mitigating measures to prevent free spreading of turbidity, which is usually also demanded by their clients and the local authorities. One possibility is the application of silt screens. These are flexible, virtually impermeable screens and come in two different types. Hanging silt screens are intended to divert the sediment-laden current towards the opening between the screen's lower edge and the bottom, which is thought to result in rapid settling of the dredging spill. Standing silt screens mostly cover the full water depth and are attached to a heavy immersion pipe at the bed. Hanging silt screens are applied most often, as they require less stringent mechanical and operational restrictions than standing silt screens.

The effectiveness of hanging silt screens when subjected to cross flow is doubted by those parties experienced with their application. Regulating parties are often less experienced in this field. This has repeatedly led to the demand for silt screens, regardless of their effectiveness given the local circumstances. It has been proved troublesome to determine the effectiveness of silt screens in the field, as their large dimensions make it difficult to chart the situation in sufficient detail. Hence this research aims to obtain insight into the most important processes determining transport of suspended sediment in the vicinity of hanging silt screens and to determine the effectiveness of hanging silt screens under varying circumstances.

An inventory of all possible mechanisms capable of transporting suspended sediment past a silt screen leads to the conclusion that silt screen 'leakage' is dominated by vertical flow diversion (between the screen's lower edge and the bed) and horizontal flow diversion (around the screen's side edges).

Furthermore, an effort is made to quantify the environmental impact potential of suspended sediment concentrations, which turns out to depend on the magnitude of these concentrations and their distance to the bed. By comparing depth-integrated values of the environmental impact potential, two different parameters constituting silt screen effectiveness are proposed. The inflow effectiveness compares values downstream of the screen with their upstream counterparts. The reference effectiveness compares downstream values with the environmental impact potential at the same location in a reference situation, without the presence of a silt screen. It should be clear that the reference effectiveness provides the most honest view on silt screen performance.

The process of vertical diversion is investigated with a two-dimensional vertical modelling approach. A numerical model is set-up, which schematises turbulence by means of large eddy simulation (LES). Its performance is validated satisfactory by means of laboratory experiments. A large series of numerical simulations with varying flow velocity, screen height, settling velocity of the sediment and upstream sediment concentration profile is conducted. The water depth is kept fixed, as this parameter is proved only to influence silt screen performance through the relative height of the screen with respect to the water depth.

The inflow effectiveness only attains a positive value for unrealistically high settling velocities and at very low flow velocities. The reference effectiveness however demonstrates the detrimental influence of hanging silt screens. The amount of free turbulence generated downstream of a silt screen leads to zero or negative reference effectiveness, especially for high settling velocities and low flow velocities. Under these favourable circumstances suspended sediment settles out rapidly anyway and silt screen-induced flow disturbance only hampers this process. Especially when upstream suspended sediment concentrations are located in the lower part of the water column, extensive turbulent mixing leads to a strong increase of the environmental impact potential and an associated decrease of silt screen effectiveness.

In addition, high near-bed velocities in the contracting jet flow caused by vertical diversion results in significantly enhanced erosion if erodible bed material is available. Hanging silt screens also have a clearly negative influence on density-driven turbidity currents, as the dense layer reaches up to a much higher position in the water column after passing underneath the screen. Finally, the duration of a dredging spill is proved not to play a role in silt screen effectiveness.

The process of horizontal diversion is assessed with a two-dimensional horizontal (2DH) modelling approach. The presence of a silt screen creates resistance to the ambient flow. When a silt screen is deployed at open water, without the presence of any lateral restriction, a part of the current will find its way past the side edges of the silt screen. This effect is shown to be stronger than the relative coverage of the water column: if the silt screen covers 50% of the water depth, somewhat less than 50% of the flow which was originally directed towards the silt screen ends up being diverted vertically. The remaining part is diverted horizontally. This counteracts the intended application of silt screens as a vertical current deflector.

An attempt is made to improve silt screen performance by applying adjustments to their design and general use. However, none of the systematically derived and tested adjustments (oblique placement with respect to the current, applying two consecutive screens, perforating the screen and extending the screen with a flap) irrefutably demonstrates a positive effect of silt screens on the spreading of suspended sediment.

This study has proved the unability of hanging silt screens in cross flow to positively influence the spreading of suspended sediment with respect to the environment. Efforts should be made to convince all parties involved in the dredging process of this finding, so that spendings on ineffective mitigation measures can be avoided and protection of the marine environment can make another step forward.

Samenvatting

Baggerwerken kunnen doorgaans een aanzienlijke vertroebeling van het omringende water veroorzaken. Gedurende de cyclus waarin bodemmateriaal wordt losgemaakt, getransporteerd en elders geplaatst, kan er bij verschillende activiteiten sediment gemorst worden. Vooral de fijnere sedimentfracties blijven meestal lang in suspensie. In de meeste kustgebieden wereldwijd vormen de resulterende wolken van vertroebeling een reëel gevaar voor het milieu. De doordringing van daglicht in de waterkolom wordt beperkt als gevolg van verstrooiing van de lichtstralen door de sediment deeltjes. Ook kan er nog op vele kilometers afstand van het baggerwerk verhoogde depositie van sediment optreden. Het eerste effect kan de activiteiten en groei van flora en fauna op de zeebodem verstoren. Het tweede effect kan vooral flora bedekken met een laag sediment. Beide effecten kunnen onherstelbare gevolgen hebben voor het milieu.

Baggerbedrijven zijn zich bewust van deze risico's. Daarom treffen zijn mitigerende maatregelen om de vrije verspreiding van vertroebeling te voorkomen, waartoe zij doorgaans ook gedwongen worden door klanten en autoriteiten. Een mogelijkheid is de toepassing van slibschermen. Dit zijn flexibele, vrijwel ondoorlatende schermen, waarvan twee verschillende types bestaan. Hangende slibschermen zijn bedoeld om de stroming met het meegevoerde sediment door de opening tussen de onderrand van het scherm en de bodem te leiden, waardoor het sediment dichter bij de bodem wordt gebracht. Dit moet het snel uitzakken van sediment bevorderen. Staande slibschermen bestrijken meestal de volledige waterdiepte en zijn bij de bodem bevestigd aan een zware, afgezonken buis. Hangende slibschermen worden het meest toegepast, aangezien dit type minder strenge mechanische en operationele eisen met zich meebrengt dan staande slibschermen.

De effectiviteit van staande slibschermen in dwarsstroming wordt betwist door partijen die ervaring hebben met deze toepassingsvorm. Regelgevende instanties hebben deze ervaring vaak niet of in veel mindere mate. Dit heeft al veelvuldig geleid tot het eisen van de toepassing van slibschermen, ongeacht hun effectiviteit onder de project-specifieke omstandigheden. Het is lastig gebleken om de effectiviteit van slibschermen in het veld te bepalen, aangezien de grote schaal het lastig maakt om de situatie voldoende in kaart te brengen. Daarom is het doel van dit onderzoek het verkrijgen van inzicht in de belangrijkste processen die een rol spelen bij het transport van gesuspendeerd sediment in de nabijheid van hangende slibschermen, alsmede het bepalen van de effectiviteit van hangende slibschermen onder wisselende omstandigheden.

Een inventarisatie van alle mogelijke mechanismen die gesuspendeerd sediment langs een slibscherm kunnen transporteren, wijst uit dat verticale uitwijking van de stroming (door de opening tussen de onderrand van het scherm en de bodem) en horizontale uitwijking (langs de zijranden van het slibscherm) in dit kader veruit het belangrijkst zijn.

Verder is de potentiële schadelijkheid van concentraties gesuspendeerd sediment gekwantificeerd. Dit kan uitgedrukt worden als het product van de concentratie en de afstand tot de bodem. Door over de waterdiepte geïntegreerde waardes met elkaar te vergelijken, kunnen twee verschillende maten voor de effectiviteit van slibschermen worden gepresenteerd. De instroom-effectiviteit vergelijkt waardes benedenstrooms van het scherm met hun bovenstroomse tegenhanger. De referentie-effectiviteit vergelijkt de benedenstroomse waarde met de waarde

op dezelfde locatie in een referentiesituatie zonder slibscherm. Het moge duidelijk zijn dat de referentie-effectiviteit het eerlijkste beeld geeft van de prestaties van slibschermen.

Verticale uitwijking is onderzocht met behulp van een tweedimensionaal verticale modellering. Er is een numeriek model opgesteld, waarin turbulentie geschematiseerd is met behulp van large eddy simulation (LES). De prestaties van het model zijn naar behoren gevalideerd aan de hand van laboratorium experimenten. Een grote reeks numerieke simulaties is uitgevoerd, waarin de stroomsnelheid, schermhoogte, valsnelheid van het sediment en het bovenstroomse concentratieprofiel werden gevarieerd. De waterdiepte is constant gehouden, aangezien er wordt aangetoond dat deze parameter de effectiviteit van slibschermen slechts beïnvloedt via de relatieve schermhoogte ten opzichte van de waterdiepte.

De instroom-effectiviteit neemt alleen een positieve waarde aan voor onrealistisch hoge valsnelheden of zeer lage stroomsnelheden. De referentie-effectiviteit toont de nadelige invloed van hangende slibschermen aan. De vrije turbulentie die benedenstrooms van het scherm wordt gegenereerd leidt tot een geringe of negatieve effectiviteit, in het bijzonder bij hoge valsnelheden en lage stroomsnelheden. Onder zulke gunstige omstandigheden zakt gesuspendeerd sediment hoe dan ook snel uit. Dit proces wordt dan geremd door de stromingsverstorende werking van een hangend slibscherm. Vooral wanneer het meeste sediment zich aan bovenstroomse zijde in het onderste deel van de waterkolom bevindt, leidt omvangrijke turbulente menging tot een sterke toename van de potentiële schadelijkheid voor het milieu en de daaruit voortvloeiende daling van de effectiviteit van het slibscherm.

Verder kan er bij beschikbaarheid van erodeerbaar bodemmateriaal een flinke verergering van de erosie optreden als gevolg van hoge stroomsnelheden dicht bij de bodem in de convergerende stroming onder het scherm. Hangende slibschermen hebben ook een negatieve invloed op dichtheidsgedreven troebelingsstromen, aangezien de sedimentvoerende laag tot veel hoger in de waterkolom reikt na het onderlangs passeren van een slibscherm. Als laatste blijkt dat de duur van een mors geen rol speelt in de effectiviteit van slibschermen.

Horizontale uitwijking is onderzocht met een tweedimensionaal horizontale modellering. De aanwezigheid van een slibscherm creëert weerstand voor de omringende stroming. Als een slibscherm op open water wordt geplaatst, buiten de invloedssfeer van gesloten randen, zal een deel van de stroming zich een weg banen langs de zijranden van het scherm. Dit effect is sterker dan de relatieve afdekking van de waterkolom: als het slibscherm 50% van de waterdiepte bestrijkt, zal iets minder dan 50% van de stroming die oorspronkelijk naar het scherm toe stroomde er uiteindelijk onderdoor gaan. Het resterende deel wijkt uit in het horizontale vlak. Dit werkt de beoogde toepassing van slibschermen als stromingsgeleider in het verticale vlak tegen.

Er is een poging ondernomen om de prestaties van slibschermen te verbeteren door aanpassingen te doen aan hun ontwerp en algemene toepassingsvorm. Geen van de systematisch afgeleide en onderzochte aanpassingen (plaatsing onder een hoek met de stroming, plaatsing van twee slibschermen achter elkaar, een geperforeerd scherm en een scherm verlengd met een flap) bewijst onomstotelijk een positief effect te hebben op de verspreiding van gesuspendeerd sediment.

Dit onderzoek heeft aangetoond dat hangende slibschermen in dwarsstroming geen positieve invloed hebben op de verspreiding van gesuspendeerd sediment ten opzichte van het milieu. Alle betrokken partijen in het baggerproces moeten worden overtuigd van deze bevinding, zodat uitgaven aan ineffectieve milieumaatregelen kunnen worden voorkomen en de bescherming van het mariene milieu weer een stap voorwaarts kan maken.

Contents

Nomenclature

B	Calibration parameter of empirical equilibrium profile for mud	$-$
B_b	Plume width prior to impingement	m
B_e	Length of edge in numerical mesh	m
C	Suspended sediment mass concentration	kg/m^3
C_0	Near-bed suspended sediment mass concentration	kg/m^3
C_b	Bed mass concentration	kg/m^3
C_{max}	Maximum SSC present in domain	kg/m^3
C_v	Suspended sediment volume concentration	$-$
C_w	WALE constant	$-$
C_*	Dimensionless SSC	$-$
D	Diffusion coefficient	m^2/s
D_p	Diameter of overflow pipe	m
E	Effectiveness parameter	%
E_d	Discontinuous effectiveness parameter	%
E_{ii}	Energy density	m^3/s^2
E_{in}	Effectiveness compared to issuing concentration profile	%
E_{ref}	Effeciteveness compared to reference run	%
$\mathbf{F}$	Summation of all body forces acting on a fluid	N
F_D	Drag force	N
F_E	Silt screen induced erosion factor	$-$
F_g	Gravitational force	N
Fr	Froude number	$-$
Fr_j	Jet Froude number	$-$
H	Energy head	m
I	Intensity of a light-beam	W/m^2
L_m	Length of numerical model domain	m
L_{50}	Downstream distance where velocity decay equals 50%	m
$\mathcal{L}$	Characteristic length scale of the flow	m
M_b	Deposited bed mass	kg/m^3
M_e	Erosion rate	$kg/(sm^2)$
P	Environmental impact potential	$-$
P_d	Discontinuous environmental impact potential	$-$
P_{in}	Environmental impact potential of issuing concentration profile	$-$
P_{ref}	Environmental impact potential of reference run	$-$
Q_L	Total discharge passing silt screen on the left side	m^3/s
Q_R	Total discharge passing silt screen on the right side	m^3/s
Q_{rel}	Relative discharge	$-$
Q_s	Discharge across edge representing part of the silt screen	m^3/s
R_E	Dimensionless rate of erosion	$-$
Re	Reynolds number	$-$
Ri	Gradient Richardson number	$-$

Ri_0	Bulk Richardson number	$-$
S	Submergence factor	$-$
Sc	Schmidt number	$-$
$\mathbf{U}$	Two-dimensional depth-averaged velocity vector	m/s
U	Undisturbed depth-averaged flow velocity in x-direction	m
U_0	Depth-averaged flow velocity between bed and structure	m/s
U_e	Ambient flow velocity near wall jet	m/s
U_f	Front velocity of turbidity current	m/s
U_t	Propagation velocity of turbidity current	m/s
$\mathcal{U}$	Characteristic velocity scale of the flow	m/s
V_p	Particle volume	m^3
W	Outflow velocity of overflow plume	m/s
W_b	Downward plume velocity prior to impingement	m/s
W_s	Width of silt screen	m
W_*	Relative silt screen width	$-$
a	Absorption coefficient of light travelling through water	m^{-1}
a_i	Calibration parameter for erosion of mud	$-$
d	Equivalent grain diameter	m
d_{50}	Median equivalent grain diameter	m
g	Gravitational acceleration	m/s^2
g'	Reduced gravitational acceleration	m/s^2
h	Undisturbed water depth	m
h_0	Minimum height between bed and structure	m
h_1	Water depth upstream of structure	m
h_2	Water depth downstream of structure	m
h_{co}	Subcritical conjugate depth	m
h_f	Frontal height of turbidity current	m
h_{rel}	Relative height: ratio of silt screen height over water depth	$-$
h_s	Height of silt screen	m
h_t	Height of turbidity current	m
i	Coordinate along the streamline	m
k	Calibration parameter for settling velocity of mud	$-$
k_w	Wavenumber	m^{-1}
k_N	Nikuradse bed roughness	m
ℓ	Travelled distance of light beam	m
m	Calibration parameter for settling velocity of mud	$-$
p	Pressure	N/m^2
r	Turbulence intensity	m/s
t	Time	s
t_s	Inflow duration of discontinuous dredging spill	s
$\mathbf{u}$	Three-dimensional velocity vector	m/s
u	Flow velocity in x-direction	m/s
$\bar{u}$	Time-averaged flow velocity in x-direction	m/s
$\tilde{u}$	Dimensionless time-averaged flow velocity in x-direction	$-$
u'	Fluctuating component of flow velocity in x-direction	m/s
u_0	Near-bed streamwise velocity	m/s
u_m	Maximum time-averaged streamwise velocity in profile	m/s
u_{m0}	Maximum time-averaged streamwise velocity within domain	m/s
u_*	Shear velocity	m/s
$\tilde{u}_m$	Dimensionless maximum streamwise velocity in profile	$-$
x_1	Streamwise coordinate where $u_m = u_{m0}$	m

x_2	Streamwise coordinate where decay of u_m is 50%	m
w	Vertical flow velocity	m/s
$\bar{w}$	Time-averaged vertical flow velocity	m/s
w_s	Settling velocity	m/s
w_{s50}	Median settling velocity	m/s
w_{s50b}	Near-bed median settling velocity	m/s
$w_{s,r}$	Settling velocity of individual mud floc	m/s
$w_{s\infty}$	Final settling velocity	m/s
$\tilde{x}$	Dimensionless x-coordinate	$-$
x_s	Characteristic settling distance	m
$\tilde{z}$	Dimensionless z-coordinate	$-$
z_1	Vertical coordinate where $\bar{u} = 0.5u_m$	m
z_b	Vertical bed coordinate	m
z_*	Dimensionless z-coordinate	$-$
α	Aspect ratio of dredging spill	$-$
β	Rotation angle of silt screen with respect to current	$^\circ$
ϵ	Relative excess density of sediment	$-$
η	Surface elevation	m
θ	Ratio of settling velocity over depth-averaged flow velocity	$-$
λ_T	Taylor length scale	m
μ	Dynamic viscosity	$kg/(ms)$
μ_c	Contraction coefficient	$-$
ν	Kinematic viscosity	m^2/s
ρ	Density of water	kg/m^3
ρ'	Characteristic density difference	kg/m^3
ρ_0	Ambient density	kg/m^3
ρ_f	Density of floc	kg/m^3
ρ_s	Dry density of sediment	kg/m^3
σ	Root-mean-square of velocity fluctuations	m/s
τ	Shear stress tensor	N/m^2
τ'	Reynolds stress	N/m^2
τ_0	Bed shear-stress	N/m^2
τ_d	Threshold bed-shear-stress for deposition	N/m^2
τ_e	Threshold bed shear-stress for erosion	N/m^2
$\langle\tau_0\rangle$	Mean bed shear-stress	N/m^2
ϕ	Slope angle	rad

Chapter 1

Introduction

By definition, dredging and reclamation works bring along changes to the environment. Various environmental effects are related to every stage in the cycle of dredging sediment, transporting and placement or further treatment (Bray, 2008). These changes are not necessarily of a detrimental type. Think for example of the removal of contaminated sediment. Nevertheless, many aspects do bring along possibly negative consequences for the environment. This topic has kept on gaining attention over the last decades as humanity became increasingly aware of its own environmental impact. One of those possibly negative consequences related to dredging and reclamation works is the spreading of suspended fine sediment, causing increased turbidity[1]. The small size of fine sediment particles enables them to remain suspended throughout the water column for long periods of time. Turbidity can be a serious threat to the aquatic flora and fauna, mainly through the processes of shading and burial. Although direct effects of turbidity may only be of a temporary nature, it can lead to permanent loss of biodiversity. All parties involved in dredging operations are set to minimise these long-term effects. When a project location is situated near vulnerable ecosystems, efforts are made to keep turbidity levels within acceptable limits outside of the dredging or reclamation area. Preventive actions to reach this goal are found in a range of different measures. Some are set to reduce the release of fine sediment, whereas others try to reduce concentrations of already suspended material. Silt screens are an example of the latter. Due to reasons explained later on in this report, many parties consider them a best management practice. Beneficial effects of silt screens regarding turbidity levels have indeed been reported (e.g. Vu et al., 2010). On the contrary, adverse effects are encountered as well (e.g. Jin et al., 2003). Altogether silt screen performance seems to depend largely on screen- and site-specific aspects. Scientific support and physical understanding of all relevant processes that determine the effectiveness of silt screens still remain fairly thin.

This research aims to determine the effectiveness of silt screens in an academic and scientific way, by gaining insight into all relevant physical processes. To that purpose, a numerical model will be set up and various laboratory experiments will be carried out. In this introductory chapter, section 1.1 sums up the sources of turbidity, whereas section 1.2 clarifies its environmental impact. In section 1.3, the purpose of silt screens is discussed. Section 1.4 presents the different types of silt screens encountered in practice. Section 1.5 gives an overview of all relevant academic and corporate research that has been carried out so far. In section 1.6 it is explained how decision making processes affect the application and perception of silt screens. The objective of this research is finally stated in section 1.7.

Chapter 2 of this report encounters the subject from a purely theoretical point of view, whereas chapter 3, 4, 5 and 6 present the results of numerical model simulations and laboratory experiments. Finally, chapter 7 and 8 contain the conclusions and recommendations.

[1] Suspended sediment concentration (SSC) and turbidity are two different approaches of the same phenomenon. Appendix D.3 elaborates on this. When indicating the presence of suspended solids in the water column, both terms will be used interchangeably.

1.1 Sources of turbidity

Bray (2008) discerns four stages constituting the dredging cycle of almost any dredging project, being dislodging, vertical transport, horizontal transport and placement. Every stage brings along a possible source of turbidity.

- During the *dislodging* stage, the differences between various types of dredging equipment can not be neglected. For Cutter Suction Dredgers (CSD) and Trailing Suction Hopper Dredgers (TSHD), both belonging to the category of hydraulic dredgers, suspension of bed material is the main goal. It is not possible to catch every suspended particle in the suction mouth. Especially the rotating movement of a CSD's cutterhead can fling about considerable amounts of suspended sediment. Backhoe Dredgers, Grab Dredgers and Bucket Ladder Dredgers, all belonging to the category of mechanical dredgers, dig into the bed material. This produces considerably less turbidity during dislodging.

- During *vertical transport* in an open container (bucket ladder dredger, backhoe dredger, grab dredger), dredged material is in direct contact with the surrounding water. The faster the container is hoisted, the more turbidity is generated. However, slowing this process down adversely affects production. The bucket of a backhoe has to be kept carefully in a horizontal position to prevent excessive spillage. Once the dredged material is raised to the free surface, a hopper or barge is loaded. All dredging equipment produces a mixture of sediment and water. However, the amount of transport water is much bigger in case of hydraulic dredgers. As this transport water limits the maximum amount of sediment in the hopper, efforts are made to discharge it. The mixture, also known as slurry, flows lengthwise through the hopper. When flowing towards the far end, big particles are able to sink to the bottom. Most of the smaller particles remain suspended and are directed out of the hopper together with the transport water. This procedure is known as overflowing and causes a plume of suspended fine sediment in the water surrounding the vessel. Modern TSHD's are often equipped with a so-called Light Mixture Over Board (LMOB) arrangement, which checks the density of incoming slurry. If it is considered too low, the whole portion is immediately redirected back into the water.

- *Horizontal transport* is done by hoppers, barges or pipelines. Some leakage might occur near the bottom doors of a hopper or barge or near pipeline joints. The spillage of suspended sediment associated with these processes is relatively small.

- A number of different *placement* techniques are used:

  - Rainbowing: the sediment-water mixture is sprayed onto the water surface, resulting in a 'rainbow' of sediment. Heavy particles will settle rapidly, but fine sediment might remain suspended for a long time.
  - Pumping ashore: the mixture is pumped into a pipeline. The pipeline ends on-shore at the location where sediment is needed. This might result in a high-density flow off the slopes of a reclamation.
  - Pumping to a spreader pontoon: the mixture is pumped into a pipeline. The pipeline ends at a movable spreader pontoon, which is able to spread the mixture over a bigger area.
  - Direct dumping: bottom doors are opened under the hopper or barge and the high-density mixture falls down the water column onto the bed. Upon impingement, clouds or near-bed currents of suspended material are formed.
  - Reversed pumping via the suction pipe: in case of a TSHD, the mixture might be redirected into the suction pipe. It enters the water column close to the bed.

The choice depends on the purpose of dredging and some site-specific circumstances. Underwater spreading of relocated material occurs due to wave and current conditions and density effects. Fine particles remain suspended for long periods of time. The biggest part of it gets dispersed and does not end up at the intended location. In case of capital dredging, the newly reclaimed land might be eroded by wave and current action or precipitation runoff. This increases turbidity levels as well.

1.2 Environmental impact

The presence and spreading of suspended sediment concentrations (SSC) does not necessarily imply negative consequences. Certain dredging and reclamation locations are confronted with relatively high levels of turbidity by nature. In order to survive, ecosystems adapt themselves to natural local circumstances (the so-called background conditions). Long periods of exposure to an unnatural level of SSC can result in irreversible impact. Dredging-induced SSC are linked to the duration of the dredging project, which is usually in the order of months to years. Especially in shallow coastal zones vulnerable aquatic flora and fauna are present.

There are five possibly negative effects of SSC for the environment:

- It affects the light transmittance of the water. Typical examples of species vulnerable to shading are fields of sea grass and coral reefs. These species drive complete ecosystems and are known to recover slowly. A lack of sunlight can lead to irreversible impact.
- Upon settling, a layer of fine sediment is formed on the bed. This can disturb the benthic community to a high degree. Fauna will probably be able to cope with such an event than better flora, since it has a higher mobility.
- It hampers the activities of animals relying on their sight when hunting. To birds especially the upper metre of the water column is of importance.
- Suspended sediment has to be kept away from certain water intake structures. Regardless of their purpose, high SSC will often pose a threat to the underlying facility.
- Turbidity at the free surface has also got an aesthetic effect. Near bathing areas, turbid water can hamper recreational activities. An additional aesthetic effect, though of less importance, is the public opinion. Turbidity always looks like a threat to the environment. This might increase the number of opponents of a certain dredging project, regardless of the real environmental damage done.

1.3 Purpose of silt screens

Whenever it is undesirable that fine suspended sediment spreads freely, a choice has to be made between different mitigating measures. All mitigating measures can be classified in a spectrum between source and receiver. The following measures can be applied according to Bray (2008), ordered from source-based to receiver-based:

- Careful selection of dredging equipment
- Modification of dredging equipment, e.g. application of closed environmental grabs
- Operational measures on board the dredgers, e.g. limiting bucket hoisting speed or overflow quantities
- Removal of fines from the dredged material, e.g. by means of a settlement pond

- Seasonal or tidal restrictions to placement in order to avoid heavy hydrodynamic conditions which promote spreading

- Containing or controlling suspended sediment, e.g. by means of a silt screen

It becomes clear that silt screens are applied at the far end of a dredging operation, relatively close to possible receivers.

The purpose of all these measures can be defined based on the environmental threats as discussed in section 1.2. Firstly, it has to be avoided that high SSC settles on vulnerable benthic species. Of course this does not mean that suspended sediment has to be prevented from settling at all. It will always do so eventually. Generally, vulnerable species are not located right next to the screen. Therefore it is a matter of making sure the fine sediment does not get transported too far in high concentrations. Secondly, the light transmittance has to be maintained at an acceptable level. Here the same argument is valid: a vulnerable receptor will not be situated exactly at the dredging site. High SSC have to be kept close to the silt screen. Finally, a clear and unclouded free surface has to be preserved because of aesthetic reasons. This goal has to be reached everywhere on the 'outer side' of the screen.

Given these different purposes, the effectiveness of silt screens can be defined. Leakage is inextricably linked to the concept of silt screens. In the context of mitigating impact of dredging operations, the effectiveness is therefore related to the degree to which the escaping fines are presented to the environment in a desirable way. In the past, the focus of research into silt screen effectiveness has always been on comparing SSC, suspended sediment fluxes and turbidity on both sides of the silt screen (JBF Scientific Corporation, 1978; Yasui et al., 1999; Jin et al., 2003; Bray, 2008; Vu et al., 2010). In this research an attempt is made to derive a more precise definition, since the various goals summed up above are not completely covered by the stated parameters. A measure for silt screen effectiveness should include the following aspects:

- The sediment has to settle as quickly as possible once it has past the silt screen. The closer it is to the bed, the shorter the settling time will be. Quantitatively this demand could be expressed as the product of a concentration and its distance to the bed. A comparison of this parameter at both sides of the screen determines whether the screen is effective at all.

- The free surface has to remain clear. Water gets already turbid at very low suspended sediment concentrations. Effectiveness is related to the position of the limit turbidity in the water column.

Not all purposes are applicable in a specific situation. Therefore the different aspects that make up silt screen effectiveness should be assessed and judged separately. A more elaborate description of the parameters which constitute silt screen effectiveness can only be presented after having discussed the theoretical part of this research. Section 2.5 continues on this topic.

1.4 Types of silt screens

Silt screens come in different shapes and with different properties, but they are always based on one of two general types. These are the hanging type and the standing type. Both are depicted in figure 1.1.

The hanging type consists of a sheet, mostly constructed from geotextile, that hangs down from floats at the free surface. To prevent the entire sheet from floating up, a weight chain is added at the lower side. When pressures on a hanging silt screen get too high, the sheet will flare and allow the current to flow underneath more easily. The anchorage construction

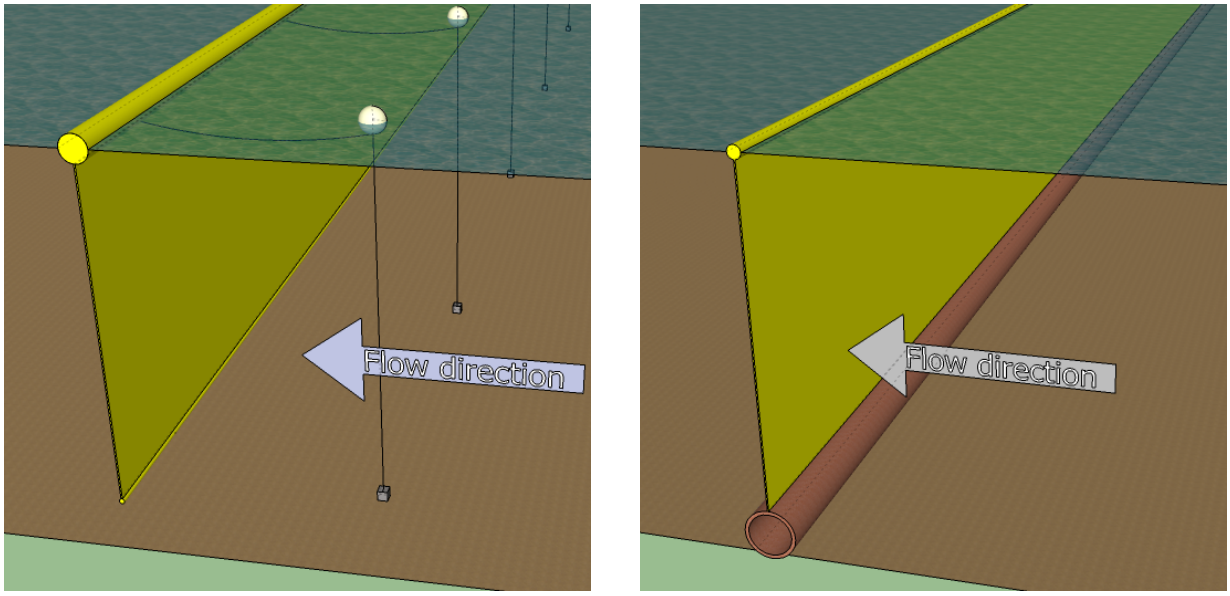

Figure 1.1: The two main types of silt screens. On the left a screen of the hanging type, on the right one of the standing type. In case of reversible flow, the hanging type needs to be anchored on both sides.

needs to have sufficient clearance. In that way the screen can move along with waves and tides. Anchorage of the bottom edge to avoid flaring induces unacceptably large forces.

In case of the standing type, the sheet is fixed to a heavy beam that lies on the bottom. Floats are attached to the top side of the sheet and pull it towards the free surface. Just like with the hanging type there is a release mechanism. Overpressure will force the floats to sink down and allow water to flow over the screen. A specific failure mechanism related to this type occurs when settled sediment piles up next to it. The sheet and sinking beam might get partially buried, which complicates removal of the barrier to a great extent.

The choice between both types is often made based on operational rather than physical arguments. Near medium and big sized dredging and reclamation activities, silt screens have to be relocated regularly to keep up with the actual dredging or dumping location. In case of a standing silt screen, relocation requires quite heavy floating equipment. Therefore contractors usually prefer hanging silt screens, which can be relocated relatively easy. This research will focus on hanging silt screens, as those are applied most often and their effectiveness is questioned the most. Figure 1.2 shows an example of hanging silt screens in dredging practice.

1.5 Current state of research

Due to its big surface area, a silt screen has to withstand large forces. Hence, much effort has been done to optimise silt screens from a mechanical point of view. Investigations regarding strength by JBF Scientific Corporation (1978) marked the beginning of silt screen research. They also addressed the effectiveness of silt screens based on analytical studies and field measurements, but only very few conclusions were drawn on that topic. Field measurement outcomes are influenced by various site-specific conditions. It becomes clear that silt screens are applied in many different geometries. In these early days, awareness of all possible environmental aspects related to dredging was still fairly low. Silt screens were especially applied around remedial dredging works, involving contaminated soils. Generally the size of remedial dredging sites is small. This enables contractors to apply a completely closed silt screen right next to the dredging site, see figure 1.3. Spreading of suspended sediment close to the dredging equipment is mostly density-driven. De Wilde (1995) and Yasui et al. (1999) concluded that silt screens in

Figure 1.2: Multiple sections of hanging silt screens as applied at a dredging project in the Middle East, courtesy Boskalis.

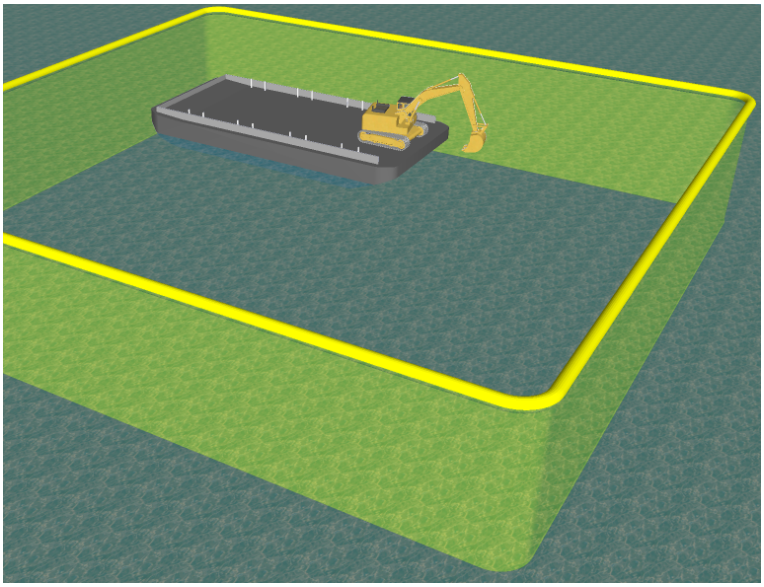

Figure 1.3: Completely closed silt screen around a remedial dredging site.

closed formation can be a very effective measure. Special attention is paid to the mechanisms leading to turbidity decay. Regarding mechanical strength and stability of silt screens, it is generally concluded that silt screens should not be applied in current velocities above 0.5 m/s or wave heights above 0.5 to 1.0 m. It is possible to improve mechanical properties of both silt screen and anchorage, but costs rapidly increase.

Gradually attention has shifted to the overall environmental impact of turbidity, regardless of contamination. In this respect, silt screens are applied in many different geometries. A report by Francingues and Palermo (2005) bundled the conclusions of various researchers into one engineering guideline. It states that a rigorous examination of silt screen performance is a remaining challenge. In Jin et al. (2003) again a series of field measurements is discussed. The complexity of the measurements poses difficulties trying to extract rigid conclusions. At least in a number of cases silt screens have proved to be ineffective.

From an academical point of view, research of Vu and Tan (2010) is worth noticing. It focuses on the performance of silt screens as a sediment control equipment, which comes very close to investigating the effectiveness. More results are still to come, but qualitative results of among others laboratory experiments have already been published. They include Particle Image Velocimetry measurements of a silt screen in a flume.

On the whole, silt screen research is heavily biased towards consideration of strength and stability during the design stage (Vu and Tan, 2009; Vu et al., 2010). Detailed and rigid conclusions on silt screen performance have not been drawn yet. For that purpose, systematic research is needed instead of incidental stand-alone field experiments. Nevertheless, the latter will be helpful in relating research outcomes to engineering practice.

1.6 Engineering practice

The actual application of silt screens as a mitigating measure always results from certain regulations limiting free spreading of suspended sediment. These regulations are usually imposed by the local government or permitting authority. In developing countries, where environmental legislation is often lacking, many project owners or financiers develop regulations themselves. However, biodiversity in a certain region can never be charted completely. Furthermore the response of aquatic flora and fauna to turbidity is known only in general terms. As all species adapt to their direct environment, the response of the same organism might differ from site to site. Therefore it is impossible to develop perfectly tailored environmental legislation. The common answer to uncertainties in engineering is found in over-dimensioning. Hence regulators will usually aim for strict environmental terms.

Likewise, the exact spreading of turbidity plumes is uncertain. Monitoring campaigns are set to keep track of SSC and turbidity at various locations surrounding a dredging or reclamation site. Nevertheless, the discrete nature of these measurements and in many cases the impossibility to perceive sub-surfacial turbidity will never lead to complete certainty regarding exceedance of SSC limits.

As a result, regulations can not be maintained strictly. So although silt screens are often applied when regulations seem to call for mitigating measures, once deployed their performance becomes less important. In addition to this, project owners often have unrealistic expectations of silt screens. They overlook operational consequences and think of silt screens as turbidity containers rather than current deflectors. Sometimes project owners even copy environmental demands, including the application of silt screens, from one project to another, regardless of varying conditions. Contractors are confronted with silt screens more often. From their experience, they know that silt screen effectiveness is rather doubtful and depends heavily on local circumstances. See appendix A for discussion of silt screen effectiveness in a number of case studies.

Currently, much effort and money is wasted on ineffective applications of silt screens, where other mitigating measures may have been more effective and cost efficient. Thorough research into silt screen effectiveness is beneficial for all parties involved:

- Environmental risks can be reduced by not relying on inappropriate mitigation measures.
- Contractors and clients are able to limit costs by only applying silt screens when they are really effective regarding local circumstances.
- Regulators are better able to judge whether it is appropriate to demand the application of silt screens given their effectiveness in a specific case.

1.7 Research objective

This research will provide increased insight into the most important processes determining silt screen effectiveness. Based on the results, a design guideline can be constructed, stating under which conditions a silt screen is an effective solution. The main research objective is formulated as follows:

To obtain insight into the most important processes determining transport of suspended sediment in the vicinity of hanging silt screens and to determine the effectiveness of hanging silt screens under varying circumstances.

Both parts of the objective are explicitly limited to hanging silt screens, because both their application and doubts about their effectiveness are the most widely spread. It will be achieved by addressing the following research questions:

1. To what extent do varying *flow velocity*, *water depth*, *relative height of the screen*, *settling velocity* and *upstream SSC profile* affect the effectiveness of a hanging silt screen in uniform cross flow?
2. Can basic adjustments to the small-scale design and large-scale application of hanging silt screens improve their effectiveness?

The first question will result in a sensitivity analysis of the effectiveness with respect to the stated parameters. A design guideline for the application of hanging silt screens in uniform cross flow can be constructed based on this analysis. By relative screen height the ratio of screen height over water depth is meant.

The second question discusses the possibility to improve silt screens. A couple of promising adjustments is developed and investigated rather than really striving to optimise silt screens. Both the small-scale design and the large-scale application are taken into account. The former focuses on adjustments to the cross-section of a hanging silt screen. For example, perforating the screen might influence the current pattern in a favourable way. By the latter, the general way in which silt screens are applied is called into question. For example, it might be advantageous to use hanging silt screens as a horizontal current deflector rather than a vertical one.

The tools used to reach the objective consist of laboratory experiments and numerical models. Their specific application in different parts of this research is closely related to the relevant physical processes. Therefore the application of these tools is explained in chapter 3.

Chapter 2

Theory

Silt screens are surrounded by a couple of different processes, literally as well as figuratively. First of all, the relevant processes regarding the effectiveness of silt screens are identified. Then the general flow field in the vicinity of a silt screen is introduced. The third section discusses a couple of basic phenomena related to suspended (fine) sediment, whereas the fourth section covers the specific case of a dredging-induced sediment spill. This chapter concludes with a way of quantifying the effectiveness of silt screens.

2.1 Key processes

First an inventory of all processes related to hanging silt screens in uniform cross flow is made. After that the processes that are of most importance to this research can be selected.

2.1.1 Inventory

When assessing the effectiveness of a silt screen, insight into the related flow and transport processes is paramount. It is known that the spreading of fines can never be stopped completely. Hence two questions arise: which mechanisms are responsible for sediment loss and which agents actually transport the sediment past the silt screen?

Four sediment loss mechanisms can be identified:

- The most obvious sediment loss mechanism is situated near the bottom. In a horizontal current, continuity forces water to get past the screen. A gap is left open between the bottom and the lower edge of the silt screen. The current is then *diverted vertically*. Nothing prevents the sediment from flowing along.

- The second mechanism is related to the horizontal plane. A silt screen has got finite dimensions and partly blocks the flow, so the current might also be *diverted horizontally* and pass the screen sideways. Engineers will always try to design a silt screen in such a way that the dredging plume does not simply end up in that current, but the mechanism can not be neglected.

- The third sediment loss mechanism is found at the free surface and is not as well-defined as the previous ones. In case of rough flow conditions, water might be splashing or *washing over* the floats. However, in case of such rough conditions many other and more severe problems will occur. The construction can not withstand these big forces and will fail. For the sake of completeness, the mechanism is not left out of these initial considerations.

- The fourth and last mechanism is related to the segmentation of a silt screen. One section of a silt screen typically has got a width of about 100 m. That is mostly shorter than the

design width of a complete screen. At the locations where two sections come together, there will not be a sand tight connection. This induces *leakage* of sediment.

The treatment of the sediment loss mechanisms has already shown a glimpse of the agents that actually transport the sediment past the silt screen.

- First of all 'external' currents can be named as one of them. In this case 'external' means that the forcing of the flow has got nothing to do with the presence of a silt screen or suspended fines. Think for example of tidal or river currents. Eventually every identifiable transporting or mixing agent, except for 'true' diffusion, can be related to the presence of flow. Nevertheless from here on these external currents are simply indicated as *flow*. Wind-driven currents belong to that category as well, but their different flow profile has to be noted.
- The second agent, being *waves*, eventually also comes down to the generation of flow. However, its specific character makes separate treatment beneficial. With waves wave-induced currents are associated. These are able to affect the spreading of turbidity. The interaction between waves and a silt screen may also lead to dynamic processes capable of transporting suspended sediment.
- The third agent is related to a somewhat different forcing mechanism, namely *buoyancy*. Turbid water obtains a slightly higher density. When it mixes with clear water, the density difference starts to drive a current. It goes without saying that fine sediment is then transported along.

Table 2.1, gives an overview of the relations between sediment loss mechanisms and agents as named above. A plus sign indicates a weak relation, a double plus sign indicates a strong relation and a zero indicates no significant relation. The numbers are used to indicate the relations in the remainder of this section.

Table 2.1: Relations between sediment loss mechanisms and agents.

		Agents		
		Flow	**Waves**	**Buoyancy**
Mechanisms	**Vertical diversion**	++ (1)	++ (2)	+ (3)
	Horizontal diversion	++ (4)	0 (5)	0 (6)
	Overwash	+ (7)	0 (8)	0 (9)
	Leakage	+ (10)	+ (11)	+ (12)

1. In case of external currents with a component perpendicular to the silt screen, the screen will start to act as a flexible baffle. Flow acceleration on the upstream side takes a major part of the suspended sediment with it. Deceleration and flow separation on the downstream side lead to a significant amount of turbulent mixing and an upward velocity component. This brings the sediment to a higher position in the water column and delays the settling process. Therefore it is an important process regarding the effectiveness of silt screens.
2. Wave-induced currents are known to have a narrow boundary layer, which leads to relatively high flow velocities near the bottom. The back and forth going character of the current leads, except for a possible residual, theoretically to zero transport. However, the presence of the silt screen makes a difference. The aforementioned flow separation will

also take place in case of wave-induced currents underneath the screen. The current pattern will not be exactly reversible anymore. This induces a nett transport. Generally silt screens are not applied in case of waves higher than about 0.5 m, but the related currents might still be significant. This becomes clear after a calculation of the order of magnitude of wave-induced currents near a silt screen. Under assumption of a water depth of 8 m and a 0.5 m swell wave with a period of 10 seconds, the velocity amplitude near the bottom according to linear wave theory (e.g. Holthuijsen, 2007) is about 0.26 m/s. This is the same order of magnitude as the maximum constant flow velocity at which silt screens can be applied.

3. The increase in density due to suspended sediment concentrations will typically be in the order of one promille. Nevertheless it will still be able to drive a current. The influence will probably only be really distinguishable in absence of external flow and waves, but the density difference will always contribute to the total flow pattern.

4. Due to the presence of a silt screen, a current will be diverted vertically as well as horizontally. The screen's geometry determines the distribution between those two mechanisms.

5. Wave-induced current does not induce a significant mass transport outside of the surf zone and away from any disturbing factors. Therefore it will not be able to transport fine sediment around the side edge of a silt screen.

6. If a part of the suspended fines ends up to the side of the screen, the concentration will be much lower than in the middle of the screen. Density effects are then negligible.

7. Rough flow conditions might be able to make water wash over the floats. As said before, regular silt screens will fail in such circumstances and will not be applied in first place.

8. Although in practice silt screens are never applied under wave conditions that are able to send water splashing over the floats, theoretically it might be the case. However, JBF Scientific Corporation (1978) proves that virtually no expected wave is able to swamp the floats.

9. As density currents take place at some distance below the free surface, overwash does not relate to this agent.

10. A current can find its way past a silt screen through the joint of two sections. When the joint is well-constructed this will not be a very strong effect.

11. The same can be said about wave-driven current. Due to the presence of the silt screen it is not perfectly reversible, but the narrow open spaces in a joint do not allow for much flow.

12. Density effects were said to be weak in case of a big gap near the bottom. In case of a smaller gap that is situated higher in the water column overpressures due to density effects are smaller. Therefore their influence is only marginal.

Silt screens are not really *preventing* the suspended fine sediment from spreading freely. They influence the way in which suspended sediment is presented to the surroundings. Sediment may get past the screen, as long as this contributes to quick settling. In principle suspended sediment is directed towards the bottom when it is transported by the contracting current. This leads to a shorter settling time. Turbulence and flow recovery downstream of the screen counteract this process. The intensity of the flow determines whether the silt screen still promotes settling. Figure 2.1 illustrates this schematically. When turbulence intensities are too low for significant turbulent mixing and the settling velocity can withstand the vertical velocity component, sediment will settle. In case sediment is forced to a position lower in the water column, the smaller

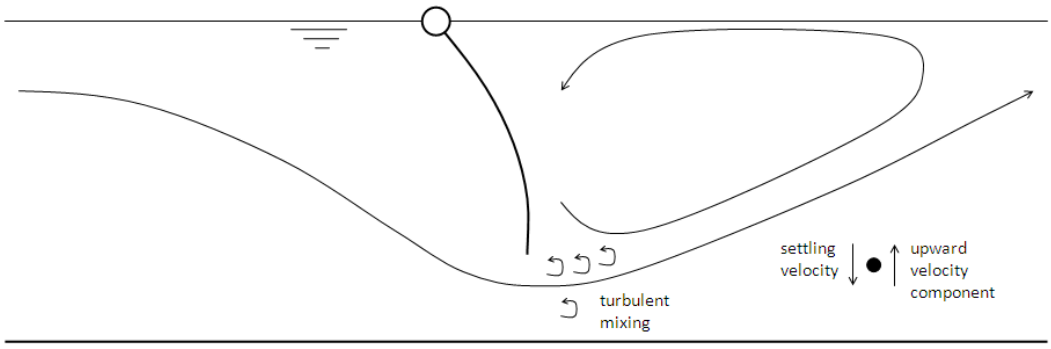

Figure 2.1: Processes regarding flow under a silt screen.

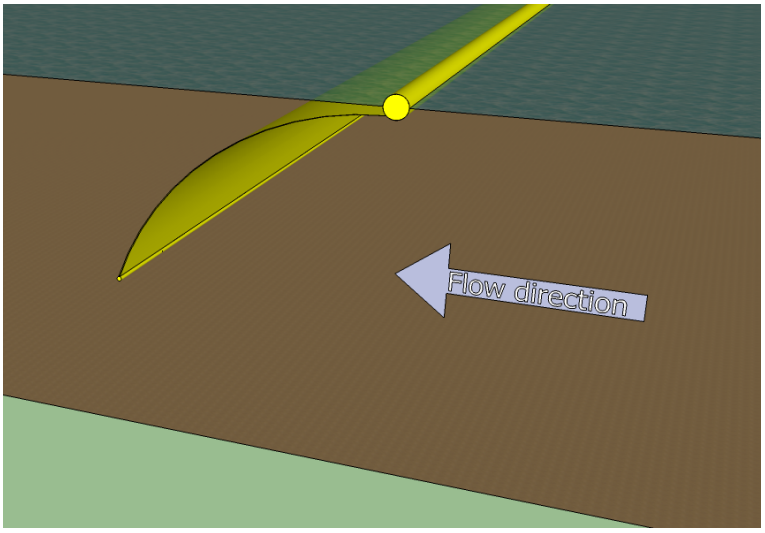

Figure 2.2: Silt screen deformed by a current.

settling time is not the only advantage. Fully developed tidal or river flow is known to have a logarithmic flow profile. Closer to the bottom the ability of the current to transport sediment is smaller. This will keep turbidity closer to the dredging site.

Two properties of the silt screen itself need to be addressed as well, being flexibility and permeability. Currents, waves and density differences lead to pressure differences between both sides of the screen. Eventually that results in deformation of the geotextile. These pressure differences will remain more or less constant under stationary conditions. The screen obtains a certain deformed shape and will stay that way until conditions change. Figure 2.2 schematically shows the way a silt screen will deform under influence of a current. Due to the deformation, the acceleration zone on the upstream side of the screen becomes more streamlined. This especially affects the current pattern upstream, but also downstream some influence will be noticeable. When the lower side of the silt screen is anchored, the deformation is of course limited within the clearance of the anchorage. However, from JBF Scientific Corporation (1978) it is known that anchoring the lower edge induces unacceptably large forces on the construction.

Silt screens are mostly made of geotextile. In theory this makes them permeable. However, the structure of the cloth is already very fine to guarantee sediment-tightness. Accumulation of sediment can result in a filter cake and marine growth might deteriorate permeability even further. On the whole it is known from Francingues and Palermo (2005) that water rather flows

around a silt screen than through it. This appears to be the path of least resistance.

2.1.2 Focus

Analyzing table 2.1, it becomes quite clear which processes are the most important regarding hanging silt screens in uniform cross flow. Vertical diversion due to flow and waves and horizontal diversion due to flow determine the effectiveness to a large extent. These three processes each require their own approach. All aspects related to vertical diversion happen in a vertical cross-section perpendicular to the silt screen. In modelling terms a 2DV approach suffices in that case. Despite the dimensional similarity, a stationary or quasi-stationary current behaves completely different from wave-induced current. Horizontal flow diversion requires the inclusion of both horizontal dimensions. In principle a 2DH approach is appropriate, but the current pattern associated with horizontal diversion might have a significant vertical component.

It is not feasible to include all three processes in this research. The differences that exist between them call for separate treatment. Wave-induced currents were said not to be perfectly reversible in the vicinity of a silt screen. Nevertheless the associated effect on suspended sediment still remains very local. The flow-related sediment loss mechanisms are capable of transporting sediment further away from the screen. Therefore the basic effectiveness of a silt screen is determined by these two flow-related processes. It becomes clear that assessing them should be the starting point of scientific research into the effectiveness of silt screens.

Besides its smaller importance, it is very difficult to investigate wave-induced currents near a silt screen. The flexibility of the screen and the degrees of freedom of the floats facilitate a nearly complete transmission of wave energy. Both aspects can not be accounted for in a regular numerical model. Very complex adjustments would be needed in that case. A physical model can represent both flexibility and movability. However, the current pattern of a wave depends heavily on the pressure distribution. A scale model will not have exactly the same proportions and properties as a real silt screen. Therefore it is questionable whether the pressure distribution can be reproduced satisfactory.

Vertical diversion will be studied most extensively, since doubts about silt screen performance are mostly related to this process. It depends on the specific application whether horizontal diversion is likely to happen, whereas vertical diversion will always take place in case of a hanging silt screen in cross flow.

Now the focus of the second research question will be determined. It consists of two parts, being adjustments to the large-scale application of silt screens and the small-scale design. As mentioned before, this topic will not be treated exhaustively. It is not aimed to optimise application and design. Yet they are included, because the tools used in this research offer a unique opportunity to study the effects of a number of promising adjustments along the way. When considering the large-scale application, silt screens are regarded as 2DH solutions influencing the horizontal velocity field. By small-scale design of silt screens, the cross-section is indicated. This is associated to regarding silt screens as a 2DV solution. The adjustments to be included in this research are systematically derived in appendix B. The following adjustments are considered promising (the codes stem from the appendix and are re-used later on in this report):

- 1a: Horizontal current diversion by deploying a silt screen obliquely with respect to the current (2DH)
- 1b: Horizontal current diversion by deploying silt screens in a V-shape (2DH)
- 2a: Promote settling due to decreased downstream turbulence by perforating the screen (2DV)
- 2b: Promote settling by extending the silt screen with a flap (2DV)

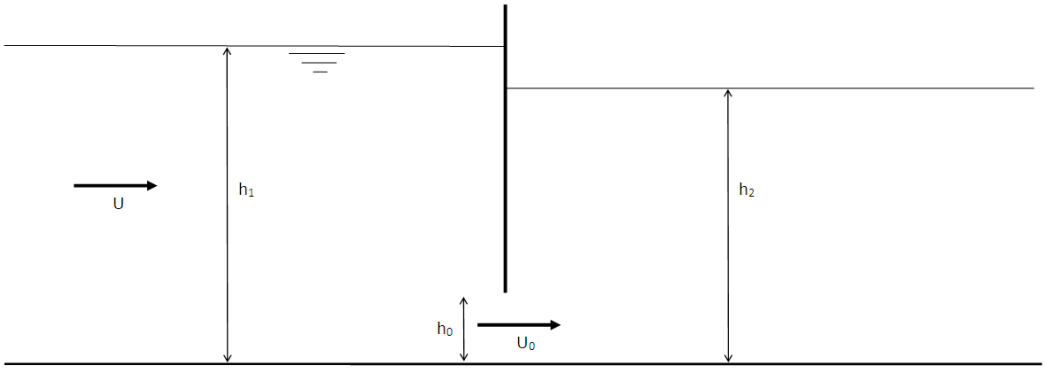

Figure 2.3: Basic geometry of 2DV flow under a baffle with all its relevant parameters.

- 3a: Extensive mixing by creating a gap between adjacent sections (2DH)
- 3b: Extensive mixing by creating a diffuser (2DH)
- 5: Halting by catching the plume in between two consecutive screens (2DV)

2.2 Flow-related phenomena

Flow is expected too be the most influential agent to the effectiveness of silt screens. It is capable of transporting suspended solids either by advection or diffusion. The presence of the screen leads to a significant increase of turbulence intensity. In this section the theoretical flow field around a silt screen is discussed, based on research by Vu and Tan (2010) and the simplified case of flow under a baffle. Appendix C contains general theory on turbulent flows (e.g. Pope, 2000).

2.2.1 Flow under a baffle

Silt screens can be thought to function as a baffle. Two-dimensional flow under a rigid vertical baffle is a popular academical case to researchers. A typical layout with its relevant parameters is given in figure 2.3. The mean underflow at the point of maximum contraction U_0 is equal to the specific discharge divided by h_0. Associated flow profiles still depend on the boundary conditions. The jet Froude number $Fr_j = U_0/\sqrt{gh_0}$ determines whether conditions are sub- or supercritical underneath the baffle. When $Fr_j > 1$ a free or submerged hydraulic jump occurs, depending on downstream water depth h_2 .

In case of a silt screen, upstream and downstream water depth h_1 and h_2 are approximately equal, since silt screens are never applied to regulate large-scale flow characteristics. The range of possible jet Froude numbers is computed based on some extreme values. Undisturbed mean flow velocity U varies between 0 and 0.5 m/s and water depth h varies between 2 and 10 m, corresponding with undisturbed Froude numbers of 0 to 0.1. Instead of h_0, the dimensionless relative baffle height $h_{rel} = 1 - h_0/h$ will be used. It varies between 0.25 and 0.75. Figure 2.4 shows that for $h_{rel} < 0.8$ and $Fr < 0.1$, which is generally the case, flow will stay subcritical. When h_{rel} and Fr are very big, theoretically supercritical flow might occur. However, for the case of silt screens some remarks have to be made. The screen is flexible, which allows for significant pressure transmission. Flow information can therefore not only travel through the narrow opening underneath the screen, but through the screen itself as well. Hence the real wave celerity in the jet will be bigger than $\sqrt{gh_0}$. Furthermore, for big values of h_{rel}, significant flaring will take place. This decreases Fr_j. On the whole it can be said that flow underneath a

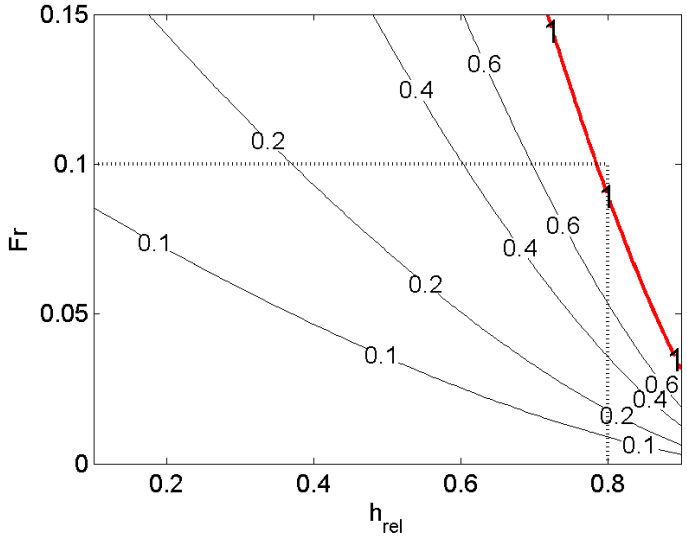

Figure 2.4: Contours of jet Froude number Fr_j as a function of undisturbed Froude number Fr and relative screen height h_{rel}. The red line indicates $Fr_j = 1$, corresponding to supercritical jet flow.

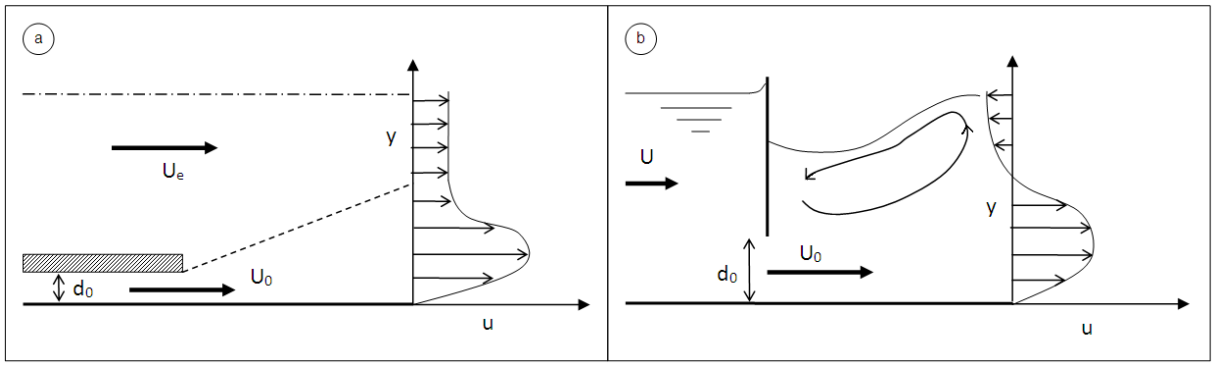

Figure 2.5: Basic geometry, parameters and downstream velocity profile of a wall jet (panel a) and a submerged hydraulic jump (panel b).

silt screen will always be subcritical.

Typical flow situations related to silt screens that have been analyzed extensively are the wall jet and the submerged hydraulic jump. They are schematically depicted in figure 2.5. The wall jet is thought to flow into an infinite halfspace and gradually spreads out. Eventually it results in fully developed wall flow with maximum velocity U_e (Launder and Rodi, 1983). A submerged jump might occur in case of a baffle. When conditions in the jet are supercritical and downstream water depth h_2 is higher than the critical depth due to some remote boundary condition, the hydraulic jump is located right next to the back wall of the baffle (e.g. Long et al., 1990). Both have some resemblance to the academical case of a rigid silt screen. However, the submerged jump is only present for supercritical jet flow. In case of an academical wall jet there is neither a closed boundary at the upstream side of the main flow nor a free surface. Therefore a wall jet will never have a zone of reversed flow. The prominent surface roller present in a submerged jump is governed by an abrupt change of flow regime, leading to more turbulence.

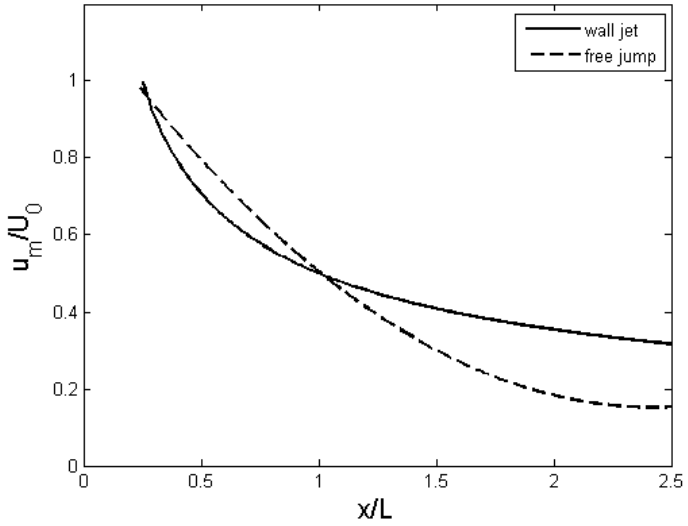

Figure 2.6: Velocity decay profile downstream of a baffle for both a free jump and a wall jet. Dimensionless maximum streamwise velocity at dimensionless downstream distance is depicted.

In case of subcritical jet flow and a back wall, reversed flow might be established due to an adverse pressure gradient. Continuity deflects the reversed flow to form a recirculation zone. This current pattern is still associated with a significant amount of velocity shear. Therefore it will lead to an increase of turbulence. In Wu and Rajaratnam (1995) the wall jet, free jump and submerged jump are assessed. From a self-similarity analysis of streamwise flow profiles it is concluded that the submerged jump forms the transition between a free jump and a wall jet. The velocity decay rate in streamwise direction was found to depend on Fr_j and the submergence factor S. The latter is equal to $(h_{co} - h_2)/h_2$, where h_{co} denotes the subcritical conjugate depth of the issuing supercritical jet flow. In general, the streamwise velocity decay profile will be wall jet-like for high values of S and free jump-like for low S. However, for low values of Fr_j, the profile stays free jump-like at much higher values of S than for high values of Fr_j. This relation has been established based on supercritical jets with jet Froude numbers down to 1.07. That is nearly critical. If the trend continues below $Fr_j = 1$, the velocity decay profile downstream of a silt screen is expected to be free jump-like. Figure 2.6 shows both types of profile in dimensionless form as found by Wu and Rajaratnam (1995). u_m is the maximum velocity in a vertical profile, x is the distance downstream of the jet opening and L is the value of x at which u_m has reduced to half of U_0. In a free jump, velocity decay rates are somewhat smoother than in a wall jet. Horizontal velocity decay corresponds to vertical expansion of the jet layer. The faster the expansion rate, the bigger vertical velocities will be. Hence vertical velocities are the lowest in a subcritical wall jet with bounded water depth, as is the case for a silt screen.

2.2.2 PIV measurements

Vu and Tan (2010) carried out laboratory experiments regarding silt screens. As a part of thorough research into silt screen effectiveness, the experiments aimed at investigating the flow field in the vicinity of a hanging silt screen. Amongst others, Particle Image Velocimetry (PIV) measurements were performed on a silt screen in both vertically fixed and loose configuration. Results of this whole-field measurement technique offer the opportunity to assess the flow in great detail. Turbulent structures down to the order of one centimeter can be recognised. The experiments largely confirm theoretical expectations. The time-averaged streamlines are

characterised by flow contraction upstream and flow separation including a recirculation zone downstream of the screen. The process of vortex shedding at the tip of the screen is visualised by successive pictures of the instantaneous flow field, see figure 2.7. These same pictures show that the theoretical, smooth recirculation zone is a time-averaged phenomenon. Instantaneously, a chaotic collection of turbulent eddies is present. This accounts for severe mixing. Time-averaged streamlines do not show this behaviour. When the screen is anchored in a vertical position, a small eddy is visible near the free surface on the upstream side. This eddy is absent when the tip is able to move freely. Apparently the deformed shape of a silt screen is not of very big importance, as the flow more or less streamlines itself by creating an upstream eddy.

2.3 Sediment-related phenomena

Eventually, research on silt screen effectiveness comes down to the behaviour of (fine) sediment around silt screens. Basic theory on the classification and morphodynamics of fine sediment is found in appendix D. Before any sediment-related phenomena are discussed, a possible misunderstanding has to be eliminated. The term 'silt screen' implies that only non-cohesive fine sediment is involved. Nevertheless, silt screens are applied under cohesive conditions as well. Dredging often takes place in a salty marine environment. Hence cohesive behaviour of sediment may not be neglected.

In this section, a qualitative assessment of suspended sediment behaviour in the theoretical flow field of section 2.2 is made, starting with a passive tracer. Step by step more elements are introduced: first the influence of the settling velocity is addressed and after that the influence of increased density is included.

2.3.1 Passive tracer in flow across a silt screen

First of all the behaviour of a passive tracer in the flow field of section 2.2 is discussed. The upper panel of figure 2.8 indicates three regions typically influencing transport of suspended material in case of flow across a silt screen. The lower panel visualises the behaviour of a passive cloud when subjected to these processes. In region 1 significant acceleration occurs. This brings along strong horizontal gradients of the streamwise velocity component. As the cloud reaches the gap it is compacted vertically by converging streamlines. In streamwise direction particles are thrust away from pursuing particles, thus dispersing the cloud horizontally. In region 2, the sudden vertical expansion leads to separation, large velocity shear and reversed flow. This is associated with high turbulence intensities and a corresponding increase in turbulent diffusion. The area of the cloud subjected to vertical mixing has been increased by dispersion in region 1. Particles are entrained into the recirculation zone, but the cloud is also spread out over the full depth of the near-bed jet flow. As a result of these diffusive processes, concentrations decrease rapidly. Region 3 is characterised by deceleration and gradual vertical expansion of the main flow. Dispersion takes place in vertical direction. The cloud was spread vertically over the jet flow, which expands to the full water depth now. Altogether the presence of the silt screen thus increases mixing effectiveness. A strong decay of concentrations in the main flow is expected in case of a passive tracer. Initial dispersion facilitates enhanced turbulent diffusion. In figure 2.8, concentrations of dissolved matter outside the main cloud were not mentioned. Large-scale turbulent structures rip off parts of the cloud, which end up in the recirculation zone. There they get diffused further. Gradually dissolved matter re-enters the main flow and is advected away from the silt screen.

In practice, suspended sediment spoiled at dredging and reclamation sites does not necessarily occur as a discrete cloud. It might also be of a continuous nature. This does not change the processes described above. The only difference is the simultaneous occurrence of all processes. So while some suspended matter has already entrained into the recirculation zone, another part

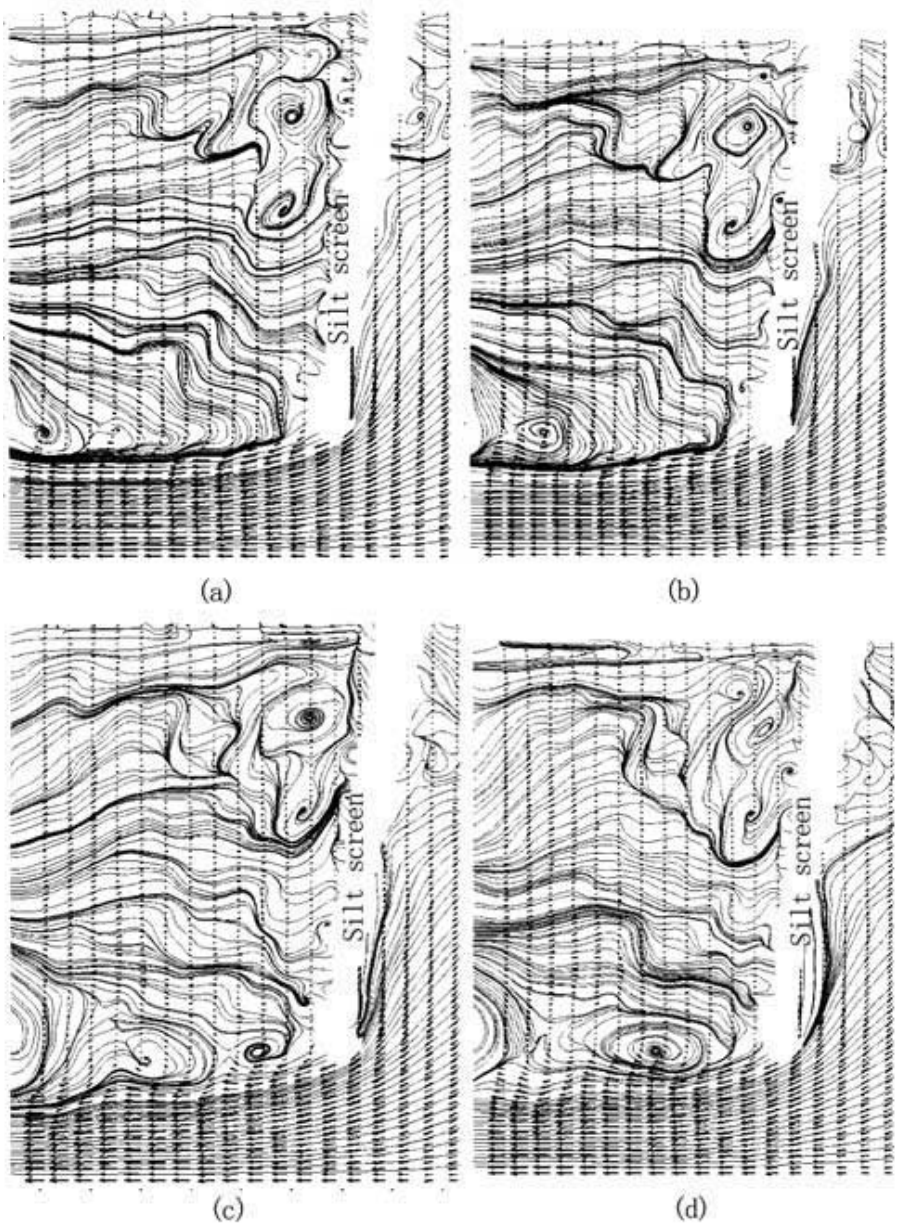

Figure 2.7: Four successive instantaneous flow fields resulting from PIV measurements by Vu and Tan (2010) at t = 17.33 s (a), t = 17.53 s (b), t = 18 s (c) and t = 18.33 s (d).

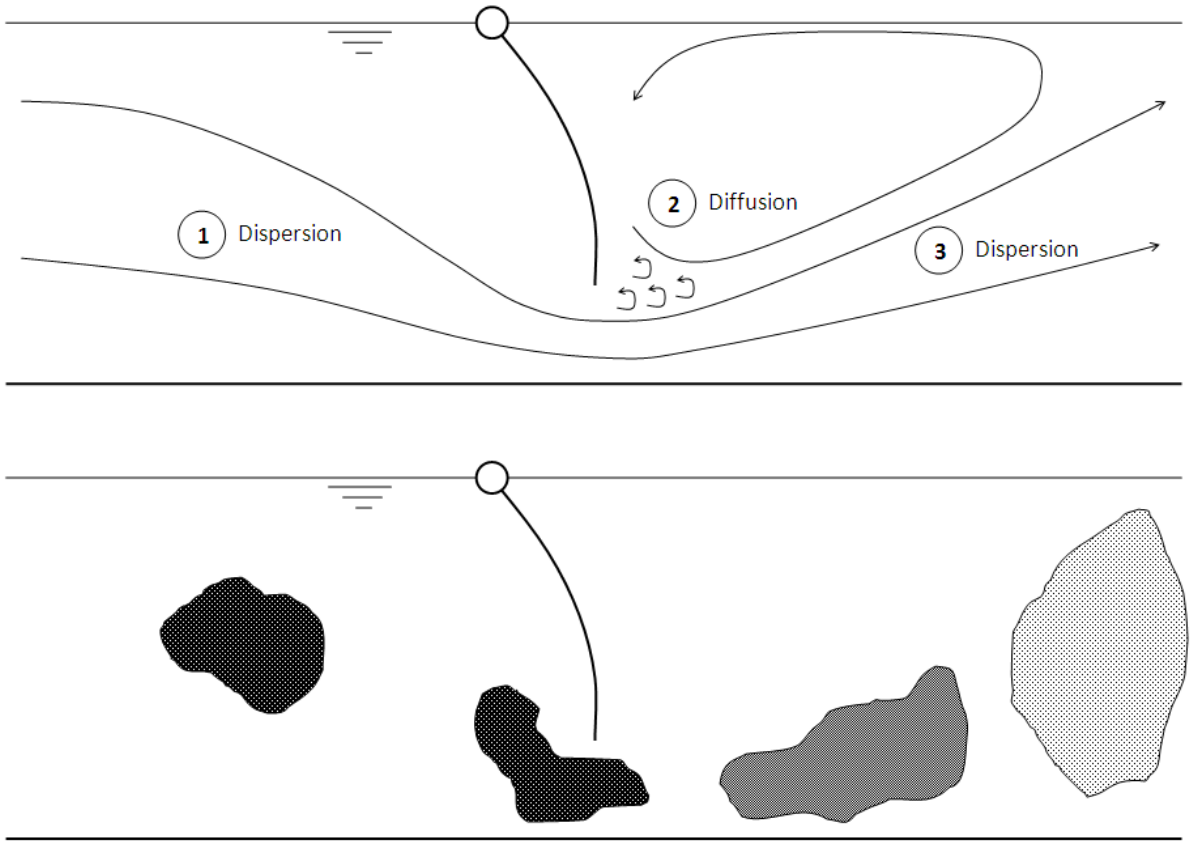

Figure 2.8: Upper panel: Transport processes in different regions of flow across a silt screen. Lower panel: transport of an initial cloud of passive material. Note how a silt screen 'stretches' the cloud as a result of dispersion, which increases the surface subjected to turbulent diffusion.

of the plume is just arriving in the jet flow. As a result turbidity levels will often be more or less equal throughout the whole water column, but it is important to be aware of the underlying processes.

2.3.2 Influence of the settling velocity

Now another element is introduced. The previous section discussed suspended sediment as a passive tracer. Now a settling velocity is introduced to account for the effect of gravity on the grains or flocs. Fine sediment is known to have a small settling velocity. Even in still and shallow water, settling times can be in the order of days. On short timescales and relatively large spatial scales, as is the case for flow across a silt screen, suspended fine sediment nearly behaves as a passive tracer.

Silt screens might be effective in drastically reducing concentrations because of two possible, favourable effects: promoting spreading or settling. The aforementioned considerations regarding settling velocity would rule out the latter, being 50% of the whole potential of silt screens. In three situations a silt screen might still promote settling of suspended sediment:

1. Upward current velocities (w) and turbulent shear stresses downstream of the silt screen are small due to very calm flow conditions. Relatively big silt grains in the order of 63 µm might still be able to settle.

2. The suspended sediment is cohesive. In salt water flocculation of cohesive sediment will be promoted. The flocs have an increased settling velocity and are therefore able to withstand upward flow velocities to a larger extent.

3. Concentrations of suspended sediment are high enough to induce density effects. The dense layer stays close to the bottom. Furthermore, stratification is able to reduce the influence of turbulent mixing.

Situation 2 and 3 lead to a substantial increase of w_s. However, they only occur in case of certain specific circumstances. Section 2.3.3 elaborates on the influence of density effects.

The influence of the settling velocity can be expressed by evaluating the dimensionless parameter w_s/w. Any dependency of w_s on different parameters is left out of consideration here, as this dependency differs for cohesive and non-cohesive sediment. The vertical flow velocity w depends approximately linearly on the horizontal flow velocity u downstream of the silt screen. u in turn varies with relative screen height h_{rel} and upstream depth-averaged flow velocity U. The relation between the average issuing jet velocity U_0 and h_{rel} is straightforward when screen deformation is neglected. In that case, U_0 is proportional to $1/(1-h_{rel})$. Far downstream of the screen, the logarithmic flow profile is restored and there is no relation anymore between u and h_{rel}. Between the screen and the point where the flow has recovered, the influence of h_{rel} gradually diminishes. The aforementioned proportionality between u and h_{rel} thus represents an upper limit of the influence of h_{rel}. Finally, it is readily seen that u is approximately proportional to the upstream depth-averaged flow velocity U. These proportionalities are summarised and elaborated upon in equation 2.1

$$\begin{aligned} & w_s && \rightarrow \frac{w_s}{w} \propto w_s \\ & w \propto \frac{1}{1-h_{rel}} && \rightarrow \frac{w_s}{w} \propto 1-h_{rel} \\ & w \propto U && \rightarrow \frac{w_s}{w} \propto \frac{1}{U} \end{aligned} \tag{2.1}$$

The potential of all three parameters only becomes clear after the range of possible values has been addressed. This is done in table 2.2. The last column is governed by the ratio of maximum

and minimum dimensionless settling velocity given the extreme parameter values.

Table 2.2: Potential of relevant parameters to influence the dimensionless settling velocity.

Parameter	**Proportionality**	**Range**	**Potential**
U	U^{-1}	$0.01 - 0.3$ m/s	30
h_{rel}	$1 - h_{rel}$	$0.25 - 0.75$	3
w_s	w_s	$0.001 - 3$ mm/s	1000

Given the big potential of w_s to influence the dimensionless settling velocity and hence the effectiveness of silt screens, settling velocities of fine sediment can not be neglected beforehand. Settling velocities of the bigger particles or flocs might well be able to counteract vertical flow velocities, especially under calm conditions.

2.3.3 Density effects

At sufficiently high SSC, the flow field can no longer be detached from the transport field. High concentrations of suspended sediment significantly affect the fluid's effective density, which might give rise to stratification. In that case, the density difference drives a turbidity current along the bed. Flow velocities in this dense layer differ largely from the theoretical flow field as derived in section 2.2. Exact concentrations at which stratification comes into play can not be found, but Winterwerp (1999) has identified the following stages for suspended fine sediment:

- *Low-concentrated mud suspension* is found at concentrations ranging from several 10 - 100 mg/l. Density differences do not play a significant role.
- *High-concentrated mud suspension (HCMS)* has concentrations between several 100 - 1000 mg/l. HCMS is transported with the main flow, but it is capable of influencing the fluid's effective viscosity and therefore interacts with the turbulent flow field.
- *Fluid mud* occurs at concentrations between a few 10 - 100 g/l. A near-bed layer of dense fluid is found. In case of dredging-induced SSC this layer is mobile and forms a turbidity current.

The specific properties of HCMS will not be taken into account here. Its effects are lumped in the settling velocity, which will be varied over several orders of magnitude throughout this research. The next section will elucidate whether stratification may be expected near a specific dredging site. Here the behaviour of turbidity currents in the vicinity of a silt screen is discussed.

At the interface between two layers of different density and with different flow velocities, exchange of fluid will take place due to breaking internal waves (Turner, 1973). This process is called entrainment. Entrainment leads to a less sharp interface with a smooth vertical density gradient over some height. The bigger the entrainment rate, the higher this transition between both layers will be. When turbulence is only generated by wall friction, the consequences of entrainment will be limited. The source of turbulence is located in the near-bottom layer. As the density difference tends to damp turbulent fluctuations, suspended transport of entrained sediment in the upper layer will be negligible. However, silt screens are a source of free turbulence, which may lead to significant turbulence and hence turbidity in the upper layer. This is a negative effect of silt screens on stratified SSC.

Computing the intensity of entrainment has been subject to discussion in literature, since some time-averaged expression has to be brought up to describe the complex interfacial instabilities causing entrainment. The starting point of all these different views is the same. The

entrainment rate is taken proportional to some characteristic velocity, which is often defined as the difference in horizontal layer-averaged velocity between both layers. Whether a silt screen magnifies or reduces this velocity difference will only become clear after numerical simulations, which are presented in chapter 4.

2.4 Spreading of dredging spills

Currents and sediment transport near silt screens can not be regarded completely separated from the source of turbidity. The latter determines the upstream vertical profile of suspended sediment concentrations. Not only does the position of a suspended particle in the water column determine where it will end up downstream of the screen, but high concentrations can also induce density effects. Whether a density-driven current occurs, is determined by upstream processes. To start with, sediment spills may be caused by a variety of possible dredging operations, all bringing along their own type of spreading. Furthermore, the influence of density differences might change during transport of the suspended sediment. These two aspects are now discussed successively. Finally, the implications for the flow and concentration profiles arriving at the silt screen are discussed.

2.4.1 Types of dredging spills

The various potential sources of turbidity (see section 1.1 for an overview) all have a different way of directing sediment into the water column. Genarally silt screens are applied as a mitigating measure near the placement site, near relatively small dredging areas and in case of overflowing. Spreading of turbidity in each of these three cases will be discussed below.

During placement, the released mixture may contain a wide gradation of sediment. The coarser grains will, as intended, settle onto the bed quickly. Only the finer particles will get transported out of the dedicated placement area. Below, specific spreading mechanisms of all placement techniques are listed. All placement methods can be classified by the relative importance of mixing-dominated spreading and density-driven spreading.

- *Rainbowing* spreads the discharged material over a large surface. The mixture will mix easily with the surrounding water. Therefore, density differences are too low to form a buoyant plume. Coarse grains settle quickly and fine particles are transported by mixing processes.

- *Pumping ashore* causes a current of dense material to enter the water column on top of the reclamation's side slope. Given the significant angle of inclination, sediment is likely to form a turbidity current down the slope.

- Placement by means of a *spreader pontoon* causes a high-density mixture to enter the water column near the free surface. When all grains present in the discharge would behave as individual particles, coarse and fine sediment would split immediately as a result of differential settling. However, the high concentrations of suspended sediment issuing from the suppletion pipe give rise to mutual influencing of particles. Particles might get pulled into the wake of another particle (cloud formation), but they might also slow down due to the return current of another particle (Winterwerp, 1999). As a result, only a part of the fine sediment will gradually get washed out of the discharge, leading to turbidity over the full water column. The remaining part is expected to descent rapidly within the plume. Upon impingement on the bottom, an axisymmetric turbidity current will be created.

- In case of *direct disposal* through bottom doors, the processes which were presented for a spreader pontoon will occur as well. However, when a hopper is emptied through a pipeline, transport water is added to fluidise the sediment. This is not needed for direct disposal, so concentrations will be higher and the processes involved in hindered settling will be stronger. More fine sediment is expected to reach the bottom quickly and spread as a turbidity current.

- *Reversed pumping via the suction pipe* leads to a near-bed discharge of high-concentrated suspension. Fine sediment is likely to spread as a turbidity current.

In terms of section 1.1, spreading near small-sized dredging areas involves the stages of dislodging and vertical transport. Silt screens near dredging sites are only considered cost-effective when the area is small. This is often the case when working with mechanical dredgers. Both dislodging and vertical transport in an open container will dispose low concentrations of suspended sediment throughout the water column. Hence, buoyancy will most likely not play a role.

Overflowing induces a negatively buoyant jet of suspended sediment, issuing at the free surface. The overflow plume solely contains fine particles, as disposing fines is the main purpose of overflowing. Depending on case-specific circumstances, the jet flow either sinks down to the bottom and forms an axisymmetric turbidity current upon impingement or mixes with the surrounding water before reaching the bed.

In summary, all dredging spills can be classified as one of the following types:

- A diffusive spill, being advected and diffused by ambient flow.

- A near-bed discharge of negative buoyancy.

- A near-surface discharge of negative buoyancy at some distance from any closed boundary.

- A near-surface discharge on top of a slope.

Based on these types, the diagram of figure 2.9 can be constructed. It shows all possible ways a dredging spill can develop into the upstream boundary condition arriving at a silt screen. In the diagram, at two positions a buoyancy criterion is mentioned. Further development of the spill depends on evaluation of this criterion, which is elaborated upon in the next section.

2.4.2 Buoyancy criterion

In dredging plume research two different scopes are distinguished, being near-field and far-field. Near-field spreading is typically associated with the density-driven (also referred to as *dynamic*) development of a plume directly upon release of sediment particles into the water column. The large-scale, mixing-dominated (*passive*) spreading of suspended sediment belongs to the far-field. Silt screens are often applied at the edge of near-field and far-field, which is the reason why two different types of upstream boundary condition were assessed in section 2.3. The buoyancy criterion mentioned in figure 2.9 differentiates between dynamic or passive propagation. First, the general form of this criterion is introduced. Then, this general form is applied to the specific cases of near-surface discharge, a propagating turbidity current and discharge on top of a slope.

The criterion we are looking for should evaluate the relative importance of buoyancy-promoting and buoyancy-destroying forces. The Richardson number expresses this ratio (e.g. Turner, 1973) and can be used as a criterion in this research. In literature, different forms of the Richardson

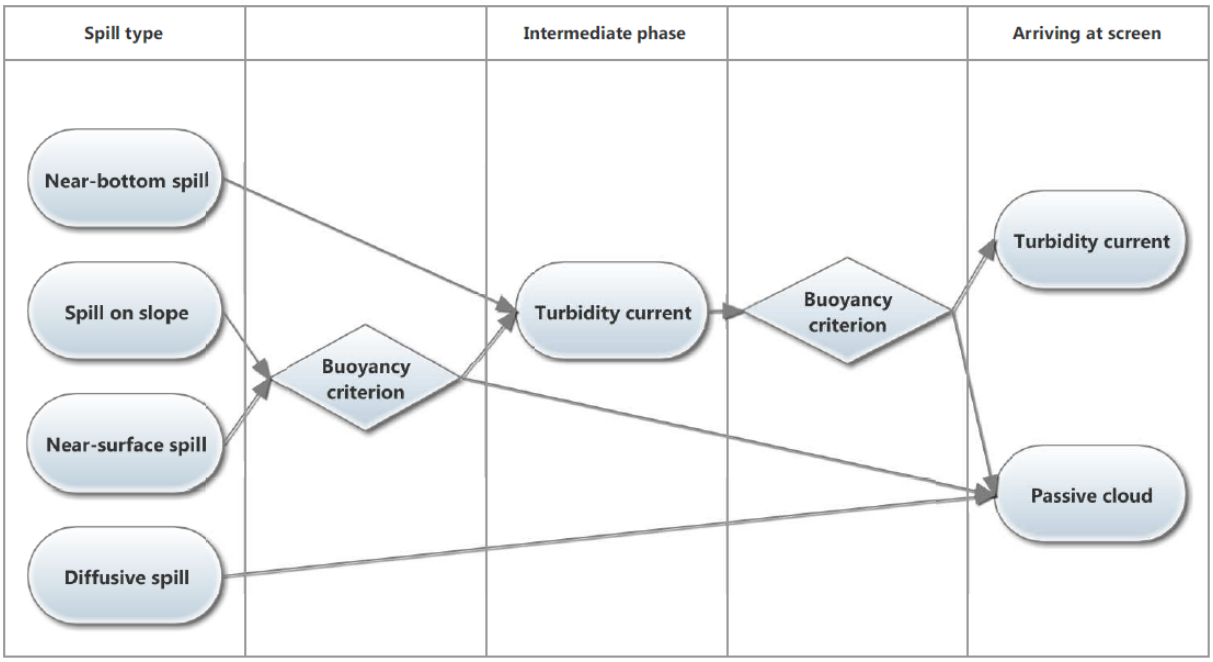

Figure 2.9: Diagram showing the possible developments from dredging spill to upstream boundary condition near a silt screen.

number are encountered. The most fundamental form is generally referred to as the gradient Richardson number Ri, see equation 2.2.

$$Ri = \frac{-g\frac{\partial \rho}{\partial z}}{\rho(\frac{\partial u}{\partial z})^2} \tag{2.2}$$

In most cases, Ri can be simplified. When dealing with steady flow, adhering to the Boussinesq and hydrostatic assumptions, the type of flow can be classified by means of the bulk Richardson number Ri_0, which is defined by equation 2.3.

$$Ri_0 = \frac{g'\mathcal{L}}{\mathcal{U}^2} = \frac{\frac{\rho'}{\rho_0}g\mathcal{L}}{\mathcal{U}^2} \tag{2.3}$$

Here, g' denotes the reduced gravitational constant, ρ' is the density difference governing the specific flow situation and ρ_0 is the reference density which characterises the ambient fluid. The characteristic length- and velocity-scales are derived from the boundary conditions.

Uniform transitional values of Ri and Ri_0 cannot be given. For Ri, analytical analysis proves that the transitional value depends on the wave-number(s) of instabilities at the density-interface and the presence of a rigid boundary (Turner, 1973). Regardless of these parameters, the analytical upper limit of the transitional value is 0.25. When Ri is higher than 0.25, buoyancy dominates mixing and stratification is stable. However, counter examples of initially turbulent flows remaining turbulent above $Ri = 0.25$ have been found. When using Ri_0, the definition of $\mathcal{L}$ and $\mathcal{U}$ are subject to debate, which obstructs the use of a general transitional value. Mostly, transitional values are derived from case-specific research. A literature review regarding the aforementioned types of dredging spills will be presented in the remainder of this section.

Near-surfacial discharges are a well-studied topic within the field of overflow plume research. Basic theory on plumes is found in e.g. Turner (1973) and Fischer et al. (1979). Field observations of physical processes in actual dredging plumes were reported in a qualitative sense

Figure 2.10: Characteristic pictures of both types of overflow plume spreading: mixing (left picture) and density-driven (right picture), Boot (2000).

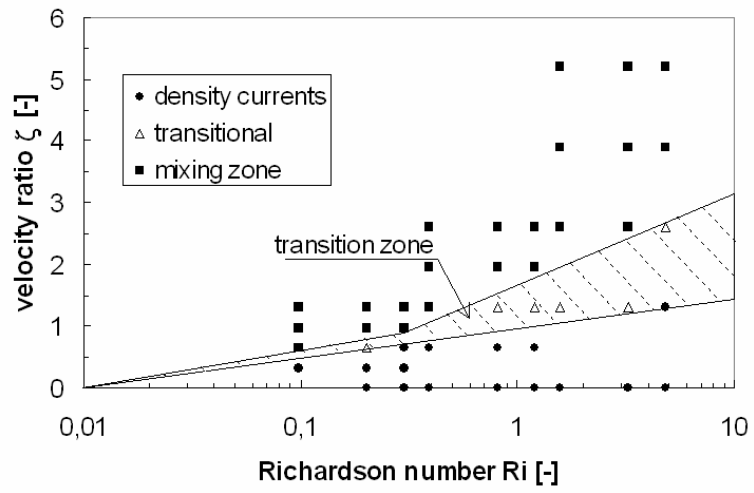

Figure 2.11: Classification of near-field overflow plume spreading (Winterwerp, 2002). Spreading is either mixing-dominated or density-driven, depending on a combination of the bulk Richardson number (horizontal axis) and a velocity ratio (vertical axis).

by Thevenot et al. (1992). Van der Salm (1998) produced the first of a still ongoing series of scientific reports on the spreading of overflow plumes. He addressed near-field as well as far-field processes and identified many possibilities for further research. Boot (2000) mainly investigated the transition between mixing-dominated and density-driven spreading of overflow plumes. His results in this field were recapitulated by Winterwerp (2002). Figure 2.10 shows examples of mixing-dominated (left picture) and density-driven (right picture) spreading. They discerned between both types of spreading based on the bulk Richardson number and the ratio between initial vertical velocity of the plume and ambient flow velocity (ζ), see equation 2.4.

$$Ri_0 = \frac{g' D_p}{W^2} \tag{2.4a}$$

$$\zeta = \frac{U}{W} \tag{2.4b}$$

D_p denotes the overflow pipe diameter, which equals the initial plume diameter, W is the vertical outflow velocity and U is the ambient horizontal depth-averaged flow velocity. Boot and Winterwerp caught their results in a diagram, which is shown in figure 2.11.

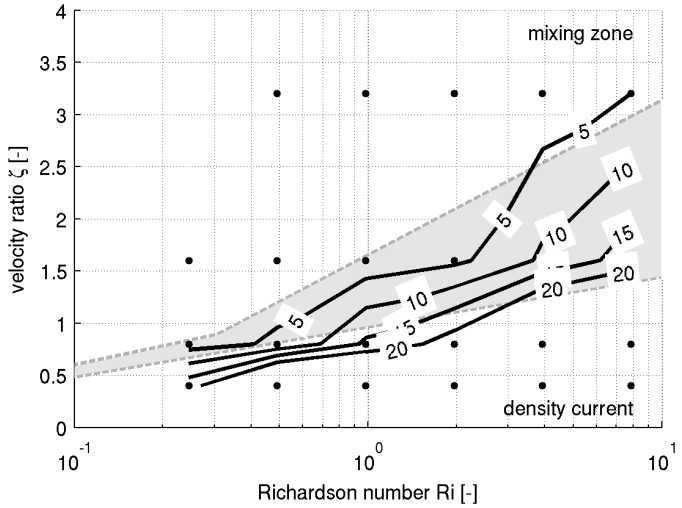

Figure 2.12: Extension of overflow plume classification by De Wit (2010). The contours indicate the transition between mixing-dominated and density-driven spreading for different water depths. The water depth is expressed as a multiple of the overflow pipe diameter D_p.

During the actual experiments, which were carried out by Boot, the water depth was kept constant at 8 times the initial overflow plume width. The type of spreading was determined right before suspended sediment reached the bottom. De Wit (2010) elaborated on this by carrying out numerical model runs with infinite water depth. The depth at which spreading of different overflow plumes shifted from initially density-driven towards mixing was documented for plumes of varying Ri_0. De Wit extended the diagram of figure 2.11 and added transition depth contours, see figure 2.12. Within the scope of boundary conditions for silt screens, especially the horizontal transition distance is a parameter of interest. Generally, interaction between plume and bed will occur prior to arrival at the silt screen. This interferes with the concept of transitional depth as investigated by De Wit.

When a density-driven plume impinges on the bed, its momentum starts to drive a radial turbidity current. Its initial height can be derived from a mass balance. Let B_b be the plume width prior to impingement, W_b the associated downward mean plume velocity, U_f the horizontal velocity of the turbidity current's front right after impingement and h_f the height of this front. Assuming that within the impingement zone sediment concentrations remain constant, the mass balance is given by equation 2.5.

$$\frac{1}{4}\pi B_b^2 W_b = 2\pi B_b h_f U_f \tag{2.5}$$

Horizontal front velocity U_f is related to h_f according to equation 2.6, where Fr is the Froude number (Bonnecaze et al., 1993). This depends on the ratio of h_f over total water depth h.

$$\begin{aligned} U_f &= Fr\sqrt{g' h_f} && (2.6)\\ Fr &= 1.19 && \text{for } 0 < \frac{h_f}{h} \leq 0.075\\ Fr &= 0.5\left(\frac{h_f}{h}\right)^{-\frac{1}{3}} && \text{for } 0.075 < \frac{h_f}{h} < 1 \end{aligned}$$

After elimination of U_f from equation 2.5 by means of equation 2.6, the initial height can be calculated iteratively. Further propagation of a radial turbidity current will be discussed below, together with the associated buoyancy criterion.

A remark has to be made regarding dynamic plumes. Even a dynamic plume will cause sediment to mix with ambient water. During the descent of a density-driven plume, some material near the plume's edge is removed by ambient currents. This process, commonly known as 'stripping', was qualitatively described by Thevenot et al. (1992). Based on literature study, Van der Salm (1998) states that about 3 to 5% of all plume material is stripped. Spreading of this stripped material is mixing-dominated due to its low concentrations. This leads to turbidity throughout the whole water column.

In case of a propagating turbidity current, whether or not radial, a characteristic length and velocity scale are readily found in the height of the current and its horizontal velocity. This is expressed by equation 2.7.

$$Ri_0 = \frac{g' h_t}{U_t^2} \tag{2.7}$$

According to Turner (1973), transitional values for Ri_0 are found between 0.1 and 0.3. Although the buoyancy criterion is straightforward, it remains very difficult to calculate the height and propagation velocity as a function of place and time for any turbidity current (Bonnecaze et al., 1993). The processes of bed-current interaction and entrainment of ambient water are difficult to parameterise. Non-continuous or radial turbidity currents and ambient currents, as is often the case in dredging practice, add up to that complexity (Bonnecaze et al., 1995; Hallworth et al., 1998). Therefore, it is unavoidable to apply numerical model simulations when the development of turbidity currents has to be predicted. To this end, yet to be published TASS software (Spearman et al., 2011) might be of great help.

Finally, discharges on top of a slope are discussed. A bottom slope adds kinetic energy to a propagating turbidity current, but it also reduces the component of gravity perpendicular to the density interface. The former increases the denominator of Ri_0, whereas the latter decreases its numerator. Therefore, downslope turbidity currents will be less stable and mix more easily with ambient water. Ri_0 is defined by equation 2.8 for this case (Turner, 1973). The bottom slope is denoted by ϕ.

$$Ri_0 = \frac{g' \cos\phi h_t}{U_t^2} \tag{2.8}$$

The transition to mixing behaviour of turbidity currents along an incline has not been studied thoroughly. Turner (1973), Simpson (1987) and Noh and Fernando (1991) only discuss the initial or steady phase of turbidity current development. Nevertheless, it is expected that a transition to mixing behaviour will not be achieved in dredging practice, as side slopes of a reclamation area are of restricted length. After having descended to a more horizontal part of the bed, the turbidity current can again be analysed by means of numerical simulation.

2.4.3 Concentration profile

One goal of the preceding considerations in this section is to determine the vertical concentration profile upstream of a silt screen. It is evident that the upstream concentration profile influences silt screen effectiveness to a great extent, as the transport capacity of the flow differs in space.

Concentration profiles may take any possible shape, depending completely on the boundary conditions. This research focuses mainly on passive concentrations, as silt screens in cross flow are usually intended to mitigate the passive part of a dredging spill. If the source of suspended sediment is located far upstream and the flow is given enough time to redistribute concentrations, an equilibrium profile will arise. When this is the case, there exists a balance between the upward sediment flux through bed erosion and turbulent diffusion and the downward flux through settling and deposition. For non-cohesive sediment, erosion and deposition fluxes remain more

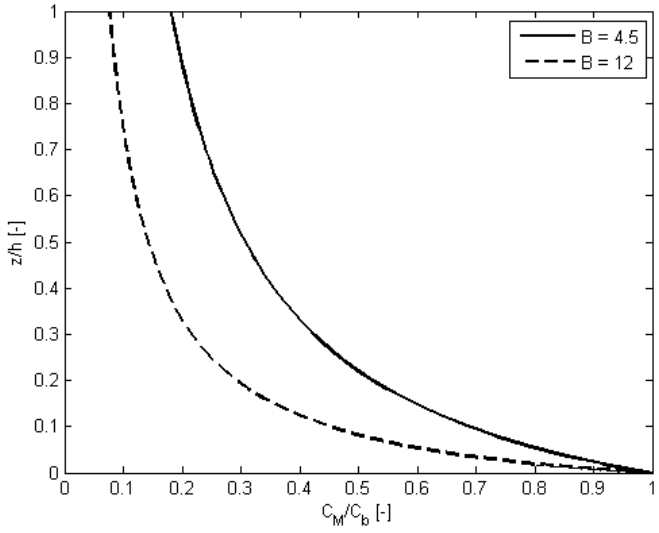

Figure 2.13: Empirical equilibrium concentration profile for cohesive sediment. The profile has only been verified for ensemble averaged data.

or less constant in stationary flow conditions. Provided that hindered settling does not play a role, this gives rise to the well-known Rouse profile.

In case of cohesive sediment, settling velocities depend on the concentration and therefore change with depth. Furthermore settling velocities are generally much smaller, which leads to a more uniform vertical distribution and a bigger dependency on flow conditions. The latter makes it difficult to predict a cohesive sediment concentration profile in a specific situation. Only through ensemble averaging it is possible to fit a parameterised profile to empirical data (Whitehouse et al., 2000). Equation 2.9 shows a dimensionless form of this empirical profile.

$$\begin{aligned} \frac{C}{C_0} &= \left(1 + B\frac{z}{h}\right)^{-\frac{1}{m}} \\ \text{with } B &= \frac{m w_{s50b}}{0.0025U} \\ w_{s50b} &= k C_0^m \end{aligned} \tag{2.9}$$

Here, C_0 is the near-bed suspended sediment mass concentration and the coefficient m is the same as the one in the simplified relation for cohesive settling velocity (equation D.4). Figure 2.13 shows two examples of this concentration profile for $B = 4.5$ and $B = 12$.

As this empirical equilibrium profile can only be found by means of ensemble averaging, it does not provide much information about individual cases. Apart from that, the concentration profile arriving upstream of a silt screen will rarely be in equilibrium. It will often depend on a combination of the spill type and local flow conditions. Therefore the upstream concentration profile will have to be varied throughout this research. Typical, schematised profiles will be used to that purpose.

2.5 Quantification of silt screen effectiveness

In order to judge any case study or model outcome in terms of silt screen effectiveness, appropriate definitions are necessary. A new approach on the quantification of silt screen effectiveness was already proposed in chapter 1. Effectiveness was said to depend on two parameters, being

(1) the product of (time-averaged) SSC and z-coordinate and (2) the vertical position of the visible turbidity limit in the water column. The former can be determined from the simulation results straightforwardly. In the remainder of this section the appropriate relation between $\bar{C}$ and z will be elaborated upon. The lack of an exact relation between turbidity and SSC impedes computation of the latter. Many different attempts of researchers to establish this relationship have resulted in so many different equations. As the product of concentration and z-coordinate assigns the highest weight to near-surface concentrations, the special disadvantage of surfacial turbidity is still incorporated indirectly.

The aforementioned product of $\overline{C}$ and z can be regarded as a measure constituting environmental impact potential. Here it is investigated whether this is a correct definition. The environmental impact of SSC can be addressed in four different ways, see table 2.3.

Table 2.3: Different views at the environmental impact potential of SSC.

		Environmental impact	
		Shading	**Burial**
Scientific field	**Physics**	• Absorption of light • Scatter	• Settling • Range of attack
	Ecology	• Stress-level of flora & fauna	• Stress-level of flora & fauna

Shading and burial of benthic species are the two main categories of environmental impact (Bray, 2008). For both aspects, two stages can be recognised in determining the impact of SSC on the environment. The presence of sediment particles in the water column invokes several physical processes, which in turn can be translated to environmental impact by means of ecological arguments.

The aspect of shading will be treated first. As light travels through a medium, its electromagnetic energy gradually gets absorbed. This is represented by the Lambert-Beer law, which prescribes the relative intensity (percentage of incoming intensity I_0, also called transmissivity) of a light beam as a function of the distance travelled ℓ. For liquids, the law is usually presented as in equation 2.10.

$$\frac{I}{I_0} = 10^{-a\ell} \tag{2.10}$$

Here, I is the intensity after a distance ℓ and a is the absorption coefficient. The presence of dissolved matter can be accounted for by adjusting a. The original form of the Lambert-Beer law only holds for monochromatic light (consisting of one single wavelength) with parallel rays in non-turbid waters. This excludes application to natural waters, as sunlight is neither monochromatic nor parallel and suspended particles in the water create turbidity. The light attenuating effect of suspended particles lies in the fact that they reflect light beams hence and forth, which is usually indicated as scatter. By doing so, the distance a light beam has to travel in order to reach a certain depth is extended. Hence more energy gets absorbed over each unit of depth, leading to a lower transmissivity. Kirk (1977) showed that the attenuation of light in

natural waters may simply be represented by a relation similar to the Lambert-Beer law, but with a much higher absorption coefficient which increases linearly with SSC.

The conversion of light intensity or transmissivity to environmental impact is much harder to establish. Ecology is not an exact science. It was briefly noted in chapter 1 that the response of species to shading and burial differs from site to site, depending on local background conditions. Nevertheless, species undergo stress from turbidity levels that have risen above the background level. Erftemeijer et al. (2012) admit that *there is still a rather poor understanding of the relationship between sediment stress and the response of most corals.* Following a literature review involving 90 case studies, they have categorised corals of different sensitivity according to the occurring suspended sediment concentrations and the observed impact. This has resulted in the upper panel of figure 2.14. It shows over which range of SSC a certain impact has been found given the coral's sensitivity to shading. Erftemeijer et al. (2012) distinguish the following categories of impact:

- No effect
- Minor sub-lethal effects (e.g. reduced growth, mucus production[1])
- Major sub-lethal effects (e.g. bleaching[2], tissue damage)
- Minor lethal effects (partial mortality)
- Major lethal effects (mass mortality)

The upper panel of figure 2.14 shows that the environmental impact aggravates more or less linearly with SSC given a certain sensitivity. This conclusion only holds for corals, but comparable studies on different species are scarce. For example, a similar literature review for sea grass meadows by Erftemeijer and Robin Lewis (2006) contains no details on the relation between sub-lethal effects and SSC. Furthermore, corals are one of the main reasons why the application of silt screens is demanded near dredging projects. Hence the use of a linear relation between the to be defined environmental impact potential and $\overline{C}$ is considered justified for shading.

Burial was named as the second hazardous impact of SSC on the environment. In physical terms, the amount of sedimentation depends on the near-bed vertical flux of suspended sediment. The higher a sediment particle is located in the water column, the longer its settling time will be. A longer settling time in turn leads to a larger horizontal distance over which the particle is expected to be advected by the current. The characteristic settling distance x_s ('range of attack') can be defined following equation 2.11.

$$x_s = \frac{Uz}{w_s} \tag{2.11}$$

The amount of sedimentation at distance x_s downstream of the reference location will be proportional to $\overline{C}x_s$. As U and w_s are background parameters which also hold when a silt screen is absent, they can be left out of consideration. Hence the product of $\overline{C}$ and z serves as an appropriate measure for the extent of sedimentation.

The aforementioned research by Erftemeijer et al. (2012) also takes into account the hazardous effects to corals of burial. The lower panel of figure 2.14 summarises the results of 102

[1] Many corals produce a certain amount of mucus. Under sediment stress the production of mucus increases. As a result, the coral consumes more energy than it produces. High SSC or prolonged shading exhausts the coral and may have lethal effects.

[2] Many corals have a symbiotic relationship with the unicellular zooxanthellae, which account for the colouring of corals. Under sediment stress zooxanthellae may be expelled by the coral, resulting in a colourless appearance. As this bleaching process develops, it becomes increasingly unlikely that the symbiosis is able to recover and the coral eventually faces lethal effects.

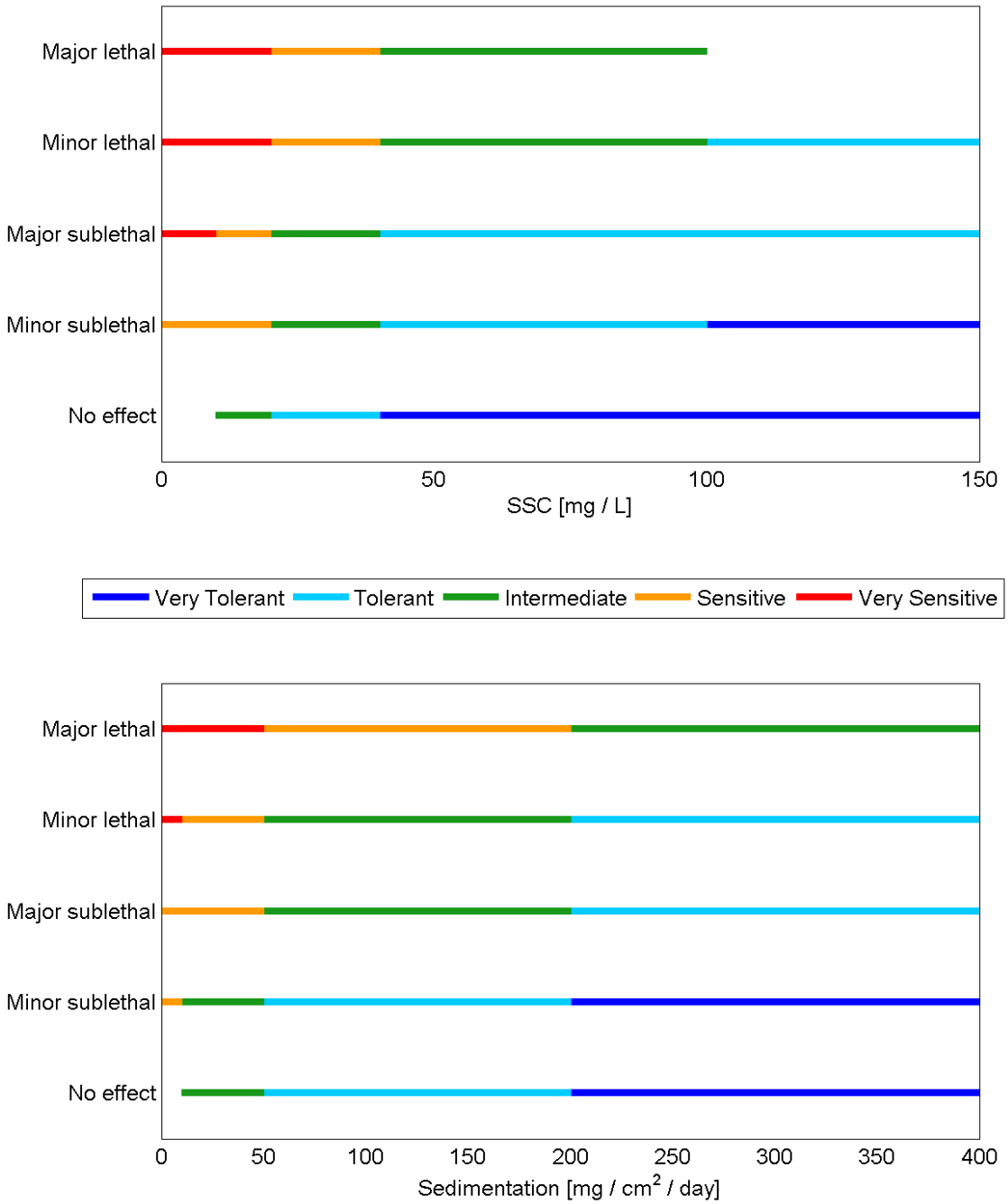

Figure 2.14: Impact of shading (upper panel) and burial (lower panel) for coral species of varying sensitivity. Modified after Erftemeijer et al. (2012).

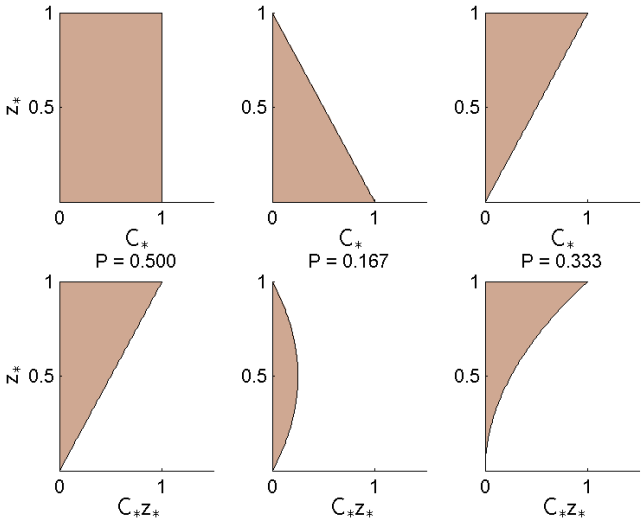

Figure 2.15: Development of the environmental impact potential. The lower panels represent the values of $C_* z_*$ of the corresponding concentration profiles in the upper panels. Integration over z_* leads to P, which is stated above each lower panel.

case studies involving burial of corals. Again, it can be argued that the relation between the sedimentation rate and the environmental impact has an approximately linear character. Combined with the physical aspects treated above, this again advocates the use of $\overline{C}z$ to define the environmental impact potential. The fact that (mobile) benthic fauna are better able to deal with burial than flora justifies the limitation of this research to corals.

For both shading and burial, a linear relationship was proved to be appropriate. The physical arguments presented for burial are of special importance, as quick settling is also beneficial regarding shading. The environmental impact potential P is now defined according to equation 2.12. z and $\overline{C}$ will be made dimensionless by means of undisturbed water depth h and the maximum upstream concentration C_{max} respectively. Through integration over z_*, the environmental impact potential only remains a function of downstream distance x.

$$P(x) = \int_0^1 z_* C_* \, \mathrm{d}z_* \tag{2.12}$$
$$\text{with } z_* = \frac{z}{h}$$
$$C_* = \frac{\overline{C(x,z)}}{C_{max}}$$

To illustrate the behaviour of P, the value of $C_* z_*$ as a function of z_* is computed for three schematic concentration profiles. The result is displayed in figure 2.15. The large contribution of near-surfacial turbidity to the impact potential is clearly shown.

The last step in parameterising silt screen effectiveness consists of converting P to a measure which expresses the actual effectiveness. In order to maximise tangibility and compliance with literature, it is favourable to express the effectiveness E as an impact reduction percentage achieved by the screen. This can be done in two ways: either by comparing a downstream value $P(x)$ with the value P_{in} belonging to the issuing concentration profile or by comparing a downstream value $P(x)$ with the value $P_{ref}(x)$ obtained at the same downstream distance in a reference situation without a silt screen. The former percentage will be referred to as E_{in},

whereas the latter will be denoted as E_{ref}. To avoid infinitely high percentages, E_{ref} is made dimensionless with P_{in}. These relations are expressed by equation 2.13.

$$E_{in}(x) = \left(1 - \frac{P(x)}{P_{in}}\right) \cdot 100\% \tag{2.13}$$
$$E_{ref}(x) = \frac{P_{ref}(x) - P(x)}{P_{in}} \cdot 100\%$$

Chapter 3

Modelling

The research objective and the focus have been determined and all relevant physical processes were studied in chapter 2. Now it can be specified how insight into the effectiveness of silt screens will be obtained given the general focus.

The first research question is applicable to both aspects of the general focus. For both horizontal and vertical diversion the effectiveness depends on a combination of flow velocity, water depth, relative screen height and sediment size. However, in present-day applications, silt screens are always intended to divert the suspended sediment vertically instead of horizontally. Therefore, determining the limiting dimensions for directing the sediment-laden flow to the screen will be the purpose of the study into horizontal diversion. Therefore, the ratio between the amount of water flowing under the screen and the amount of water passing the screen laterally under varying width and height of the screen, water depth and flow velocity will be checked. A 2DH model contains all the required features to study this process. In a model based on the shallow water equations, the silt screen will be represented as a baffle by applying a discharge relation at a series of internal cell boundaries.

Vertical diversion can be investigated in a 2DV approach. The associated flow field is known to be very turbulent. In a numerical model, turbulence can be schematised in various ways. The possibilities range from a constant turbulent viscosity to more sophisticated solutions such as Large Eddy Simulation (LES). Nevertheless it still remains a numerical representation. In a physical model turbulence is present by nature, but the length scales are much smaller than in reality. This limits the size of turbulent structures. When both a numerical and a physical model are applied, the results of the numerical model can be validated by means of the experimental data. Figure 3.1 visualises the investigated relations between model scale and model nature. Modelling at three different levels should lead to reliable conclusions regarding the fourth level.

The modelling activities carried out in the scope of this research can thus be divided into three parts: laboratory experiments, a 2DV numerical model and a 2DH numerical model. The different goals per activity are defined below.

The purpose of the laboratory experiments consists of the following aspects:

- The prime purpose is *obtaining validation data for the numerical model*. High-frequency measurements of local velocities at regular spatial intervals provide data to compare time-averaged velocity profiles and turbulence parameters.

- Furthermore, *observing the spreading of dye* provides qualitative information on both the instantaneous and the time-averaged flow field. This information is used to verify the numerical model. All dye injections are captured on video.

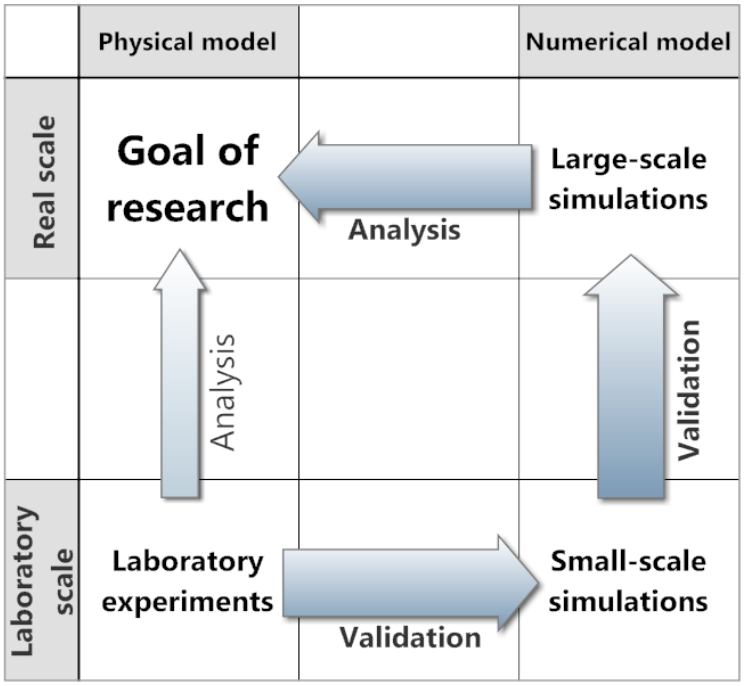

Figure 3.1: Relations between model scale and model nature concerning the 2DV modelling part.

- The final aspect is *investigating the effect of a number of promising adjustments to the silt screen.* The laboratory experiments are only suitable for the 2DV adjustments: perforation of the screen (adjustment 2a), extending the screen with a flap (2b) and applying an additional silt screen downstream of the first one (5). The investigation consists of detailed velocity measurements and observing the spreading of dye.

The specific goals of the 2DV numerical modelling activities are listed below:

- The main part of the 2DV numerical model consists of *quantifying the effectiveness of hanging silt screens under varying flow velocity, water depth, relative screen height, settling velocity and upstream SSC profile.*
- The 2DV numerical model will also be used to *investigate the effect of a number of promising adjustments to the hanging silt screen.* Only applying an additional silt screen (5) is feasible in the applied numerical model.

Finally, the 2DH numerical model aims at the following goals:

- The model is used to *determine the influence of flow velocity, water depth, relative screen height and relative screen width on the distribution of vertically and horizontally diverged discharges.*
- By also varying the angle of incidence, it is possible to *assess the screen's ability to act as a current deflector*, which corresponds to adjustment 1a and 1b.

The two numerical codes used for this research are described in appendix F. The academical Dflow3D code will be used for the 2DV approach, whereas the more commercial FINEL2D code will be used for the 2DH approach.

Chapter 4

Vertical diversion

The most important processes determining silt screen effectiveness were said to be vertical and horizontal diversion. This chapter presents investigations into the former. Results have been obtained by means of numerical as well as physical modelling. Both have constituted their own set of valuable observations, but the physical model tests mainly serve as validation data to the numerical model. Section 4.1 discusses the laboratory experiments. After explaining the experimental set-up and the different measurement scenario's, the results are presented. These results already give rise to some considerations regarding the flow field. Suspended sediment transport is added in section 4.2, which addresses the numerical model simulations. Successively, the model set-up, validation by means of the laboratory data, the simulation scenario's and the simulation results are presented. The section will end with a self-similarity analysis of the flow field.

4.1 Physical model

A silt screen scale model has been placed in a flume at the Fluid Mechanics Laboratory of the Delft University of Technology. Section 4.1.1 deals with the experimental set-up, the actual series of experiments is discussed in section 4.1.2 and the results are presented in section 4.1.3.

4.1.1 Set-up

The experiments are conducted in a laboratory flume of 14 m length, 40 cm width and at maximum 35 cm depth. It is schematically depicted in figure 4.1. Discharge and water depth

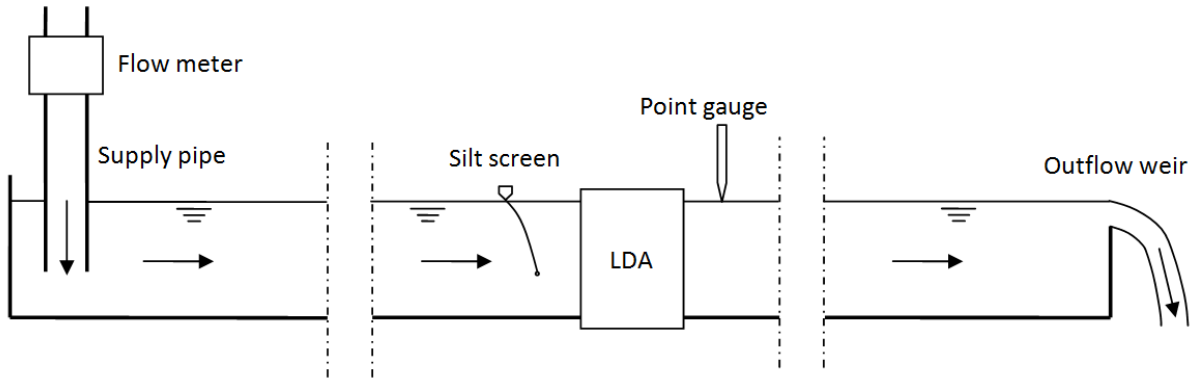

Figure 4.1: The experimental set-up used for this research consists of a long flume of 14 m length, 40 cm width and at maximum 35 cm depth.

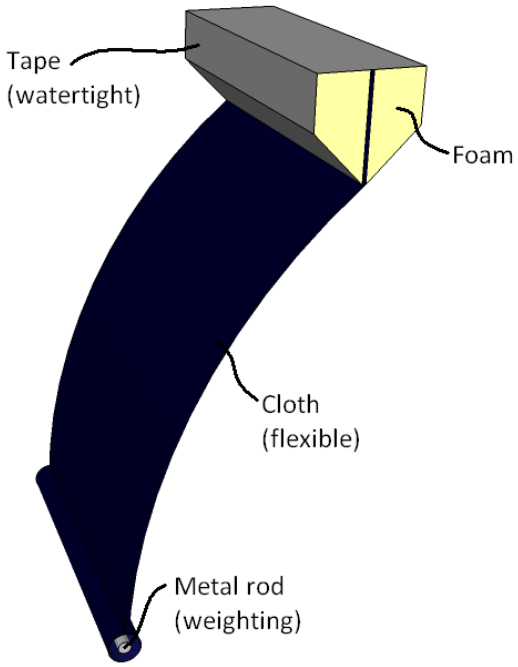

Figure 4.2: The silt screen scale model as applied in the flume.

are controlled by a valve in the supply pipe and a weir at the downstream end of the flume. The construction of the silt screen scale model is shown in figure 4.2. The upper bar is made of rigid foam, so as to clamp the bar in between the flume's side walls. The screen itself consists of a cloth. Synthetic material might guarantee complete water tightness, but its mechanical properties can not be scaled correctly. A flexible cloth has proved to be practically water tight and behaves more like a real, large-scale silt screen. The weight chain of a real silt screen is accounted for by a metal rod.

The following measuring instruments are used:

- Measurements of local velocities are made by means of *Laser Doppler Anemometry (LDA)* with a sampling rate of 500Hz. This leads to very detailed measurements of the turbulent fluctuations. The operating principles of LDA are explained in appendix E. Figure 4.3 shows the locations in the flow where velocity timeseries will be collected.
- The discharge is measured by means of a *flow meter* and a *Rehbock weir*.
- Water depths at various locations are measured by means of a *point gauge*.
- A *videocamera* serves to capture all dye injections on video, so that they can be studied extensively.

Furthermore the deformed shape of the screen is documented in order to use real deformations in the numerical model.

4.1.2 Scenarios

A series of different conditions is applied to the experimental setup described above. Each experiment is characterised by a unique combination of flow parameters, silt screen geometry and measurements.

Determination of the possible flow parameters is done by scaling a field situation down to flume

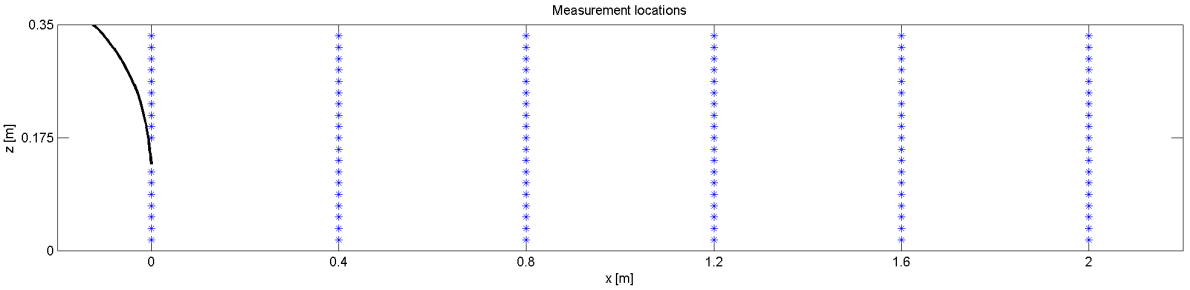

Figure 4.3: The blue markers show the locations where velocity timeseries will be collected by means of LDA. They form 6 profiles of 19 measurements each. A hypothetical position of the silt screen is indicated in black. Its lower edge serves as reference point for the horizontal coordinates.

dimensions. In principle, both the Froude number Fr and the Reynolds number Re of the laboratory flow should equal Fr and Re of the field situation. By doing so, uniformity of the influence of inertia and uniformity of the turbulence properties are guaranteed. However, Re is proportional to the water depth, whereas Fr is inversely proportional to the square-root of the water depth. Adhering to both numbers is therefore impossible. Changing Fr leads to unacceptably deformed flow situations and has to be avoided. Changing Re is less rigorous, as long as the flow remains well inside the turbulent regime ($Re \gg 3000$). There is no strict rule prescribing the lower limit for Re, since the sensitivity of measurements to the Reynolds number varies from case to case. The flow downstream of a silt screen is obviously dominated by turbulent structures originating from flow separation. On the one hand, scaling can be said to have a very disadvantageous effect. Re is changed, although turbulence plays an important role in this specific research. On the other hand, the presence of the screen significantly increases turbulence intensities, which is not accounted for by Re. This might prevent the flow from switching incidentally to laminar conditions. A comparison of numerical model runs at both scales offers more certainty about the influence of Re.

Three different field scenarios will be scaled down to laboratory dimensions. These scenarios are chosen so as to cover the whole range of flow parameters at which silt screens may be applied. They are listed in table 4.1 and are coded from 1 to 3. Subscript F denotes 'Field', whereas subscript L denotes 'Laboratory'.

Table 4.1: Three combinations of flow parameters that are scaled down to laboratory dimensions.

	(1)	**(2)**	**(3)**
U_F [m/s]	0.2	0.3	0.5
d_F [m]	5	5	5
Re_F [-]	$9.1 \cdot 10^5$	$1.4 \cdot 10^6$	$2.3 \cdot 10^6$
Fr_F [-]	0.029	0.043	0.071
Fr_L [-]	0.029	0.043	0.071
d_L [m]	0.35	0.35	0.35
U_L [m/s]	0.053	0.079	0.1323
Re_L [m]	$1.7 \cdot 10^4$	$2.5 \cdot 10^4$	$4.2 \cdot 10^4$

Furthermore, seven different types of silt screens are used throughout the experiments. The first two types, being A and B, are regular silt screens with different relative screen heights. All

other types are used to investigate the adjustments as discussed previously. The screen types are coded from A to G, see table 4.2.

Table 4.2: Different types of silt screen used during the experiments with their respective code.

A	Regular screen, $h_{rel} = 0.5$
B	Regular screen, $h_{rel} = 0.75$
C	Moderately perforated screen, $h_{rel} = 0.75$
D	Heavily perforated screen, $h_{rel} = 0.75$
E	Screen extended with a flap, $h_{rel} = 0.5$
F	Screen with 1 additional weight chain, extended with a flap, $h_{rel} = 0.75$
G	2 screens after another, $h_{rel} = 0.75$

Screen A and B are investigated under all three flow conditions (experiments 1A, 1B, 2A, 2B, 3A and 3B). All adjustments are investigated under flow condition 2 (experiments 2C, 2D, 2E, 2F and 2G). Experiment 1B, 3A and 3B have an LDA sampling duration of 100 seconds. As this does not lead to satisfactory convergence after time-averaging, experiment 1A, 2A and 2B have a sampling duration of 200 seconds.

The deformation of a silt screen is governed by the hydraulic load and the weighting along the bottom edge of the screen. The weighting of the scale model should be such that its deformations resemble those of the respective field scenario. However, field measurements of silt screen deformations are not available. Efforts to compute the shape of a screen in uniform current by means of a simplified model have not proved to be of any use. Finally a weighting of about 1.24 kg/m has been chosen in case of the A and B experiments, since this leads to a realistic order of magnitude of deformations.

4.1.3 Results of laboratory experiments

This section will present the results as obtained from the laboratory experiments. The effectiveness of silt screens can only be determined after transport processes have been investigated with the numerical model. However, the laboratory results are used to describe the turbulent flow field of flow being diverted vertically by a silt screen.

The results of experiment 2A are shown as an example. Any observation mentioned hereafter is supported by the other laboratory runs. Figure 4.4 shows time-averaged flow velocities. Raw data of time-averaged vertical velocity $\bar{w}$ all show the same constant deviation of +0.01 m/s with respect to the expected velocity field (near the bottom and the free surface, $\bar{w}$ should equal zero). Hence all data regarding $\bar{w}$ have been corrected manually. The theoretical flow field as described in chapter 2 clearly applies to the experiments. Right downstream of the screen a near-bottom jet flow and a near-surface recirculation zone exist. The approximate extent of the recirculation zone is indicated with a dotted line, based on the vertical position where the integral of horizontal velocities equals zero. Downstream of the recirculation zone, the jet flow spreads out over the full water column and the flow gradually recovers towards a logarithmic velocity profile. In this region $\bar{w}$ still attains a non-zero value. This is caused by the combination of deceleration in the lower part of the water column and acceleration in the upper part. The upward flow of momentum associated with the upward flow velocities facilitates these streamwise velocity gradients.

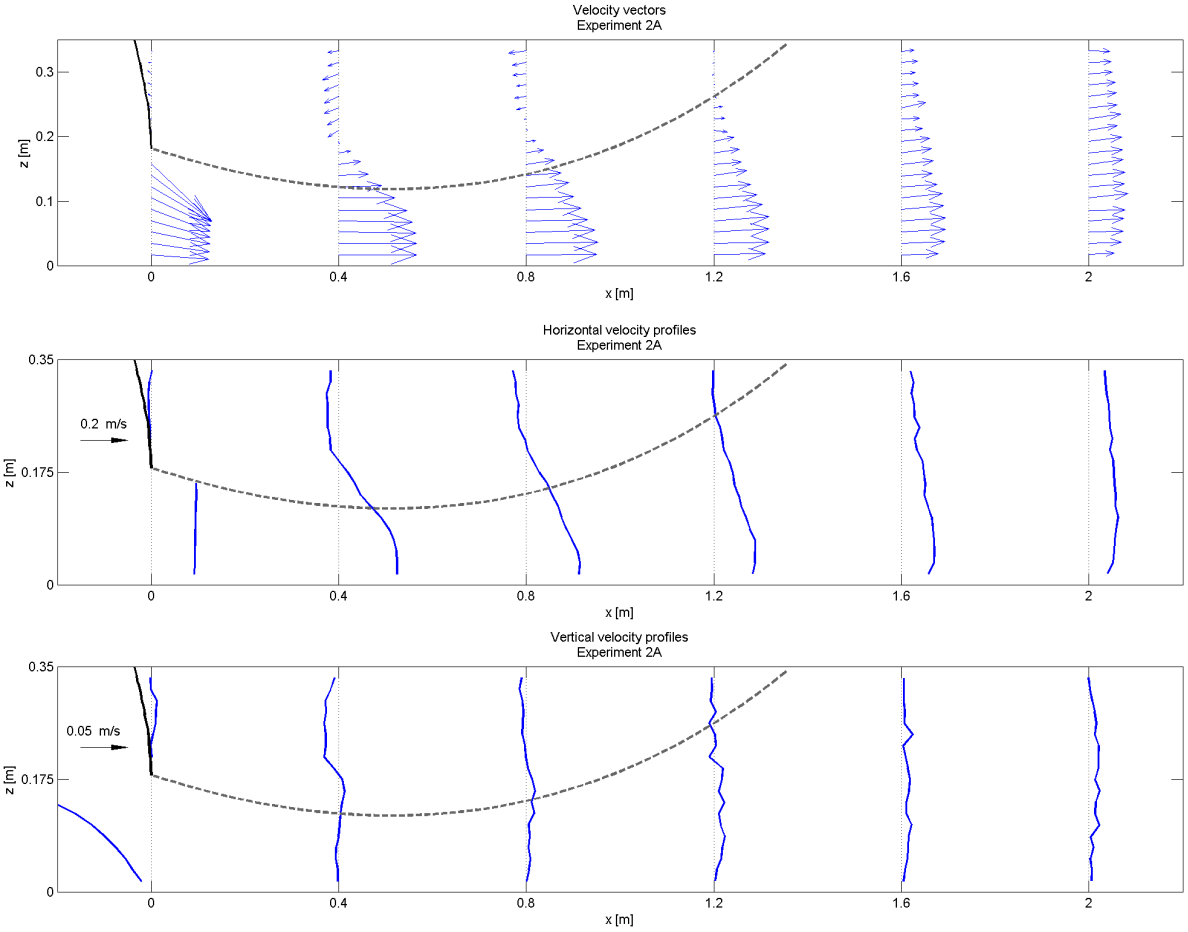

Figure 4.4: Time-averaged velocity plot for laboratory run 2A. The actual deformation of the silt screen is indicated by the solid black line. The dotted line shows an approximation of the recirculation zone boundary. The upper panel shows velocity vectors, whereas the middle and lower panel show profiles of horizontal and vertical velocity $\bar{u}$ and $\bar{w}$ respectively.

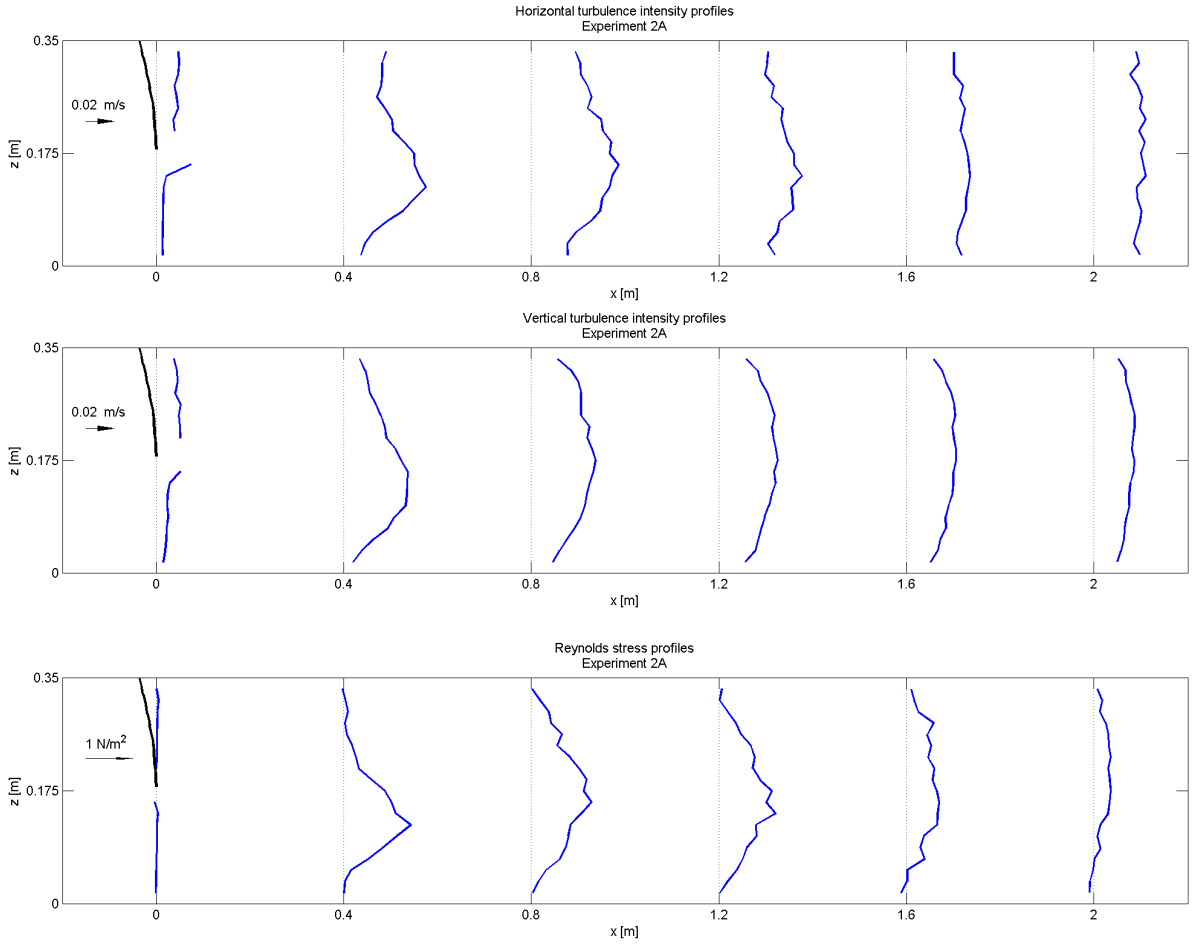

Figure 4.5: Turbulence parameters for laboratory run 2A. The upper and middle panel show horizontal and vertical turbulence intensities r_u and r_w respectively. The lower panel shows Reynolds stress τ'_{uw}.

Furthermore a number of turbulence parameters has been derived from the LDA timeseries. These are shown in figure 4.5. The highest turbulence intensities and Reynolds stresses are encountered right downstream of the silt screen's bottom edge. The flow separation taking place at that location constitutes a mixing layer, which grows bigger downstream until it covers the whole water depth. In this mixing layer, the velocity shear causes Kelvin-Helmholtz instabilities to develop. This is clearly visible in figure 4.6, which shows a snapshot of a dye injection during experiment 2B. Two small curling vortices are visible, whereas a bigger and more diffused vortex can be seen in the left part of the picture.

The dye injection of figure 4.6 may not be used to judge the effectiveness of silt screens, as it concerns a passive tracer. However, especially the turbulent shear stress serves as a measure for turbulent transport of dissolved or suspended matter. It is fruitful to compare profiles of $\bar{u}$, $\bar{w}$, r_u, r_w and τ'_{uw} for different laboratory experiments in order to say something about the degree of flow disturbance induced by the silt screen.

Figure 4.7 shows horizontal and vertical time-averaged velocity profiles for experiments 2A and 2B. Experiment 2B shows a more intense jet flow and recirculation zone, due to the bigger blockage of the water column. As a result, the recirculation zone of experiment 2B is longer and flow recovery takes a longer downstream distance.

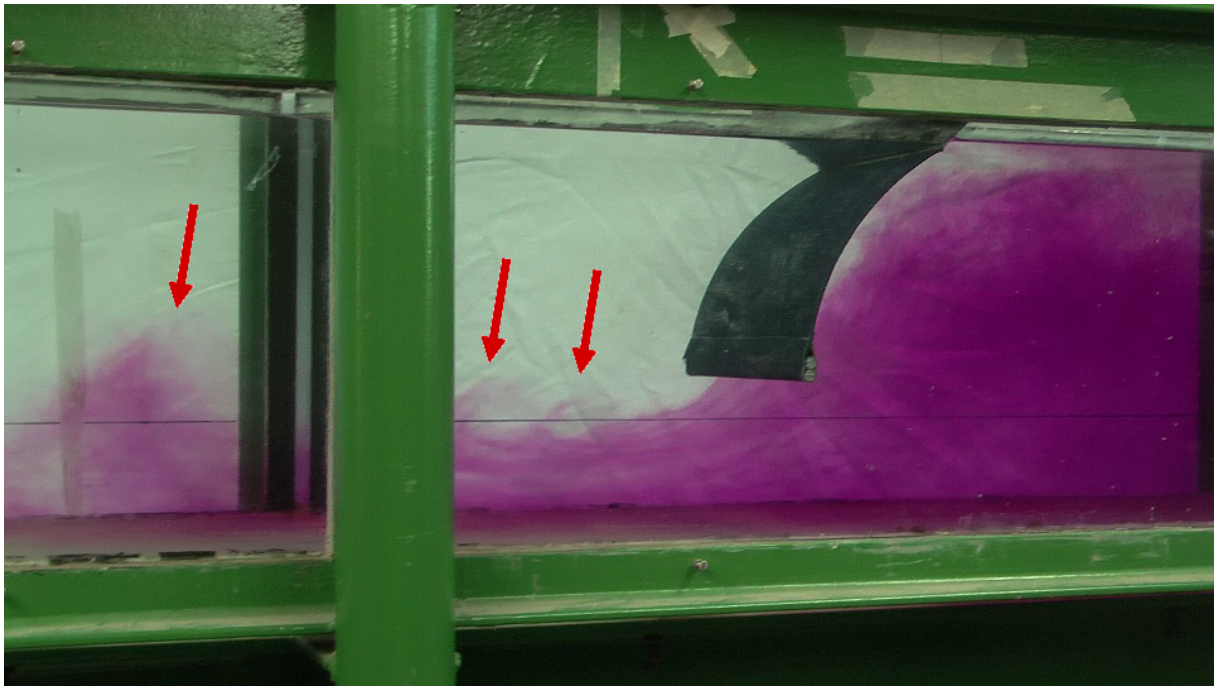

Figure 4.6: Snapshot of a dye injection during laboratory experiment 2B. Immediately downstream of the silt screen's bottom edge two curling vortices are visible, resulting from Kelvin-Helmholtz instability. Further to the left a more developed and diffused vortex can be seen.

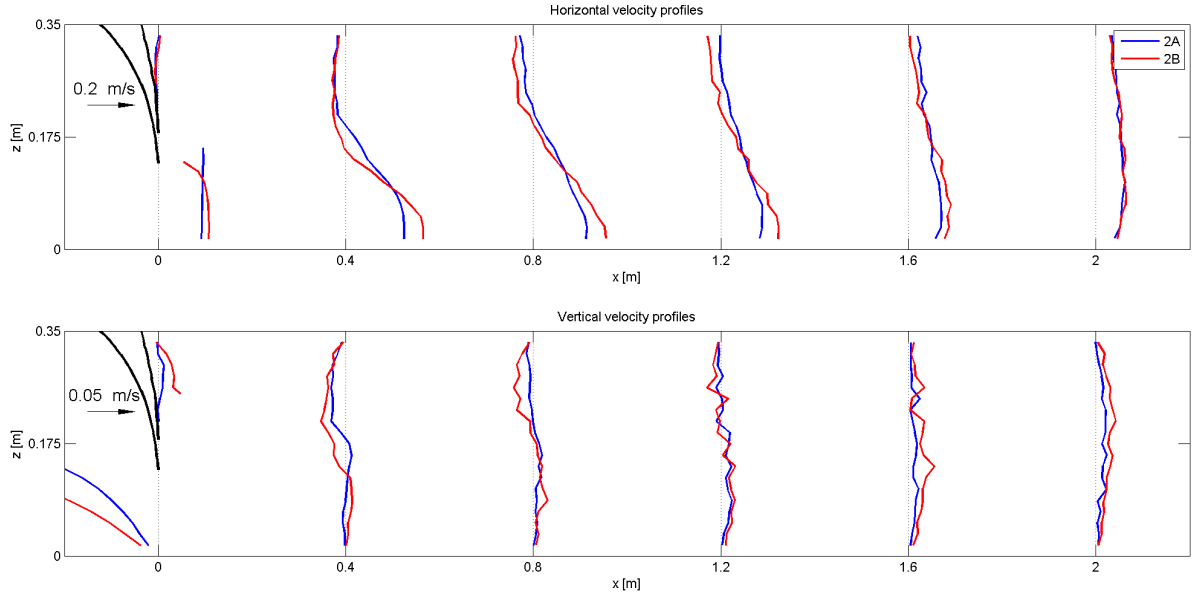

Figure 4.7: Comparison of time-averaged horizontal and vertical flow velocities for experiment 2A and 2B.

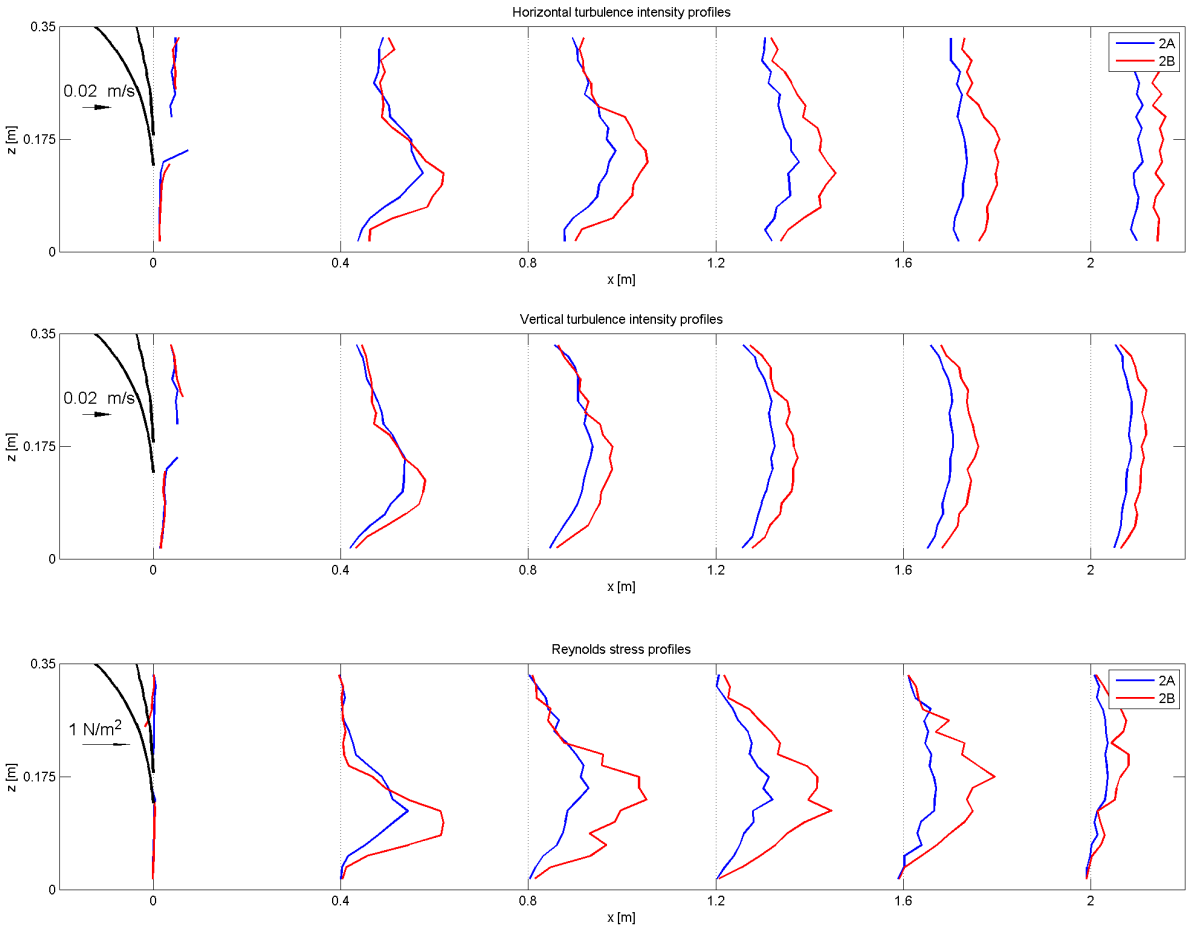

Figure 4.8: Comparison of turbulence parameters for laboratory experiments 2A and 2B.

A comparison of turbulence parameters for the same experiments is made in figure 4.8. With respect to experiment 2A, the peak of all 2B profiles is shifted downward due to the lower position of the screen's bottom edge. The bigger blockage of the water column leads to a higher velocity shear and more production of turbulence. This is reflected by higher peak values of r and τ'_{uw}.

The comparison between run 2A and 2B discussed above focused on the influence of relative screen height h_{rel}. Now the influence of varying depth-averaged horizontal flow velocity U will be assessed by comparing run 1A and 2A. In figure 4.9 the velocity profiles are shown. The maximum jet flow velocity is higher in experiment 2A, but due to the bigger specific discharge the recirculation zone does not necessarily have to be more pronounced as well. Moreover, as a result of the bigger screen deformation and associated lower effective h_{rel}, experiment 2A has a slightly shorter recirculation zone.

Turbulence parameters of both experiments are displayed in figure 4.10. The vertical position of the peak values is equal due to the comparable effective relative screen heights. Figure 4.9 already showed that the bigger jet velocities of experiment 2A lead to a bigger velocity shear. This is associated with more turbulence production, which results in higher peak values of r and τ'_{uw}.

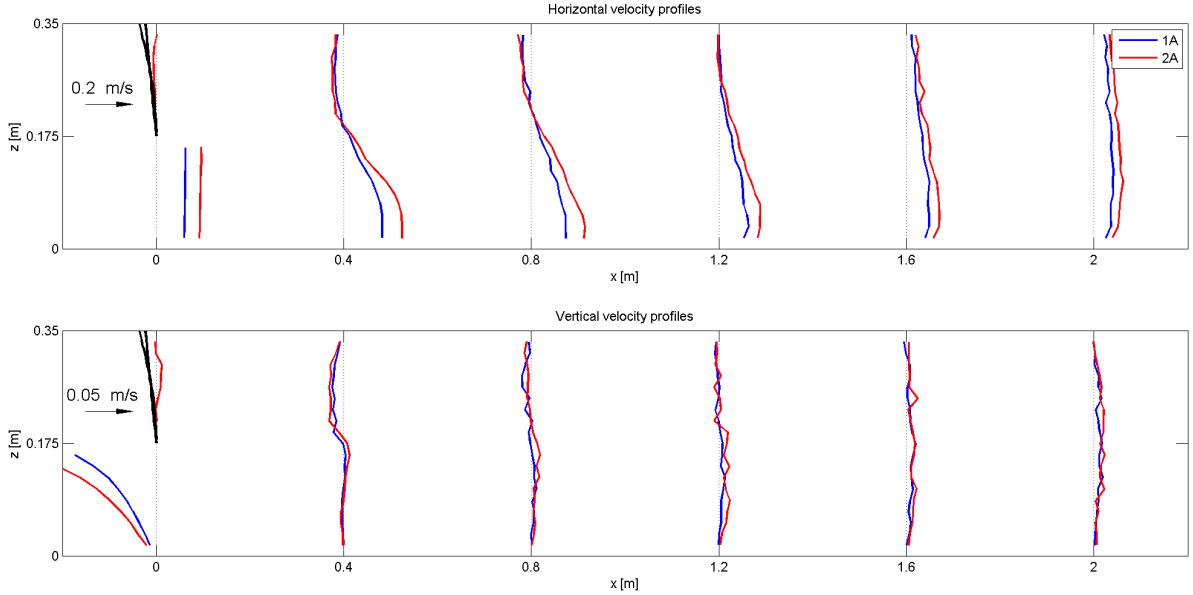

Figure 4.9: Comparison of time-averaged horizontal and vertical flow velocity for experiment 1A and 2A.

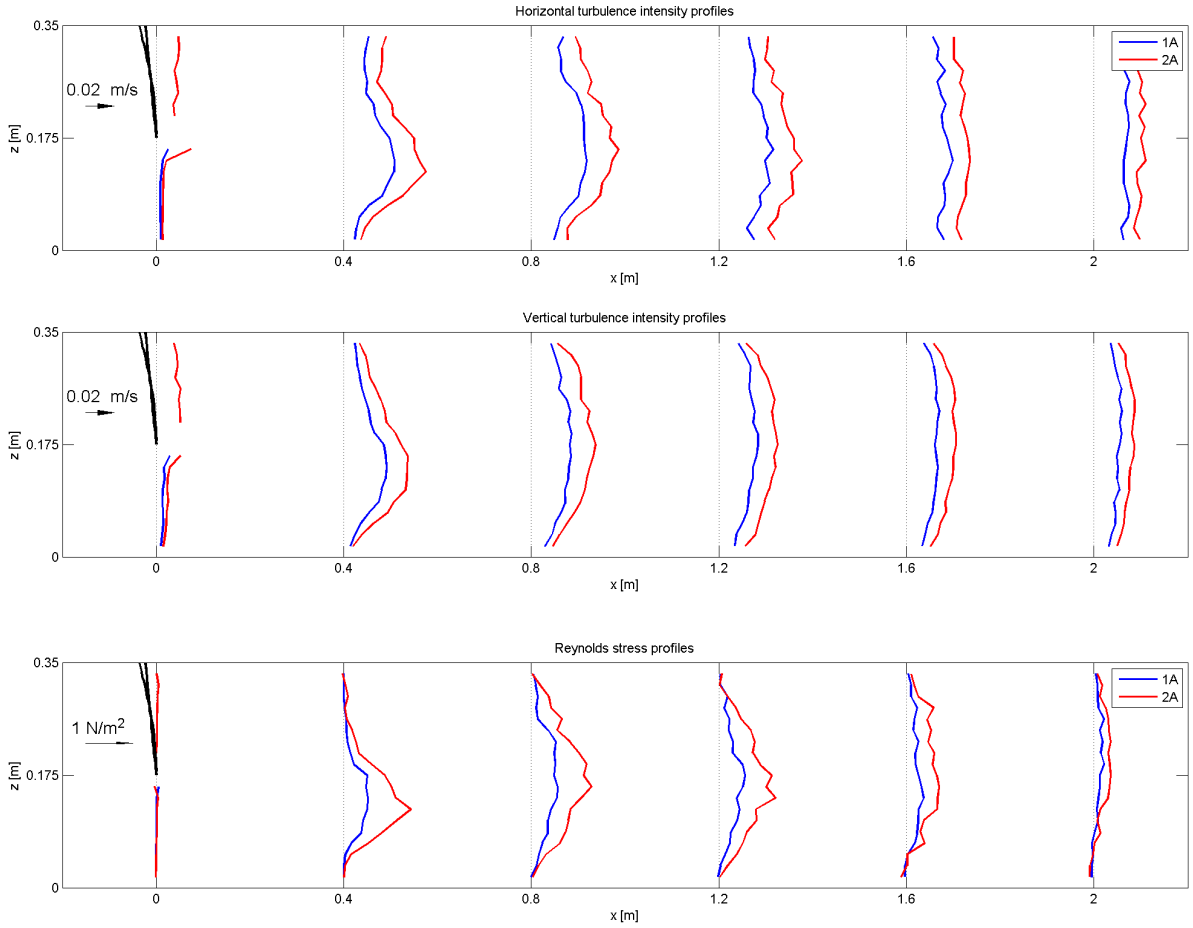

Figure 4.10: Comparison of turbulence parameters for experiment 1A and 2A.

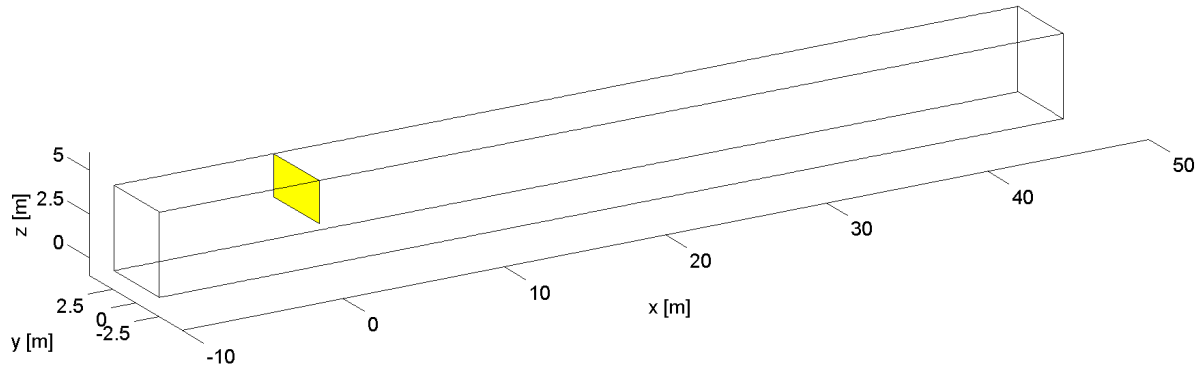

Figure 4.11: Boundaries of the numerical domain as used for large scale simulations. The silt screen is represented by a series of impermeable grid cells.

4.2 Numerical model

The 3D LES model described in appendix F.2 has been used to simulate vertically diverted flow past a silt screen. Before the actual simulation results are presented, an overview of the model set-up is given and the model's performance is validated. Treatment of the results will start with deriving the relevant parameters which represent silt screen effectiveness. Finally, self-similarity analysis will be applied to the simulated flow field.

4.2.1 Set-up

It has been argued before that a 2DV model approach suffices to analyse all relevant processes related to vertical diversion. However, two-dimensional turbulence behaves fundamentally different from three-dimensional turbulence as encountered in practice (Rivera, 2000). The process of vortex stretching, which is responsible for breaking down turbulent eddies into smaller ones until dissipation takes place, does not apply in the two-dimensional case. On the contrary, eddies are merged into bigger eddies by a process named vortex cannibalisation. Hence the LES model needs a third dimension in order to function properly. As long as the third dimension is at least as big as the water depth, it will not be a limiting factor for turbulent length scales present in the flow.

The model boundaries are depicted in figure 4.11. As indicated by the yellow surface, the silt screen is accounted for by inserting a vertical series of impermeable grid cells. Horizontal deformations of the screen are not taken into account, but the relative screen height is determined from the deformations measured in the laboratory. This simplification hardly influences the results, as the exact shape of the screen is only of minor importance. By creating an upstream recirculation zone the flow more or less shapes its main streamlines in a natural way. This behaviour was also observed from PIV-measurements by Vu and Tan (2010).

Based on the outer grid geometry, a grid cell size has to be chosen. When the grid cell size lies within the inertial range of turbulent fluctuations, SGS models are expected to perform well. The transitional length scale of anisotropic to isotropic turbulence can be estimated by means of the Taylor microscale λ_T. It is not very straightforward to determine λ_T from the laboratory experiments. However, it is known that λ_T lies in the order of 1 mm for laboratory experiments and 10 cm for river flow. The more the flow is dominated by bigger length scales, the bigger the allowable grid cell size. Despite these theoretical considerations, it is primarily a matter of available computational power that prescribes a lower limit for the grid cell size. A satisfactory balance between accuracy of the results and computational time has to be established. A grid cell size of 1 cm for the laboratory scale runs and 12.5 cm for the real scale meets this demand.

For the full scale simulations this results in a grid resolution of 450 x 40 x 40 and 720,000 grid cells in total. Simulations at laboratory scale make use of a grid resolution of 400 x 35 x 35 and 490,000 grid cells in total.

The numerical grid has been defined. Some model input parameters still have to be determined, being the simulated time span, the Schmidt number and the bed roughness. The latter will be part of the validation procedure and is therefore discussed in the next section.

In order to determine an appropriate time span for the simulations, two different aspects have to be covered. On the one hand, the averaging time of the simulations has to be sufficiently large to discern consistent turbulence parameters. On the other hand, the flow and SSC fields will need some spin-up time to reach a stationary condition (in a time-averaged sense). The durations required to meet these demands are presented in table 4.3. Suspended sediment concentrations call for a longer spin-up time than flow velocities, since the domain initially does not contain any sediment concentrations and the exchange flow in and out of the recirculation zone requires a long time to reach an equilibrium.

Table 4.3: Required spin-up time and averaging time for numerical model simulations.

	Laboratory scale		**Real scale**	
	Velocities	Concentrations	Velocities	Concentrations
Spin-up time	100 s	n/a	200 s	2000 s
Averaging time	360 s	360 s	360 s	360 s

The Schmidt number is used for computation of the sub-grid scale diffusion of SSC. Values of Sc encountered in literature are always based on empirical data. Although it can be reasoned that transport of a scalar is more effective than transport of momentum in most cases, corresponding to $Sc < 1$, exact values are not known. Moreover, Sc is expected to vary in space, depending on local flow conditions. The LES model used in this research makes use of a constant Schmidt number. According to Tominaga and Stathopoulos (2007), the range of Schmidt numbers encountered most often in Reynolds-averaged Navier-Stokes models is 0.7 - 0.9. In LES models, Sc is only needed to determine the sub-grid scale turbulent mass flux. Antonopoulos-Domis (1981) shows that a sub-grid scale Schmidt number of 0.5 is appropriate for fitting LES results to experimental data obtained in isotropic turbulence. Therefore $Sc = 0.5$ is adopted in this research. As the LES model partly calculates the turbulent fluctuations, it is dominated by advection. Therefore the sensitivity of SSC to varying Sc can be shown to remain very small.

4.2.2 Validation

In order to prove that the numerical model predicts the correct behaviour of flow and suspended solids in case of vertical diversion past a silt screen, its results have to be validated. To this end, the laboratory dataset described in section 4.1 may be used. As this dataset has been obtained at laboratory scale, only a numerical model at this same scale can be validated directly. However, by comparing normalised parameters of laboratory and real scale model simulations, confidence can be gained about the real scale performance. The last part of this section deals with the validation of a reference simulation without a silt screen.

The laboratory dataset does not contain data of suspended solids transport. Because the scalar transport equations largely resemble those for momentum, validation of the latter provides information on the former. Only the Schmidt number and the settling velocity discern between both sets of equations. It was argued before that Sc hardly influences the transport field due to the dominant role of advection in the LES model. The settling velocity is one of the parameters

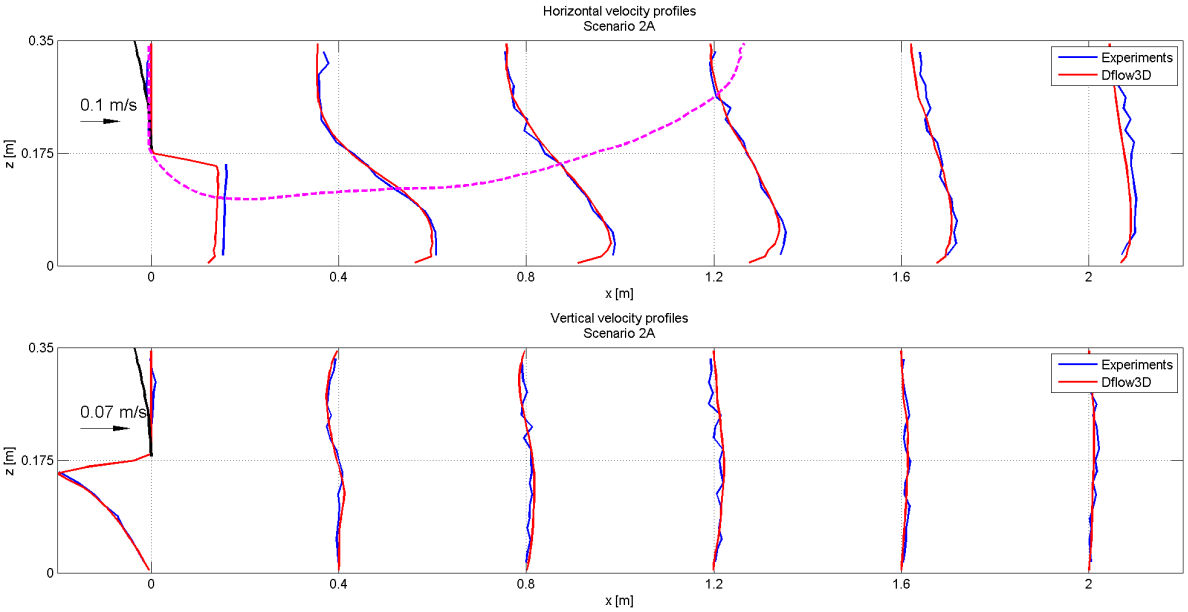

Figure 4.12: Time-averaged velocity validation plot for laboratory experiment 2A. Nikuradse bottom roughness k_N is set to 10^{-4} m.

of interest in this research and will be varied throughout the model runs. Therefore the model's performance regarding scalar transport does not have to be addressed separately and will be considered as validated together with the flow field.

The Nikuradse bottom roughness k_N is the only parameter which is varied throughout the validation process. The purpose of varying it is not to determine the laboratory flume's bottom roughness, but to fit the simulation data as close as possible to the experimental data. For application to the real scale simulations this analysis of bottom roughness is useless, since only an academical situation is assessed. A default value of 0.01 m is used in these simulations.

Validation of the model takes place based on five different flow parameters, being horizontal time-averaged flow velocity $\bar{u}$, vertical time-averaged flow velocity $\bar{w}$, horizontal turbulence intensity r_u, vertical turbulence intensity r_w and Reynolds stress τ'_{uw}. Furthermore the energy spectrum will be assessed and a comparison is made between laboratory and real scale numerical simulations. Again, laboratory experiment 2A is used as an example. Validation figures for all other laboratory scenario's are included in appendix G.

Horizontal time-averaged flow velocities are predicted very well by the model. Within the tested range of k_N, model predictions and laboratory measurements differ on average between 10% and 15% of the depth-averaged velocity. The upper panel of figure 4.12 shows a comparison of $\bar{u}$ for laboratory experiment 2A and a numerical model run with k_N set to 10^{-4} m. The LES model data are interpolated to the same vertical profiles as the laboratory data. The mean difference between experiments and model simulations is 13% of the depth-averaged velocity with a standard deviation of 1%. Both right downstream of the screen and in the zone of flow recovery some deviations are visible. The laboratory flow appears to return to a logarithmic flow profile quicker than the simulated flow. A higher value of k_N in the numerical model would give rise to a more intense redistribution of momentum, which improves the model's performance in the zone of flow recovery. However, right downstream of the screen the boundary layer is shallower in the laboratory experiments. Here, a lower bed roughness would be an improvement. Most other runs show this same tendency. The applied bottom roughness of 10^{-4} m appears

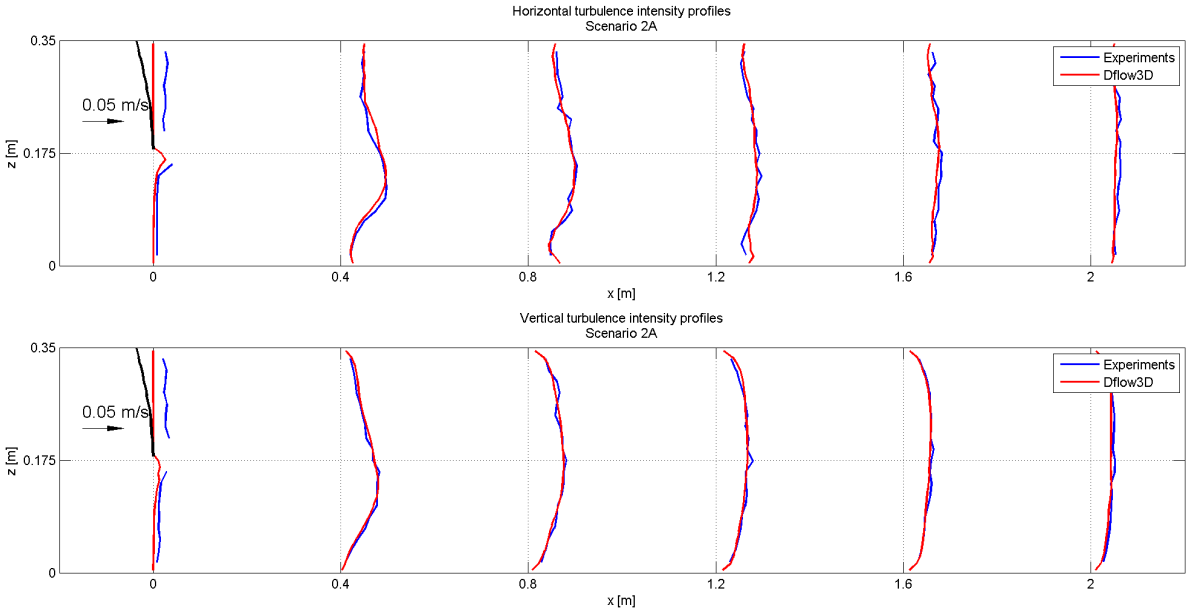

Figure 4.13: Turbulence intensity validation plot for laboratory experiment 2A. Nikuradse bottom roughness k_N is set to 10^{-4} m.

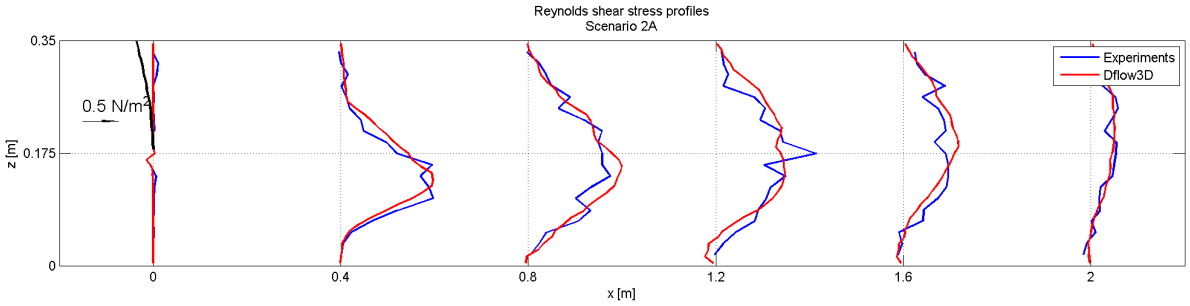

Figure 4.14: Reynolds stress validation plot for laboratory experiment 2A. Nikuradse bottom roughness k_N is set to 10^{-4} m.

to be the best compromise.

The lower panel of figure 4.12 shows a comparison of vertical time-averaged flow velocity $\bar{w}$. The numerical model appears to mimic vertical flow velocities well. Downstream of the recirculation zone, Dflow3D predicts slightly lower values of $\bar{w}$. Nevertheless, the redistribution of momentum by positive values of $\bar{w}$ can be recognised.

Horizontal and vertical turbulence intensities of the same laboratory experiment and numerical model run are shown in figure 4.13. The mean difference of r_u is 9% of the depth-averaged value with a standard deviation of 6%. For r_w a mean of 7% and a standard deviation of 5% apply. The most upstream profile at $x = 0$ m has been excluded from these percentages, as the small turbulence intensities of this profile induce large relative deviations. Model performance concerning turbulence intensities is remarkably well. Persistent deviations throughout all scenarios are absent.

A comparison of Reynolds stresses τ'_{uw} is depicted in figure 4.14. On average, the numerical

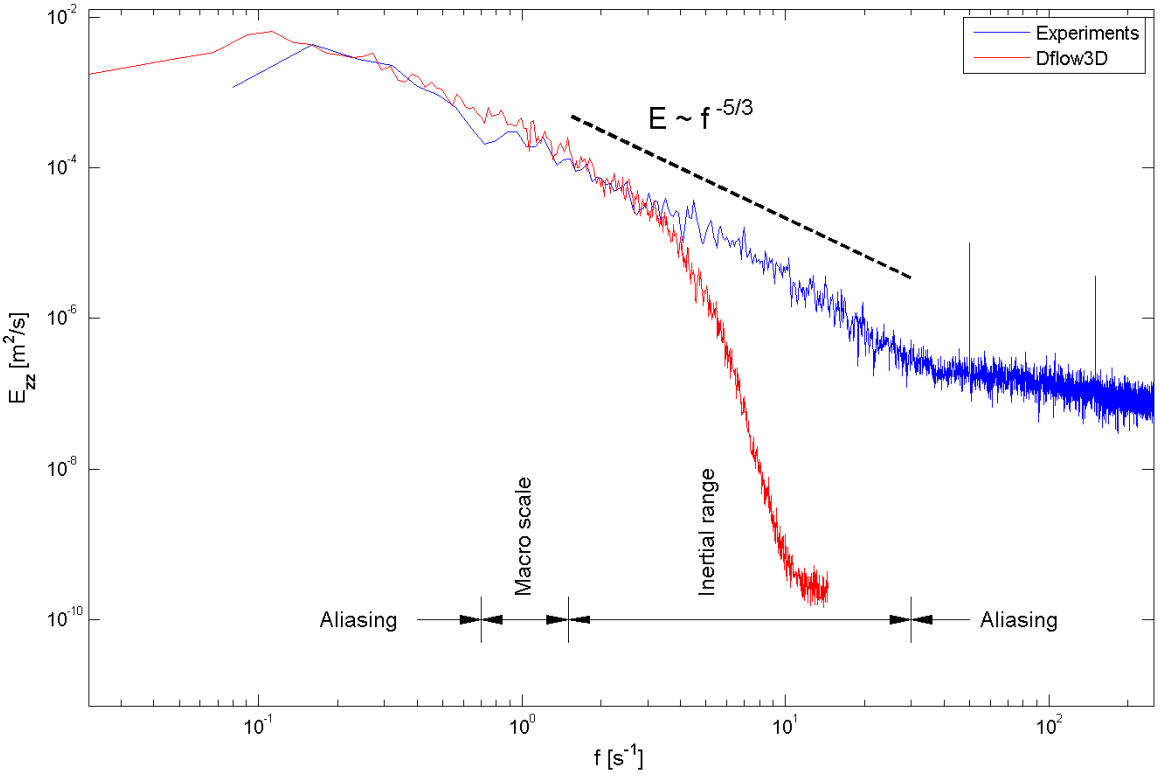

Figure 4.15: Comparison of energy-density spectra of vertical velocity v in the frequency domain for laboratory run 2A and its corresponding numerical model run. Both spectra clearly show an inertial sub-range, adhering to the Kolmogorov $-5/3$ scaling.

model differs 26% of the depth-averaged value with a standard deviation of 20%, again excluding the profile at $x = 0$ m. Compared to the validation of velocity and turbulence intensity, model performance concerning Reynolds stresses seems worse based on these quantitative values. However, it should also be noted that the laboratory data of τ'_{uw} contain more scatter, which increases deviations. In a qualitative sense, the Reynolds stress comparison looks very satisfying. The magnitude and vertical position of the peak value is quite sensitive to variations of k_N, but as was already argued before, this validation does not aim to determine the laboratory flume's bottom roughness.

A different way of validating the numerical model is found in assessing the energy spectra of both the laboratory experiments and the numerical model (see appendix C.3 for background theory on one-dimensional energy-density spectra of turbulent flows). When the calculated velocity is stored at every timestep, a single-point timeseries is extracted from the numerical model. After determining the autocovariance function and carrying out a Fourier transformation, the one-dimensional energy-density spectrum is obtained in the frequency domain. Figure 4.15 shows the result of this procedure for vertical velocity v in a laboratory timeseries and its corresponding numerically calculated timeseries with k_N again set to 10^-4 m. The timeseries stem from laboratory run 2A, at a location 120 cm downstream of the silt screen at half-depth. A couple of things stand out from these spectra:

- Both spectra show a clear $f^{-5/3}$ scaling, which follows from theory after applying Taylor's hypothesis to the commonly known $k^{-5/3}$ scaling. Regarding the grid cell size considerations presented in section 4.2.1, this means that the numerical model simulations partly

cover the inertial range. Hence, the SGS model is expected to perform well.

- For $f > 4$ s^{-1}, the wavelength approaches the grid cell size of the numerical model. The energy-density contained in the numerical model decreases accordingly.
- The spectrum obtained in the laboratory positively deviates from the $f^{-5/3}$ line for high wave numbers. Energy contained in wavenumbers which are higher than can be measured by means of the LDA is erroneously interpreted to belong to lower wavenumbers (aliasing due to lack of resolution).
- At the low wavenumber side, the spectrum should be limited by the large-scale geometry. Especially in the numerically calculated spectrum, energy is assigned to wavelengths larger than the water depth of 0.35 m. This phenomenon is linked to describing spatial turbulent structures by means of single-point velocity components. Energy contained in turbulent structures passing by obliquely with respect to the reference frame is erroneously assigned to lower wavenumbers (aliasing due to obliqueness). For the numerical model simulations this process continues down to lower frequencies, as it is based on a longer time series than the laboratory data. Hence aliasing may generate lower frequencies.
- The laboratory data show two distinct spikes at 50 Hz and 150 Hz. These spikes most certainly stem from the electricity mains. The spike at 150 Hz is clearly a higher harmonic of the one at 50 Hz. A spike representing the Strouhal frequency, that is the frequency at which vortex shedding takes place at the silt screen's lower edge, appears to be absent. It is probably not distinct enough.

Conclusively, the energy-density of laboratory experiments and LES model is comparable over the range of wavenumbers represented by both flows and the sub-grid scale of the numerical model is considered small enough to contain merely isotropic turbulence.

Up to this point, only numerical model runs at laboratory scale have been validated. Now two numerical model runs at laboratory and real scale will be compared. Unfortunately it is not possible to prove that Froude scaling really applies to vertical diversion past a silt screen. As a result of the way in which bed roughness is imposed in the numerical model code, the role of the Reynolds number is minimised. Nevertheless, the two most extreme laboratory simulations (1A and 3B) are now scaled to larger dimensions by keeping Fr fixed. Figure 4.16 shows a comparison of successively $\bar{u}$, $\bar{w}$, r_u, r_w and τ'_{uw} for scenario 3B on laboratory scale and its corresponding large-scale run (see table 4.1). The latter has a bed roughness of 10^{-2} m. As expected, the flow scales nearly exactly with Fr. Only minor deviations occur, which might even decrease further by fine-tuning of k_N. The same comparison is shown in figure 4.17 for run 1A, which represents the least turbulent conditions. Deviations are again very small.

The definition of effectiveness parameters in section 2.5 has made clear that the behaviour of suspended solids in a reference situation, i.e. without a silt screen, is of importance to this research. Hence, model performance of a reference simulation has to be validated as well. The absence of a silt screen poses difficulties in creating enough flow disturbance to get real turbulent flow going in the LES code. It takes many water depths for the bed friction alone to create realistic turbulent wall flow. Hence a sophisticated upstream velocity boundary condition is applied, which makes use of a synthetic eddy method (SEM). For further details on SEM, reference is made to Jarrin et al. (2006). In short, it means that multiple coherent structures are superimposed at the inflow boundary, adhering to a number of statistical properties of 'real' turbulent eddies.

In order to check the performance of SEM in a reference simulation, vertical profiles of turbulence parameters are compared to direct numerical simulation (DNS) data of turbulent

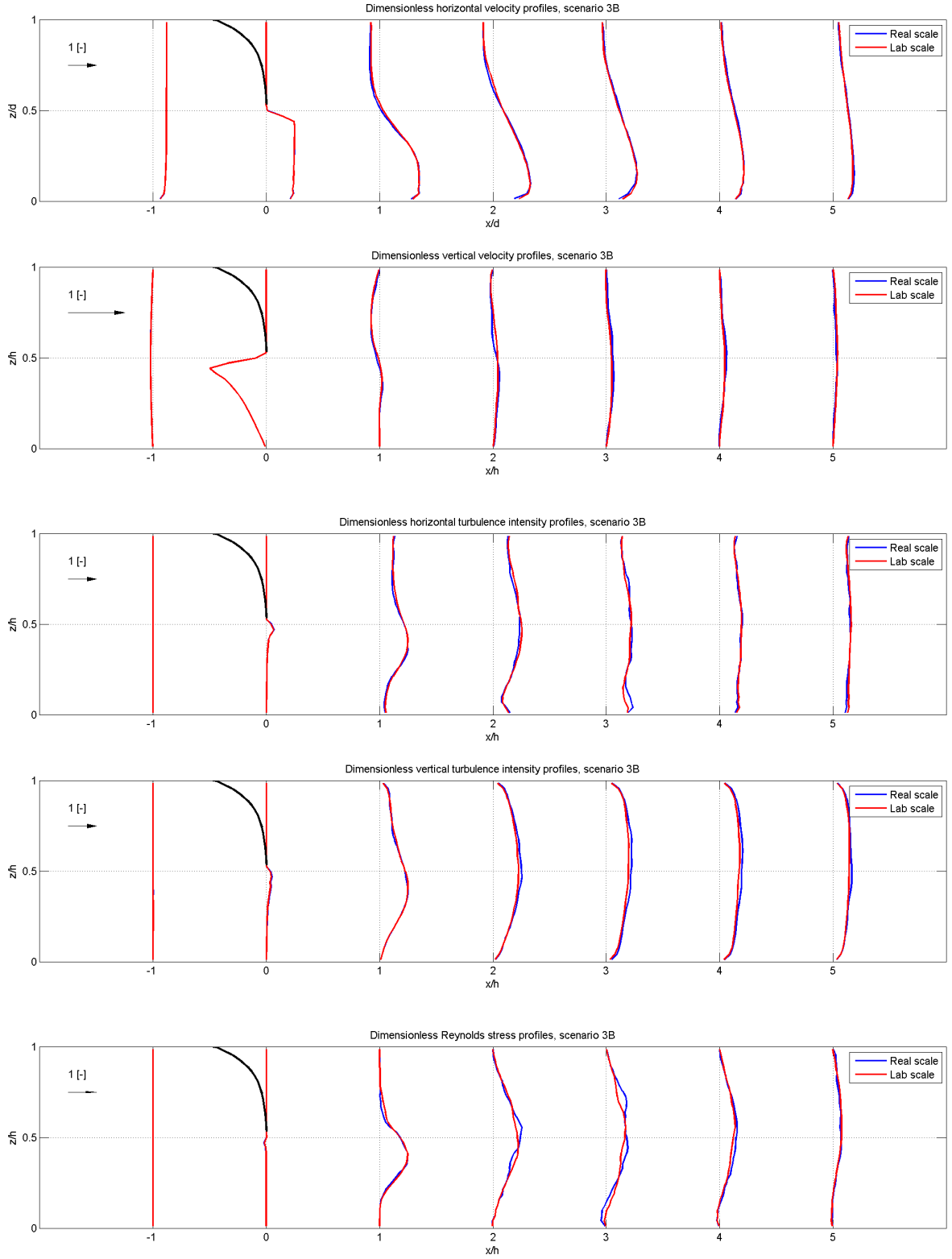

Figure 4.16: Comparison of time-averaged velocities, turbulence intensities and Reynolds stress for scenario 3B in numerical simulations at laboratory scale and real scale. The flow situation scales almost perfectly with the Froude number, which is more or less forced by imposing the law of the wall in the numerical model code.

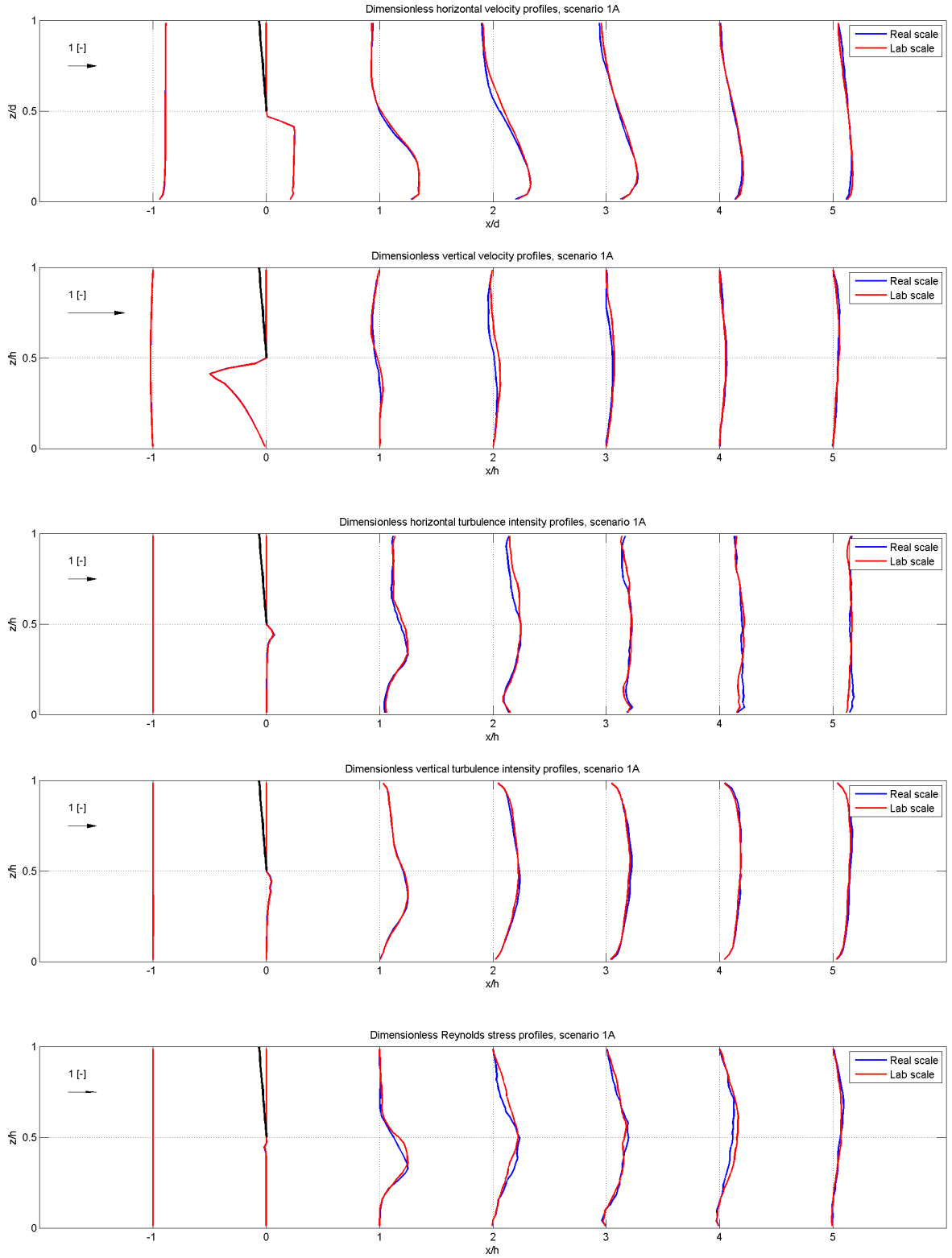

Figure 4.17: Comparison of time-averaged velocities, turbulence intensities and Reynolds stress for scenario 1A in numerical simulations at laboratory scale and real scale. Again, scaling with the Froude number applies very well to this scenario.

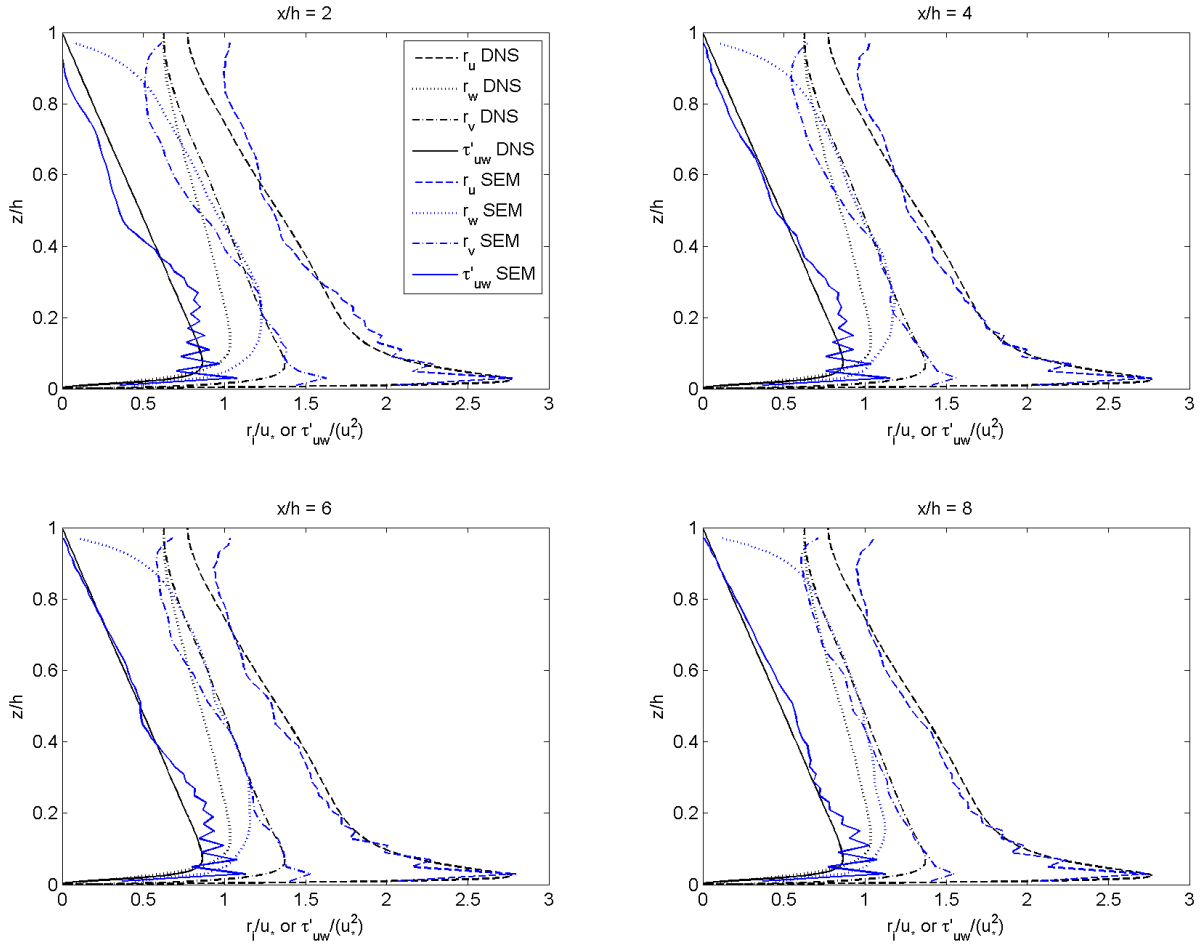

Figure 4.18: Comparison of dimensionless turbulence parameter profiles in channel flow between Dflow3D results using the synthetic eddy method (SEM) and direct numerical simulation (DNS) data by Moser et al. (1999). The dimensionless downstream coordinate is indicated above each panel.

channel flow as obtained by Moser et al. (1999). Figure 4.18 shows dimensionless profiles of r_u, r_v, r_w and τ'_{uw} at four different x-coordinates. Based on these profiles, the turbulent flow field in reference simulations is considered validated. Much higher averaging times do not lead to a significant increase of agreement with the DNS dataset.

4.2.3 Scenarios

The Dflow3D model described above will now be used to determine silt screen effectiveness as a function of several relevant parameters. These are listed below.

- The most important sensitivity parameters of this research are *relative silt screen height* h_{rel}, *depth-averaged flow velocity* U, *settling velocity* w_s and the *upstream SSC profile*. Numerical model runs with combinations of the parameter values listed in table 4.4 and the upper three concentration profiles shown in figure 4.19 will form a basic dataset. The influence of all other parameters in the remainder of this list and the lower three concentration profiles will be judged by comparing a few alternative runs to the basic dataset.

- The basic dataset is obtained with the *water depth* kept fixed at 5 m. A different wa-

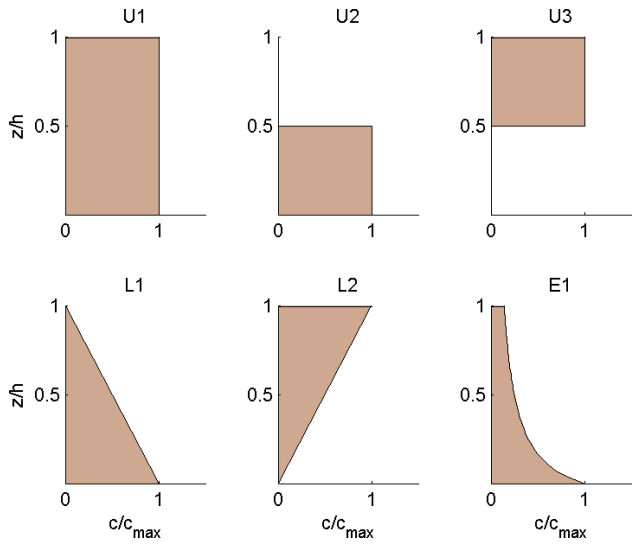

Figure 4.19: Issuing dimensionless concentration profiles used in the Dflow3D runs. The associated codes (U = 'uniform', L = 'linear', E = 'empirical') are mentioned above each profile. Only the uniform profiles are part of the basic dataset. For the empirical profile, $B = 6$ (see equation 2.9).

ter depth will certainly lead to a different silt screen effectiveness. However, the actual effectiveness will be determined as a function of dimensionless numbers (discussed in section 4.2.4). There is no need to include varying water depth in the basic dataset, as the associated dimensionless numbers are already changed by varying other parameters. To confirm the choice of dimensionless numbers, some alternative runs will be carried out with a water depth of 10 m.

- The *continuity of the issuing sediment concentration profile* may influence silt screen effectiveness to some extent. When a dredging spill persists over a longer period of time, equilibrium concentrations are reached throughout the whole model domain. The equilibrium concentrations result from a balance between sediment inflow, deposition and the transport field. As soon as equilibrium concentrations are reached, the spill is considered continuous. If the upstream end of the spill reaches the screen before a balance has been reached, the spill has got a discontinuous character. If this is the case, the time needed for the spill to pass the screen is an additional parameter of interest. The basic dataset mentioned above consists of runs with a continuous spill. Alternative runs with a discontinuous dredging spill will have passage times of 100 and 500 seconds.

- In section 2.3.3 the difference between passive and stratified turbidity was already mentioned. In the basic dataset, the maximum concentration at inflow is kept constant at 100 mg/l, which results in a passive plume. The influence of a silt screen on a passing *turbidity current* is investigated by means of additional simulations.

- In order to avoid mixing up different processes which influence SSC, *erosion* of the bed is disabled in the basic dataset. The properties of the sediment constituting the bed introduce a whole new range of sensitivity parameters, since the sediment in the plume will often not have the same properties as the sediment in the bed. By means of some alternative runs, a qualitative assessment will be made of the influence of erosion. Silt screens give rise to high near-bed velocities in the downstream jet flow. Hence it is expected that silt screens promote erosion.

- The turbulent flow field around a silt screen is mainly governed by free turbulence, resulting from flow separation near the screen's bottom edge. However, the contribution of bottom turbulence might still be significant. This is investigated by varying the *bed roughness*.

Table 4.4: Different values assigned to the parameters constituting the basic Dflow3D dataset.

h_{rel} [-]	0.25	0.5	0.75	
U [m/s]	0.05	0.1	0.3	0.5
w_s [mm/s]	10	1	0.01	

The different codes assigned to all parameter variations are omitted in this report, since individual runs will only be mentioned sporadically. Should the case arise, relevant parameters are stated explicitly.

4.2.4 Results of numerical model simulations

The effectiveness of silt screens according to each scenario described in section 4.2.3 can now be determined. Accessibility of the results can be increased by categorising all scenarios based on a set of dimensionless numbers. This dimensional analysis is very straightforward, as the parameters of interest are depth-averaged horizontal flow velocity U, undisturbed water depth h, settling velocity w_s and silt screen height h_s. It is readily seen that the two dimensionless groups following from this set are relative screen height $h_{rel} = h_s/h$ and velocity ratio $\theta = w_s/U$. h_{rel} is a measure for the degree of flow disturbance caused by the silt screen. Due to the significant deformations, in the context of simulation results h_{rel} is used to denote the relative screen height based on the effective screen height after deformation. The physical meaning of θ can be explained as the angle between the 'attacking' velocity U and the 'defending' velocity w_s. This angle is found e.g. when tracking a sediment grain which is released in a time-averaged uniform flow field without a silt screen. It is proportional to the horizontal range of attack. In the remainder of this section, the effectiveness of silt screens as a function of h_{rel} and θ when facing a continuous and a discontinuous spill will be determined consecutively.

Continuous spill

The basic dataset was said to consist of continuous spill simulations. In total, 78 basic simulations have been conducted, 30 of which have concentration profile U1, 18 have profile U2 and another 30 have profile U3. As an example, a run with $\theta = 10^{-1}$, $h_{rel,eff} = 0.5$ and concentration profile U1 will be presented first.

Figure 4.20 shows snapshots of u and C in the upper and lower panel respectively. The equilibrium situation has been reached already. The intense turbulent fluctuations generated by the silt screen are visible in both figures. It should be noted that θ is very high. Especially the settling velocity of 10 mm/s will virtually never be encountered in nature when dealing with fine sediment. Despite this favourable value, still a significant amount of suspended sediment is whirled up towards the free surface.

Although the functioning of the model is illustrated very well by these snapshots, quantitative information regarding effectiveness will have to be determined from time-averaged parameter values. Because one of the two different effectiveness parameters uses the results of a reference simulation without the silt screen, this reference simulation is incorporated in the analysis. Figure 4.21 shows time-averaged dimensionless SSC of the original simulation (upper panel) and its reference simulation (lower panel). Values are averaged over the domain width (y-direction). It stands out from these plots that on the one hand the silt screen manages to

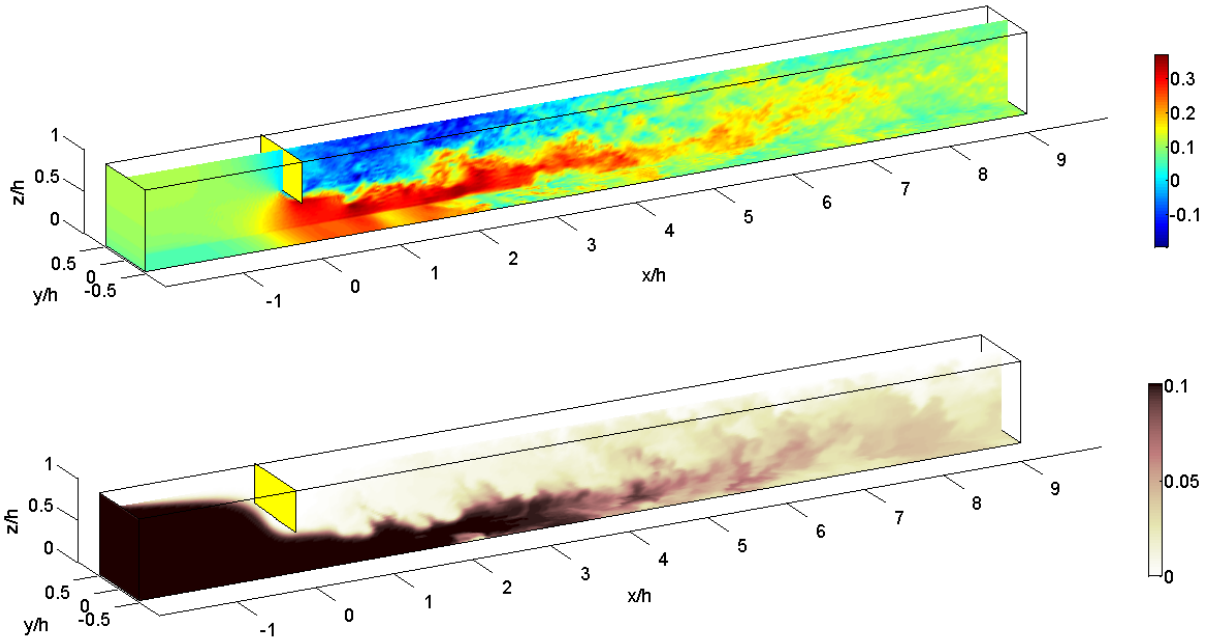

Figure 4.20: Instantaneous streamwise velocity u in m/s (upper panel) and suspended sediment concentration C in g/l (lower panel) for a Dflow3D simulation with $U = 0.1$ m/s, $h_{rel} = 0.5$, $w_s = 10$ mm/s and concentration profile U1.

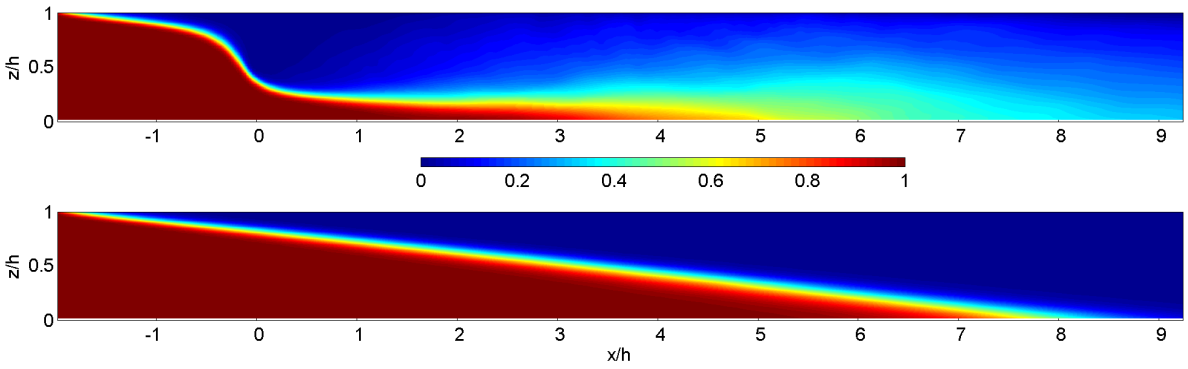

Figure 4.21: Dimensionless suspended sediment concentrations C_* for the example simulation (upper panel) and the associated reference simulation (lower panel).

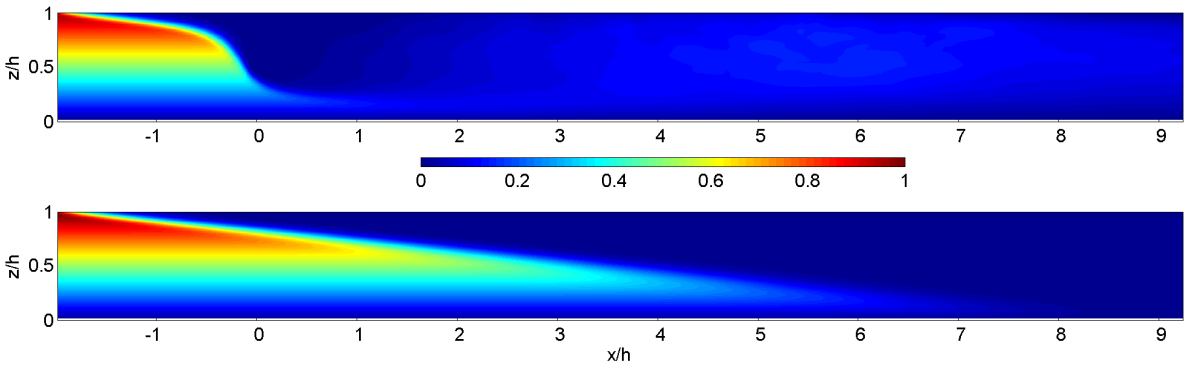

Figure 4.22: Unintegrated environmental impact potential for the example simulation (upper panel) and its reference simulation (lower panel).

reduce the maximum concentration, but on the other hand it leads to more SSC near the free surface with respect to the reference simulation. These near-surfacial concentrations are only low. The reference simulation clearly shows that a big settling velocity is not only favourable in case of a silt screen, but results in rapid settling anyway. Theoretically, the balance between settling and turbulent mixing should give rise to a Rousean sediment profile in the reference simulation. Due to the big settling velocity, the equilibrium profile has only very low concentrations and virtually all sediment is deposited. Simulations with a smaller value of θ will show more distinct Rouse profiles.

Before P is computed from C_* and z_*, an intermediate step is taken to illustrate how P is constructed. Figure 4.22 shows the non-integrated impact potential. Again, the reference run is shown in the lower panel. Although the near-surfacial suspended sediment concentrations caused by the silt screen are only low, they result in a significant impact potential due to their big z-coordinate. In the reference run, all the sediment settles gradually without too much mixing. As soon as the region of high SSC does not extend too high in the water column, the impact potential quickly approaches zero.

Integration over z_* now results in graphs of $P(x)$ for both simulations. This is shown in the upper panel of figure 4.23. Locally, the silt screen does what it is intended to by reducing the impact potential. However, further than about four times the water depth downstream, the reference run shows lower values of P. The middle panel shows $E_{in}(x)$ of the simulation with a silt screen. A maximum effectiveness of 92% is reached, but this quick win partly diminishes further downstream. At about 6 times the water depth downstream of the screen, the settling velocity starts to dominate the transport field again. Finally, in the lower panel $E_{ref}(x)$ is shown. When compared to the reference simulation, the silt screen has a negative effectiveness of -17% at 7 times the water depth downstream. This percentage gradually reduces towards 0 further downstream, since eventually all sediment is deposited in both simulations.

The presented example simulation has a very high settling velocity (w_s = 10 mm/s). To give an impression of the full range of settling velocities, figure 4.24 shows the impact potential and effectiveness for a run with w_s = 0.01 mm/s. All other parameters remain the same. Due to the small w_s, downstream of the screen SSC spreads out over the full water column again. Equilibrium concentrations are more or less equal to the inflow concentration. During the reference simulation, hardly any settling occurs within the length of the numerical domain. Therefore the reference SSC profile at $6h$ downstream of the silt screen closely resembles the inflow profile. As a result E_{in} and E_{ref} do not differ noticeably.

All runs of the basic dataset are treated in a similar manner. The contour lines in figure 4.25

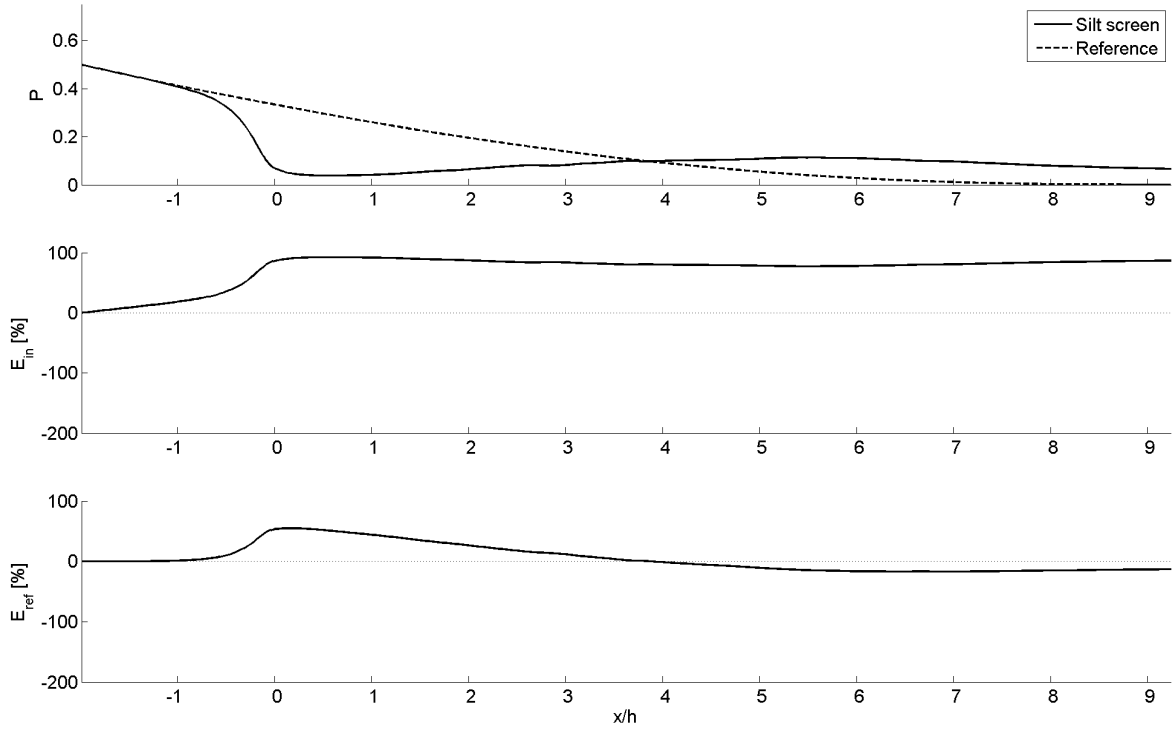

Figure 4.23: Environmental impact potential P (upper panel), inflow effectiveness E_{in} (middle panel) and reference effectiveness E_{ref} (lower panel). The fundamental difference between both effectiveness parameters is shown by their different implications: judging from E_{in} the screen is effective, but judging from E_{ref} it is not.

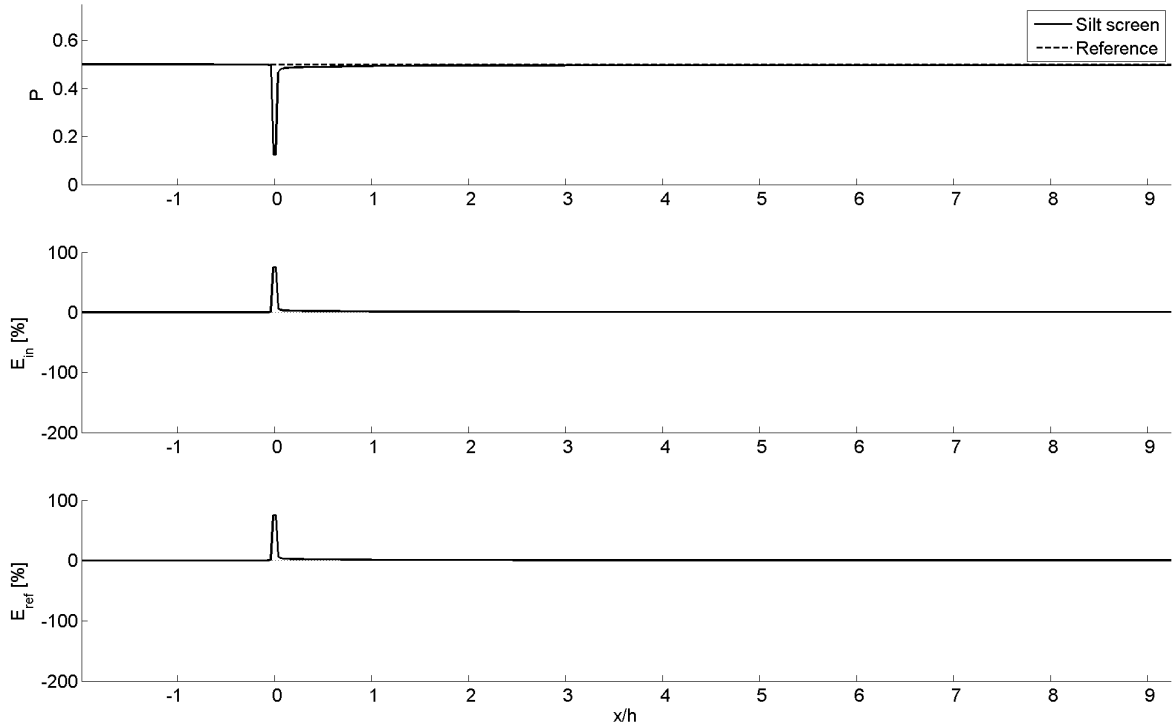

Figure 4.24: Environmental impact potential P (upper panel), inflow effectiveness E_{in} (middle panel) and reference effectiveness E_{ref} (lower panel) for a simulation with $w_s = 0.01$ mm/s. The absence of significant settling leads to maximum concentrations throughout the whole domain.

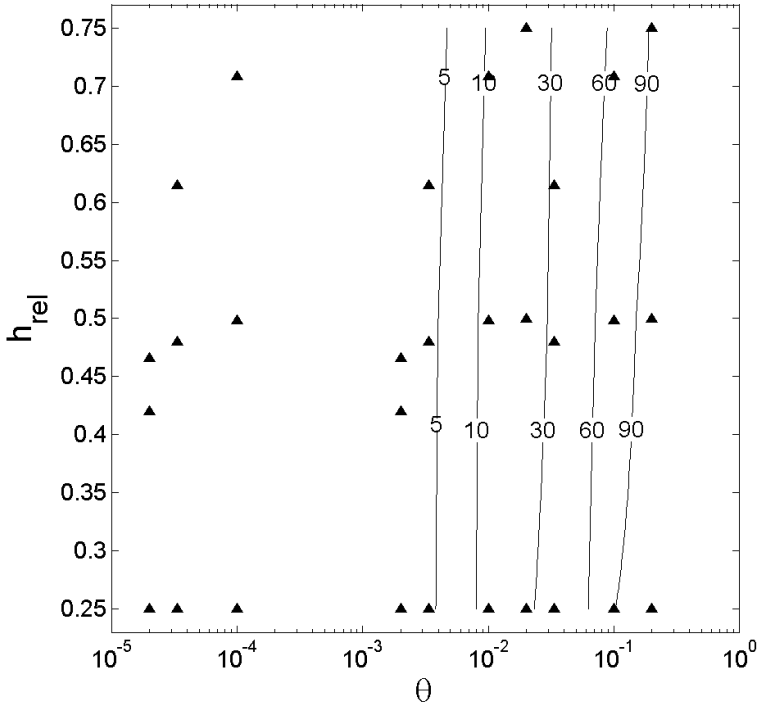

Figure 4.25: Inflow effectiveness $E_{in}(6h)$ is displayed for issuing SSC profile U1 as a function of θ and h_{rel}. The black markers indicate the actually obtained data points. $E_{in}(x)$ will never attain a negative value for inflow profile U1, as P is at its maximum for this profile.

represent the values of $E_{in}(6h)$ for concentration profile U1 as a function of h_{rel} and θ. Note that θ is displayed on a logarithmic scale. In appendix H all effectiveness plots which are discussed in this section are presented together with the original values of the data points. Iso-effectiveness contours are constructed from interpolation. Suppose a field situation with water depth $h = 10$ m, screen height $h_s = 5$ m after deformation, flow velocity $U = 0.05$ m/s and settling velocity $w_s = 0.1$ mm/s. In that case, $h_{rel} = 0.5$ and $\theta = 2 \cdot 10^{-3}$. From figure 4.25 it follows that $E_{in}(6h)$ is in between 0 and 5%. Figure H.4 in appendix H reveals an inflow effectiveness of about 3%. It is clear that especially the bigger values of θ result in high effectiveness due to more deposition. For low values of θ, effectiveness approaches zero. Mixing fully dominates the downstream transport field in that case. In the complete domain, concentrations are almost equal to the inflow concentration. Diffusion is only able to lower maximum concentrations and since profile U1 consists of the maximum concentration over the full water depth, negative values of E_{in} can not be reached. The effectiveness asymptotically decreases towards zero for disadvantageous conditions.

A relation between E_{in} and h_{rel} can only be noticed for bigger values of θ. A higher h_{rel} means more disturbance of the flow, which counteracts the increased settling at higher θ. Significant effectiveness only occurs when θ is higher than about $5 \cdot 10^{-1}$, which is not likely to occur in practice.

In figure 4.26 the inflow effectiveness $E_{in}(6h)$ is given for concentration profile U2. Again, a positive relation between E_{in} and θ can be seen for higher values of the latter. In addition, a clearly negative relation exists between the effectiveness and h_{rel}. In contrast to profile U1, profile U2 is already in its most positive form at inflow. Therefore, positive effectiveness can only be reached through extensive settling and low mixing. This is the case for high θ and low h_{rel}, but as the figure shows this does not result in positive effectiveness within the region of

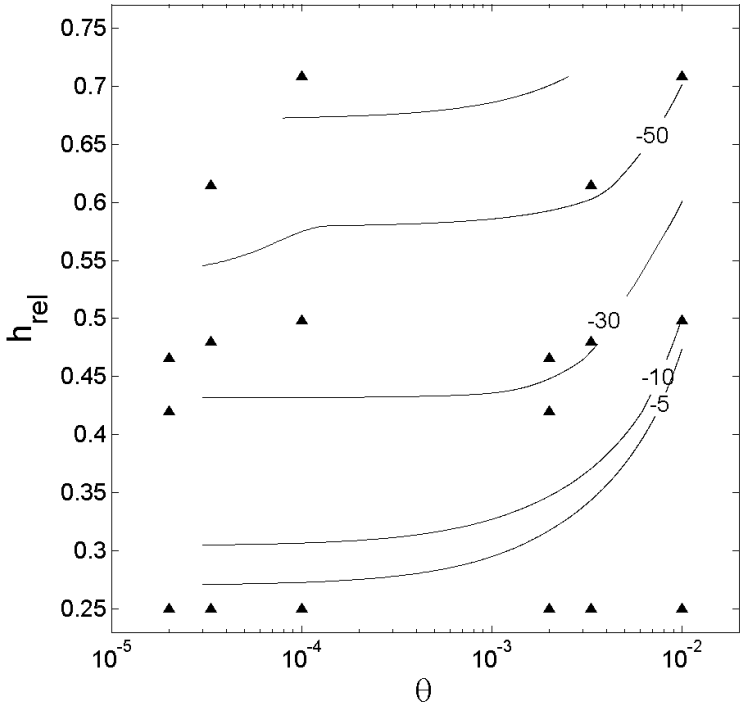

Figure 4.26: Inflow effectiveness $E_{in}(6h)$ for issuing SSC profile U2.

realistic θ values.

The inflow effectiveness of simulations with concentration profile U3 is presented in figure 4.27. The high inflow concentrations near the free surface imply that the inflow profile is in its most damaging form. Negative effectiveness does therefore not occur. The right part of the figure closely resembles the effectiveness pattern for profile U1, but deviations occur in the left part. For low values of θ, a positive relation exists between E_{in} and h_{rel}. The relative screen height is a measure for flow disturbance and hence mixing. For increasing h_{rel}, downstream mixing intensifies and diffusion towards the lower half of the water column results in slightly positive effectiveness.

Up to this point, only E_{in} has been regarded. Of both silt screen effectiveness parameters, this is the most favourable one. Only for unrealistically high values of θ, concentration profiles U1 and U3 were significantly reduced by the screen. Now $E_{ref}(6d)$ will be discussed. This is only done for profile U1 and U3, as no consistent effectiveness pattern can be found in the h_{rel}-θ plane for profile U2. However, discussion of E_{in} already showed that silt screens will always have a negative influence on inflow profiles of type U2.

In figure 4.28 E_{ref} is displayed for profile U1. The positive effectiveness for higher θ has completely vanished. Apparently, a favourable settling parameter is more advantageous in the undisturbed situation than it is in case of a silt screen. At very high θ, the effectiveness becomes less negative again. Between values of about $2 \cdot 10^{-2}$ and $2 \cdot 10^{-1}$, the effect of the favourable velocity ratio is already noticeable, but screen-induced mixing is still able to counteract settling. This also leads to a relation between E_{ref} and h_{rel} in the aforementioned region. A bigger relative screen height represents more intense mixing, but also leads to a lower z-coordinate of SSC immediately downstream of the screen. The balance between both effects results in a

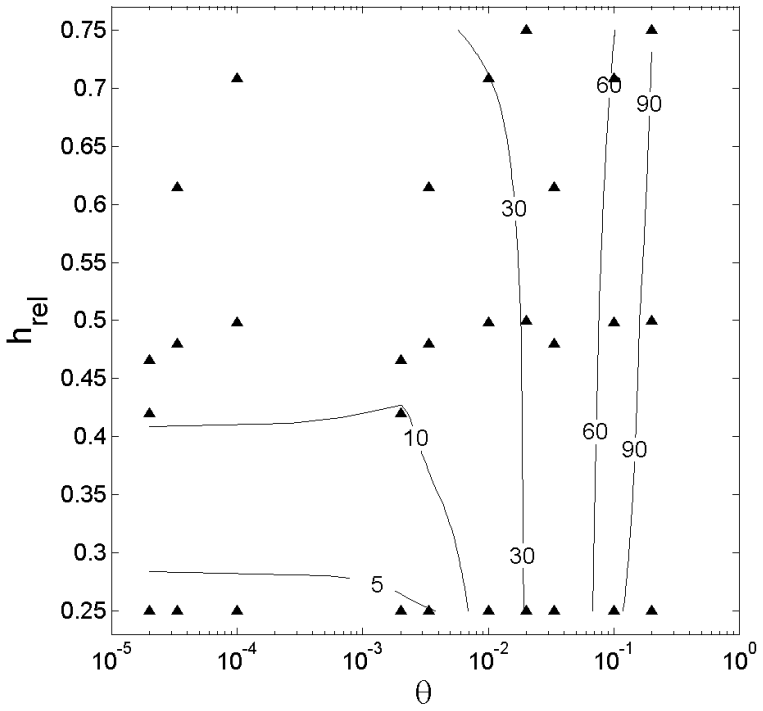

Figure 4.27: Inflow effectiveness $E_{in}(6h)$ for issuing SSC profile U3.

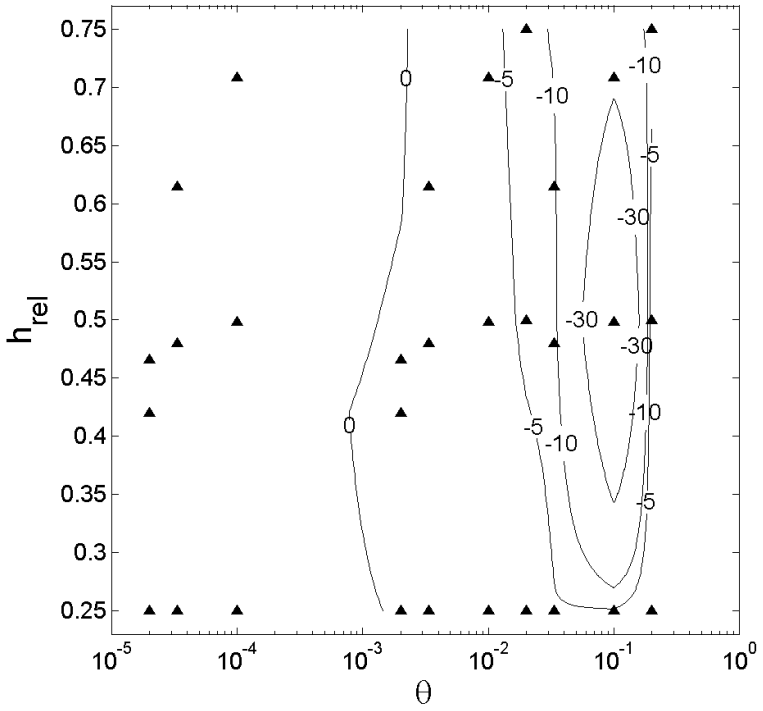

Figure 4.28: Reference effectiveness $E_{ref}(6h)$ for concentration profile U1.

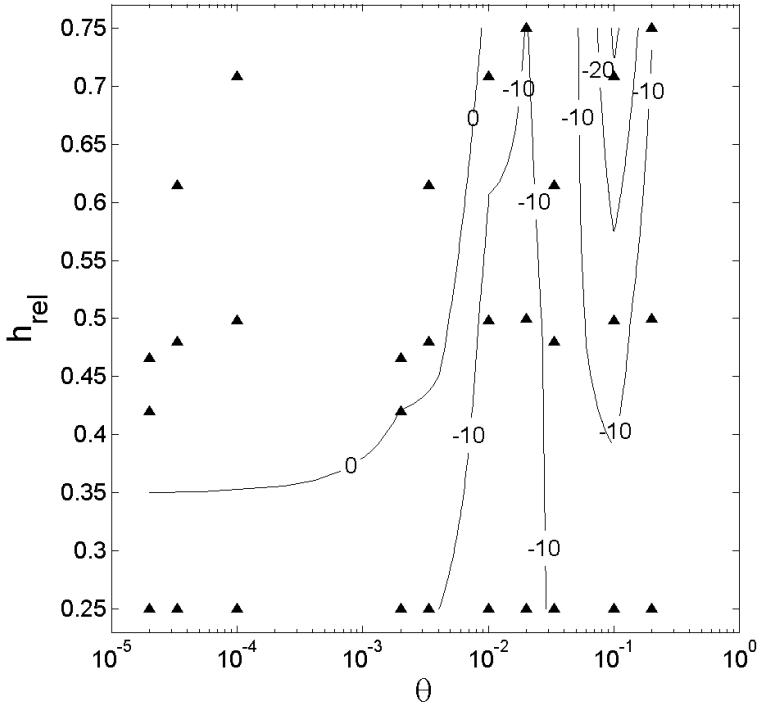

Figure 4.29: Reference effectiveness $E_{ref}(6h)$ for concentration profile U3.

minimum effectiveness around $h_{rel} = 0.5$. Small positive effectiveness still occurs for very low θ, but the percentage remains far too low to make silt screens meaningful.

Finally, E_{ref} is shown for profile U3 in figure 4.29. It is difficult to establish consistent relations between h_{rel}, θ and E_{ref}. Only the positive relation between E_{ref} and h_{rel} for low values of θ, stands out, which was also noticed for E_{in}. Significantly positive reference effectiveness is not reached within the displayed, realistic parameter space.

On the whole, a couple of things are made clear by this analysis:

- Only under very favourable settling circumstances, the downstream screen-induced mixing is dominated by settling. These circumstances are not likely to be encountered in nature.

- When settling circumstances are very favourable, this does not only improve silt screen performance, but it also leads to quick settling in the undisturbed situation. In fact, the screen-induced mixing (with a negative influence on SSC) always dominates the local divergence effect (positive influence) of a silt screen.

- Regarding the concentration profile, it is noticed that silt screens have an explicitly unfavourable influence when SSC only occur in the lower part of the water column. Near-bed concentrations should be left undisturbed, since their settling time is already greatly reduced by their position.

Continuous spill - Alternative simulations

Now the alternative scenarios will be discussed. The full list was provided in section 4.2.3. The alternative simulations are characterised by their values of θ and h_{rel}, which enables comparison with figures 4.25, 4.26, 4.27, 4.28 and 4.29.

First, the influence of a different water depth will be assessed. The basic dataset was obtained at a water depth of 5 m. If silt screen effectiveness scales with h_{rel} and θ, the alternative simulations with a water depth of 2.5 m should not show any difference concerning effectiveness. Table 4.5 contains the effectiveness percentages obtained for simulations with a water depth of 2.5 m.

Table 4.5: Simulations with $h = 2.5$ m. The 'basic' column indicates the corresponding percentage at $h = 5$ m.

θ	$\mathbf{h_{rel}}$	**Profile**	$\mathbf{E_{in}(6h)}$	Basic	$\mathbf{E_{ref}(6h)}$	Basic
$3.3 \cdot 10^{-3}$	0.25	U1	5%	0 to 5%	-1%	-5 to 0%
$3.3 \cdot 10^{-3}$	0.48	U1	5%	0 to 5%	-1%	-5 to 0%
$3.3 \cdot 10^{-3}$	0.61	U1	5%	0 to 5%	-1%	-5 to 0%

All effectiveness percentages correspond with their position in the h_{rel}-θ plane of figure 4.25 and 4.28. Hence, silt screen effectiveness may be regarded independent of water depth, which also overrules the Froude number as a relevant scaling parameter for silt screen effectiveness.

Furthermore, the remaining three concentration profiles have been applied as an upstream boundary condition. Simulations with profile L1, L2 and E1 (see figure 4.19) were carried out, along with their associated reference simulations without a silt screen. The results are listed in table 4.6.

Table 4.6: Simulations with concentration profiles L1, L2 and E1.

θ	$\mathbf{h_{rel}}$	**Profile**	$\mathbf{E_{in}(6h)}$	$\mathbf{E_{ref}(6h)}$
10^{-2}	0.25	L1	15%	-3%
10^{-2}	0.71	L1	-19%	-37%
10^{-2}	0.25	L2	14%	-9%
10^{-2}	0.71	L2	25%	2%
10^{-2}	0.25	E1	15%	6%
10^{-2}	0.71	E1	-11%	-19%

Profile L1 can be seen as an intermediate profile between U1 and U2. This also follows from the effectiveness values. For low values of h_{rel}, profile L1 resembles profile U1 in terms of silt screen effectiveness. At higher values of h_{rel} profile L1 behaves more like profile U2. The presence of a vertical concentration gradient in the inflow profile results in stronger dependence on h_{rel}.

In the same way, profile L2 can be thought of as an intermediate profile between U1 and U3. Again the concentration gradient in the inflow profile induces dependence on h_{rel}.

Finally, profile E1 is more or less an intermediate profile between U1 and L1. The relationship between the effectiveness and h_{rel} still exists, but is less explicit than with profile L1.

With the next alternative simulations, the influence of bed erosion is investigated. The erosion rate M_e (see appendix D.2.1) has been set to 10^{-4} kg/(sm^2), which is a moderate value. The

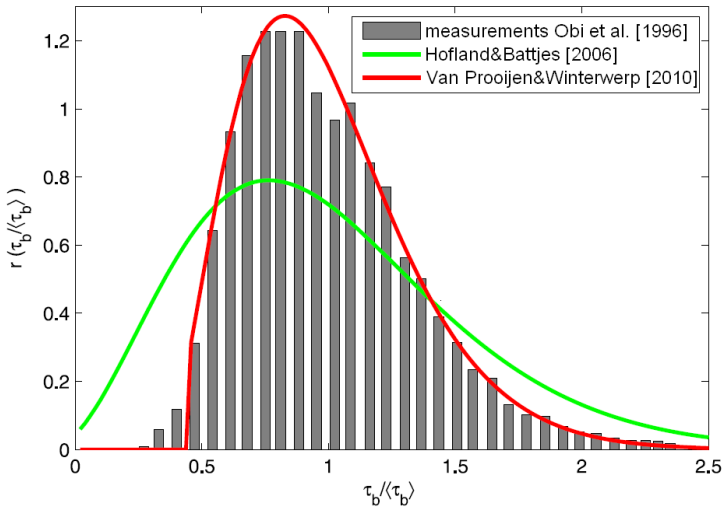

Figure 4.30: Probability density distributions of dimensionless bed shear stress as derived by Obi et al. (1996), Hofland and Battjes (2006) and Van Prooijen and Winterwerp (2010). Modified after Van Prooijen and Winterwerp (2010).

threshold bed shear-stress for erosion τ_e is chosen to be 0.15 N/m^2. An unlimited amount of bed material is available for erosion. Table 4.7 lists the results.

Table 4.7: Simulations with bed erosion.

θ	$\mathbf{h_{rel}}$	**Profile**	$\mathbf{E_{in}(6h)}$	Basic	$\mathbf{E_{ref}(6h)}$	Basic
$2 \cdot 10^{-5}$	0.47	U2	-63%	-50 to -30%	-54	n/a
$2 \cdot 10^{-5}$	0.47	U3	9%	10 to 30%	2%	0 to 10%

More sediment is now added to the water column by bed erosion. Flow contraction underneath the silt screen results in a bigger bed shear stress and more erosion accordingly. This only appears to have a significant, negative influence when a negative vertical concentration gradient is present (profile U2). This gives rise to rapid upward diffusion of the eroded sediment. When the gradient is positive (profile U3), hardly any influence of bed erosion is observed.

A more generalised quantification of silt-screen induced erosion is obtained by determining the dimensionless erosion rate (equal to the excess bed shear stress) for every simulation. Time-averaged flow fields are used in order to determine the near bed velocity u_0. The approach followed here differs from the linear formulation presented in appendix D (Partheniades, equation D.7). Instead, the formulation proposed by Van Prooijen and Winterwerp (2010) is used, which produces a more realistic onset of erosion. Figure 4.30 shows the probability-density function of dimensionless bed shear stress as found by different authors. The heavy right-hand side tail of the distributions results from extreme instantaneous velocities in the turbulent flow field. It gives rise to a non-zero erosion rate when the time-averaged bed shear stress $\langle \tau_0 \rangle$ is lower than the critical bed shear stress τ_e. This is in contradiction with Partheniades' equation. Van Prooijen and Winterwerp (2010) have reworked the distribution derived by Hofland and Battjes (2006) and combined it with the linear erosion formulation. The resulting analytical expression for the dimensionless rate of erosion R_E may be represented by a third order polynomial, see equation 4.1. With respect to equation D.7, R_E is equal to the mass flux $\mathrm{d}m/\mathrm{d}t$

divided by M.

$$\begin{aligned} R_E &= 0 && \text{for } \frac{\langle\tau_0\rangle}{\tau_e} < 0.52 \\ R_E &= a_1\left(\frac{\langle\tau_0\rangle}{\tau_e}\right)^3 + a_2\left(\frac{\langle\tau_0\rangle}{\tau_e}\right)^2 + a_3\left(\frac{\langle\tau_0\rangle}{\tau_e}\right) + a_4 && \\ R_E &= \frac{\langle\tau_0\rangle}{\tau_e} - 1 && \text{for } \frac{\langle\tau_0\rangle}{\tau_e} > 1.7 \end{aligned} \tag{4.1}$$

In this equation, $a_1 = -0.144$, $a_2 = 0.904$, $a_3 = -0.823$, $a_4 = 0.204$, M is the dimensional erosion rate and $\langle\tau_0\rangle$ is the mean bed shear stress, which follows straightforwardly from $\langle\tau_0\rangle = \rho u_*|u_*|$. Shear velocity u_* is determined with Nikuradse's equations for rough and smooth walls, which will not be treated in detail here. Again, $\tau_e = 0.15$ N/m^2 is adopted as the critical bed shear stress for erosion.

The dimensionless rate of erosion $R_E(x, y)$ is now integrated over the length of the model domain L_m along the central axis ($y = 0$). The ratio of this integrated rate of erosion in a run with silt screen over the same parameter in the associated reference run is a measure for silt screen induced erosion and is called the silt screen induced erosion factor F_E, see equation 4.2.

$$F_E = \frac{\int_0^{L_m} R_E(x,0)\mathrm{d}x}{\int_0^{L_m} R_{E,ref}(x,0)\mathrm{d}x} \tag{4.2}$$

Unfortunately, the presence of a silt screen increases the bed shear stress over a stretch which continues well outside the model domain. Furthermore F_E depends non-linearly on τ_e. Hence it is not possible to present general, absolute values of the increase of erosion, but the values of F_E obtained with the model results still give a good view of the relative increase for all scenarios. It appears that F_E is a function of Fr and h_{rel}. Figure 4.31 shows contours of equal F_E in the Fr-h_{rel} plane. The triangular markers indicate the actually obtained dataset. The contours are constructed from interpolation. It appears that F_E mainly depends on the relative screen height. Only for low Froude numbers a significant dependency on Fr is found. Although the values of F_E presented in the figure may not be regarded as absolute erosion enhancement factors, they are still a good indication for the order of magnitude of this factor. Bearing this in mind, it can be concluded that silt screens greatly enhance erosion.

Now, the influence of the bed roughness on silt screen effectiveness is investigated. The basic dataset was obtained using a Nikuradse bed roughness k_N of 0.01 m. Alternative runs have been conducted with $k_N = 0.05$ m. The results are listed in table 4.8.

Table 4.8: Simulations with higher bed roughness.

θ	$\mathbf{h_{rel}}$	**Profile**	$\mathbf{E_{in}(6h)}$	Basic	$\mathbf{E_{ref}(6h)}$	Basic
10^{-2}	0.25	U1	13%	10 to 30%	0%	-5 to 0%
$2 \cdot 10^{-5}$	0.47	U1	0%	0 to 5%	0%	0 to 5%

These percentages do not differ from the ones obtained for $k_N = 0.01$ m. This underlines that the flow and transport field around a silt screen is highly dominated by screen-induced free turbulence rather than bottom-induced wall turbulence.

Finally, the influence of a silt screen on a turbidity current is assessed. To this end the passive concentration of 0.1 g/l used in the basic dataset is increased to 50 g/l. Furthermore, $U = 0.3$ m/s, $h_{rel} = 0.5$, $h = 5$ m and the inflowing sediment concentrations obey to profile U2. Figure

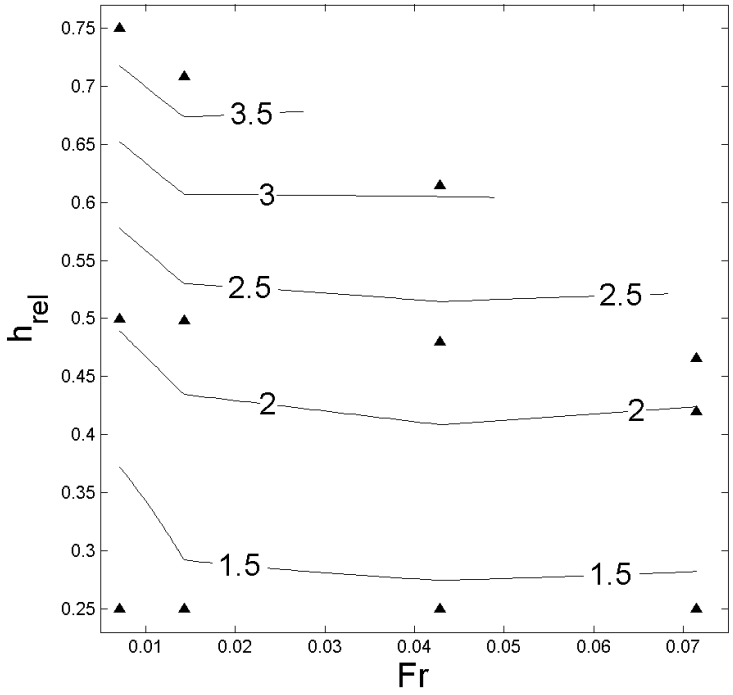

Figure 4.31: Values of the silt screen induced erosion factor F_E in the dimensionless Fr-h_{rel} plane.

4.32 displays the resulting SSC of the simulation itself (upper panel) and its associated reference simulation (lower panel). Profiles of streamwise velocity $\bar{u}$ are added in white. The results clearly show a two-layer stratified flow. The silt screen only protrudes into the upper layer. Flow contraction and hence reduction of the pressure in the upper layer gives rise to a vertical expansion of the turbidity current. Although a part of the turbidity current is slowed down by the expansion, continuity requires that the flux of suspended sediment does not change. Only if the low velocity of the dense layer allows for rapid deposition, the silt screen has a beneficial influence on the turbidity current. Figure 4.33 proves that this is not the case. The decreased rate of deposition and the higher environmental impact potential of the downstream flow profiles lead to the conclusion that silt screens do not have a favourable influence on turbidity currents. There is no reason to believe that different values of Fr or h_{rel} lead to a fundamentally different behaviour.

Discontinuous spill

It was mentioned in section 4.2.3 that the occurrence of an equilibrium concentration field differentiates between continuous and discontinuous dredging spills. After having discussed the former above, the effectiveness of discontinuous dredging spills will be addressed below. The big difference in case of a discontinuous spill is constituted by the much bigger SSC gradients, since the region downstream of the silt screen has not been filled with sediment up to the equilibrium concentrations.

The behaviour of a discontinuous spill is demonstrated in figure 4.34. The figure shows four consecutive snapshots of SSC for a simulation with $U = 0.3$ m/s, $h_{rel} = 0.5$, $w_s = 10^{-4}$ mm/s, $C_{max} = 0.1$ g/l, concentration profile U1 and spill inflow duration $t_s = 100$ s. Reference is made to the theoretical analysis of transport processes as presented in chapter 2. The influence of upstream dispersion through differential (mean) advection and downstream turbulent diffusion

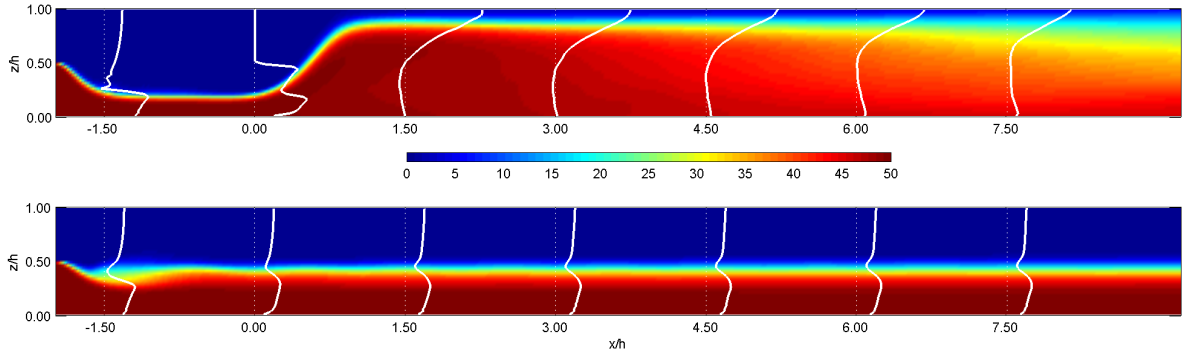

Figure 4.32: Simulation of a turbidity current passing a silt screen (upper panel) and a reference simulation without a silt screen (lower panel). The colourscale represents time-averaged concentrations $\bar{C}$ (g/l) and the white profiles represent streamwise time-averaged velocity $\bar{u}$.

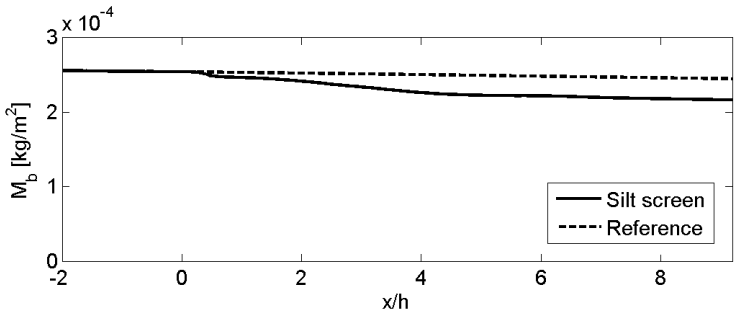

Figure 4.33: Bed mass M_b deposited along the central axis of the numerical domain at the end of the simulation (t = 2360 s). The increased velocity shear due to deceleration in the dense layer in case of a silt screen leads to less favourable settling conditions.

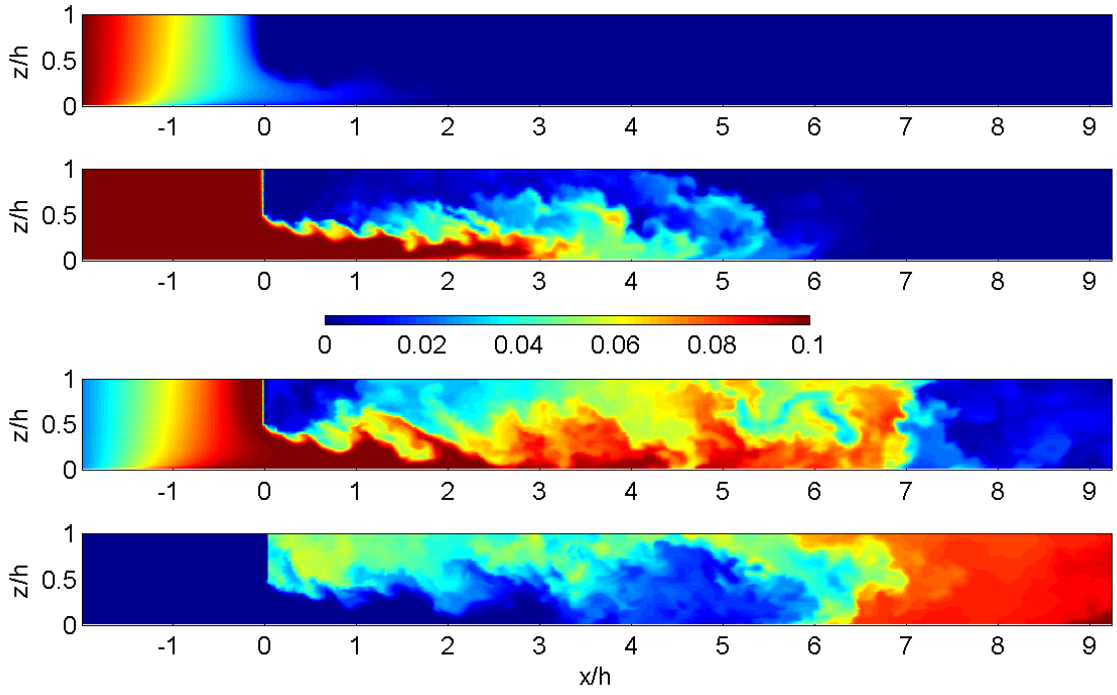

Figure 4.34: Four consecutive stages in time of suspended sediment concentrations (g/l). The inflow duration of the spill is 100 seconds. From top to bottom, the panels represent $t = 55$ s, $t = 100$ s, $t = 145$ s and $t = 235$ s respectively.

can be distinguished. Concentrations are effectively reduced and hence spread out over a larger volume of water. As a result of the relationship between z and P, reduction of concentrations alone is not necessarily beneficial from an environmental point of view. Only if SSC is kept low enough in the water column a significant reduction of P can be achieved. Because no equilibrium concentration has been reached yet, $P(x,t)$ is still a function of both downstream distance and time. The upper panel of figure 4.35 shows timeseries of both $P(6h,t)$ and $P(-2h,t)$. Apparently the peak value is reduced, but the spill is given a hazardous trailing edge, with fairly low concentrations at high positions in the water column. For discontinuous spills, integration of $P(6d,t)$ over the time domain is still needed to obtain an absolute measure for the environmental impact potential. Therefore, the discontinuous environmental impact potential is defined as $P_d(x) = \int_0^\infty P(x,t)\,\mathrm{d}t$. The lower panel of figure 4.35 shows the evolution of this integral in time for both $x = 6h$ and $x = -2h$. According to expectations after having seen the upper panel, the integral at $x = 6h$ attains more or less the same value as the integral at $x = -2h$. The inflow effectiveness for discontinuous spills $E_{in,d}$ can now be computed according to equation 4.3.

$$E_{in,d}(x) = \frac{P_{in,d} - P_d(x)}{P_{in,d}} \cdot 100\% \tag{4.3}$$

Analogous to the method for continuous spills, reference simulations without a silt screen allow for the computation of $E_{ref,d}$, see equation 4.4.

$$E_{ref,d}(x) = \frac{P_{ref,d}(x) - P_d(x)}{P_{in,d}} \cdot 100\% \tag{4.4}$$

The development of $P(x,t)$ and its integral over time for $x = 6h$ and $x = -2h$ during a reference run is now shown in the upper and lower panel of figure 4.36 respectively. During a reference run, the geometry of the spill hardly changes as it translates through the domain, except for

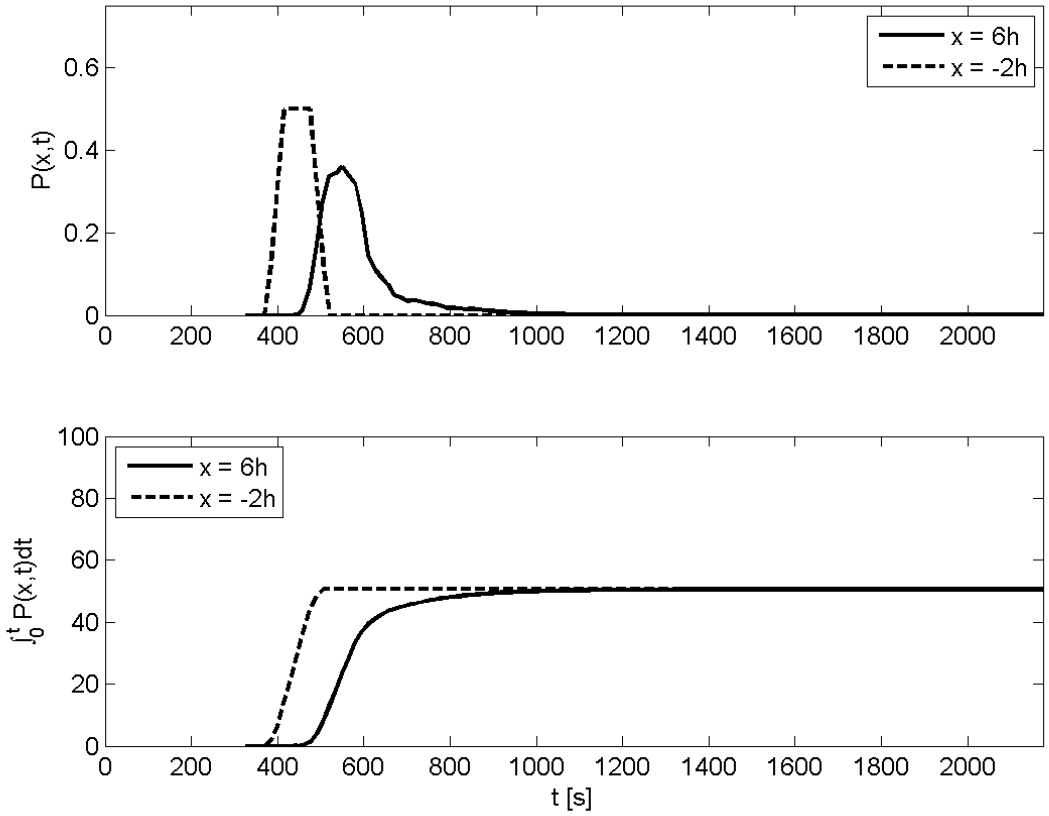

Figure 4.35: Development of environmental impact parameters in time for the same discontinuous run. The upper panel shows $P(x,t)$ for $x = 6h$ as well as $x = -2h$. The lower panel shows the same curves integrated over the time domain $\int_0^t P(x,t)\,\mathrm{d}t$.

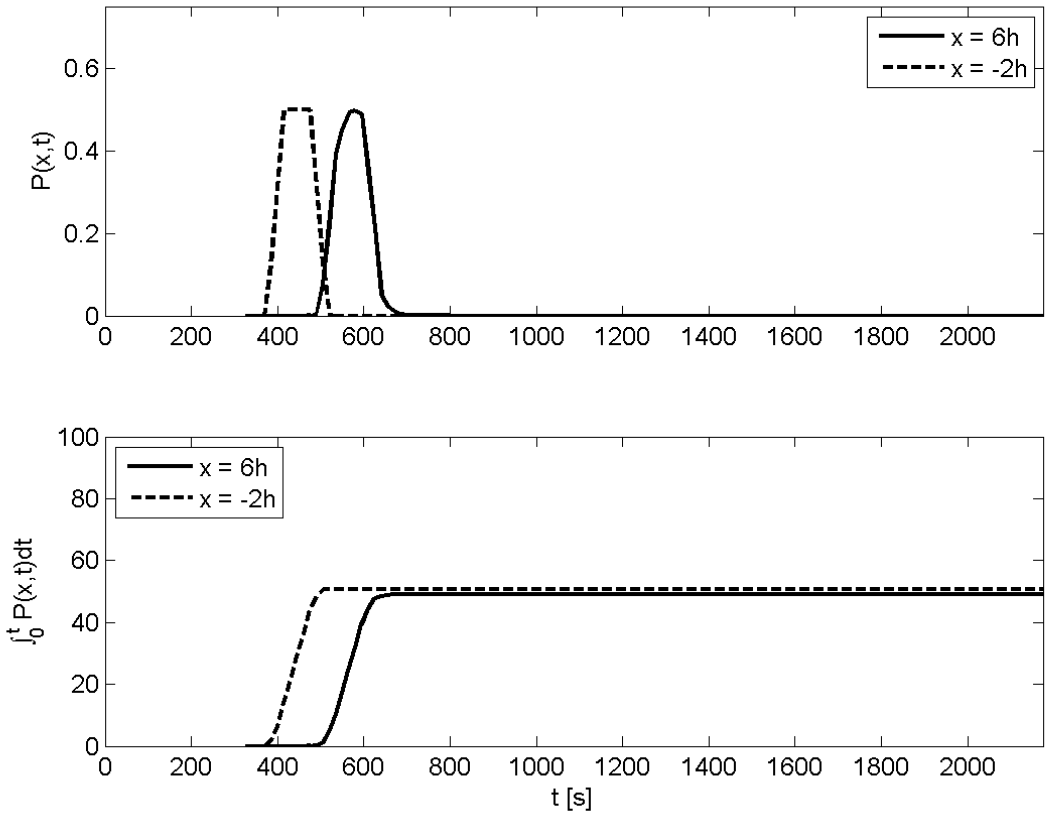

Figure 4.36: Development of environmental impact parameters in time during the reference simulation. $P(6h, t)$ and $P(-2h, t)$ are shown in the upper panel and their time-integrated counterparts are shown in the lower panel.

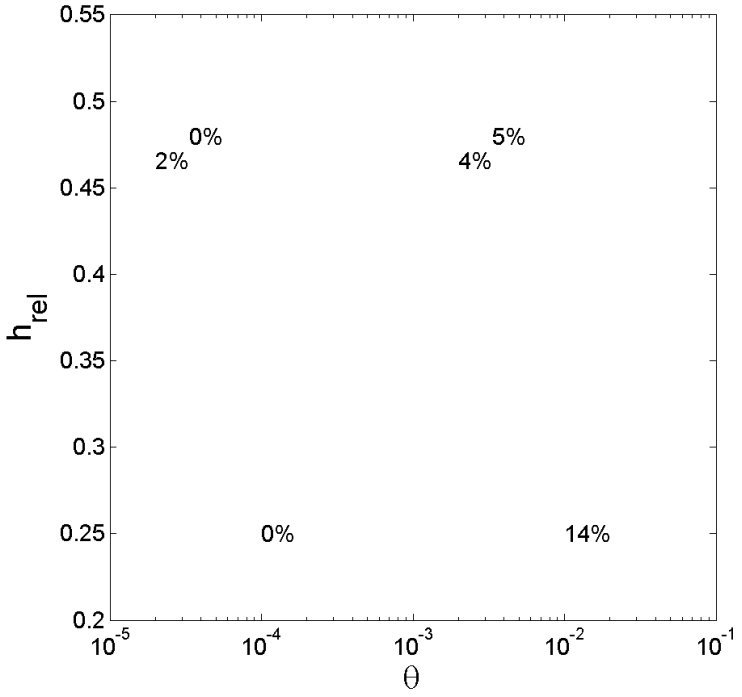

Figure 4.37: Discontinuous inflow effectiveness $E_{in,d}(6h)$ as a function of θ and h_{rel} for concentration profile U1.

some settling and some longitudinal diffusion. The former leads to a very slight decrease of the time-integrated impact potential over downstream distance x. From the lower panels of figure 4.35 and 4.36, the value of $E_{ref,d}(6h)$ belonging to this example simulation can be determined.

In total, 24 discontinuous dredging spills have been simulated. For inflow duration t_s the values 100 s and 500 s were adopted. With the incorporation of t_s as a relevant parameter, an additional dimensionless number can be constructed, see equation 4.5.

$$\alpha = \frac{Ut_s}{h} \tag{4.5}$$

In physical terms, α represents the aspect ratio of the dredging spill, being the ratio of its initial length over the water depth. It is a measure for the length of spill boundary exposed to large concentration gradients. Big values of α imply a (geometrically) long spill, which has less potential to mix thoroughly with ambient clear water. For small values of α this is the other way around. For continuous spills, α goes to infinity. Figure 4.37 shows the discontinuous inflow effectiveness $E_{in,d}(6d)$ for concentration profile U1 in the dimensionless θ-h_{rel} plane. The figure does not reveal dependency of the effectiveness on α. However, every data point represents the mean value of two simulations with different values of α. It is found that the effectiveness depends only marginally on α (deviations remain within 3%) and is largely determined by h_{rel} and θ. Only 6 data points are obtained, but yet they show a clear trend. For increasing θ, the effectiveness increases as well. Thus, the more settling can take place, the higher the discontinuous inflow effectiveness gets. This corresponds to the previously drawn conclusions regarding continuous spill. A relation with h_{rel} is less evident. At higher θ a slightly negative relation seems to exist between $E_{in,d}$ and h_{rel} as a result of extensive mixing at higher relative screen height. The values in figure 4.37 correspond well to those obtained for continuous spill (figure 4.25).

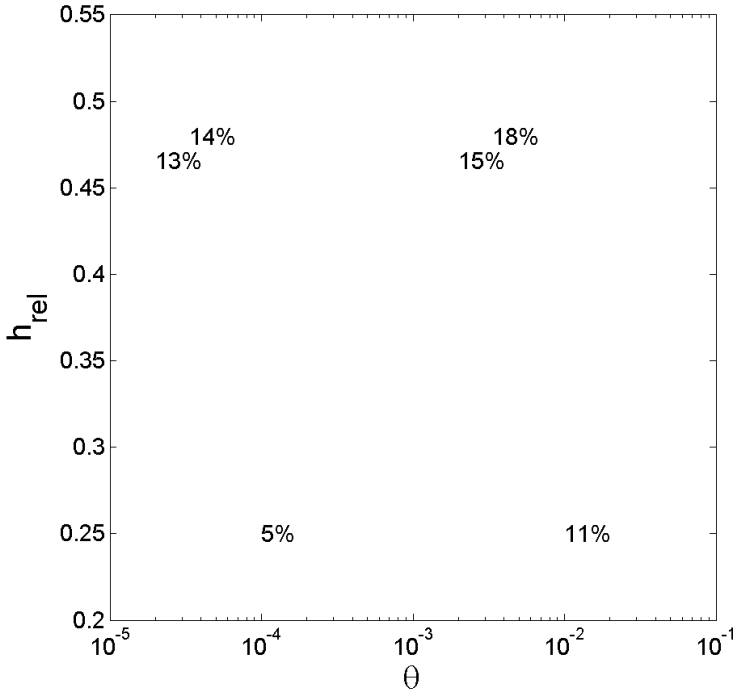

Figure 4.38: Discontinuous inflow effectiveness $E_{in,d}(6h)$ as a function of θ and h_{rel} for concentration profile U3.

A similar analysis can be carried out for inflow profile U3. The result is shown in figure 4.38. Again, the effectiveness is displayed as a function of h_{rel} and θ. Deviations due to varying α range up to 6%. In contrast to inflow profile U1, now a positive relation exists between $E_{in,d}$ and h_{rel}. More intense screen-induced mixing transports more sediment to lower z-coordinates. Again, the results for discontinuous spills with inflow profile U3 closely resemble those for continuous spills (figure 4.27).

The lower panel of figure 4.36 already revealed that in a reference simulation P_d only changes very slowly over downstream distance x. Therefore, the discontinuous reference effectiveness $E_{ref,d}(6h)$ is expected to be of the same order as $E_{in,d}(6d)$. $E_{ref,d}(6d)$ is shown in figure 4.39 and 4.40 for profile U1 and U3 respectively. Only the data points with $h_{rel} = 0.25$ show significant differences with the continuous reference effectiveness E_{ref}. This is caused by the fact that these data stem from simulations with $U = 0.1$ m/s. The smaller intensity of wall turbulence gives rise to a high Richardson number. Instable horizontal (profile U1) or vertical (profile U3) stratification leads to a collapse of the concentration profile during reference simulations. Negative buoyancy moves high concentrations to a lower position in the water column, which effectively decreases P. This behaviour is considered an artifact of the schematic sediment profiles with sharp concentration gradients and is therefore ignored. The values of $E_{ref,d}$ at higher h_{rel} are of the same order as their counterparts for continuous spill (figure 4.28 and 4.29).

In summary, the effectiveness of silt screens may be regarded insensitive to the inflow duration of the dredging spill. Although concentrations are reduced stronger for a short inflow duration, the percentage of the total sediment mass passing at every downstream z-coordinate is equal for continuous and discontinuous spills.

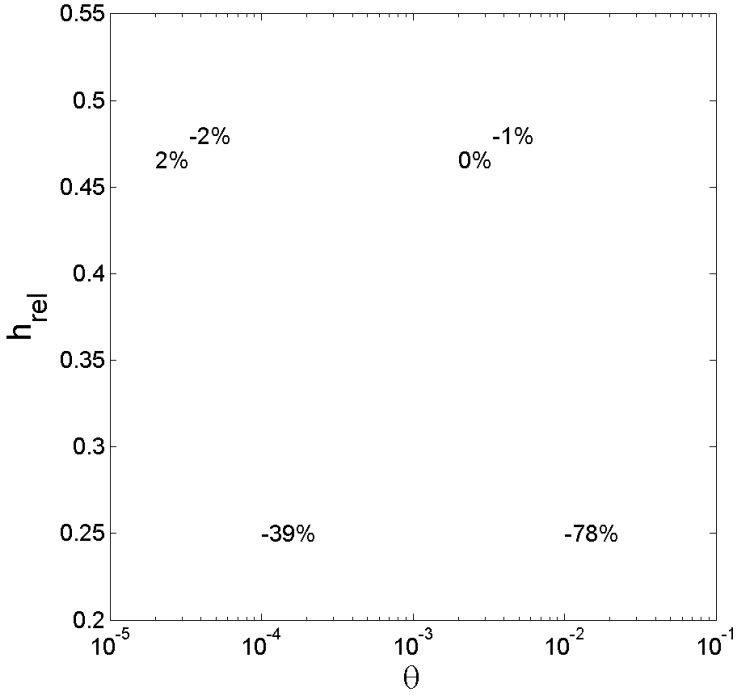

Figure 4.39: Discontinuous reference effectiveness $E_{ref,d}(6h)$ as a function of θ and h_{rel} for concentration profile U1.

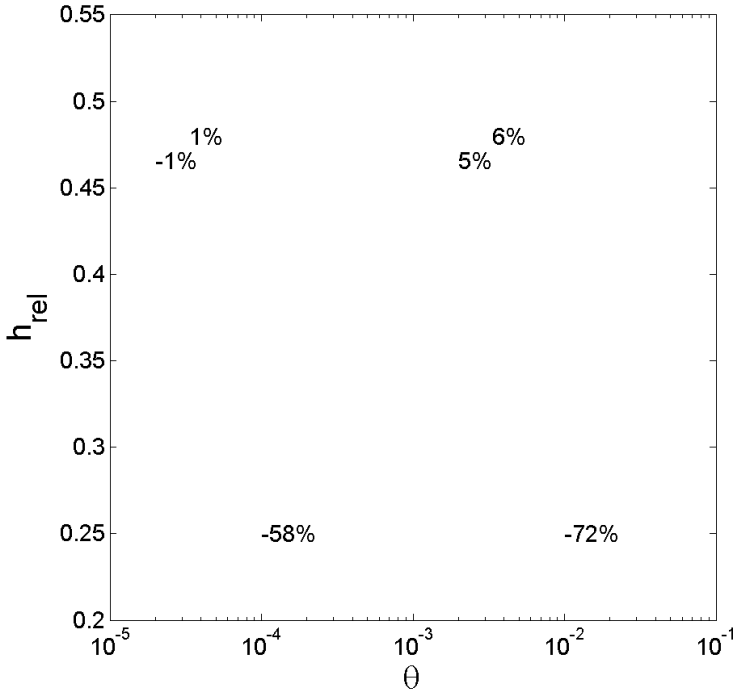

Figure 4.40: Discontinuous reference effectiveness $E_{ref,d}(6h)$ as a function of θ and h_{rel} for concentration profile U3.

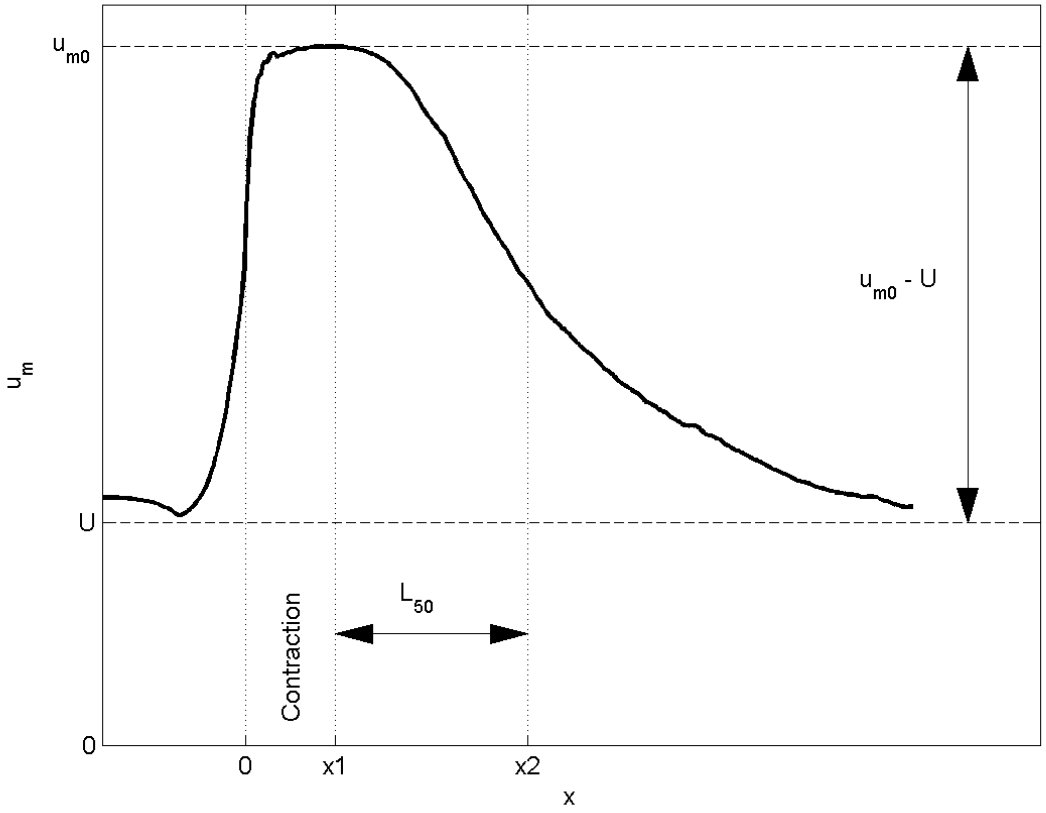

Figure 4.41: Parameters used to derive dimensionless forms of u_m and x.

4.2.5 Self-similarity analysis

In section 2.2, some aspects of self-similarity were addressed for hydraulic jumps and wall jets. Here, self-similarity analysis is applied to the numerical model results regarding vertical diversion. The findings can be related to those of section 2.2.

First of all, the evolution of $u_m(x)$ is addressed, being the maximum time-averaged streamwise velocity in every vertical profile. $u_m(x)$ reaches a maximum near the point of biggest flow contraction. Further downstream it decreases towards the maximum value occurring in a logarithmic flow profile. A dimensionless form of $u_m(x)$ is obtained following equation 4.6. In figure 4.41 all parameters used in this self-similarity analysis are indicated.

$$\tilde{u}_m(x) = \frac{u_m(x) - U}{u_{m0} - U} \tag{4.6}$$

U denotes the undisturbed depth-averaged streamwise flow velocity and u_{m0} is the maximum value of $u_m(x)$. U is used here as a measure for the maximum velocity occurring in an undisturbed logarithmic flow profile.

Furthermore, x is made dimensionless by means of length scale L_{50}, being the horizontal distance between the positions x_1 where $u_m(x) = u_{m0}$ and x_2 where $u_m(x) = U + 0.5(u_m(x) - U)$, corresponding to 50% velocity decay. This is expressed by equation 4.7.

$$\tilde{x} = \frac{x - x_1}{L_{50}} \tag{4.7}$$

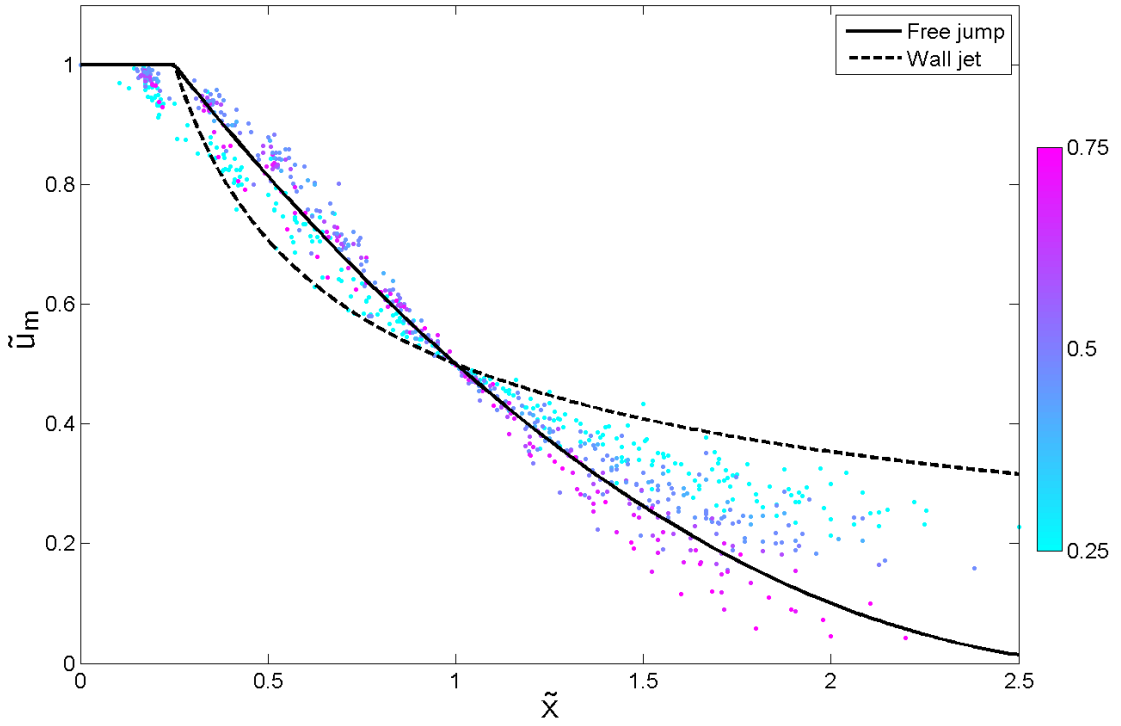

Figure 4.42: Dimensionless velocity decay profiles for silt screens (markers, colourscale indicates relative screen height h_{rel}), free jumps (solid line) and wall jets (dotted line).

The use of L_{50} as a horizontal scaling parameter for velocity decay has been proposed by Long et al. (1990) in their study of submerged hydraulic jumps. They found that this parameter leads, rather than any parameter related to the initial jet height, to the best collapse of velocity decay profiles onto a single line. Their approach was adopted by various authors later on (e.g. Wu and Rajaratnam, 1995; Dey and Sarkar, 2006; Dey et al., 2010). This also follows from analysis of the silt screen data, as scaling with parameters related to the screen height does not yield consistent results.

For every simulation of the basic dataset, 11 data points have been extracted from the simulation results downstream of the point of maximum flow contraction. Furthermore, the presented relations of $u_m(x)$ for free jumps and wall jets (see figure 2.6) have been reworked to match the definitions of $\tilde{u}_m$ and $\tilde{x}$. Figure 4.42 shows the result. Although the data show a high degree of scatter, the figure reveals dependency of the velocity decay on h_{rel}. It can roughly be said that for high h_{rel} the profile is free jump-like, whereas for low h_{rel} it is more wall jet-like.

Now the vertical profiles of time-averaged streamwise velocity are assessed. This calls for new definitions. A dimensionless form of $\bar{u}$ is obtained by means of the maximum velocity u_m in each vertical profile, see equation 4.8.

$$\tilde{u}(z) = \frac{\bar{u}(z)}{u_m} \tag{4.8}$$

The z-coordinate is made dimensionless by means of z_1, being the vertical position where $\bar{u} = 0.5u_m$ and $\partial u/\partial z < 0$. This results in $\tilde{z}$, see equation 4.9.

$$\tilde{z} = \frac{z}{z_1} \tag{4.9}$$

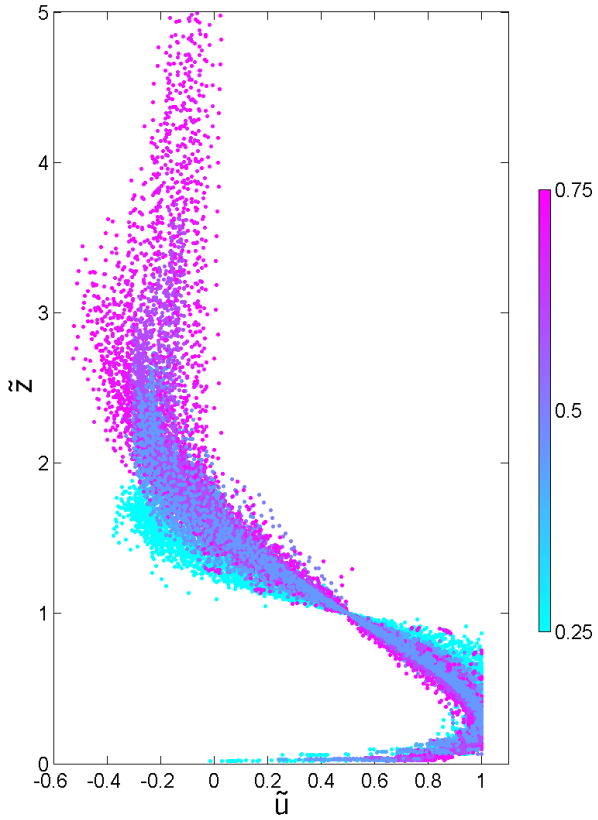

Figure 4.43: Vertical profiles of dimensionless streamwise time-averaged velocity $\tilde{u}$. The colourscale indicates relative screen height h_{rel}.

Reference height z_1 is only defined within the recirculation zone and in the first phase of flow recovery. Again, the use of z_1 as a relevant scaling parameter for vertical profiles of $\bar{u}$ was proposed first by Long et al. (1990) and adopted by Wu and Rajaratnam (1995), Dey and Sarkar (2006) and Dey et al. (2010). For their wall-jet and submerged jump data as well as the silt screen data, parameters related to the initial jet height do not lead to satisfactory collapse of the $\tilde{u}$-profiles. For every simulation of the basic dataset a number of velocity profiles has been extracted downstream of the point of maximum flow contraction. All profiles are plotted in dimensionless form in figure 4.43. Again a lot of scatter is present in the data. The profiles reveal dependency of $\tilde{u}(\tilde{z})$ on h_{rel}. Even for the same value of h_{rel} the profiles do not collapse onto a single line. This might be caused by dependency on the Froude number.

Chapter 5

Horizontal diversion

Depending on the specific application of a silt screen, a cross current might be able to flow around the side edges. The presence of a silt screen will induce some surface elevation at the upstream side. If the side edges do not connect to a slope or quay wall, the free surface will exhibit a lateral slope. This induces horizontal diversion of the cross current. Depending on the screen's geometry, a certain distribution will be established between horizontally and vertically diverted flow. Determining this distribution as a function of flow velocity, water depth, silt screen width and silt screen height is the aim of this chapter.

As indicated in chapter 3, horizontal diversion will be modelled by means of a 2DH CFD model constructed with the FINEL2D code. The set-up and characteristics of this model are discussed in section 5.1. Section 5.2 deals with the different scenarios which are investigated with the model. Finally, the results of the simulations are presented in section 5.3.

5.1 Set-up

FINEL2D solves the shallow water equations by means of the finite element method. This allows for the use of unstructured, triangular grids. The model's external boundaries form a large rectangle at some distance from the silt screen. The screen itself is represented as an internal boundary. On each edge belonging to the internal boundary, the discharge relation presented in equation 5.1 is imposed. It is derived from applying conservation of energy upstream and conservation of momentum downstream.

$$Q_s = B_e \mu_c (1 - h_{rel}) h \sqrt{2g(H_1 - h_2)} \tag{5.1}$$

In this equation, Q_s is the discharge across the edge, B_e is the length of the edge, μ_c denotes the contraction coefficient, $H_1 = h_1 + U_1^2/2g$ is the upstream energy head and h_2 is the downstream water depth. It should be noted that this relation only holds for the subcritical flow regime. In chapter 2 it was already shown that the assumption of subcritical flow is justified. The contraction coefficient is not a constant, but varies with the boundary conditions. However, from the experiments and simulations regarding vertical diversion it has been determined that $\mu_c = 0.6$ is a close approximation for all conditions.

When the external boundaries are situated too close to the silt screen, the distribution of discharges is influenced by the boundary conditions. Therefore the model's geometry is made dependent on the width of the silt screen W_s. Sensitivity analysis has led to the geometry presented in figure 5.1. The grid resolution can be seen to vary in space, with the finest grid cell size next to the silt screen and coarsening towards the external boundaries.

It is mentioned in appendix F.3 that FINEL2D does not include turbulent shear stresses and is therefore limited to flows dominated by advection. The downstream 'wake' of a silt screen

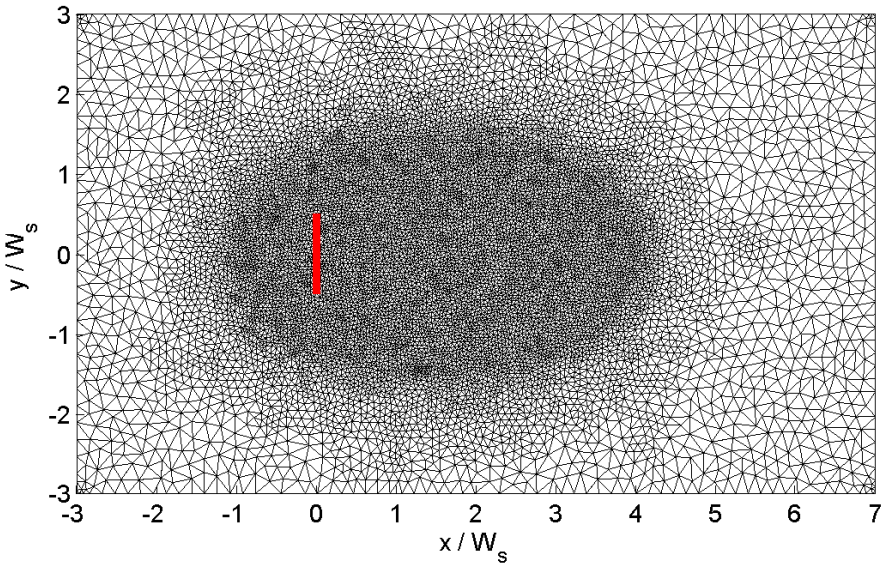

Figure 5.1: Geometry of the 2DH model. The red line indicates the position of the silt screen, which is modelled as an internal discharge boundary.

is certainly influenced by turbulent diffusion, making the results concerning this region rather doubtful. However, this study focuses on the upstream process of horizontal diversion, which is dominated by advection. The water level right downstream of the silt screen still appears in the discharge relation (equation 5.1). However, sensitivity analysis has shown that Q_s is hardly influenced by the downstream flow conditions. For example, under certain conditions the wake does no longer exhibit stationary behaviour and attains the character of a vortex street. FINEL2D can not be trusted unconditionally on correct prediction of this behaviour, but the predicted discharge across the silt screen is still consistent with other simulations.

5.2 Scenarios

Before the actual 2DH simulation scenarios are discussed, the relevant parameters will be derived from dimensional analysis. Inclusion of the second horizontal dimension introduces the silt screen's width W_s as an additional parameter. Just like the screen's height, it is made dimensionless through dividing by the water depth. The resulting parameter $W_* = W_s/h$ is a measure for horizontal diversion. The bigger W_*, the more difficult it will be for the current to flow around the side edges of the screen. The Froude number, based on undisturbed U and h, serves as a measure for the load acting on the silt screen. A higher load will induce more horizontal diversion.

Horizontal diversion itself can be quantified as the rate of the vertically diverted discharge over the total inflowing discharge along the width of the screen. With n the number of grid edges constituting the silt screen, the relative discharge Q_{rel} is given by equation 5.2.

$$Q_{rel} = \frac{\sum_1^n Q_s}{UhW_s} \cdot 100\% \tag{5.2}$$

The relative discharge denotes the percentage of the flow which is being diverted vertically. It should be clear that vertical diversion is the intended effect of a silt screen, whereas horizontal diversion should be limited as much as possible. This corresponds to a high relative discharge.

Now the actual 2DH simulation scenarios are presented. Table 5.1 lists the different values of

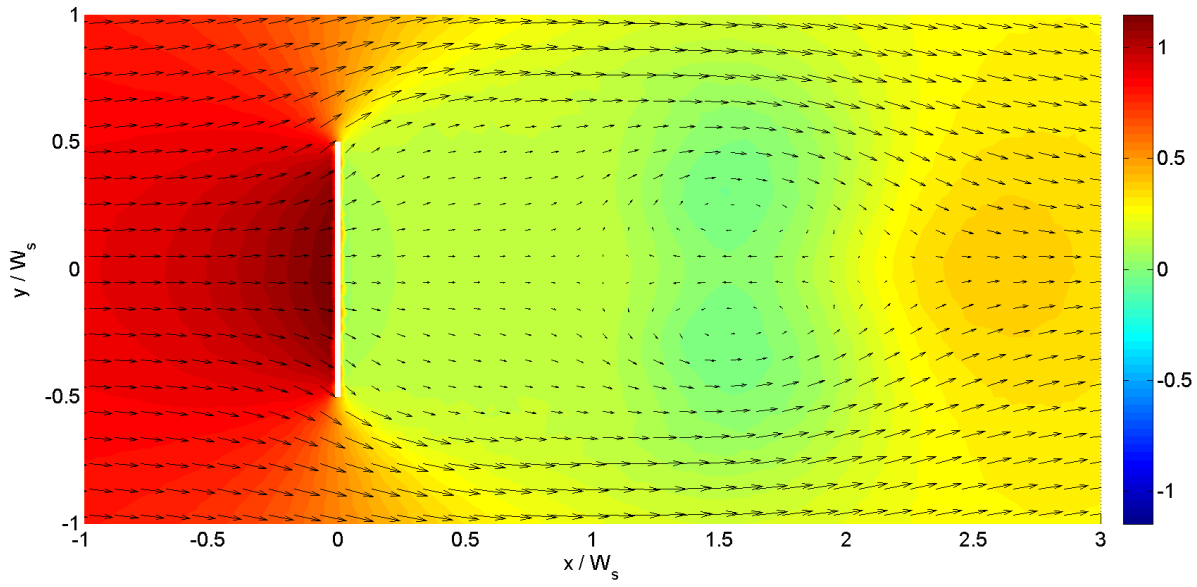

Figure 5.2: Surface elevation (colourscale, in mm) and velocity vectors for a 2DH numerical simulation in FINEL2D, with $h_{rel} = 0.5$, $U = 0.1$ m/s and $W_* = 20$. The water depth is kept constant at 5 m throughout all simulations.

all relevant parameters.

Scenarios are put together by various combinations of these values. The Froude number is

Table 5.1: Different values assigned to the parameters constituting the basic Dflow3D dataset.

h_{rel} [-]	0.25	0.5	0.75	
U [m/s]	0.1	0.3	0.5	
W_* [-]	10	20	50	100

varied by means of the undisturbed depth-averaged flow velocity, whereas the water depth is kept constant at 5 m.

5.3 Results

This section will deal with the results of the 2DH numerical simulations. Before the full dataset is analysed, the results of an arbitrary scenario are discussed in order to demonstrate the model's behaviour.

Figure 5.2 shows the results of a simulation in the near vicinity of the silt screen with $h_{rel} = 0.5$, $U = 0.1$ m/s and $W_* = 20$. The colourscale represents surface elevation in mm, the vector arrows represent depth-averaged flow velocity and the white line indicates the position of the silt screen. Due to a build-up of pressure on the upstream side, the free surface attains a gradient in both horizontal directions. The lateral gradient tends to bend the current away from the silt screen, which constitutes the process of horizontal diversion. At about two times the screen width downstream, two big counterrotating eddies are formed. Although this behaviour corresponds with the observed velocity gradient in y-direction, the model is not expected to predict the downstream flow field with great accuracy. For the sake of clarity, figure 5.3 shows the absolute horizontal depth-averaged velocity on a colourscale. The highest flow velocities occur in two plume-shaped regions downstream of the screen's tips. This flow pattern corresponds

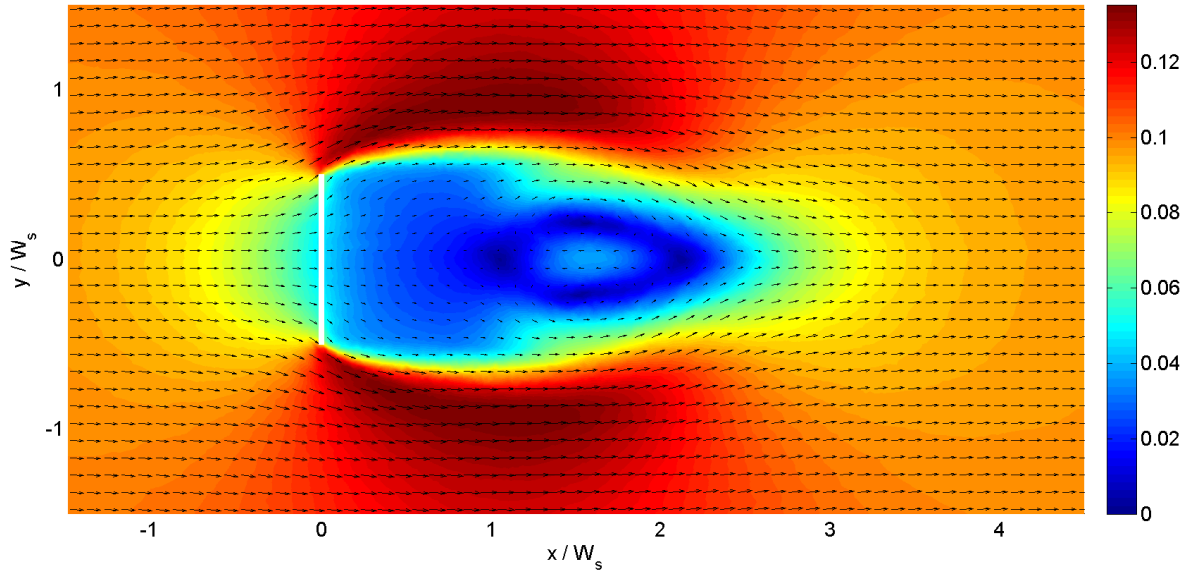

Figure 5.3: Absolute horizontal depth-averaged velocity (colourscale, in m/s) and the associated velocity vectors for the same simulation.

well with the flow pattern around blunt objects, e.g. a groyne (Schiereck, 2001).

The discharge through the grid edges representing the silt screen is shown in dimensionless form in figure 5.4. The solid line represents the relative specific discharge $q_{rel} = Q_s/(B_e U h)$ as a function of the screen's y-coordinate. Zero horizontal diversion corresponds with the dotted line. The ratio of the surface underneath the solid line over the surface underneath the dotted line is equal to Q_{rel}. The influence of horizontal diversion intensifies towards the side edges.

By evaluating the ratio of these integrals, Q_{rel} is determined for all simulations. These percentages are shown in figure 5.5 as a function of Fr/W_* and h_{rel}. The black markers show the actual datapoints. Contours of equal Q_{rel} are determined from interpolation. The dimensionless parameter Fr/W_* is a measure for the ease of horizontal diversion, whereas h_{rel} represents the resistance against vertical diversion. Some trivial features can be recognized in the figure straight away:

- For an infinitely long silt screen, Fr/W_* approaches zero. In that case, Q_{rel} approaches 100%, as flow around the screen's side edges will not be possible.
- For $h_{rel} = 0$, the flow is not hampered by the screen and Q_{rel} should equal 100%. A negative relation between Q_{rel} and h_{rel} is visible in the figure, but linear extrapolation of the contours towards $h_{rel} = 0$ leads to a smaller relative discharge than 100%. Therefore, a stronger relation between both parameters will exist for small relative screen heights.
- For $h_{rel} = 1$, the screen blocks the flow completely and Q_{rel} should equal 0%. This also follows from linear extrapolation of the contours.

Horizontal diversion is an unwanted effect of silt screen application at open water. Only if the vast majority of a dredging spill passes underneath the silt screen, possibly favourable effects of vertical diversion might take place. The figure shows that this is only bound to happen at extremely low Froude numbers and/or extremely long silt screens. In any case, the relative screen height should be kept small in order to promote vertical diversion. A certain degree of horizontal diversion can never be avoided. This leads to increased dispersion and diffusion of the dredging spill, which decreases effectiveness.

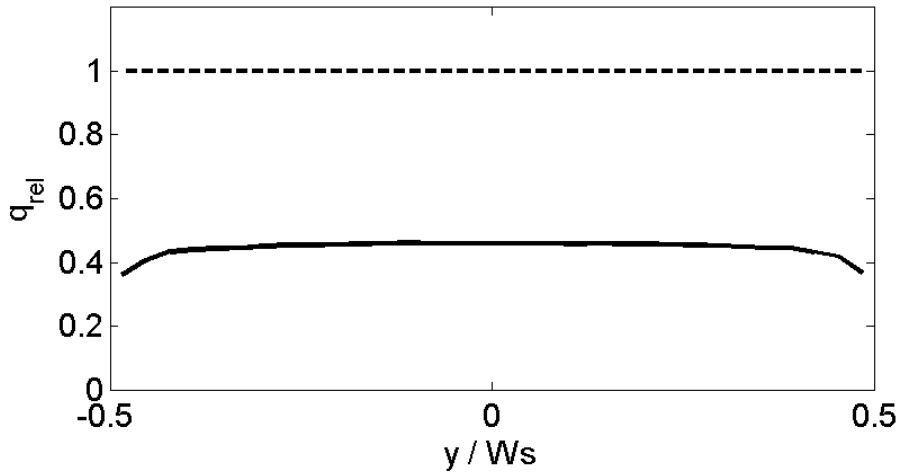

Figure 5.4: Relative specific discharge q_{rel} through the grid edges representing the silt screen (solid line). The horizontal axis shows the lengthwise coordinate of the screen. In case of no horizontal diversion, the solid line equals the dotted line.

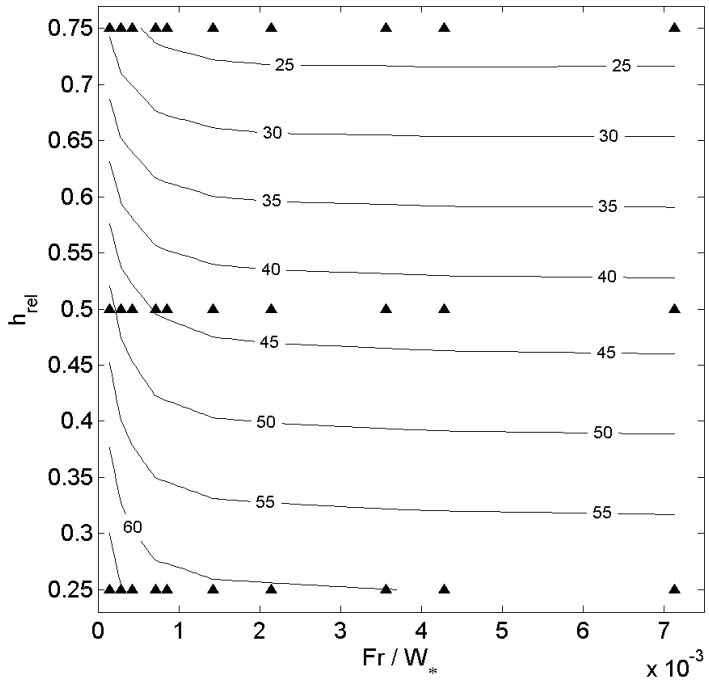

Figure 5.5: Relative discharge Q_{rel} as a function of Fr/W_* and h_{rel}. The actually obtained data are indicated by black triangles. Contour lines are constructed by means of interpolation.

Chapter 6

Adjustments

The secondary goal of this research is to test a number of promising adjustments to the hanging silt screen. These adjustments are divided into two categories. Adjustments to the large-scale application involve the use of 'ordinary' hanging silt screens in new formations. They are discussed in section 6.1. Adjustments to the small-scale design involve actual adaptations to the silt screen itself. These are dealt with in section 6.2.

It is stressed that this chapter does not aim to deliver a ready-to-use improved design for hanging silt screens. If conclusions regarding a promising adjustment are positive, further research should be conducted in order to determine its feasibility, its constructability and its behaviour under various circumstances.

6.1 Large-scale application

In appendix B a number of different large-scale applications of hanging silt screens are listed. These include oblique placement of the screen with respect to the current, V-shaped placement, leaving a gap between adjacent sections of the screen, application as a diffuser and placing two screens after another. However, some remarks have to be made regarding these applications:

- Although oblique placement and V-shaped placement might seem comparable applications, there is an important difference. Both options aim at diverting the plume horizontally in a streamlined way. Discharge 'through' the screen will only cease if pressure differences between both sides are kept small. In case of V-shaped placement, a downstream wake with low pressures is unavoidable, which induces a significant amount of vertical diversion. This drawback does not necessarily hold for oblique screen placement, since the current might bend completely into the wake at the downstream side of the screen. Theoretically there would be no pressure difference between both sides. Because of these considerations, only oblique placement is actually investigated.

- The adjustments aiming at extensive mixing of the plume should be investigated in a 2DH set-up. In this research, 2DH modelling is done by means of FINEL2D. Exclusion of turbulent shear stresses from the governing equations and high numerical diffusion limit the use of this code to flows dominated by advection. Therefore it is not possible to include these adjustments in this research. From chapter 4 and 5 it is known that extensive diffusion often leads to a negative effectiveness. Furthermore it is not very likely that diffusing a turbidity plume by means of silt screens reduces concentrations far enough to fit within environmental legislation. Hence these adjustments are not considered very promising.

Now, oblique placement and application of two silt screens will be discussed consecutively in the remainder of this section.

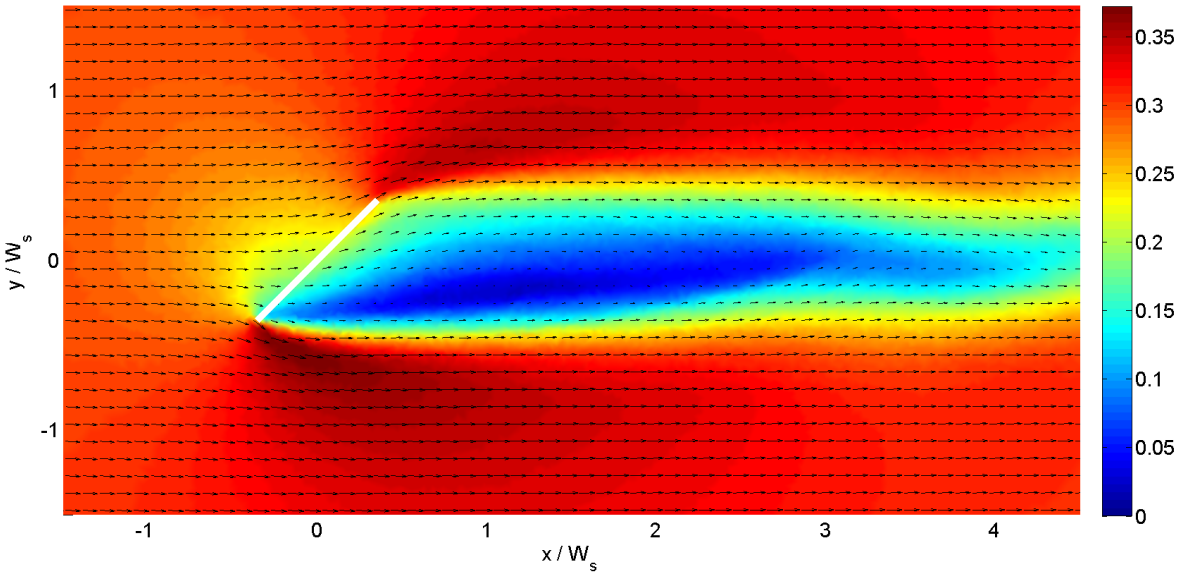

Figure 6.1: Absolute depth-averaged horizontal flow velocity (colourscale, m/s) and the associated velocity vectors in the near vicinity of an obliquely placed silt screen with $d = 5$ m, $h_{rel} = 0.5$, $U = 0.3$ m/s, $W_* = 20$ and $\beta = 45°$.

6.1.1 Oblique placement

The result of a FINEL2D simulation with an obliquely placed screen is shown in figure 6.1. This concerns a simulation with $U = 0.3$m/s, $h_{rel} = 0.5$, $W_* = 20$ and silt screen rotation angle $\beta = 45°$. The colourscale and vector arrows both indicate absolute depth-averaged horizontal flow velocity. The obliquely placed screen does not function as intended:

- The regions of high flow velocity downstream of both tips indicate that horizontal diversion is still taking place to both sides. Ideally, all diverted fluid should end up to the left side of the screen (as seen from the upstream side). This process can be quantified by determining how many percent of the inflowing discharge at the upstream model boundary ends up passing the silt screen left (46.3%), right (47.7%) or underneath (6.0%). It appears that the obliquely placed screen diverts flow to the unintended side rather than to the intended side.

- Furthermore, the screen still has a long wake with low flow velocities. The big pressure difference leads to a significant discharge through the screen. When compared to a perpendicular screen, the influence of β on Q_{rel} can be expressed as the ratio of the total discharge through the screen at angle β over the total discharge through a perpendicular screen of the same width when projected on the y-axis: $Q_{rel}(\beta)/(Q_{rel}(0)\cos\beta) \cdot 100\%$. For the current simulation, that results in 117%. Apparently, the obliquely placed screen attracts a bigger percentage of the total discharge than a perpendicularly placed screen.

These observations hold for all simulations. Figure 6.2 shows the ratio of the total discharge passing the screen on the left side over the right side, Q_L/Q_R, as a function of β. The solid lines connect simulations with equal h_{rel}, U and W_*. A clear relationship between these parameters and the discharge ratio can not be found. Nevertheless, except for one simulation, obliqueness of the silt screen diverts the biggest part of the current to the right.

In figure 6.3, Q_{rel} is shown as a function of β. Again, the solid lines connect simulations with equal conditions. For all conditions, Q_{rel} grows as β grows, indicating that oblique placement

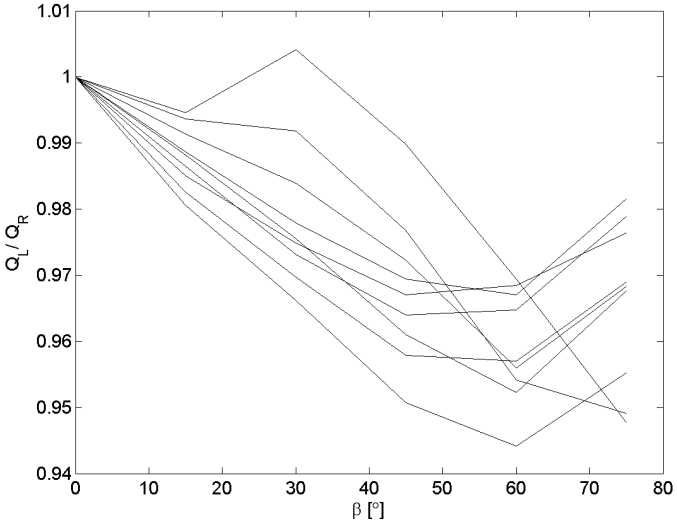

Figure 6.2: Ratio between total discharge passing the screen at the left side over the right side, as seen from the upstream side. Except for one simulation, a rotated screen diverts the biggest part of the discharge towards the right side.

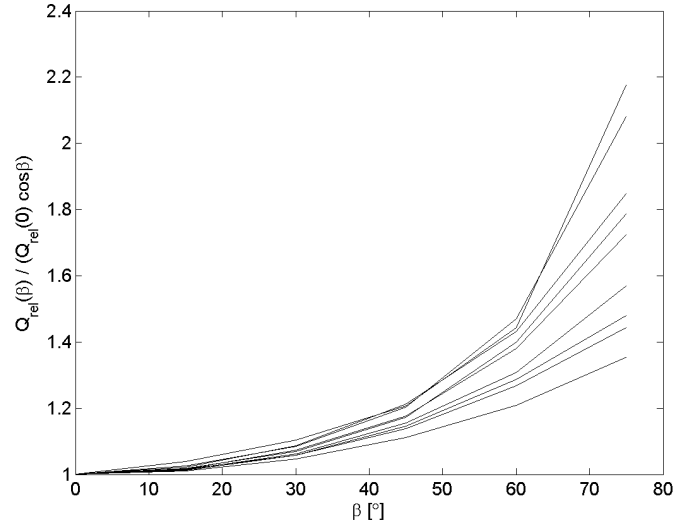

Figure 6.3: Relative discharge Q_{rel} as a function of rotation angle β. Q_{rel} represents the ratio of the total discharge passing the oblique screen over the discharge through a perpendicular screen of the same width when projected on the y-axis.

attracts a bigger part of the current to the silt screen.

Altogether, oblique placement leads to less horizontal diversion, which is contrary to the intended effect. Furthermore, the biggest part of the current is diverted around the upstream tip of the screen, which is contrary to the intended effect as well. So only if the turbidity plume is located in the upper half of figure 6.1, the silt screen redirects the plume towards the intended direction. Though it should be noted that this effect is even stronger with the screen placed perpendicular to the current.

6.1.2 Two silt screens

In appendix B, placing two consecutive silt screens is presented as a possible way of 'halting' a turbidity plume. In between both screens a fixed recirculation zone will form, which might absorb a significant part of an initial turbidity plume. However, an exchange current will be formed between the recirculation zone and the main flow. Eventually all turbidity will end up downstream of both screens, which indicates that the halting effect is only of temporary nature. Nevertheless this adjustment is expected to result in extensive horizontal dispersion. Concentrations might be brought low enough in the water column to reduce the environmental impact potential.

First, the performance of Dflow3D in case of two consecutive silt screens is validated by comparing numerical simulation results to the results of laboratory experiment 2G. Figure 6.4 shows $\overline{u}$, $\overline{w}$, r_u, r_w and τ'_{uw} respectively from top to bottom. The numerical model performs fairly well, although it underestimates the maximum time-averaged streamwise velocity downstream of the second silt screen. The resulting smaller velocity shear consequently affects the turbulence parameters. The smaller maximum jet velocity seems to result from a slightly different relative screen height. Due to the discrete nature of the numerical grid, h_{rel} can not be implemented at its exact value. Hence it is very likely that the observed differences between the physical and numerical models do not stem from fundamental errors produced by the numerical code. There is no reason to believe that Dflow3D performs worse with two silt screens than with a single one.

Now the simulation results regarding silt screen effectiveness are presented. Again a distinction is made between continuous and discontinuous spills. The former is addressed first. Simulations were conducted with $h_{rel} = 0.75$, $U = 0.3$ m/s, $w_s = 1$ mm/s, $d = 5$ m and concentration profiles U2 and U3. Time-averaged SSC for profile U2 is depicted in figure 6.5. The lower panel shows the reference simulation. Due to its low position in the water column, the biggest part of the plume passes both screens with the main flow. Only very low concentrations are stored in the first recirculation zone. Downstream of the second silt screen, extensive dispersion and diffusion spreads SSC equally over the full water depth. This behaviour is similar to the situation with one screen. The integrated environmental impact potential and both effectiveness parameters are shown in figure 6.6. At a distance of 30 m downstream of the second screen, $E_{in}(9h) = -66\%$ and $E_{ref}(9h) = -65\%$ are found. Figure 4.26 predicts a less negative value of $E_{in}(6d)$ in case of a single screen with $h_{rel} = 0.75$ and $\theta = 3.3 \cdot 10^{-3}$. Apparently two screens cause even more sediment to end up in the upper part of the water column.

Figure 6.7 shows suspended sediment concentrations for profile U3. The first recirculation zone is filled with high concentrations. As the plume is continuous, an equilibrium situation has been reached. Hence, the recirculation zone absorbs as much sediment as it releases into the main flow. Continuity now requires that the flux of SSC passing the second screen is the equal to the flux passing the first screen. Compared to a situation with only one screen, increased mixing might be the only difference. $P(x)$, $E_{in}(x)$ and $E_{ref}(x)$ are presented in figure 6.8. The

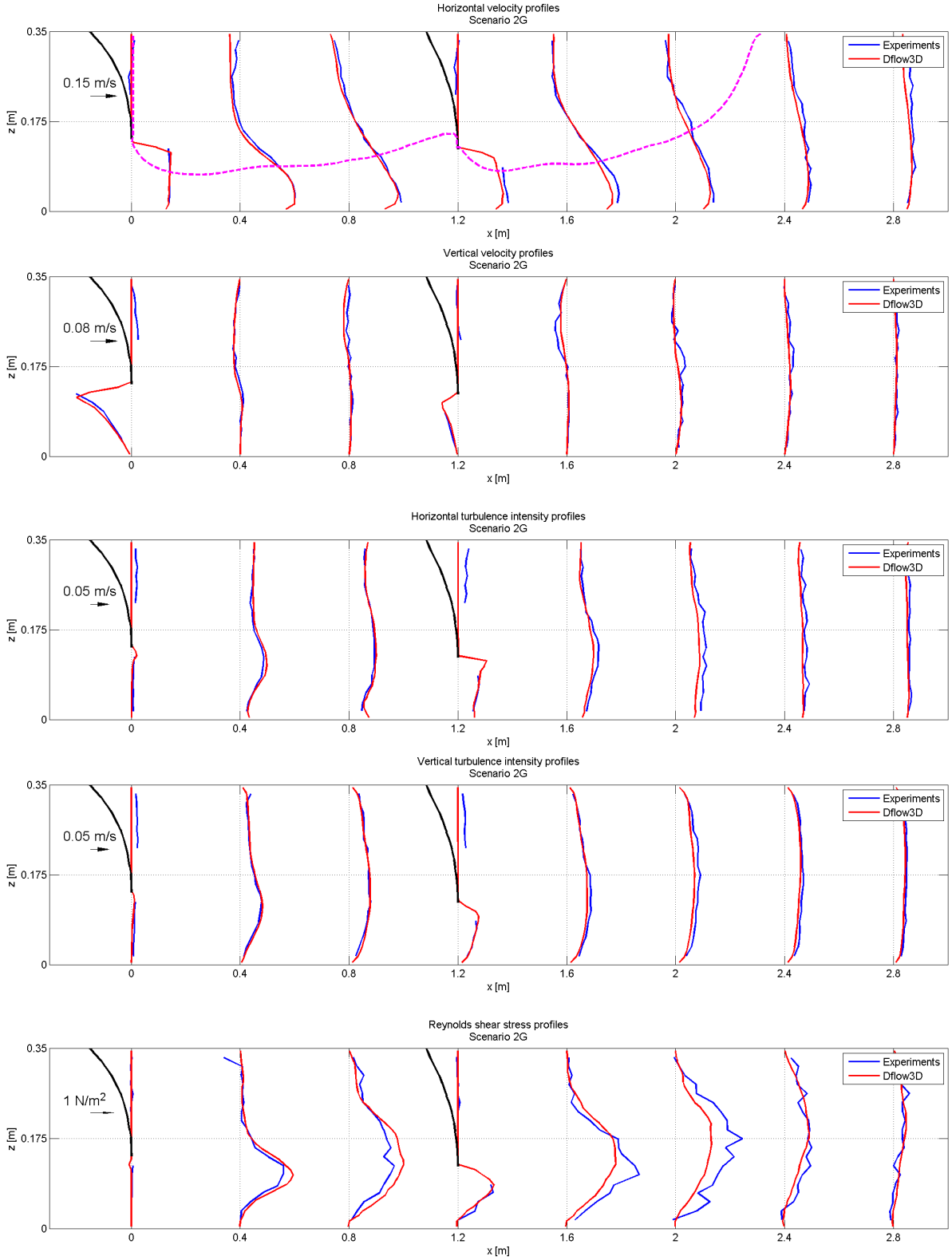

Figure 6.4: Validation plot for laboratory run 2G. From upper to lower panel, the time-averaged velocities $\overline{u}$ and $\overline{w}$, turbulence intensities r_u and r_w and Reynolds stress τ'_{uw} are shown.

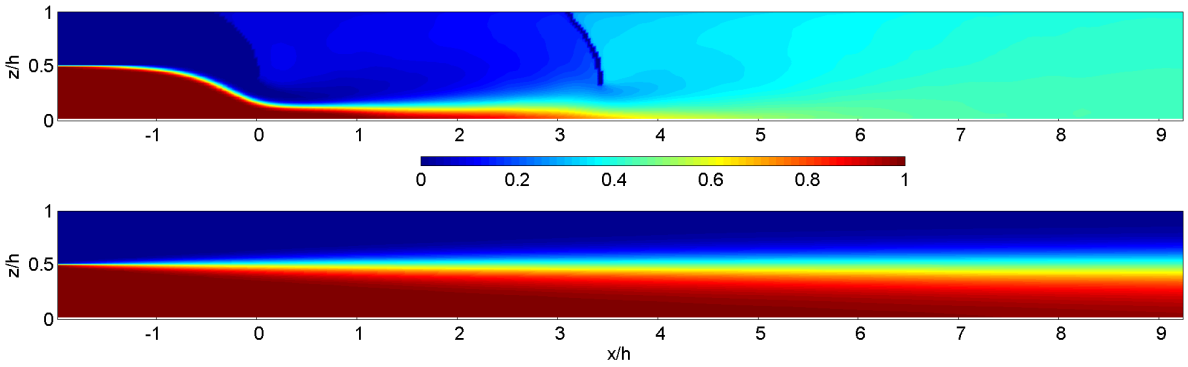

Figure 6.5: Time-averaged suspended sediment concentrations $\overline{C}$ for a numerical simulation with two silt screens. Inflowing concentration profile U2 is applied.

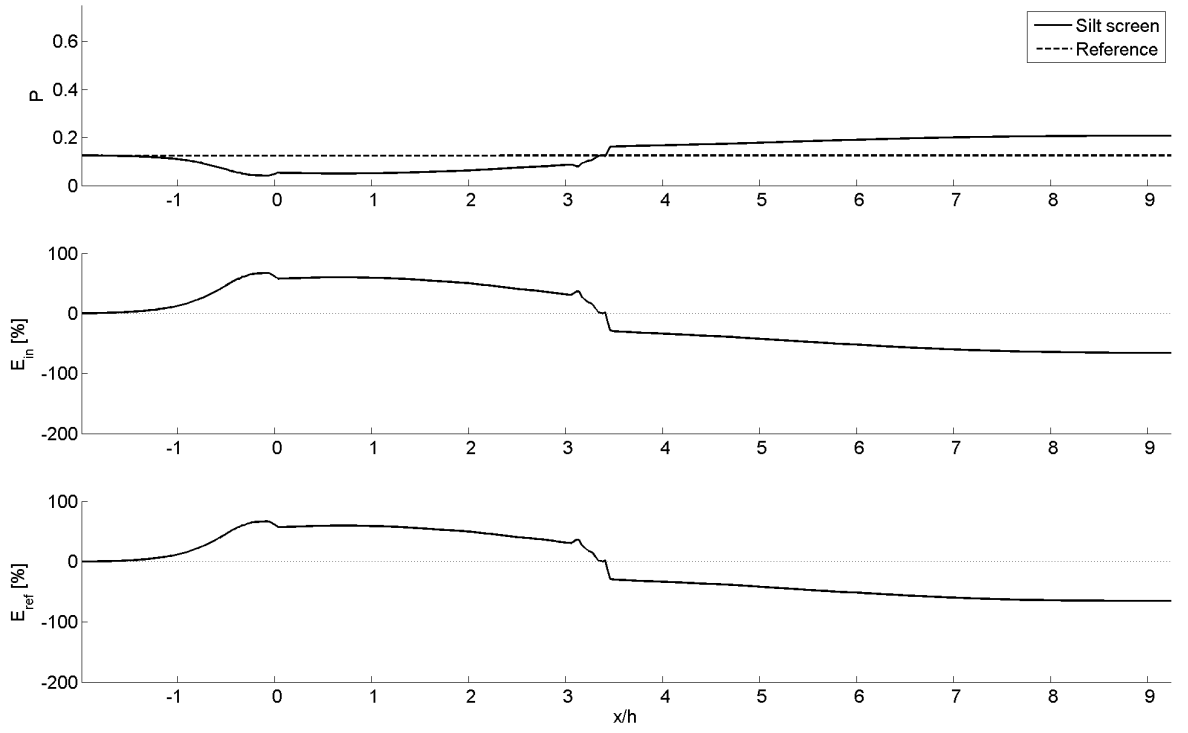

Figure 6.6: Environmental impact potential $P(x)$ (upper panel), inflow effectiveness $E_{in}(x)$ (middle panel) and reference effectiveness $E_{ref}(x)$ (lower panel) for a numerical simulation with two silt screens and concentration profile U2.

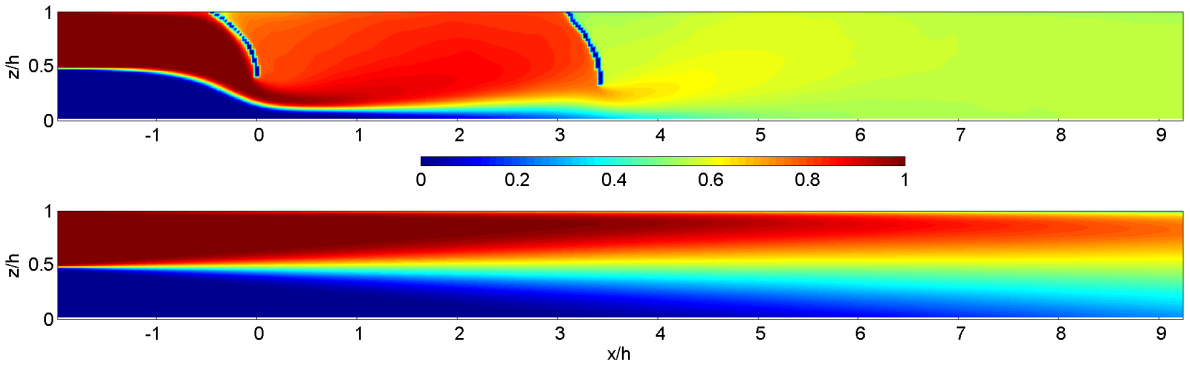

Figure 6.7: Time-averaged suspended sediment concentration $\overline{C}$ for a numerical simulation with two silt screens. The concentration profile is U3.

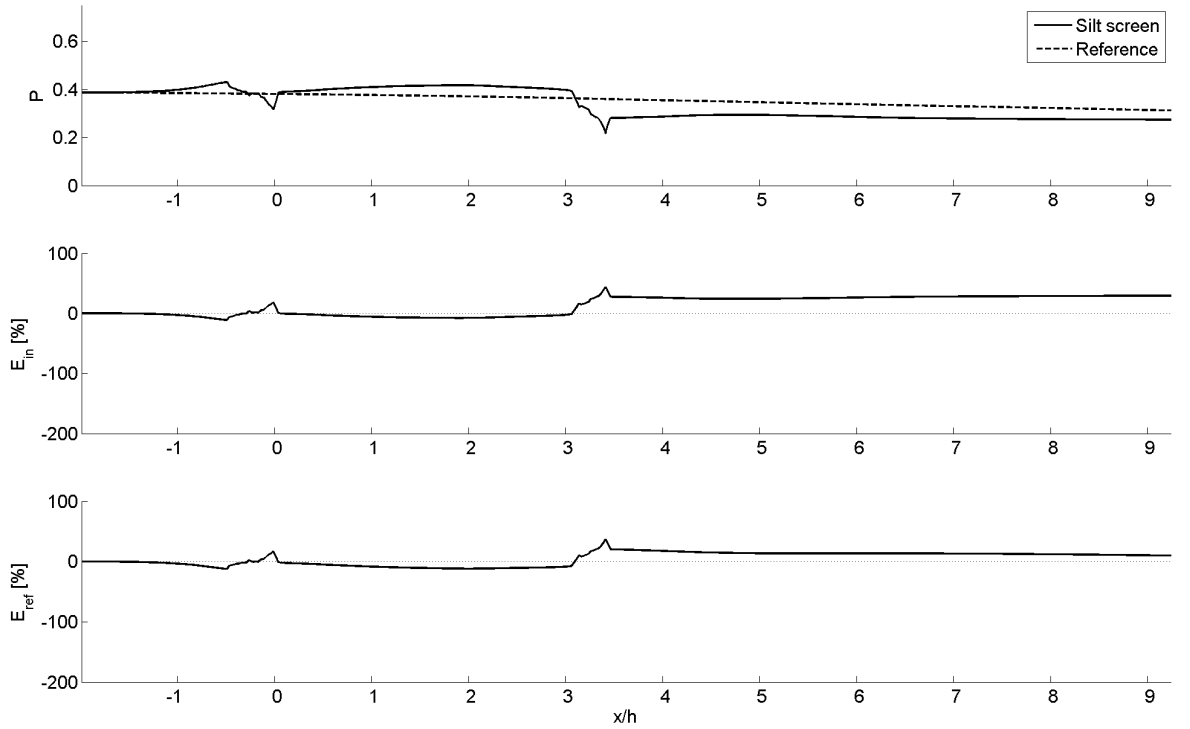

Figure 6.8: $P(x)$, $E_{in}(x)$ and $E_{ref}(x)$ for a numerical simulation with two screens and concentration profile U3.

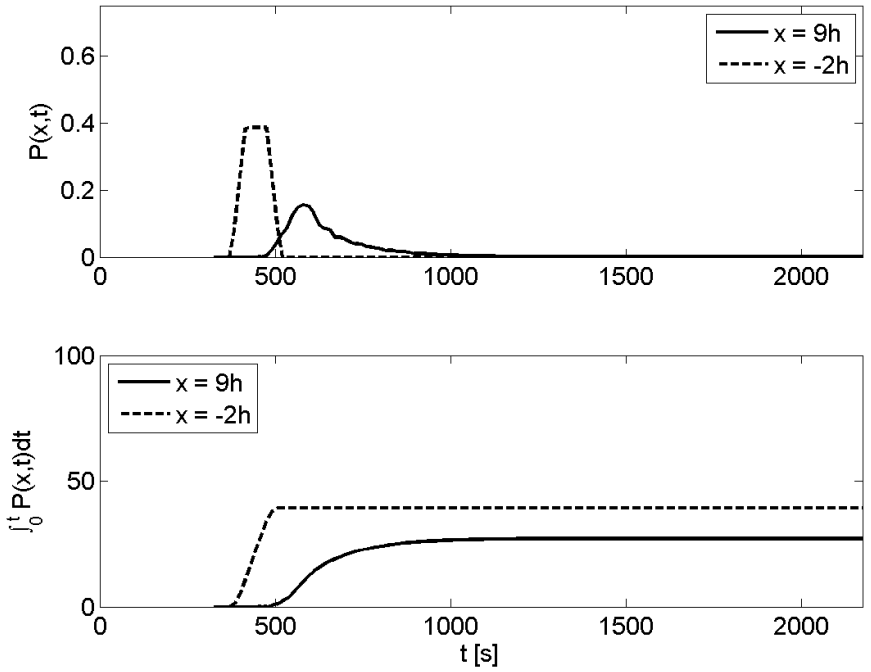

Figure 6.9: Discontinuous impact parameters for a simulation with two silt screens, concentration profile U3 and an inflow duration of 100 s. The upper panel shows the environmental impact potential as a function of time both at inflow and at $6h$ downstream of the second screen. The lower panel shows the development of both integrals in time.

values at 30 m downstream of the second screen are only a little bit higher than the values predicted by figure 4.27 and 4.29: $E_{in}(9h) = 29\%$ and $E_{ref}(9h) = 10\%$. Probably the higher value results from increased vertical mixing, which directs more sediment towards the lower half of the water column.

Fundamentally different behaviour is expected for discontinuous plumes. The increased horizontal dispersion will lead to lower concentrations over a longer period of time. In chapter 4 it was argued that such a diffusive trailing edge is only beneficial if concentrations are brought to a lower position in the water column.

Figure 6.9 shows $P(x,t)$ and its integral in time for both the inflow profile and the profile at six times the water depth downstream of the second screen. The inflow profile is U3 and inflow duration $t_s = 100$ s. The discontinuous effectiveness parameters are $E_{in,d}(9d) = 31\%$ and $E_{ref,d}(9d) = 12\%$. In this simulation, $\alpha = 6$, $\theta = 3.3 \cdot 10^{-3}$ and $h_{rel} = 0.75$ when screen deformations are not taken into account. The presented values of $E_{in,d}$ and $E_{ref,d}$ are slightly more positive as those for a comparable simulation with only one screen, see figure 4.38 and 4.40. This can be explained by the more intense downstream mixing imposed by two silt screens instead of one. Inflow profile U3 is diffused over the full water column more effectively, which leads to a lower environmental impact potential. This is solely the effect of intense mixing. Due to the extended stretch over which increased bed shear stress occurs, the amount of deposition is expected to decrease and the amount erosion is expected to increase. Hence conclusions regarding the application of two consecutive silt screens may only be moderately positive when facing a discontinuous spill with most upstream SSC located at high z-coordinates.

6.2 Small-scale design

Some of the adjustments which are suggested in appendix B involve modifications to the design of silt screens. These adjustments are a perforated screen and extension of the lower edge with a flap. For technical reasons, both adjustments can not be implemented in Dflow3D. Therefore the analysis is limited to the laboratory experiments.

6.2.1 Perforated screen

Conventional hanging silt screens completely block a part of the water column. This leads to high jet velocities underneath the screen and big velocity gradients downstream. Continuity requires dispersion of the jet flow over the full water depth. Increased turbulent diffusion due to the big velocity gradient leads to extensive mixing of suspended sediment concentrations. In that way the impermeability of silt screens undermines their objective to reduce the environmental impact potential.

A possible design adjustment to overcome these drawback is to make a silt screen partially permeable. The resulting decrease of velocity shear accordingly leads to less dispersion and diffusion. However, a permeable silt screen will also allow for a part of the turbidity plume to pass through the screen. This gives rise to SSC in the upper part of the water column. Whether the beneficial or the detrimental effect of a perforated screen dominates the resulting situation is not known beforehand.

A number of important notions must be kept in mind when designing perforated silt screens.

- The detrimental effect of perforation can be limited by applying a permeability gradient over depth. Ideally, the screen's permeability should decrease from 100% near the lower edge to 0% near the free surface.
- The size of the perforations governs the size of the turbulent structures issuing from them. Transport of suspended solids is mainly associated with the biggest structures in the flow. As increased mixing should be prevented, small holes are preferred.

The first notion can not be realised without changing the design of conventional silt screens drastically. This research into possible improvements should start with assessing what can be done with relatively simple adjustments.

Two laboratory experiments are conducted with perforated silt screens. The design as applied in experiment 2D is depicted in figure 6.10. This design leads to an average permeability of 8%. Figure 6.11 shows the results of experiment 2D and experiment 2B, which serves as a reference experiment with an impermeable screen. The upper panel, showing time-averaged horizontal flow velocity $\overline{u}$, indicates that both the maximum jet flow velocity and the maximum return velocity are decreased. This matches expectations, since the discharge of the jet flow is lower than the total discharge. Less velocity shear also leads to significantly less turbulence production, which is reflected by r_u, r_w and τ'_{uw} in the lower three panels. The same trends, though less explicit, are observed for experiment 2C, which has a permeability of only 3%.

Unfortunately these laboratory experiments only give an indication of the beneficial effect of perforated silt screens, as the output is limited to flow-related parameters. Although the decrease of Reynolds stresses is quite spectacular given the low average permeability of the screen, information on the detrimental effect is needed to give a final judgment on this design adjustment.

Without further research, it is not known where optimisation of silt screen permeability leads to. It might be the case that effectiveness keeps increasing for increasing permeability. If this is the case, silt screen effectiveness is optimal for 100% permeability, corresponding to no screen at all.

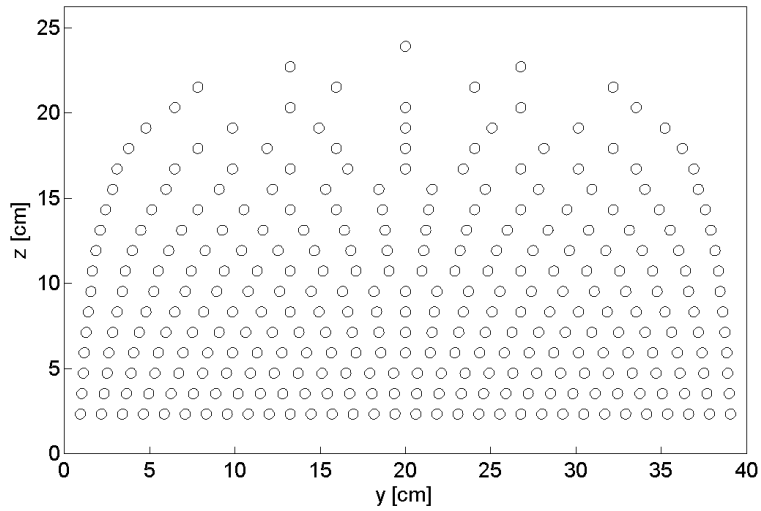

Figure 6.10: Design of the perforated silt screen as used in laboratory experiment 2D. The holes have a diameter of 6 mm. On average, the screen has a permeability of 8%.

6.2.2 Extending with a flap

Both the laboratory experiments and the numerical model simulation show that downstream mixing is governed by vortex shedding from the screen's lower edge. A common way to suppress this process in the near-field is often sought in applying a rigid extension parallel to the main flow direction. Talstra (2011) applied this design adjustment to a shallow lateral expansion. He concludes that the extension simply creates a dead zone and shifts the flow field downstream over a distance equal to the length of the extension. No significant change of any turbulence quantity is observed. As the flow pattern of vertical diversion is 2DV oriented instead of 2DH, as is the case for a shallow lateral expansion, the different role of gravity might give rise to different behaviour.

A laboratory experiment has been conducted with an unweighted extension of the cloth below the weight bar. An important requirement for the extension is that it should act as a stiff plate. If it is flexible, vortex shedding from the weight bar is not suppressed and the extension simply moves along with the vortices like a flag. Due to mechanical scaling effects of the screen's fabric, the unweighted extension remains stable in the laboratory. At real scale some weighting should be applied near the tip.

The results of this experiment, coined experiment 2E, are depicted in figure 6.12. Experiment 2A is used as a reference experiment without an extension. Both experiments have the same depth-averaged flow velocity but a different effective h_{rel}. The typical differences for that situation were explained in figure 4.7 and 4.8. It is striking that experiment 2E, with a larger effective h_{rel}, behaves as if it has a lower h_{rel} than experiment 2A. Probably this is because experiment 2A has got a bigger contraction coefficient μ_c. The flap more or less streamlines the screen's shape. As the real convergence of streamlines is determined by a combination of both h_{rel} and μ_c, a reduction of the maximum jet flow velocity is accomplished. Besides this effect, extending a silt screen with a flap has no beneficial influence on the flow field.

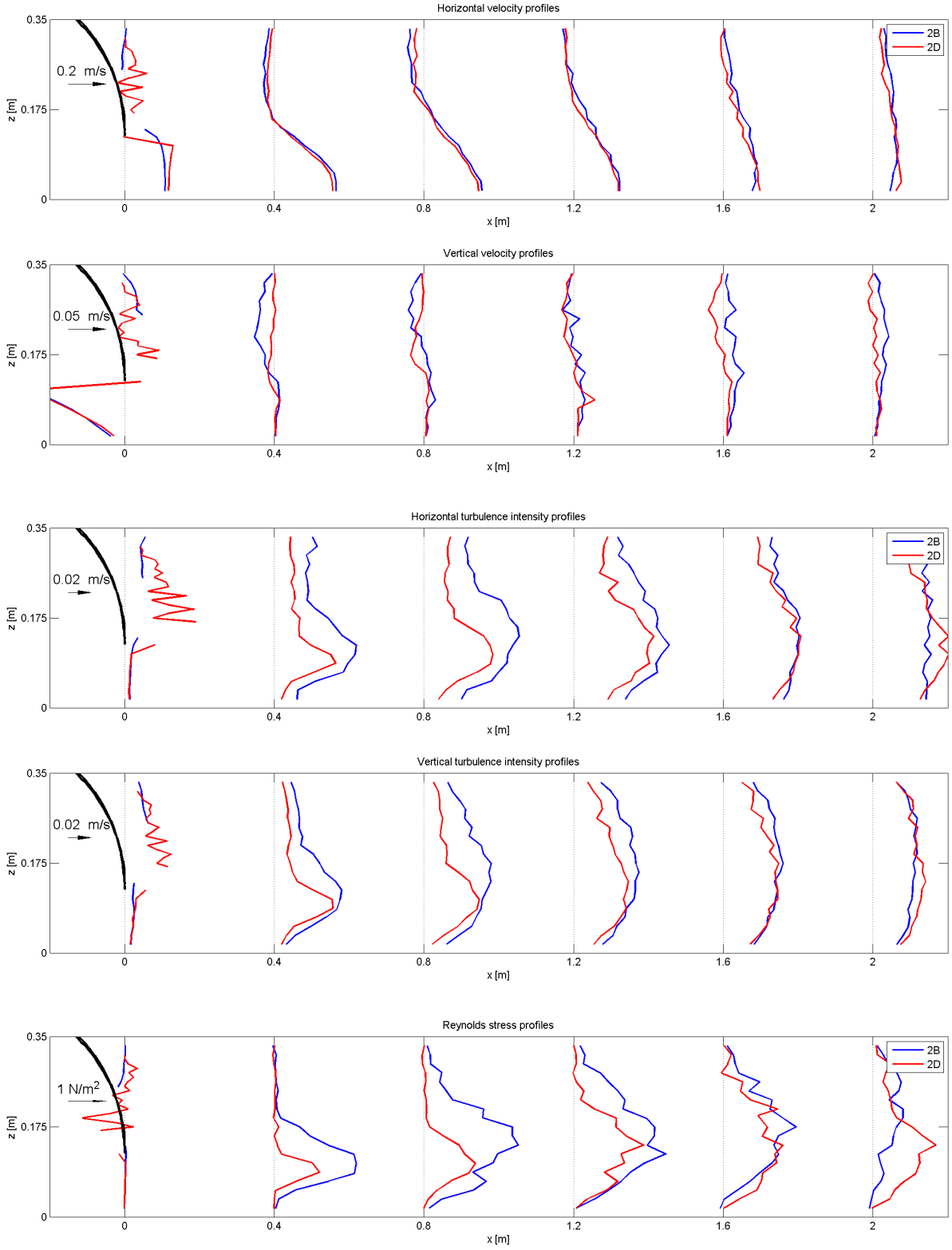

Figure 6.11: Comparison of a laboratory experiment with a perforated screen (experiment 2D) and its reference experiment (2B). From top to bottom the panels show $\overline{u}$, $\overline{w}$, r_u, r_w and τ'_{uw}.

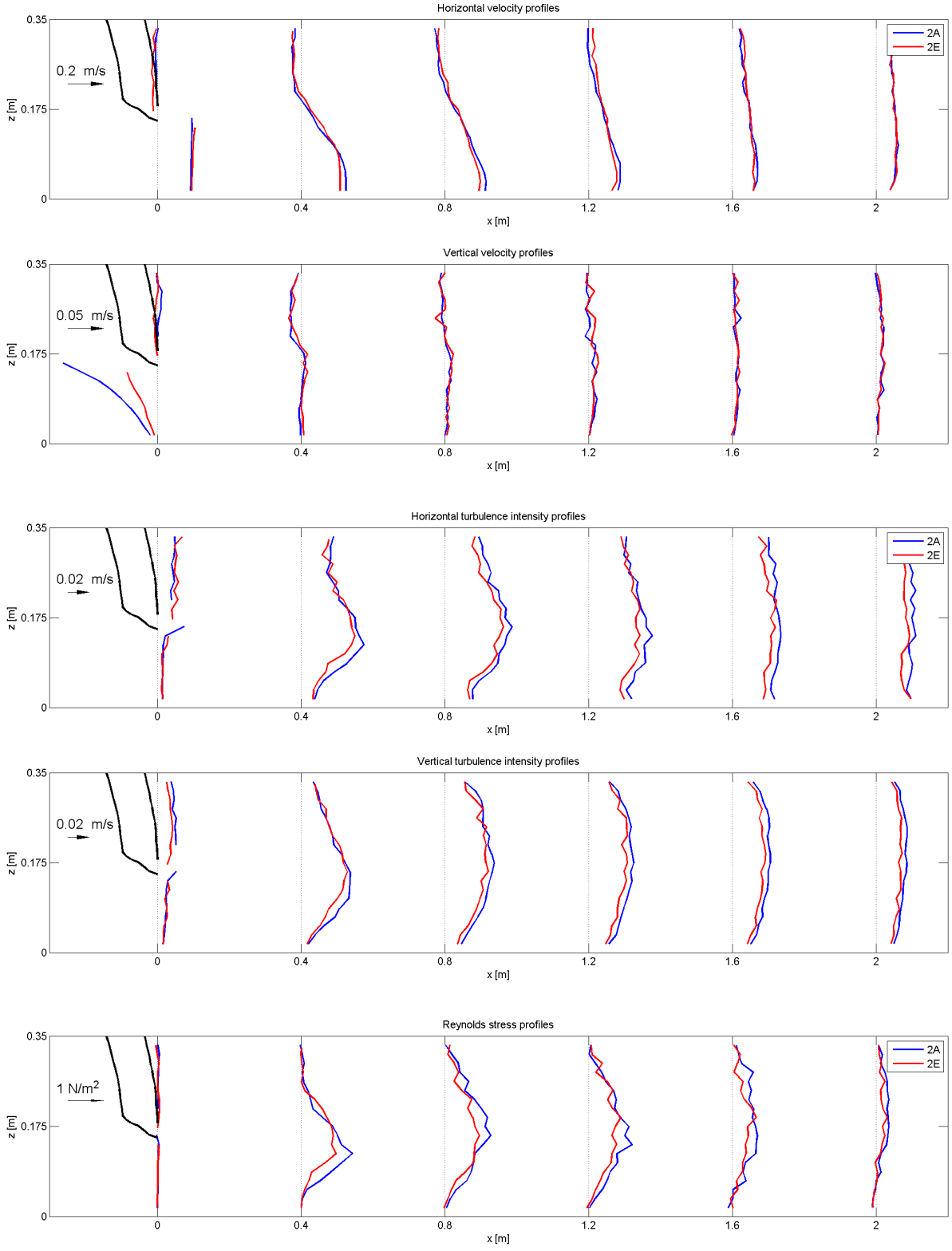

Figure 6.12: Results of laboratory experiment 2E. The silt screen has been extended with a rigid flap. Experiment 2A is shown as a reference. From top to bottom the panels show $\overline{u}$, $\overline{w}$, r_u, r_w and τ'_{uw}.

Chapter 7

Conclusions

In this thesis the effectiveness of hanging silt screens in cross flow has been investigated. It is known that in present-day dredging practice hanging silt screens are considered an effective environmental measure under mild flow conditions. After fundamental research, involving literature study, physical modelling and numerical modelling, it becomes clear that earlier reports on hanging silt screen effectiveness have been too positive.

The findings of this research are formulated in 9 conclusions:

1. Vertical diversion of sediment-laden flow caused by hanging silt screens has a negative effect on the spreading of suspended sediment, regardless of local conditions and silt screen geometry.

2. The effectiveness of silt screens is insensitive to the duration of a dredging spill. The screen gives rise to large diffusion in streamwise direction, but the influence of the screen remains equally negative.

3. If a dredging spill is mainly situated in the lower half of the water column, silt screens have the most negative impact.

4. Comparing downstream SSC to upstream SSC results in a too positive view on silt screen effectiveness. All relevant parameters should be compared to the same situation without a silt screen. Values within five times the water depth downstream of the silt screen are not representative, as the negative effects need some distance to develop.

5. The definition of the 'badness' of suspended sediment, coined 'environmental impact potential' in this research, should include the influence of SSC values and their height above the bed.

6. If erodible bed mass is available, a silt screen will lead to increased erosion.

7. Application of hanging silt screens on open waters causes a significant amount of horizontal flow diversion. This counteracts the intended usage of silt screens as a vertical current deflector and brings along increased dispersion and diffusion of SSC.

8. Oblique placement of a silt screen with respect to the current can not be used for intended horizontal diversion of a complete dredging spill. It is counterproductive in two ways: (1) the biggest part of the current is diverted to the unintended side and (2) vertical diversion increases per unit of projected screen width.

9. None of the application or design adjustments investigated in this research irrefutably demonstrates a positive effect of silt screens on the spreading of suspended sediment.

Bearing these conclusions in mind, it is interesting to revisit the case studies which were previously treated in appendix A. The knowledge gained through this research is applied to the same cases in appendix I, which leads to interesting findings. Especially the occurrence of horizontal diversion seems to be ignored in a number of cases.

Chapter 8

Recommendations

The effectiveness of hanging silt screens in cross flow is not an isolated topic in dredging practice. The application of silt screens is surrounded by a complex decision making process, which was briefly explained in chapter 1. Most recommendations are aimed at integrating the conclusions of this research into the (environmental) management practice of dredging works. All recommendations are listed below:

1. Make an effort to convince all parties involved in dredging practice of the ineffectiveness of hanging silt screens in cross flow. In that way requests from clients or local authorities for silt screen application in unfavourable circumstances can be avoided or rejected successfully. This leads to a better protection of the environment and helps both clients and dredging companies to save expenses on useless mitigation measures.

2. Investigate whether the environmental impact potential as defined in this research can be of use when quantifying environmental impact of dredging projects. A new definition was brought up here, as an appropriate way of quantifying the environmental risks of SSC appeared to be lacking. It is expected that the environmental impact potential can be applied to many different projects, especially those involving numerical modelling. The exact definition might be subject to debate amongst researchers in the field of ecology. Further improvements to the environmental impact potential are encouraged here.

3. Contrary to hanging silt screens in cross flow, standing silt screens covering the entire water depth have been proved successful in retaining dredging-induced SSC under very calm flow conditions. However, standing silt screens have the disadvantage of much stricter operational, mechanical and hydrodynamical constraints. It is therefore recommended to optimise guidelines for the application of standing silt screens covering the entire water depth.

4. Do not put effort into developing beneficial adaptations to the design or application of hanging silt screens in cross flow. The adaptations proposed and investigated in this research were deduced systematically with the help of experts in the fields of silt screen application, marine biology, turbulent flows and suspended sediment transport. As these adaptations show no proof of a potential increase in silt screen effectiveness, successful adaptations are considered non-existent.

Some additional remarks have to be made regarding certain approaches applied and choices made in this research. As these remarks are not expected to influence the conclusions in any possible way, they are not posed as full recommendations requiring further action or research. Nevertheless they are listed below for the sake of completeness:

- The use of the synthetic eddy method (SEM) to create a fully turbulent upstream velocity boundary in reference simulations was mentioned in section 4.2.2. SEM was not applied to

the 2DV simulations with a silt screen, as this led to a better validation of the downstream flow field. To comply with the reference simulations, it would have been sound to impose the synthetic eddy method at the upstream velocity boundary in all 2DV simulations.

- As an upstream sediment boundary, schematised SSC profiles were imposed. The uniform profiles, which contain no vertical concentration gradient at all or a very sharp one, were used the most frequently. Such profiles will never be encountered in practice. Although the results obtained with more realistic profiles, like the linear ones, could be readily linked to the basic dataset, it would have been better when both linear profiles had been applied in the basic dataset.
- Some trouble was encountered with implementing the deformed shape of a silt screen in the numerical grid of Dflow3D. Although the model's performance has been validated satisfactory using vertical screens, it might have been worth the effort to correct this technical issue.

References

Antonopoulos-Domis, M. (1981). Large-eddy simulation of a passive scalar in isotropic turbulence, *Journal of Fluid Mechanics* **104**: 55–79.

Bonnecaze, R. T., Hallworth, M. A., Huppert, H. E. and Lister, J. R. (1995). Axisymmetric particle-driven gravity currents, *Journal of Fluid Mechanics* **294**: 93–121.

Bonnecaze, R. T., Huppert, H. E. and Lister, J. R. (1993). Particle-driven gravity currents, *Journal of Fluid Mechanics* **250**: 339 – 369.

Boot, M. (2000). *Near-field verspreiding van het overvloeiverlies van een sleephopperzuiger*, Master's thesis, Delft University of Technology, Delft, Netherlands.

Bray, R. N. (ed.) (2008). *Environmental aspects of dredging*, Taylor & Francis, Leiden, Netherlands.

De Wilde, J. J. (1995). Slibschermproeven, *Technical report*, WL Delft Hydraulics, Delft, Netherlands.

De Wit, L. (2010). Near field 3D CFD modelling of overflow plumes, *in* Dobson (2010).

Dey, S., Nath, T. K. and Bose, S. K. (2010). Submerged wall jets subjected to injection and suction from the wall, *Journal of Fluid Mechanics* **653**: 57–97.

Dey, S. and Sarkar, A. (2006). Response of velocity and turbulence in submerged wall jets to abrupt changes from smooth to rough beds and its application to scour downstream of an apron, *Journal of Fluid Mechanics* **556**: 387–419.

Dobson, J. (ed.) (2010). *Proceedings of World Dredging Congress XIX*, Chida.

Erftemeijer, P. L. A., Riegl, B., Hoeksema, B. W. and Todd, P. A. (2012). Environmental impacts of dredging and other sediment disturbances on corals: A review, *Marine Pollution Bulletin* **64**: 1737–1765.

Erftemeijer, P. L. A. and Robin Lewis, R. R. (2006). Environmental impacts of dredging on seagrasses: A review, *Marine Pollution Bulletin* **52**: 1553–1572.

Fischer, H. B., List, E. J., Koh, R. C. Y., Imberger, J. and Brooks, N. H. (1979). *Mixing in Inland and Coastal Waters*, Academic Press, San Diego, USA.

Francingues, N. R. and Palermo, M. R. (2005). Silt curtains as a dredging project management practice, *Technical report*, U.S. Army Engineer Research and Development Center, Vicksburg, USA.

Hallworth, M. A., Hogg, A. J. and Huppert, H. E. (1998). Effects of external flow on compositional and particle gravity currents, *Journal of Fluid Mechanics* **359**: 109–142.

Hinze, J. O. (1975). *Turbulence*, McGraw-Hill, New York, USA.

Hofland, B. and Battjes, J. A. (2006). Probability density function of instantaneous drag forces and shear stresses on a bed, *Journal of Hydraulic Engineering* **132**: 1169–1175.

Holthuijsen, L. H. (2007). *Waves in Oceanic and Coastal Waters*, Cambridge University Press, Cambridge, UK.

Jarrin, N., Benhamadouche, S., Laurence, D. and Prosser, R. (2006). A synthetic-eddy-method for generating inflow conditions for large-eddy simulations, *International Journal of Heat and Fluid Flow* **27**: 585–593.

JBF Scientific Corporation (1978). An analysis of the functional capabilities and performance of silt curtains, *Technical report*, U.S. Army Corps of Engineers, Vicksburg, USA.

Jin, J. Y., Chae, J. W., Song, W. O., Park, J. S., Kim, S. E., Jeong, W. M., Yum, K. D. and Oh, J. K. (2003). Behavior of currents and suspended sediments around a silt screen, *Ocean and Polar Research* **25**: 399–408.

Kang, H. S., Chester, S. and Meneveau, C. (2003). Decaying turbulence in an active-grid-generated flow and comparisons with large-eddy simulation, *Journal of Fluid Mechanics* **480**: 129–160.

Kirk, J. T. O. (1977). Attenuation of light in natural waters, *Australian Journal of Marine and Freshwater Research* **28**: 497–508.

Launder, B. E. and Rodi, W. (1983). The turbulent wall jet - measurements and modeling, *Annual Review of Fluid Mechanics* **15**: 429–459.

Long, D., Steffler, P. M. and Rajaratnam, N. (1990). LDA study of flow structure in submerged hydraulic jump, *Journal of Hydraulic Research* **28**: 437–460.

Moser, R. D., Kim, J. and Mansour, N. N. (1999). Direct numerical simulation of turbulent channel flow up to $Re_\tau = 590$, *Physics of Fluids* **11**: 943–945.

Nederlands Normalisatie-instituut (2000). *NEN-EN-ISO 7027*, Delft, Netherlands.

Nicoud, F. and Ducros, F. (1999). Subgrid-scale stress modelling based on the square of the velocity gradient tensor, *Flow, Turbulence and Combustion* **62**(3): 183–200.

Noh, Y. and Fernando, H. J. S. (1991). Gravity current propagation along an incline in the presence of boundary mixing, *Journal of Geophysical Research* **96**(C7): 12,586–12,592.

Obi, S., Inoue, K., Furukawa, T. and Masuda, S. (1996). Experimental study on the statistics of wall shear stress in turbulent channel flows, *Intenational Journal of Heat and Fluid Flow* **21**: 576–581.

Pope, S. B. (2000). *Turbulent Flows*, Cambridge University Press, Cambridge, UK.

Rivera, M. K. (2000). *The inverse energy cascade of two-dimensional turbulence*, PhD thesis, University of Pittsburgh.

Schiereck, G. J. (2001). *Introduction to bed, bank and shore protection*, Delft University Press, Delft, Netherlands.

Simpson, J. E. (1987). *Gravity Currents in the Environment and the Laboratory*, Ellis Horwood, Chichester, UK.

Spearman, J., De Heer, A. F. M., Aarninkhof, S. G. J. and Van Koningsveld, M. (2011). Valdation of the TASS system for predicting the environmental effects of trailing suction hopper dredgers, *Terra et Aqua* **125**: 14–22.

Talstra, H. (2011). *Large-scale turbulence structures in shallow separating flows*, PhD thesis, Delft University of Technology, Delft, Netherlands.

Thevenot, M. M., Prickett, T. L. and Kraus, N. C. (1992). Tylers beach, virginia, dredged material plume monitoring project, *Technical report*, U.S. Army Corps of Engineers, Vicksburg, USA.

Tominaga, Y. and Stathopoulos, T. (2007). Turbulent schmidt numbers for CFD analysis with various types of flowfield, *Athmospheric Environment* **41**: 8091–8099.

Turner, J. S. (1973). *Buoyancy effects in fluids*, Cambridge University Press, Cambridge, UK.

Van der Salm, R. (1998). *Milieuvriendelijke zandwinning: De verspreiding van overvloeiverlies*, Master's thesis, Delft University of Technology, Delft, Netherlands.

Van Prooijen, B. C. and Winterwerp, J. C. (2010). A stochastic formulation for erosion of cohesive sediments, *Journal of geophysical research* **115**: 15 pp.

Van Rijn, L. C. (2005). *Principles of sedimentation and erosion engineering in rivers, estuaries and coastal seas*, Aqua publications, Blokzijl, Netherlands.

Vu, T. T. and Tan, S. K. (2009). A review of the current state-of-the-arts on the application of silt screens as sediment control equipment in open water, *in* S. K. Tan and Z. Huang (eds), *Asian and Pacific Coasts 2009*, World Scientific Publishing, pp. 60–66.

Vu, T. T. and Tan, S. K. (2010). Laboratory investigation of hydraulic performance of silt screens, *in* Y. S. Wu, S. Q. Dai and H. Liu (eds), *Proceedings of the 9th International Conference on Hydrodynamics*, China Ocean Press, pp. 307–312.

Vu, T. T., Tan, S. K. and Doorn-Groen, S. (2010). A case study of silt screen performance, *in* Dobson (2010).

Whitehouse, R. J. S., Soulsby, R. L., Roberts, W. and Mitchener, H. J. (2000). *Dynamics of estuarine muds*, Thomas Telford Publishing, London, UK.

Winterwerp, J. C. (1999). *On the dynamics of high-concentrated mud suspensions*, PhD thesis, Delft University of Technology, Delft, Netherlands.

Winterwerp, J. C. (2002). Near-field behavior of dredging spill in shallow water, *Journal of waterway, port, coastal and ocean engineering* **128**: 96–98.

Winterwerp, J. C. (2003). On the sedimentation rate of cohesive sediment, *in* J. P. Y. Maa, L. P. Sanford and D. H. Schoellhamer (eds), *Estuarine and coastal fine sediment dynamics*.

Wu, S. and Rajaratnam, N. (1995). Free jumps, submerged jumps and wall jets, *Journal of Hydraulic Research* **33**: 197–212.

Yasui, A., Deguchi, I. and Ono, M. (1999). Performance of silt protector in three dimensional flow, *in* J. S. Chung, T. Matsui and W. Koterayama (eds), *The Proceedings of The Ninth (1999) International Offshore and Polar Engineering Conference*, International Society of Offshore and Polar Engineers.

Appendix A

Case studies

Definition of all problems and processes related to silt screens in this report is partly based on knowledge and experience of dredging company Boskalis. In order to relate this research to dredging and reclamation practice, a number of case studies will be discussed in this appendix. Boskalis has done an effort to investigate silt screen effectiveness during a project. The well-documented results are discussed in section A.1. In literature, some case studies on silt screen effectiveness are found as well. These are discussed in section A.2.

A.1 Experiments by Boskalis

Dredging company Boskalis has been involved in a reclamation project in the Middle East. Since the reclamation site is situated in the vicinity of a vast coral reef, monitoring and mitigation of suspended sediment is a key activity of the project. A series of silt screen experiments has been carried out. By means of measuring buoys and a monitoring vessel, structured measurements were made of three different applications of a hanging silt screen and five of a standing one.

In one of three cases concerning the hanging type, suspended sediment concentrations were caused by overflowing of a trailing suction hopper dredger (TSHD). A screen of 6 m deep was positioned perpendicular to the main (tidal) flow direction. The depth was 13 m and the mean current velocity was about 0.1 m/s. The relative height of the screen is about 0.5 and flow conditions are moderate. Fine sediment was observed to get trapped in the downstream recirculation zone. Turbidity measurements suggest that the overflow plume was mixed through the whole water column by the silt screen. As a result, conclusions regarding silt screen effectiveness are negative. Nevertheless it does not become clear whether fine sediment ends up in the recirculation zone by horizontal or vertical diversion. The former might be the case, since the screen width is smaller than the plume width. So possibly a wider screen might have led to different conclusions.

Both other investigated applications of hanging silt screens were related to reclamation activities. Within a semi-enclosed reclamation, filling was done by means of a spreader pontoon. Along most of the open boundary a hanging silt screen was deployed. In one case, the distance between spreader and screen was about 800 m, allowing most of the suspended sediment to settle before reaching the silt screen. Accordingly, measurements of screen effectiveness were not very useful. Measurements regarding the second case gave proof of a high-density layer of suspended sediment moving along the bottom part of the water column. Over the silt screen, the height of this layer decreased slightly. Therefore conclusions were fairly positive.

All other experiments concerned the standing type of silt screen. They were related to construction of a bund for enclosed reclamation. A straight section of standing silt screen covering the full water depth of 8 m was replaced several times as construction of the bund proceeded.

Tidal flow of 0.2 m/s was mainly directed parallel to the screen. Only during slack tide, minor perpendicular flow velocities occurred. Except for one case where the silt screen was placed at a useless location, all experiments led to significant reduction of suspended sediment concentrations. Wave action and rotating flow direction during slack tide induced a small increase of near-bed suspended sediment concentrations on the 'outer' side of the screen. Waves also created an additional source of turbidity. Despite the small wave heights of 0.5 to 1.0 m, wave breaking at the newly reclaimed bund caused resuspension of fine sediment. Nevertheless, concentrations during such an event remained low when compared to concentrations during reclamation.

Two additional experiments were carried out regarding a full-depth standing silt screen perpendicular to the tidal flow. Except for one case of damage to a float, the screen was able to resist flow forces fairly well. Suspended sediment concentrations reduced over the screen in both cases. Conclusions were therefore positive, although in one case it was questioned whether a silt screen was needed at all regarding the small maximum concentrations.

In chapter 1 it was mentioned that in most situations hanging silt screens are preferred over standing silt screens. During this specific project, specific circumstances made standing silt screens competitive. Dredging activities were partly carried out by means of cutter suction dredgers (CSD). As a CSD is a stationary vessel, it needs tug assistance to move from site to site. Therefore, heavy floating equipment was already present at the project site, allowing for easy relocation of the standing silt screen.

A.2 Case studies in literature

More results on field measurements regarding silt screens have been published by various authors. Obviously, field measurements bring along practical limits to the amount of detail that can be achieved. The big scales do not allow for measurements of all relevant parameters in every specific region surrounding the silt screen. Therefore results are often susceptible of multiple interpretations, as was also noticed for the Boskalis experiments.

Jin et al. (2003) carried out measurements near a hanging silt screen of 3 m depth in water of 5.5 m depth. Suspended sediment originated from dredging activities by a grab dredger and a backhoe at about 300 m from the screen. Perpendicular tidal current velocities ranged from 0.2 to 0.3 m/s. Flow velocities and concentration profiles were measured at multiple locations on both sides of the silt screen. Published results show a negative influence of the silt screen on suspended sediment. Concentration profiles at the downstream side nearly always exceed those at the upstream side. Fluxes of suspended fine sediment on either side are of the same order of magnitude. During a moderate storm, concentrations reach values comparable to those during active dredging. This raises questions about background concentrations and the necessity to apply a silt screen in this specific case.

Vu et al. (2010) have reported on measurements near a big hanging silt screen (13 x 400 m) in deep water (22.5 m). Conditions were quite severe, as the depth-averaged perpendicular flow velocity varied between 0.2 and 0.6 m/s. Although both water depth and flow velocity are well out of the range of traditional silt screen applicability, moderately positive results are published. A small reduction of suspended sediment concentration and flux is achieved throughout the whole water column. Surprisingly, the results show no clear correlation with the flow velocity. One would expect a fair amount of vertical mixing downstream of the screen in case of 0.6 m/s currents. This does not follow from the results. Unfortunately no visual feedback has been published.

A.3 Mutual conclusions

Although the case studies discussed above do not cover the full range of all possible silt screen applications, they still offer useful information. With respect to the current research, the following conclusions can be drawn:

1. Hanging silt screen performance is highly variable. Judgments range from very negative to fairly positive.
2. Established guidelines on the applicability of silt screens regarding flow velocity and water depth do not always seem to hold. Negative performance has been reported within the traditional range of applicability and vice versa.
3. Standing silt screens covering the full water depth can be applied successfully in certain situations, oriented perpendicular as well as parallel with respect to the current.
4. The existence of a recirculation zone near the free surface downstream of a hanging silt screen has been verified.
5. Erosion of newly reclaimed land by waves forms an additional source of suspended fine sediment.

Appendix B

Possible applications

In this appendix a systematic inventory of all possible applications of hanging silt screens is made. This process is split in two main parts. Firstly, all possibilities for preventing high concentrations of suspended sediment from reaching vulnerable flora and fauna are listed. Secondly, the different applications of hanging silt screens are assessed per possibility from step one.

Figure B.1 depicts the situation of a dredging plume heading straight at vulnerable flora and fauna. Five options exist to prevent high sediment concentrations from reaching them: horizontal diversion (1), settling (2), extensive mixing (3), removal (4), halting (5).

Now an inventory of all different applications of hanging silt screens can be made. Table B.1 presents them ordered by mechanism from step one. Possible drawbacks are included as well, so as to assess feasibility.

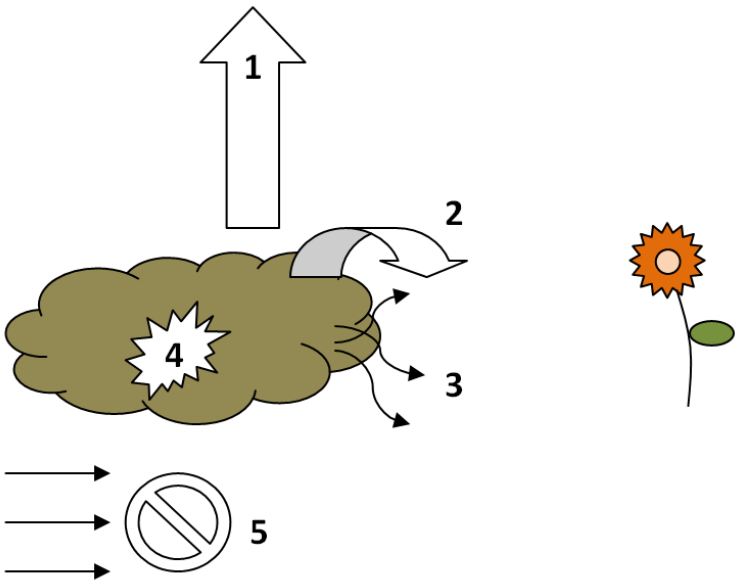

Figure B.1: Schematic overview of all possibilities for preventing high concentrations of suspended sediment from reaching vulnerable flora and fauna. The numbers refer to horizontal diversion (1), settling (2), extensive mixing (3), removal (4) and halting (5).

Table B.1: Possible applications of hanging silt screens.

	Application	Possible drawbacks
1a	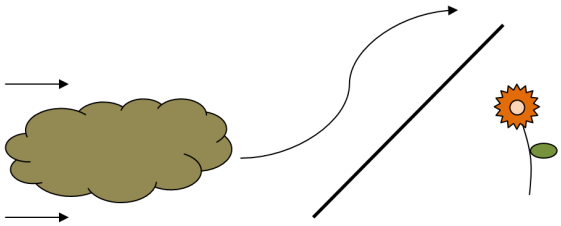	**Obliquely placed screen** • Vulnerable area is too big
1b	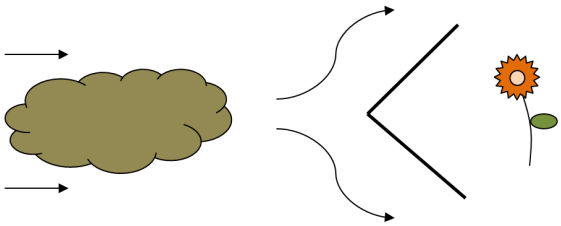	**V-shaped screen placement** • Vulnerable area is too big • Leakage near joint • Unintended vertical diversion
2a	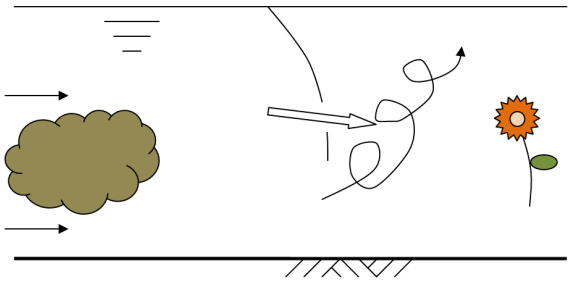	**Perforated screen** • Tensile strength of screen is lowered • Adverse effect • Complicated construction
2b	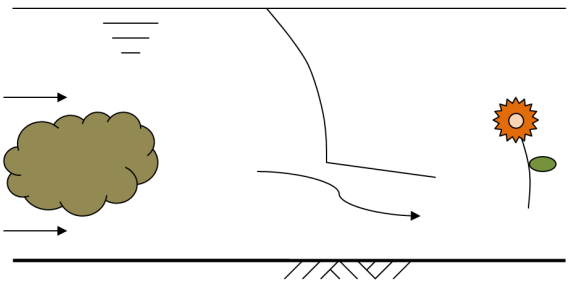	**Screen extended with flap** • Mixing downstream of flap • Complicated construction

	Application	Possible drawbacks
3a	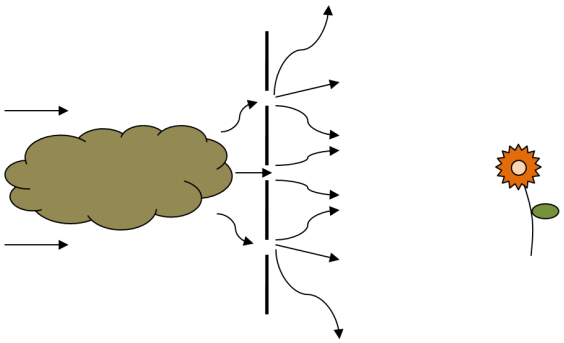	**Gap between sections** • Concentrations not reduced sufficiently
3b	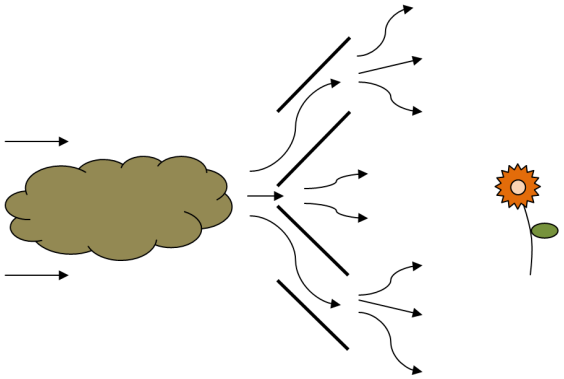	**Diffuser** • Concentrations not reduced sufficiently • Complicated placement
4	Not achievable by means of a silt screen	
5	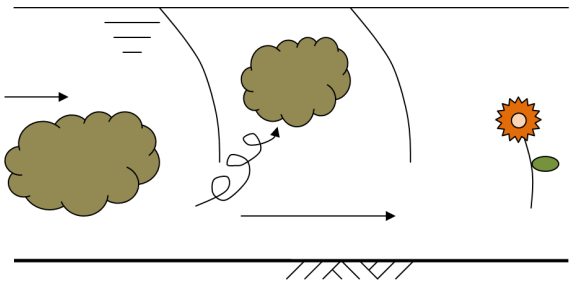	**Two silt screens** • Amount of silt screens doubled

Appendix C

Turbulence

When looking at a detailed time series of flow velocity measurements, one might observe something like figure C.1. Above a certain combination of flow parameters rapid velocity fluctuations occur. This is the result of turbulence. It has been defined by Hinze (1975) as follows: *'Turbulent fluid motion is an irregular condition of flow in which the various quantities show a random variation with time and space coordinates, so that statistically distinct average values can be discerned'.* Turbulence is characterized by three-dimensional flow structures of different length scales with a high degree of vorticity. At some point they are generated, then move on with the flow while developing further and eventually die out. This process is visualized clearly by for example smoke, whirling its way up through the air.

C.1 The onset of turbulence

The Reynolds number is a measure for turbulence. It represents the ratio of inertia over viscosity. This ratio can be used to illustrate the onset of turbulence. Panel 1 of figure C.2 depicts an initially laminar flow. Three streamlines lie nicely parallel to each other, but due to some reason left out of consideration a velocity difference appears. From Bernoulli's law it follows that pressure decreases between contracting streamlines, whereas it increases between diverging streamlines. Panel 2 shows that the pressure difference leads to curvature of the middle streamline, followed by an additional centrifugal force working in the same direction. Viscosity counteracts that process. Only when viscous forces are able to withstand inertial forces, these disturbances can be eliminated. This is generally the case for low flow velocities, small length scales, small fluid density and/or high viscosity. The flow is then said to be laminar. If not, the disturbances enhance themselves as illustrated in panel 3 and 4. One can imagine that this leads to the development of three-dimensional flow structures.

Via this generation of turbulence, energy is transferred from the mean motion to the turbulent motion. The principle of figure C.2 is valid in a range of different length scales. Therefore turbulent structures will be present from the biggest scales in a certain flow situation onto very small scales. Only at the smallest scales velocity gradients are high enough to allow for viscous dissipation of kinetic energy into heat. Turbulence can thus be seen as an intermediate stage in the dissipation of energy. The process of big whorls breaking down into ever smaller whorls until dissipation comes into play is known as the energy cascade. It has been mentioned before that the degree of turbulence can be expressed by means of the Reynolds number. It was said to represent the ratio of inertia over viscosity. Equation C.1 shows this in a parametrical way.

$$Re = \frac{\text{Inertia}}{\text{Viscosity}} = \frac{\rho \mathcal{U}\mathcal{L}}{\mu} = \frac{\mathcal{U}\mathcal{L}}{\mu/\rho} = \frac{\mathcal{U}\mathcal{L}}{\nu} \tag{C.1}$$

When Re is less than about 2,300 the flow can be characterized as laminar. In case Re is higher than about 4,000 the flow becomes turbulent. All values in between belong to the transitional

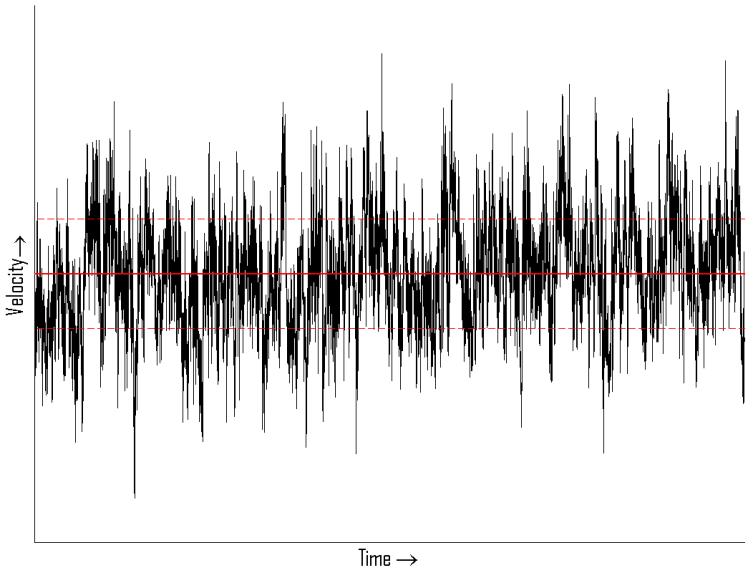

Figure C.1: Turbulent time series from research by Kang et al. (2003).

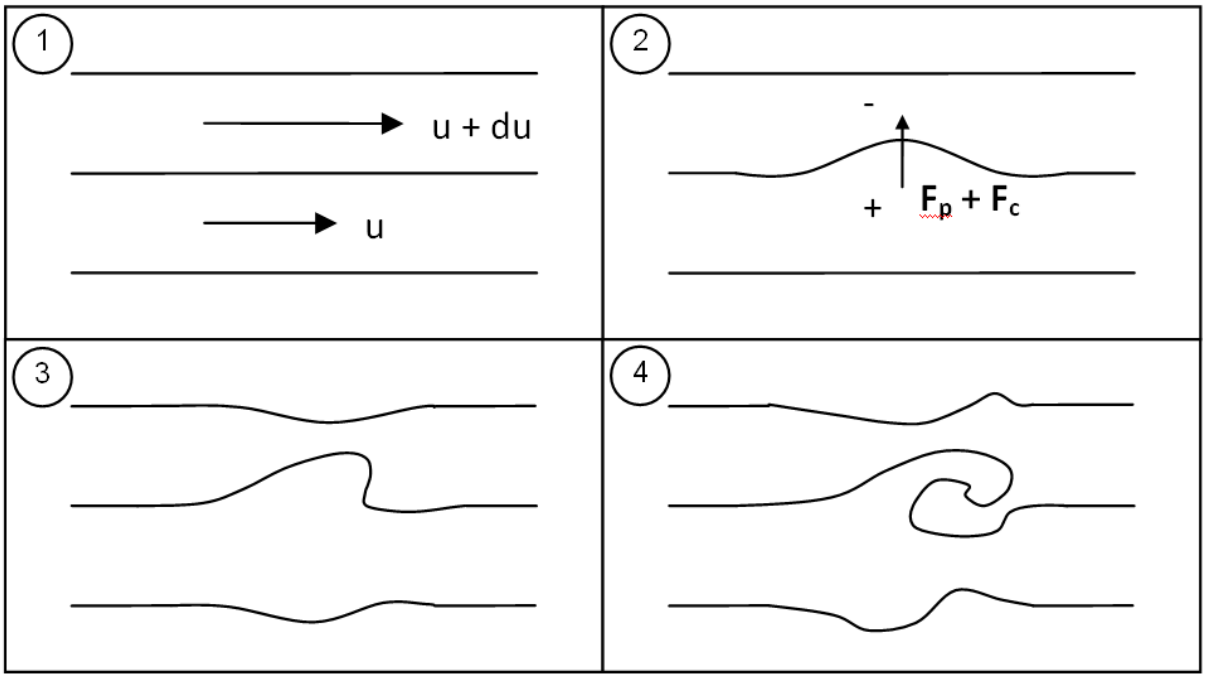

Figure C.2: Four successive stages in the onset of turbulence.

zone. The behaviour of the flow in this transitional zone can be explained by referring to figure C.2. An initial disturbance as displayed in panel 1 is needed to get the generation of turbulence going. Small disturbances can still be eliminated in the transitional zone, but bigger ones develop into fully turbulent structures. The flow then obtains a variable state, with sudden outbreaks of turbulence and periods of calm, laminar flow. Above Reynolds numbers of 4,000, disturbances continuously create new turbulent structures. The flow then really can be identified as turbulent.

The Reynolds number tells something about the character of a certain flow situation. It does not specify anything about the spatial distribution of turbulence within that situation. The statistical description of turbulence offers a solution. In the time series of figure C.1, the thick red line indicates the mean value of all measured velocities. The complete signal u is thought to be the sum of the mean velocity $\bar{u}$ and a fluctuating component u'. This is called the Reynolds decomposition. The dotted red lines mark the bandwidth of velocities within one standard deviation (σ) of $\bar{u}$. For a Gaussian distributed signal, this σ is equal to the root-mean-square value of all turbulent fluctuations. The latter can be used as a typical order of magnitude, called the turbulence intensity r. The square of σ is the variance of all velocity fluctuations. It is a measure of the kinetic energy contained in turbulent motions. Such velocity measurements can be obtained everywhere in the flow. In that way the spatial distribution of turbulence can be assessed.

C.2 Types of turbulence

Theoretically it is possible to generate laminar flow of any desired Reynolds number, as long as no disturbances are generated. In a laboratory situation one can create flows along very smooth surfaces and with a minimum amount of internal shear. In that case flow is able to remain laminar up to fairly high Reynolds numbers. In hydraulic engineering practice however, sufficiently disturbing elements will always be present and the above-mentioned limits for Re are respected. Only one feature is responsible for the generation of turbulence, being a velocity gradient. Velocity gradients can have two different causes. This accordingly divides turbulent flows into two main categories: wall flow and free flow.

The term wall flow relates to flows that are governed by the proximity of a closed boundary. Viscosity prescribes a no-slip condition at the boundary surface. In case of a current, flow velocities away from the wall are non-zero. This will always result in a velocity gradient perpendicular to the wall. When a certain flow condition holds long enough, a boundary layer will develop. In the boundary layer the influence of the wall is noticeable and flow velocities get higher with increasing distance from the wall.

Remote from a closed boundary, one speaks of free flow. Velocity gradients and the associated generation of turbulence can still occur. Mixing layers, jets and wakes are identified as the three main types of free turbulence. Grid turbulence and plumes might also be named in this respect. Grids are used in laboratory situations to create more or less homogeneous turbulence. Plumes form a somewhat separate category, since they are driven by density differences. Most free flows are characterized by self similarity. Velocity profiles perpendicular to the mean flow direction at varying distance from the source of free turbulence are of the same shape.

An initial wall flow can transform into free flow. This process is known as flow separation. It occurs near sudden geometrical changes, like man-made structures or bedforms. The main flow is then not able to follow the curvature of the boundary. When the cross-sectional width increases, continuity forces the flow to slow down. Near the boundary flow velocities are already very small. Therefore a negative velocity gradient in the direction of the mean flow can easily give rise to negative velocities in that region. Hence a recirculation zone exists downstream of the separation point. Between the main flow and the recirculation zone transverse velocity gradients are big. There a mixing layer develops with high turbulence intensities. At some

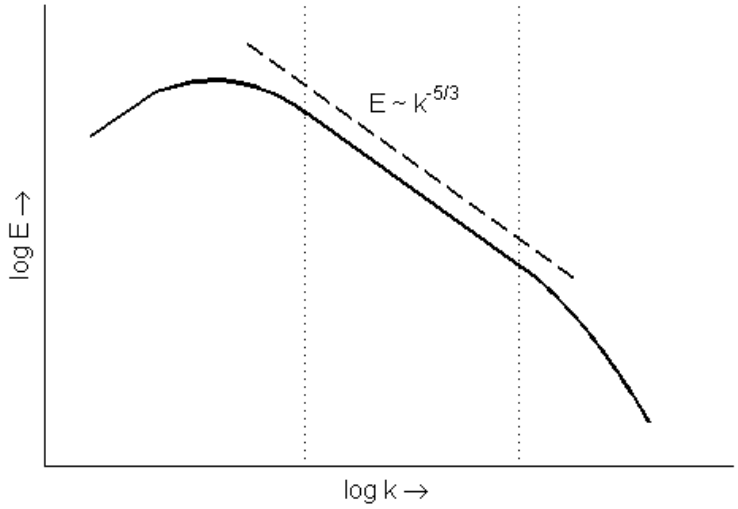

Figure C.3: Typical shape of the one-dimensional energy-density spectrum of a turbulent flow.

distance downstream of the disturbance, flow recovery takes place. A new boundary layer gradually develops based on the downstream geometry.

C.3 Turbulent kinetic energy

It was already briefly mentioned that the generation of turbulence transfers energy from the mean flow to the turbulent fluctuations, which eventually leads to dissipation. The energy of a turbulent flow is distributed over the mean flow and the turbulent motions. This becomes clear after applying the Reynolds decomposition to the total energy of the flow per unit volume, see equation C.2.

$$E = \frac{1}{2}\rho\overline{uu} = \underbrace{\frac{1}{2}\rho\overline{uu}}_{E_m} + \underbrace{\frac{1}{2}\rho\overline{u'u'}}_{E_t} \tag{C.2}$$

As energy is passed on from large to small scales, it is interesting to analyse how the turbulent kinetic energy (TKE) E_t is distributed over the length scales. A turbulent timeseries can be seen as the sum of the signals of all passing eddies. Therefore, all length scales of the turbulent flow should be represented in it. However, a single-point timeseries merely contains information on time scales and not on length scales. To make the conversion, an assumption is needed about the way turbulent structures travel through the space domain. This assumption is provided by Taylor's hypothesis, also known as the frozen turbulence approximation. It states that the velocity field, being a collection of 'frozen' turbulent eddies, translates through the space domain at constant velocity. When considering a single-point timeseries, the frozen velocity field travels along the local streamline at mean velocity. Therefore, projecting the velocity components onto the streamline and multiplying the sample times with the mean velocity results in an approximation of the spatial distribution of velocities along the streamline. Due to the coupling between the time and space domains the spatial coordinates are reversed, but this does not affect the analysis.

By taking the Fourier transform of the autocovariance of the converted turbulent timeseries and integrating over the three dimensional wavenumber space, the one-dimensional energy-density spectrum is obtained. Typically the spectrum is shaped like the solid line in figure C.3. The left-hand side of the figure represents the large, energy containing eddies. The right-hand side represents the length scales at which dissipation takes place. The part in between,

commonly known as the inertial subrange, contains the energy cascade. Based on dimensional considerations, energy-density can be shown to scale with $k_w^{-5/3}$ in the inertial subrange.

Appendix D

Fine sediment

Fine sediments form a separate part of sediment theory. They are mainly distinguished by small particle sizes and accordingly small weights. Nevertheless, chemical aspects turn out to be at least as important. Section D.1 discusses the basic properties of fine sediment. In section D.2 erosion, transport and deposition of fines are addressed. Finally section D.3 clarifies similarities and differences between SSC and turbidity. An elaborate description of fine sediment dynamics is found in e.g. Whitehouse et al. (2000), on which this appendix is largely based.

D.1 Properties of fine sediment

All particles with an equivalent diameter d smaller than 63 μm are classified as fine sediment. Within this category an important difference exists between silt and clay. This difference is characterized by particle size as well as particle nature. Particles having a diameter between 2 and 63 μm are officially recognized as silt. Smaller ones are said to be clay particles. Although these limits are roughly adhered to, the most decisive aspect is particle nature. Silt particles are comprised of quartz minerals, just like sand. Therefore, silt can simply be thought to act as sand grains with very small particle diameters. Clay however consists of clay minerals (primarily kaolinite, illite, chlorite and montmorillonite). Because of their specific properties, clay minerals mainly form a plate-like structure. These clay particles are much less stable than silt grains in a chemical sense.

One of the most relevant parameters of sediment regarding morphologic research is its settling velocity w_s. Sediment particles are suspended in the surrounding water instead of dissolved. Besides flow-related and chemical forces, gravity is the most important force acting on a particle. When releasing a particle in stagnant water, its fall velocity will reach a constant value after an initial start-up phase. This is due to a balance between gravity and the drag force. The drag force F_D acting on a falling particle depends on the flow characteristics. For small Reynolds numbers $Re = w_s d/\nu$, viscosity dominates inertia. This generally holds for falling fine sediment particles in water. In that case, Stokes' Law is applicable and F_D is calculated according to equation D.1. Particles are schematised as spheres.

$$F_D = 3\pi\mu d w_s \tag{D.1}$$

The gravitational force acting on a submerged spherical particle of density ρ_s and volume V is given in equation D.2. When drag force and gravitational force F_g have reached a balance, the final fall velocity $w_{s\infty}$ follows from equation D.3.

$$F_g = (\rho_s - \rho) g V_p = (\rho_s - \rho) g \frac{1}{6}\pi d^3 \tag{D.2}$$

$$\begin{aligned} F_D &= F_g \\ 3\pi\mu d w_{s\infty} &= (\rho_s - \rho) g \frac{1}{6}\pi d^3 \\ w_{s\infty} &= \frac{(\rho_s - \rho) g d^2}{18\mu} \end{aligned} \tag{D.3}$$

Final fall velocities are always relatively small. The acceleration phase is very brief and the equilibrium situation is reached quickly. As a result, $w_{s\infty}$ will simply be indicated as w_s. Settling velocities of fine sediment are in the order of 0.01 mm/s, whereas coarser ones typically have settling velocities in the order of 1 cm/s. This leads to an important difference of behaviour between both types. For water depths in the order of 10 m, settling times of fine and coarse particles are 10^6 s and 10^3 s respectively. The settling velocity of fine sediment is easily overruled by an upward vertical flow velocity, increasing settling times even further. The more or less floating behaviour of fines elucidates the troubles faced fighting turbidity.

It was already mentioned briefly that clay is less stable than silt in a chemical sense. The plate-like clay particles formed by clay minerals possess ionic charges. Their edges are positively charged, their faces negatively. Other charged particles can get attracted by these electrostatic forces. Water might contain free cations (positively charged) and anions (negatively charged). When clay gets in touch with water, cations form a layer on the plate faces and anions collect around the edges. The charged clouds surrounding clay particles are able to cling together. Organic material can be adsorbed as well. Long polymer chains offer an effective way of gathering particles together in flocs. Hence the process is called flocculation. Big empty spaces in these aggregates are filled with water, giving flocs a water content of 90 to 98% under natural conditions.

Flocs are formed due to attractive forces. However, the magnitude of these forces decreases rapidly with distance. Therefore particles have to be brought into contact with each other in order to achieve cohesion. The processes of collision and cohesion are therefore the most important ones regarding flocculation. Cohesion has been discussed above. Collisions between particles can have three different causes: Brownian motion, internal shear and different settling velocities. From analogy with diffusion, it becomes clear that Brownian motion is only able to cause collision of particles on a small scale. The range of different settling velocities depends on the chemical and biological characteristics of water and sediment. Internal shear plays a dual role. It is both a floc promoting and limiting process. Turbulence comes with internal shear. When turbulence intensities are high enough, aggregates start disintegrating again.

Flocculation is not just an interesting side effect of clay. It influences the physical parameters regarding suspended sediment to a great extent. Due to the large water content of flocs, their density ρ_f decreases to about 1100 kg/m^3. The equivalent diameter of a floc may vary from microns to millimeters. The increase of d tends to have a bigger influence on w_s than the decrease of ρ_f. Therefore flocculation is able to magnify settling velocities drastically.

In a natural environment, fine sediment will virtually never consist of only one type. Clay, silt and sand particles are found mixed up in varying proportions, together with organic material, water and sometimes gas. The mixture is mostly indicated as 'mud'. The clay content and chemical properties of the surrounding water determine whether sediment is cohesive or not.

Whether or not cohesive, one single value of the settling velocity will never be applicable to every particle in a specific situation. Grains and flocs coexist in a variety of sizes, each with its own settling velocity. Therefore it comes down to a settling velocity *distribution*. For non-cohesive sediment in low suspended concentrations, settling velocities are readily linked to the grain size distribution. In case of cohesive sediment, the composition of flocs may vary significantly. The Stokesian settling velocity according to equation D.3 does not hold, since flocs can not be schematised as homogeneous spheres. Various authors have reported on cohesive

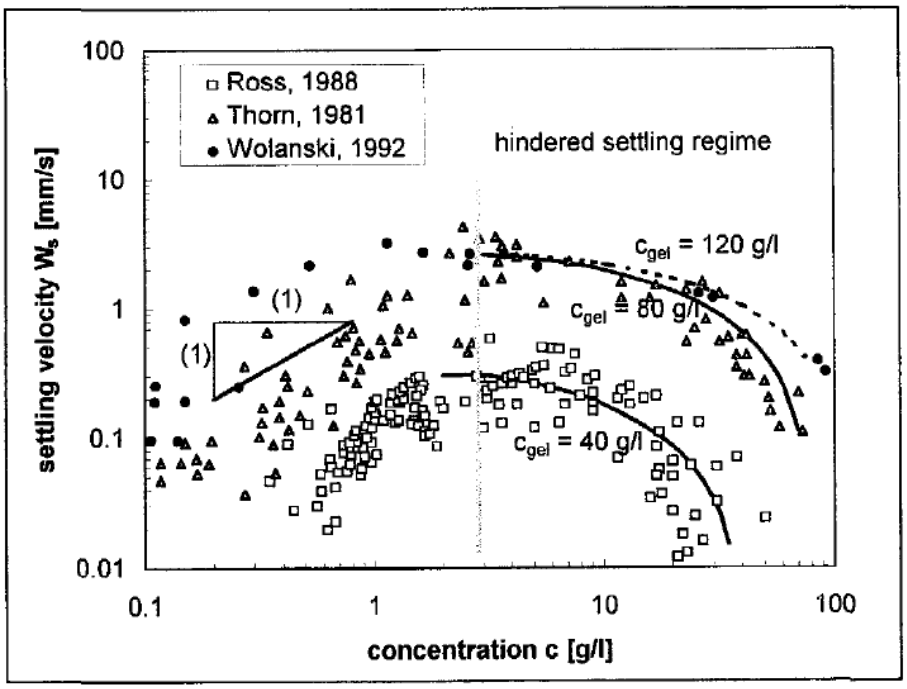

Figure D.1: Experimental data relating the settling velocity of mud flocs to the suspended sediment concentration (Winterwerp, 1999).

settling velocity distributions. At low concentrations, a very simple relation like equation D.4 may be used, but with caution.

$$w_{s50} = kC^m \tag{D.4}$$

Here w_{s50} denotes the median settling velocity, i.e. the settling velocity exceeded by 50% of all flocs, C is the suspended sediment mass concentration and k and m are coefficients. Whitehouse et al. (2000) propose $k = 0.001$ and $m = 1.0$. Low concentrations are defined as lower than 3000 mg/l. Winterwerp (1999) expanded equation D.3 to calculate the settling velocity of individual mud flocs. This resulted in equation D.5.

$$w_{s,r} = \frac{\alpha}{18\beta}\frac{(\rho_s - \rho_w)g}{\mu}D_p^{3-n_f}\frac{D^{n_f-1}}{1 + 0.15Re_p^{0.687}} \tag{D.5}$$

Here, α, β and n_f are coefficients depending on the shape of the floc, D_p is the diameter of primary mud particles, D is the floc diameter and $Re_p = w_{s,r}D/\nu$ is the particle Reynolds number. The left-hand side of figure D.1 shows the relation between settling velocity of mud flocs and suspended sediment concentration for various experimental datasets. The line indicating a 1-in-1 slope represents equation D.4 with $k = 0.001$ (note the unit mm/s on the vertical axis) and $m = 1.0$. It appears that especially coefficient k varies from case to case.

The right-hand side of figure D.1 shows the process of hindered settling. At high suspended sediment concentrations, settling flocs interfere with each other and the surrounding flow of fluid. This reduces the settling velocity, which is expressed by the decaying line at the right-hand side of figure D.1. Winterwerp (1999) distinguishes seven processes affecting the settling velocity of individual particles in a suspension:

- A falling particle of finite dimensions gives rise to *return flow and wake formation.* Surrounding particles are slowed down by the return flow, but accelerated when pulled into the wake.

- Return flow and wake formation involve velocity gradients. This *dynamic or flow effect* leads to a change in pressure distribution, added mass of the particles and hydrodynamic drag.
- *Particle-particle collisions* lead to a direct exchange of momentum between particles. As collisions lead to a loss of energy, on average particles are slowed down.
- *Particle-particle interactions* are the combined effect of attracting and repelling forces between particles due to e.g. electrical charges.
- The presence of particles in a fluid leads to an *increase of viscosity*. As individual particles are thought to fall in the surrounding suspension, their settling velocity is decreased.
- The argument that individual particles fall in the surrounding suspension can be used as well to discuss the *increase of density* of the fluid. Individual particles are slowed down by their higher buoyancy.
- When a particles are pulled into the wake of another particle, this might induce *cloud formation*. The cloud starts to behave as a large grain, which leads to an increase of settling velocity.

The onset of hindered settling happens above concentrations of 1 g/l, which is the upper limit of concentrations measured near silt screens. However, closer to the source of turbidity, hindered settling will come into play.

D.2 Erosion, deposition and transport

The real importance of (fine) sediment to hydraulic engineers is its ability to get transported by a current. Or to put it different: its impotence to remain in position. Above a certain limit of flow parameters, sediment gets eroded from the bed. It is then transported by the current. Under influence of its settling velocity, every particle is deposited back onto the bed eventually. Three consecutive subsections address the processes of erosion, deposition and transport.

D.2.1 Erosion

Equations for erosion of cohesive beds are mostly based on the threshold bed shear-stress τ_e. The value of τ_e is related to some parameter representing bed density. Either bulk-density ρ_B = mass of mixture/volume of mixture or bed-concentration C_b = mass of grains/volume of mixture is used for this purpose. The formulation of Thorn and Parsons is commonly used and is given in the empirical equation D.6.

$$\tau_e = E_1 C_b^{E_2} \tag{D.6}$$

E_1 and E_2 are dimensional coefficients. Their values are subject to debate and may vary slightly from situation to situation. Whitehouse et al. (2000) state that the values $E_1 = 0.0012$ and $E_2 = 1.2$ give the best fit in general (with C_b in g/m^3).

Based on τ_e, the empirical equation D.7 by Partheniades is applicable to compute the rate of erosion dm/dt. The rate of erosion denotes the dry mass of cohesive sediment eroded per unit area per unit time.

$$\begin{aligned} \frac{dm}{dt} &= M_e\left(\frac{\tau_0}{\tau_e} - 1\right) && \text{for } \tau_0 > \tau_e \\ \frac{dm}{dt} &= 0 && \text{for } \tau_0 \leq \tau_e \end{aligned} \tag{D.7}$$

Dimensional coefficient M_e is known as the erosion rate. From literature study, Van Rijn (2005) reports values between 10^{-5} and $5 \cdot 10^{-4}$ kg/(sm^2), depending amongst others on mineral composition, organic material and salinity. τ_0 is the bed shear-stress and the term $(\tau_0/\tau_e - 1)$ is called the relative excess bed shear-stress.

D.2.2 Deposition

Due to the settling velocity, suspended particles tend to return to the bed. Therefore the main parameter regarding deposition is the median settling velocity w_{s50}. In case of still water, there is no sediment movement but settling. The rate of deposition dm/dt then depends solely on w_{s50} and C_0. The latter denotes the near-bed concentration of suspended sediment. Equation D.8 shows this relation.

$$\frac{dm}{dt} = -C_0 w_{s50} \tag{D.8}$$

In case of flowing water, the above equation needs modification. Increasing bed shear stress will decrease the deposition flux. Whitehouse et al. (2000) proposes to use a threshold bed shear-stress for deposition τ_d, above which deposition completely ceases. In mathematical terms this relationship is expressed by equation D.9.

$$\begin{aligned} \frac{dm}{dt} &= -(1 - \frac{\tau_0}{\tau_d}) C_0 w_{s50} && \text{for } \tau_0 < \tau_d \\ \frac{dm}{dt} &= 0 && \text{for } \tau_0 \geq \tau_d \end{aligned} \tag{D.9}$$

The notion of one threshold bed shear-stress for deposition does only hold under assumption of homogeneous suspended sediment. For varying grain or floc sizes, every particle has got its own value of τ_d. When used in combination with the median settling velocity w_{s50}, values between 0.06 and 0.10 Nm^{-2} are suggested for τ_d by Whitehouse et al. (2000).

Winterwerp (2003) argues that a threshold bed shear-stress for deposition does not exist. He considers it an apparent effect resulting from a threshold bed shear-stress for resuspension of deposited material. In this research, these findings are incorporated by assigning an infinitely high value to τ_d.

Furthermore it is possible to introduce sediment fractions. The total collection of particles is broken down into discrete fractions, each with its own τ_d, w_s and C_0. Calculation of the rate of deposition is done per fraction. Summation over all fractions gives the total deposition flux.

D.2.3 Transport

Transport of suspended sediment can be explained best by setting up a mass balance. This exercise is closely related to the basic equations governing two- and three-dimensional flow and transport models. Therefore it is discussed in the corresponding section on basic equations in appendix F. For now the treatment of theory on suspended sediment transport is restricted to a couple of important notions.

Generally, transport of suspended sediment is simplified to transport of a passive tracer with an additional vertical velocity due to settling. On the whole, three different processes can be recognised: advection, diffusion and dispersion. The latter term is sometimes used ambiguously in fluid mechanics. Here, dispersion indicates the direct effect of velocity gradients in the mean motion on a cloud of suspended material. Different parts of the cloud are advected at different velocities. As a result, the cloud starts deforming. It should be noted that dispersion only changes the shape of the cloud, while the volume remains the same. Therefore dispersion does not influence concentrations directly, although it is able to increase the surface area subjected to diffusion. Depending on the boundary conditions, spreading can be governed by different processes.

As we have seen already, cohesive sediment brings along some complications regarding settling velocity. As expressed in equation D.4, the median settling velocity depends on the concentration of suspended sediment rather than grain size. In general, concentrations vary in vertical direction. Hence the settling velocity of cohesive sediment varies in vertical direction as well. Closer to the bed, concentrations are higher. This leads to a higher settling velocity. The opposite is valid closer to the free surface.

D.3 Turbidity

The terms suspended sediment concentrations (SSC) and turbidity have been used interchangeably. They are closely related indeed. In fact SSC and turbidity are different measures for the same phenomenon. The use of suspended sediment concentrations is very straightforward. It is equal to the weight of all suspended sediment particles present in a predefined volume of water. This is an exact measure, although it requires some steps to determine SSC given a certain volume of water.

Turbidity, in the context of dredging operations, is concerned with the presence of suspended sediment particles in water as well. As the international standard NEN-EN-ISO 7027 (2000) defines it, turbidity is a reduction of transparency of a liquid caused by the presence of undissolved matter. Hence, it focuses on visual aspects rather than exactly measurable quantities. Two units are commonly used to express turbidity, being the Nephelometric Turbidity Unit (NTU) and Jackson Turbidity Unit (JTU). The former is used in this report. Its measurement is based on the amount of reflection of a light beam pointed at the suspension. The use of NTU does not belong to exact science, since a direct link to SSC can not be made. NTU values do not only vary with SSC, but also with shape, reflective properties and colour of sediment particles. Despite this disadvantage compared to SSC, turbidity is still commonly used as a quantity in hydraulic engineering because of the simplicity of measurements. These can simply be carried out by means of a so-called nephelometer. Nevertheless, one should always be aware of the shortcomings.

Appendix E

Laser Doppler Anemometry

Local velocities were said to be measured by means of Laser Doppler Anemometry (LDA). This is an optical measurement technique, which makes use of laser beams. The general application of the instrument is depicted in figure E.1. A single laser beam passes through an acousto-optic modulator (also known as a Bragg cell). By means of acoustic waves, the Bragg cell splits the laser beam into two separate beams. These adopt the frequency of the acoustic waves, which is far lower than the frequency of the electromagnetic laser frequency. The beams are focused by means of a lens, so as to create an intersection of both beams within a fluid under an angle θ. Within the intersection, the beams create an interference pattern based on the Bragg cell's acoustic frequency. The interference pattern is indicated in the bottom left corner of figure E.1.

Fine suspended particles within the fluid scatter the laser light when they pass through the intersecting beams. The scattered light, which has attained a Doppler shift with respect to the issuing light, is recorded by a receiver. The velocity can now be derived from this Doppler shift. This is done by means of figure E.2. The two green laser beams consist of successive crests (black lines) and troughs. It is readily seen that the crests intersect along straight lines, called fringes. The Doppler frequency, that is the difference between the issuing and recorded frequencies, modulates the amplitude of the recorded signal. When a particle moves through a fringe it scatters a high light intensity and in between fringes it scatters a low light intensity. When the fringe spacing δ is known, the velocity of the particle can be calculated from the Doppler shift of the scattered signal. The fringe spacing depends on the wave length λ of the laser beams. It is derived by means of the right-hand side of figure E.2. First, λ and δ are defined:

$$AF = EB = \lambda$$
$$DC = \delta$$

The crests are directed perpendicular to the direction of propagation. This yields:

$$\angle ACB = \theta$$

Triangle ABC is an isosceles triangle and AF, BE and CD are its altitudes. Four similar triangles can be discerned:

$$\triangle ACD \sim \triangle BCD \sim \triangle ABE \sim \triangle BAF$$

Due to similarity of triangle ABE and triangle ACD, angle ABE is found:

$$\angle ABE = \angle ACD = \theta/2$$

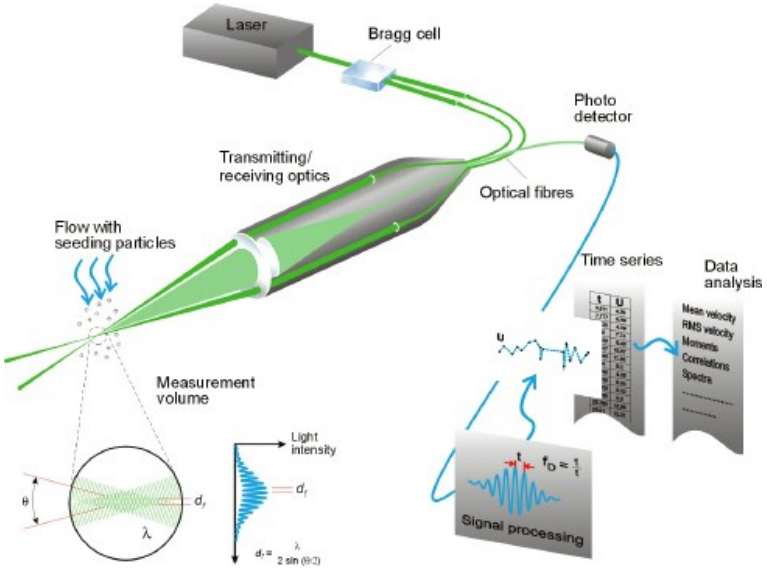

Figure E.1: The working principle of LDA (http://www.dantecdynamics.com/).

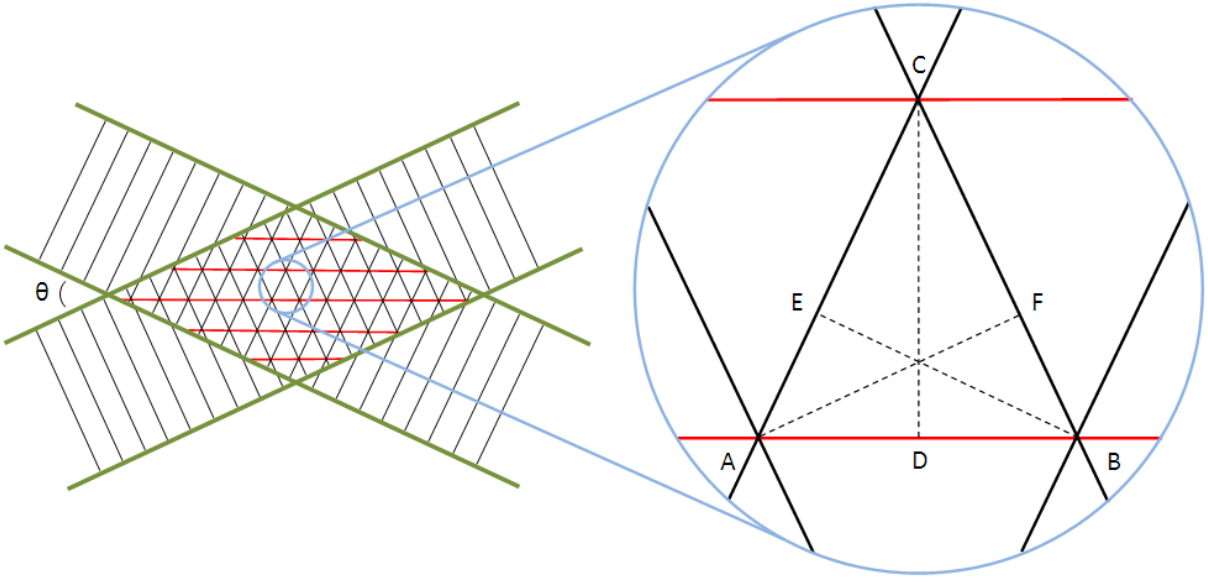

Figure E.2: The interference pattern of two crossing laser beams.

With the help of some trigonometry, δ can be expressed in terms of λ and θ:

$$AB = \frac{AF}{\cos \theta/2} = \frac{\lambda}{\cos \theta/2} = 2AD = 2CD \tan \theta/2 = 2\delta \frac{\sin \theta/2}{\cos \theta/2}$$

$$\delta = \frac{\lambda}{2 \sin \theta/2}$$

Let the recorded Doppler frequency be f_D. Now the particle's velocity u can be calculated:

$$u = f_D \delta$$

However, the sign of u can still not be determined. Irrespective of which way the particle moves through the fringes, the recorded Doppler shift will be the same. Therefore, the frequency of one of both laser beams is given a small, known shift f_s. This causes the fringes to move slowly at a speed v_s, which equals:

$$v_s = f_s \delta$$

Now the recorded amplitude modulation has got a frequency of $f_s + f_D$ or $f_s - f_D$, which takes away the directional ambiguity.

Appendix F

Numerical models

For this research, use is made of two computational fluid dynamics (CFD) models. The fully 3-dimensional Large Eddy Simulation code Dflow3D is used to investigate the process of vertical diversion. The 2-dimensional horizontal (2DH) code FINEL2D is applied to study horizontal diversion. Section F.1 will deal with the basic equations governing flow and transport. After that, section F.2 presents the specifics of Dflow3D and section F.3 treats those of FINEL2D.

F.1 Basic equations

Generally, incompressible 3-dimensional flows of a Newtonian fluid are described by means of the continuity equation and the incompressible Navier-Stokes equation. The former is presented by equation F.1 and follows from a mass balance.

$$\frac{\partial \rho}{\partial t} + \nabla \cdot (\rho \mathbf{u}) = 0 \tag{F.1}$$

The continuity equation implies that the velocity field is free of divergence. The incompressible Navier-Stokes equations can be derived from the momentum balance and are presented by equation F.2.

$$\frac{\partial \rho \mathbf{u}}{\partial t} + \nabla \cdot (\rho \mathbf{u}\mathbf{u}) = -\nabla p + \nabla \cdot \tau + \rho \mathbf{F} \tag{F.2}$$

Here, $\mathbf{u}$ denotes the 3-dimensional velocity vector, p is pressure, τ is a shear stress tensor and all body forces like Coriolis and gravity are lumped in $\mathbf{F}$.

Transport of suspended solids is can be described by means of a transport equation for (volume) concentration C_v. This is given in equation F.3.

$$\frac{\partial C_v}{\partial t} + \nabla \cdot (\mathbf{u} C_v) = \nabla \cdot (D \nabla C_v) \tag{F.3}$$

In this equation, D is the diffusion coefficient.

Turbulent fluctuations occur down to very small length scales. Solving for all these length scales and their associated time scales in a CFD model is known as direct numerical simulation (DNS). These are computationally very expensive, which limits the domain size to a large extent. A solution is found in applying the Reynolds decomposition to the Navier-Stokes equation. The non-linear advection term creates an extra term stemming from the fluctuating velocity component. Equation F.4 shows the resulting Reynolds-averaged Navier-Stokes (RANS) equation.

$$\frac{\partial \rho \bar{\mathbf{u}}}{\partial t} + \nabla \cdot (\rho \bar{\mathbf{u}} \bar{\mathbf{u}}) + \nabla \cdot \tau' = -\nabla p + \nabla \cdot \tau + \rho \mathbf{F} \tag{F.4}$$

$$\text{with } \tau' = \rho \overline{\mathbf{u}'\mathbf{u}'}$$

The extra term represents the gradient of the so-called Reynolds stresses or turbulent shear stresses τ'. These still contain the fluctuating velocity component and require simplification in order to speed up numerical simulation. Methods to close the Navier-Stokes equations are known as turbulence models. Many turbulence models focus on finding an expression for the Reynolds stresses based on the averaged velocity vector, but different and more sophisticated models exist as well.

F.2 Dflow3D

Dflow3D is an academical CFD model optimised for the use of Large Eddy Simulation (LES). It is a rigid lid model, meaning that the model has a constant depth instead of a free surface. LES is a turbulence model which makes use of averaging in space instead of averaging in time. The bigger length scales of the turbulent energy-density spectrum contain the anisotropic part of all turbulent fluctuations and are therefore responsible for most of the shortcomings of time-averaged turbulence models. In LES, turbulent length scales are represented down to the grid cell size. The more isotropic part of the energy spectrum is filtered out of the equations by filtering over one or more grid cells. In the inertial range, the key function of smaller length scales is extracting energy from the bigger length scales in order to keep the energy cascade going. This process can be approximated quite well by means of a sub-grid scale (SGS) stress term. The resulting filtered equation looks much like the RANS equation, except for the fact that the overbars represent averaging in space and the Reynolds stresses have been replaced by the sub-grid stress τ_{sgs}, see equation F.5.

$$\frac{\partial \rho \bar{\mathbf{u}}}{\partial t} + \nabla \cdot (\rho \bar{\mathbf{u}} \bar{\mathbf{u}}) = -\nabla p + \nabla \cdot \tau + \nabla \cdot \tau_{\mathbf{sgs}} + \rho \mathbf{F} \tag{F.5}$$

An additional model is now needed to compute τ_{sgs}. In this study, the wall-adapting local eddy-viscosity (WALE) model is used (Nicoud and Ducros, 1999) with a WALE constant C_w of 0.325.

Transport of suspended solids is computed by means of equation F.3. D is determined from the kinematic viscosity as $D = \nu/Sc$, where Sc is the Schmidt number. The kinematic viscosity used in Dflow3D is the sum of the molecular kinematic viscosity and the SGS kinematic viscosity computed by the WALE model. The value of Sc is discussed further in chapter 4.

F.3 FINEL2D

FINEL2D is a 2DH CFD model based on the shallow water equations. If the horizontal length scales of a flow are much bigger than the vertical length scales, vertical accelerations may be assumed to equal zero. This leads to a hydrostatic pressure distribution. Integrating the continuity equation and Navier Stokes equation over depth and applying the Boussinesq approximation regarding buoyancy results in equations F.6 and F.7 respectively.

$$\frac{\partial \eta}{\partial t} + \nabla \cdot (h\mathbf{U}) = 0 \tag{F.6}$$

Here, $h = \eta + z_b$ denotes the actual water depth with η the surface elevation and z_b the vertical bed coordinate, and $\mathbf{U}$ is the two-dimensional depth-averaged velocity vector.

$$\frac{\partial h\mathbf{U}}{\partial t} + \nabla \cdot (h\mathbf{U}\mathbf{U}) + gh\nabla\eta - \frac{1}{\rho}\tau_{\mathbf{b}} = 0 \tag{F.7}$$

Bed shear stress is represented by the vector $\tau_{\mathbf{b}}$. It should be noted that turbulent shear stresses are left out of consideration in FINEL2D. This restricts the use of the code to flows dominated by advection.

Appendix G

Validation figures

Validation of the CFD model Dflow3D is done by means of the laboratory experiments conducted for this research. An elaborate description of validation scenario 2A is given in section 4.2.2. This appendix contains figures for all scenario's.

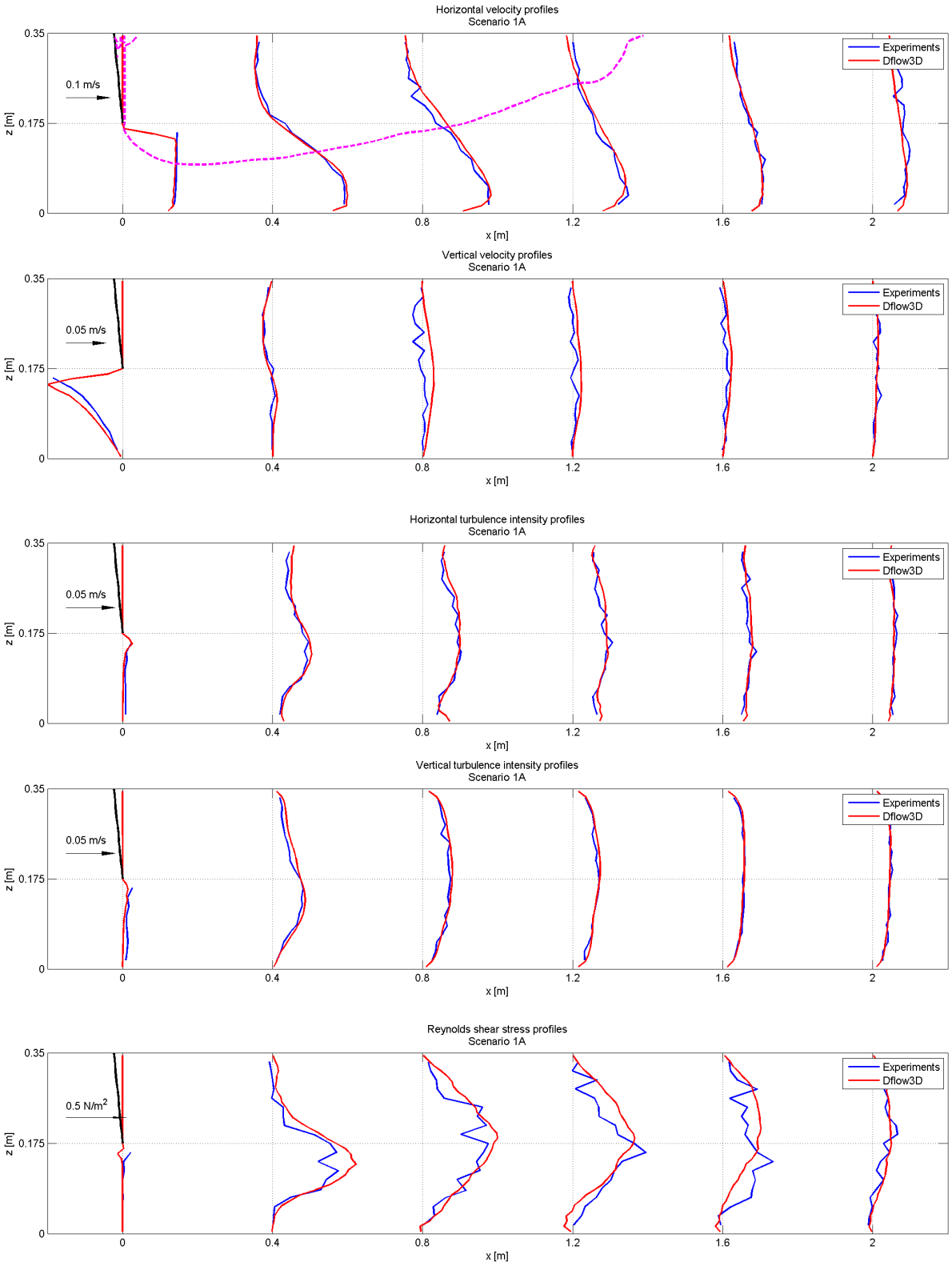

Figure G.1: Validation of the numerical model for laboratory scenario 1A.

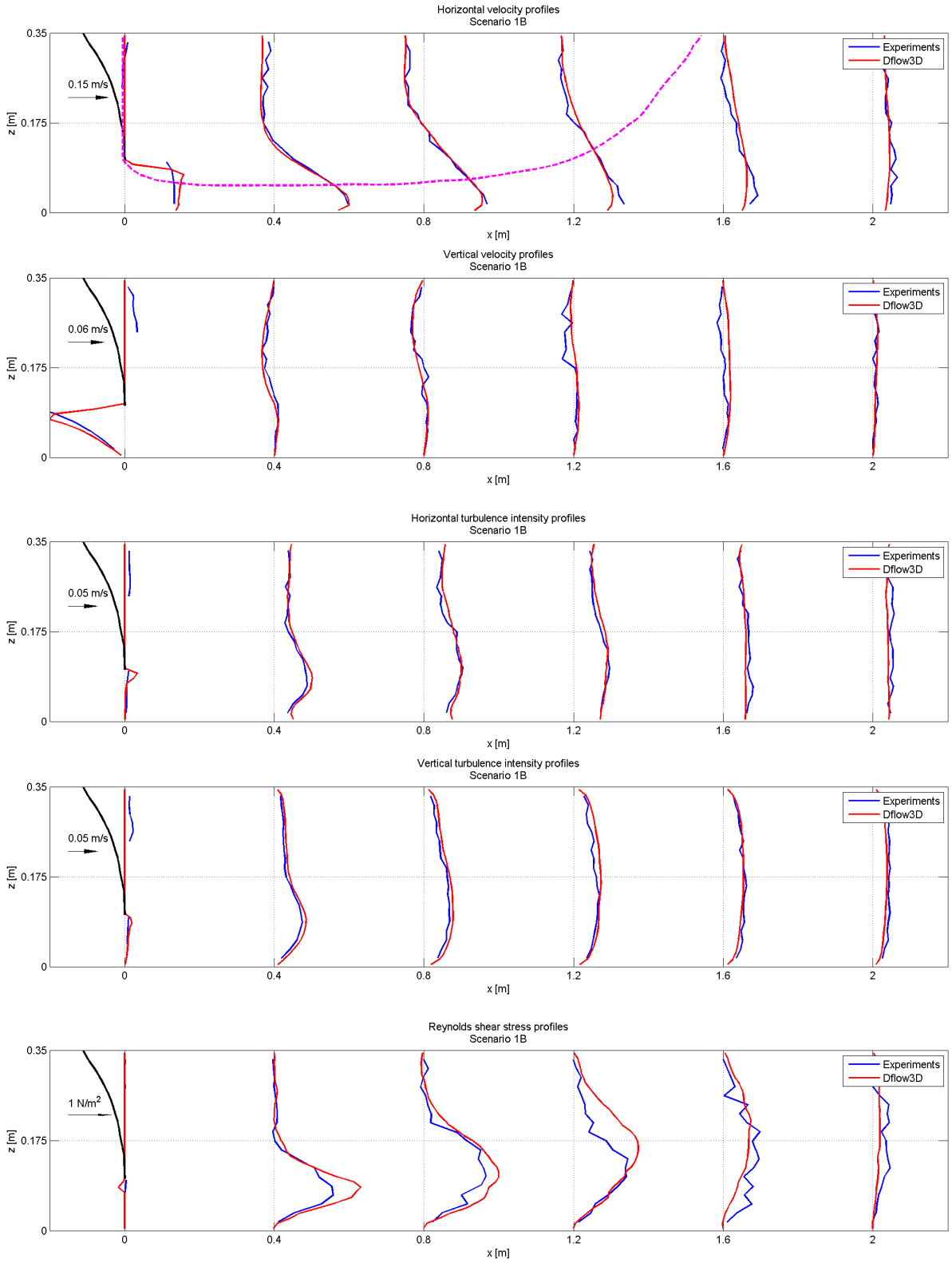

Figure G.2: Validation of the numerical model for laboratory scenario 1B.

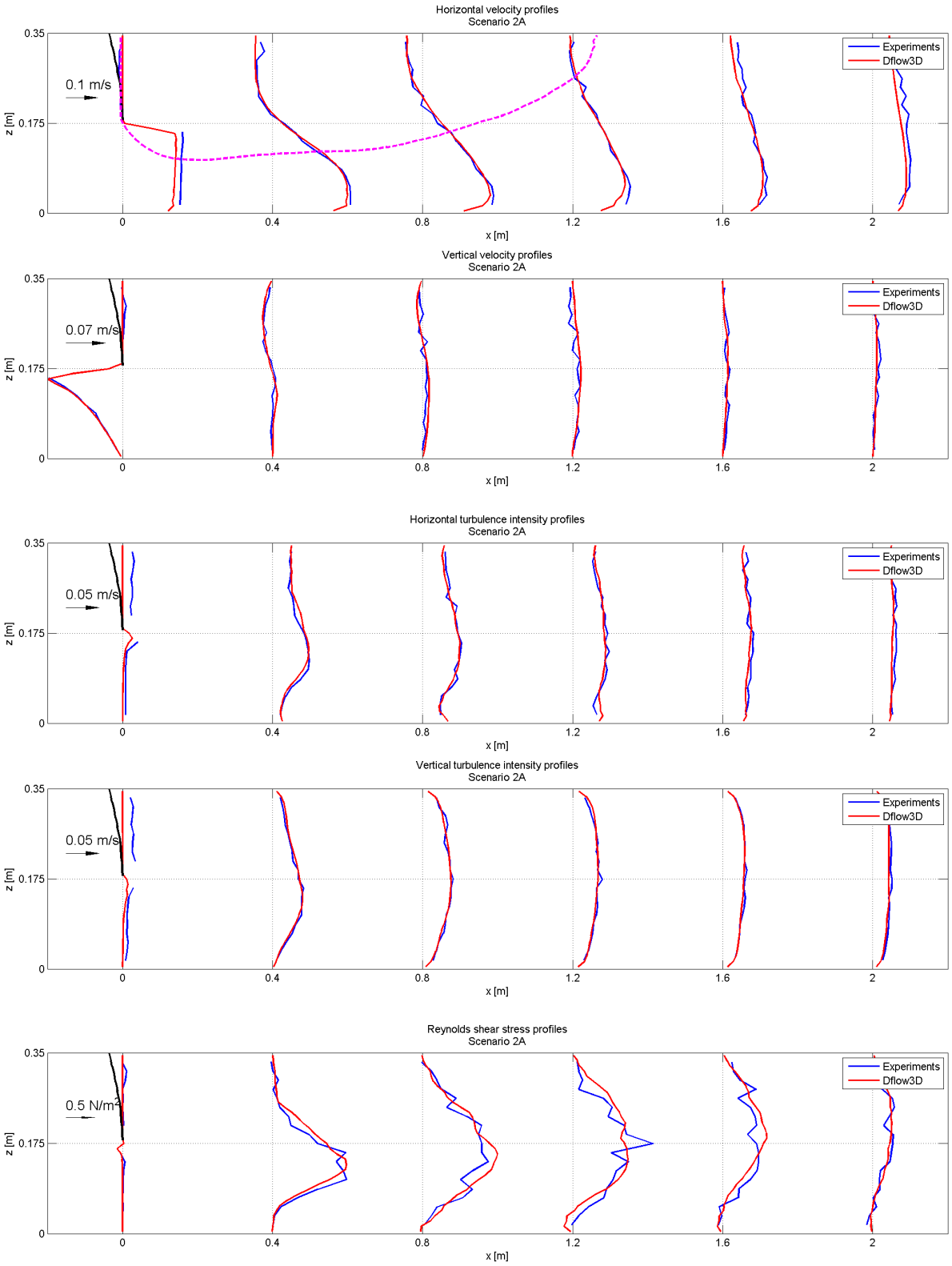

Figure G.3: Validation of the numerical model for laboratory scenario 2A.

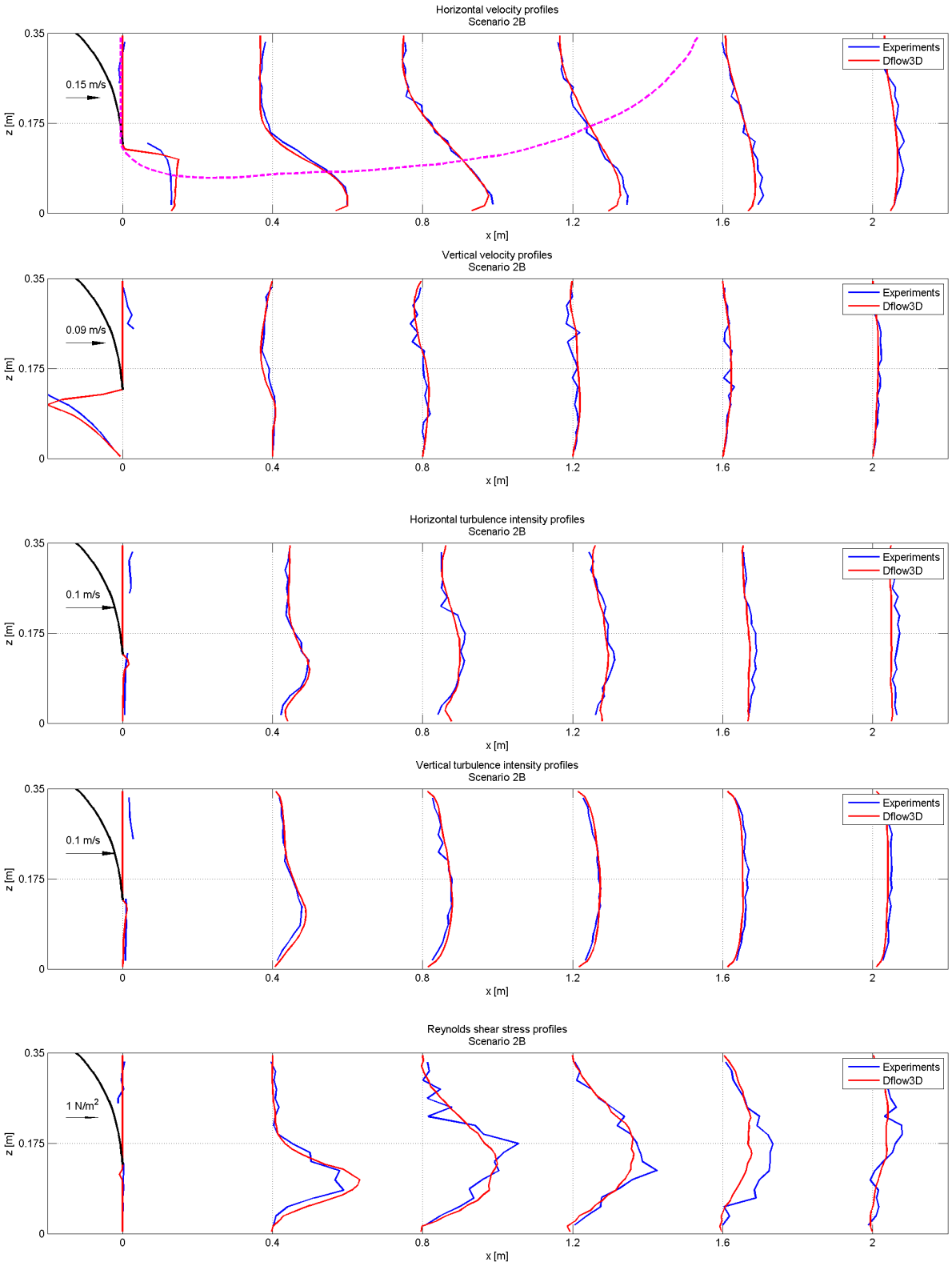

Figure G.4: Validation of the numerical model for laboratory scenario 2B.

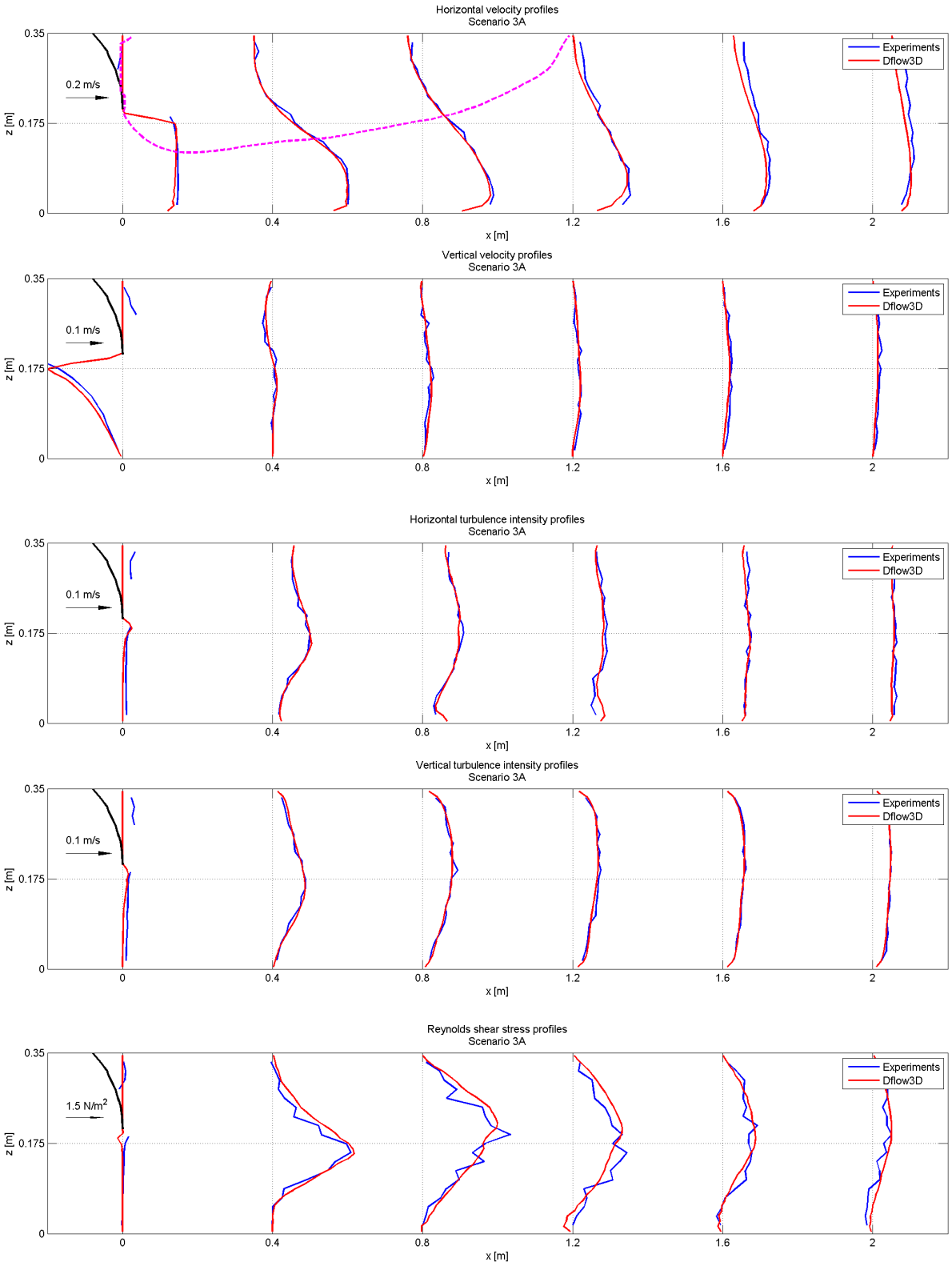

Figure G.5: Validation of the numerical model for laboratory scenario 3A.

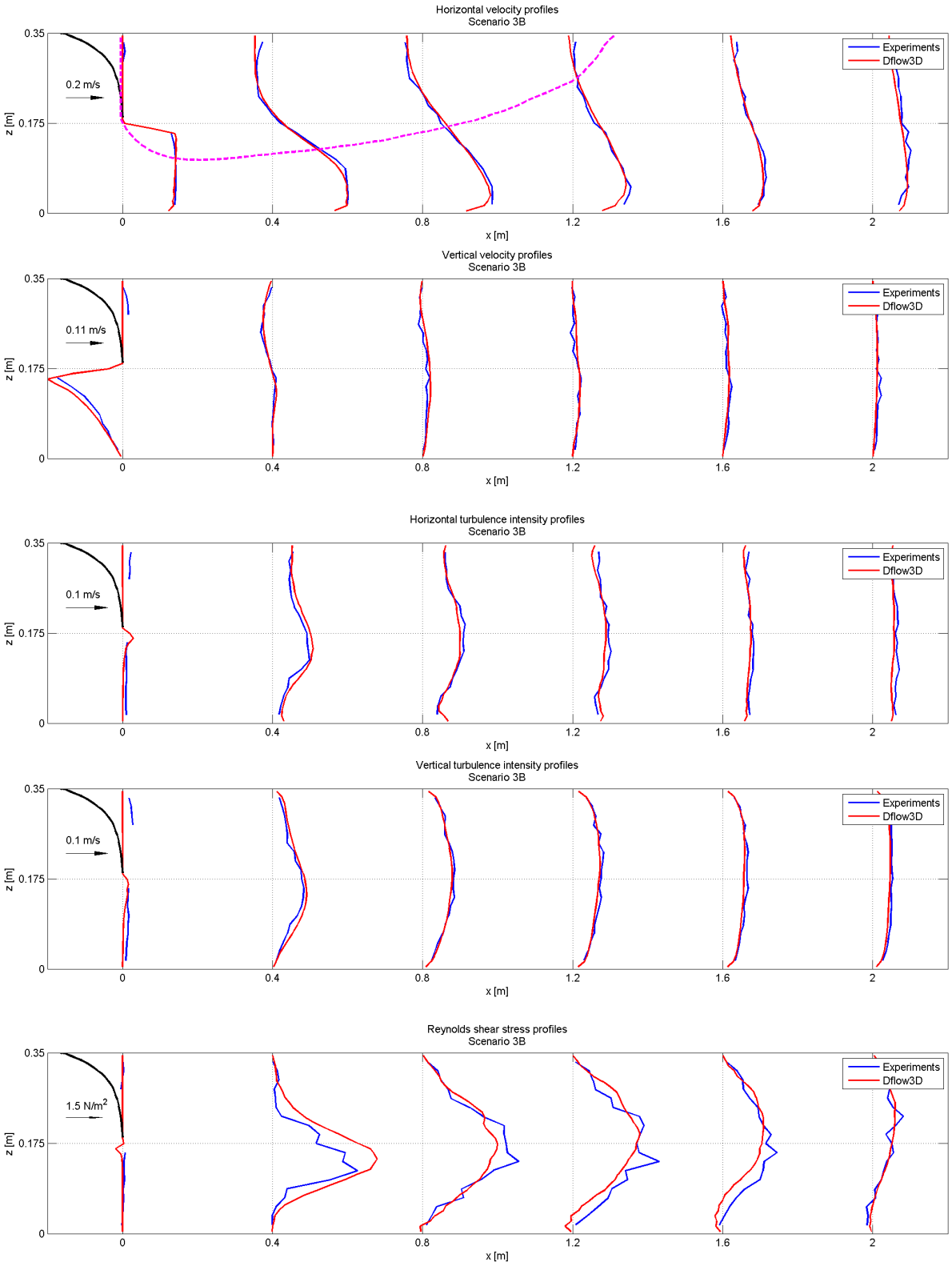

Figure G.6: Validation of the numerical model for laboratory scenario 3B.

Appendix H

Effectiveness figures

In this appendix, plots of $E_{in}(6h)$ and $E_{ref}(6h)$ are presented together with the actual data points.

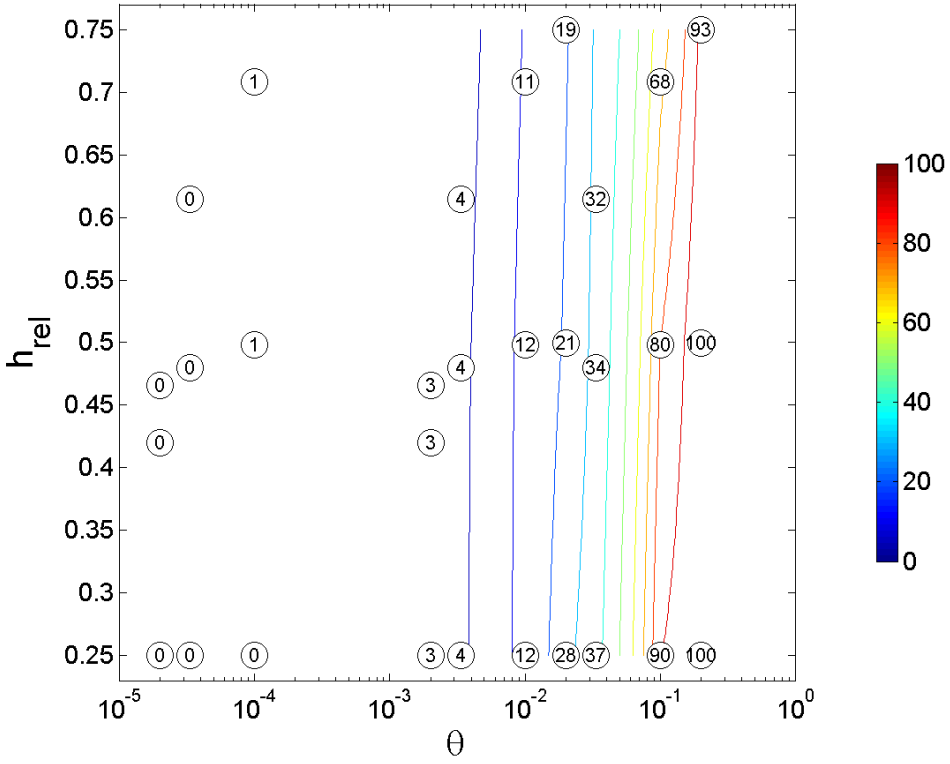

Figure H.1: Inflow effectiveness $E_{in}(6h)$ for profile U1 (%).

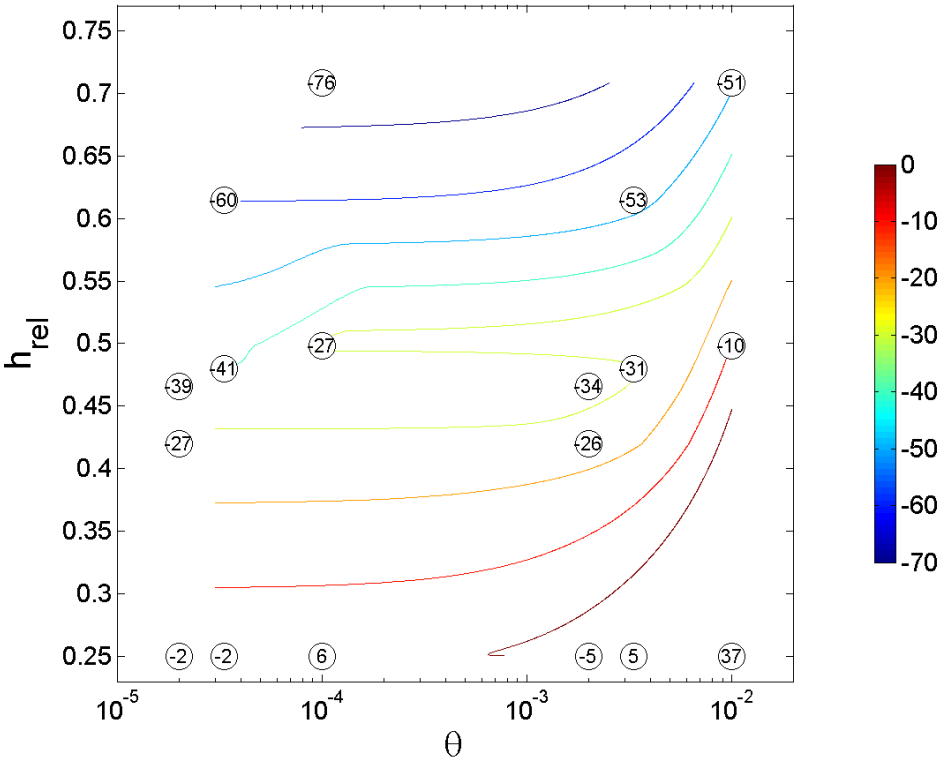

Figure H.2: Inflow effectiveness $E_{in}(6h)$ for profile U2 (%).

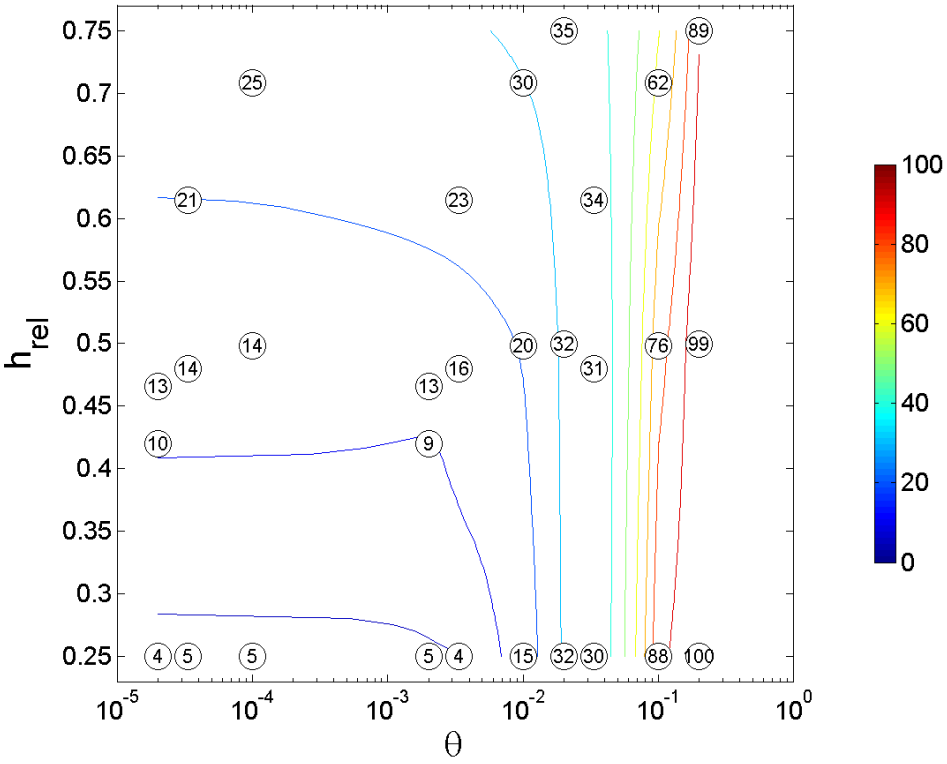

Figure H.3: Inflow effectiveness $E_{in}(6h)$ for profile U3 (%).

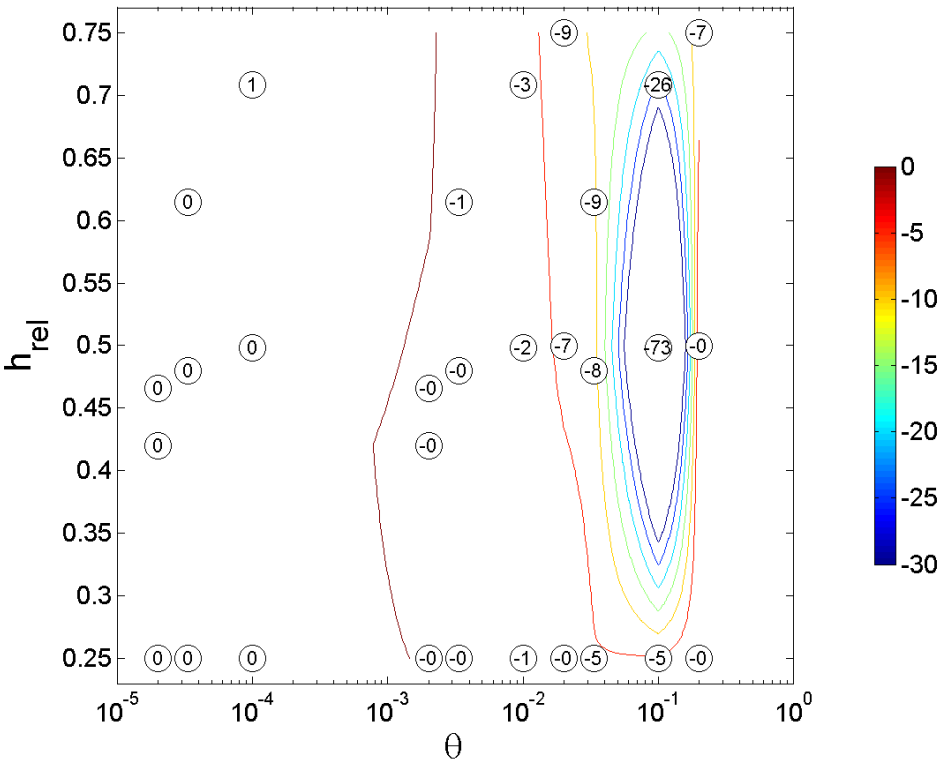

Figure H.4: Reference effectiveness $E_{ref}(6h)$ for profile U1 (%).

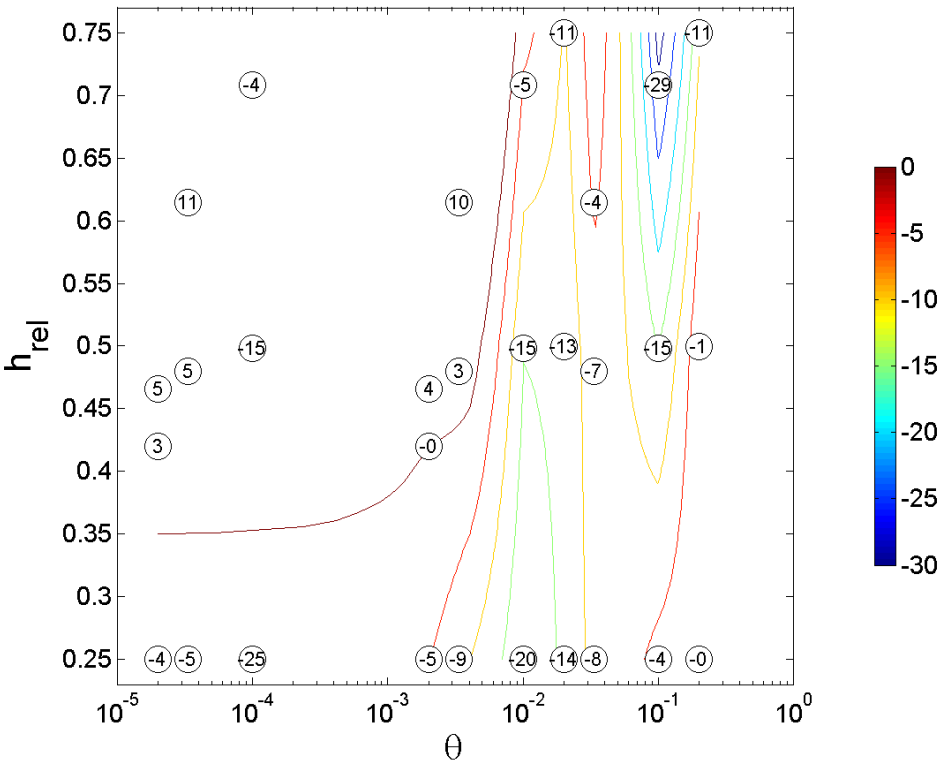

Figure H.5: Reference effectiveness $E_{ref}(6h)$ for profile U3 (%).

Appendix I

Case studies revisited

Appendix A treated a couple of case studies regarding silt screen effectiveness, stemming from both internal research by dredging company Boskalis as well as published research by Vu et al. (2010) and Jin et al. (2003). The case studies and the associated conclusions are now re-examined, bearing in mind the knowledge gained from this research.

I.1 Experiments by Boskalis

Boskalis conducted three field measurements regarding silt screens of the hanging type. Their specifications are recalled in table I.1.

Table I.1: Specifications of silt screen field experiments by Boskalis.

	Case (1)	**Case (2)**	**Case (3)**
Geometry	Open water	Semi-enclosed reclamation	Semi-enclosed reclamation
h	13.5 m	9 m	6 m
h_{rel}	0.5	0.66	1
W_*	20	54	25
U	0.1 m/s	very small	very small
Conclusions	Negative	Neutral	Positive

Neutral conclusions were drawn on silt screen effectiveness in case 2, as no dredging-induced turbidity reached the screen. This observation is endorsed here, so case 2 is left out of further consideration.

Case 1 deals with a linear silt screen at open water, which is therefore susceptible to horizontal as well as vertical diversion. Both processes are recognised by the authors during the passage of an overflow plume. Figure I.1 shows three consecutive phases of this event. In the left panel the plume is mainly located upstream (to the left of the screen). The last few meters upstream show a fairly clear free surface, indicating that the sediment-laden main flow is diverted vertically. Downstream of the screen some turbidity has already been mixed into the recirculation zone, judging from the moderately turbid free surface. The middle panel shows the screen being surrounded by turbidity as a result of horizontal and vertical diversion. Finally, the left panel proves the existence of a downstream recirculation zone. After the main part of the plume has moved out of sight, significant suspended sediment concentrations persist immediately downstream of the silt screen.

Turbidity was measured at several depths while sailing circles around the screen with a survey vessel. Around 75 m upstream of the screen, turbidity values range from 5 NTU near

Figure I.1: Three consecutive images of an overflow plume passing a hanging silt screen (at $t =$ 11:11, 11:24 and 12:25). Courtesy Boskalis.

the free surface to 30 NTU near the bed. This is in fair agreement with profile L1 or E1 as used in this research. At 25 m downstream of the screen, a more or less uniform turbidity profile is found with values between 10 and 15 NTU. The following conclusions are drawn by the authors:

- A silt screen at deep water, placed perpendicular to the main current with a relative screen height of 0.5 is not an effective measure to mitigate dredging induced turbidity.
- The silt screen causes additional stirring of fine sediment into the water column, which increases plume decay times.
- Successful application of silt screens at deep water demands at least (1) increased screen height to block a larger part of the water column and (2) extended screen width to cover a wider variety of flow directions.
- As the adaptations proposed above might not be feasible, it is recommended to focus efforts on the development of operational measures to minimise the release of fine sediments together with sound skills for plume prediction.

Although the effectiveness of the screen is correctly judged, a number of remarks can be made regarding these conclusions:

- The big water depth is mentioned indirectly as a factor which negatively influences silt screen performance. This research has proved that the influence of water depth on silt screen effectiveness is negligible. However, the authors might implicitly associate a smaller water depth with smaller flow velocities and the presence of land masses which prevent horizontal diversion. Although that would at least improve the inflow effectiveness in a relative sense, a truly effective hanging silt screen does not exist.
- Increasing the (relative) height of the silt screen does not lead to effective mitigation of suspended sediment. It only induces more horizontal diversion and more intense downstream mixing.
- Increasing the screen width is suggested as way of preventing excessive horizontal diversion. It is true that increasing W_* leads to a bigger relative discharge, but this effect is limited (see figure 5.5). Within the range of realistic W_*, the part of incoming discharge being diverted vertically will never get much higher than 50%.

Case 3 concerns the application of a hanging silt screen just outside the open end of a semi-enclosed reclamation. Turbidity is caused by a cutter suction dredger pumping dredged material into the reclamation through a pipeline. This causes high suspended sediment concentrations on the inner side of the screen, ranging from several 100 to 1000 mg/l. The authors assume the

existence of near-bed turbidity currents, since the sheltered environment is expected to have virtually no mixing. The associated high Richardson number allows for stable stratification. Turbidity values measured on the outer side of the screen are 4 to 8 times lower than those on the inner side, which leads the authors to the following conclusions:

- Systematic variation of mid-depth turbidity values with the tidal level confirm the occurrence of density-driven currents. A sudden increase of turbidity is observed when the sensor touches the dense layer.
- The strong decrease of measured turbidity values from the inner to the outer side of the silt screen shows that the screen effectively blocks part of the fine sediment present in the dense layer.
- This decrease can not be fully attributed to the presence of a silt screen, as a turbidity current would show a certain degree of settling anyway.
- Effective functioning of the silt screen finds further confirmation from the observation that the screen, by the time that it was pulled out, was partly buried under a layer of sediment.

The following remarks have to be made regarding these conclusions:

- The high effectiveness of the silt screen can largely be attributed to it's coverage of the entire water column. The screen is partly buried under a layer of sediment, which means that its lower edge touches the bed. This puts the screen out of the scope of this research, as it does not allow for vertical diversion. Such a configuration is only feasible in very weak cross currents.
- Burial of the screen's lower edge might cause trouble during removal. The typical advantage of hanging silt screens over standing screens, being the absence of the need for heavy floating equipment, does not hold in this case.

I.2 Case studies in literature

In literature, two case studies of silt screen effectiveness were encountered. Their relevant parameters are summarised in table I.2.

Table I.2: Specifications of silt screen case studies encountered in literature.

	Jin et al. (2003)	**Vu et al. (2010)**
Geometry	Open water	Open water
h	5.5 m	22.5 m
h_{rel}	0.6	0.5
W_*	80	18
U	$0.2 - 0.3$ m/s	$0.3 - 0.6$ m/s
Conclusions	Negative	Positive

Jin et al. (2003) investigated the effectiveness of a hanging silt screen at open water. Turbidity was caused by three mechanical dredgers, operating at 220 to 330 m from the silt screen. Ebb-tidal currents are directed from the dredging site perpendicularly to the screen. An extensive measurement campaign is conducted, see figure I.2. The six measurement locations indicated by solid black dots numbered 1-1 to 2-3 are of special interest, as well as locations A1 and A2. Vertical SSC profiles are obtained at paired locations upstream and downstream of the

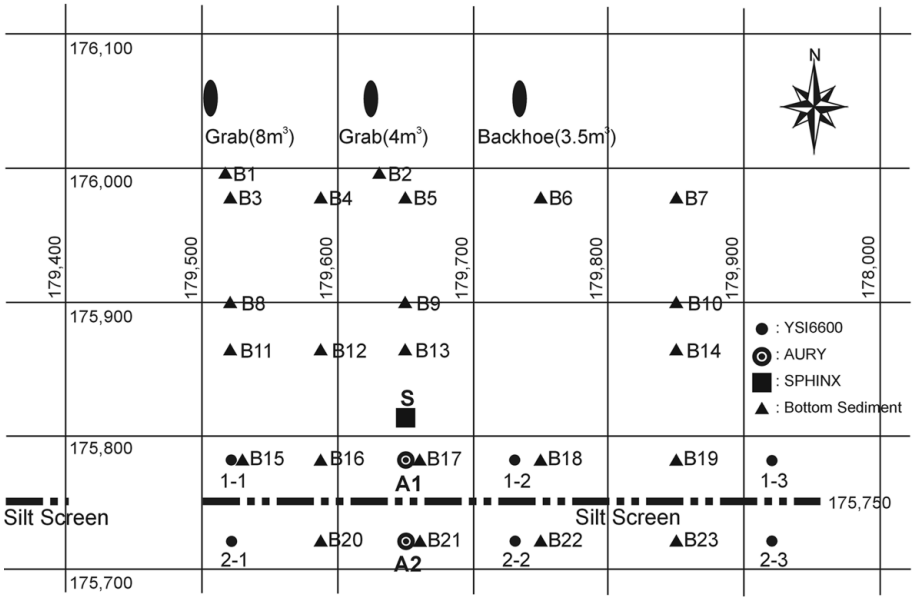

Figure I.2: Overview of case study into silt screen effectiveness by Jin et al. (2003).

screen, represented by the solid black dots. During ebb-tidal current, virtually all measurements show that downstream SSC profiles exceed the upstream ones up to 100%. Upstream SSC values mostly range from 5 mg/l near the free surface to 10 mg/l near the bed. At locations A1 and A2, mid-depth values of flow velocity and SSC are obtained. It stands out that downstream flow velocities are about half as high as the upstream values. This phenomenon systematically switches along with the tidal current direction. Jin et al. (2003) conclude as follows:

- The flow velocity at 30 m downstream of the silt screen is about half that found at the same distance upstream.
- Even for a relatively weak storm period, SSC increases up to the value caused by dredging.
- Depth-averaged SSC downstream of the screen is higher by 60% with respect to the upstream side. This contradicts the major purpose of the screen, which is to reduce SSC.
- Screen efficiency evaluated by the SSC flux at mid-depth is about 55%. Considering the higher SSC downstream, however, depth-integrated flux downstream may be comparable to that upstream.
- Considering the above results, the silt screen of the fixed hanging type installed from the surface to about half of the water depth does not confirm a mitigation measure against the spreading of suspended sediment plumes generated by dredging in the study area, where the mean flow velocity ranges from 20 to 30 cm/s.

The negative conclusions are confirmed here. However, a number of remarks should be made:

- Jin et al. (2003) completely ignore the presence of horizontal diversion. As the screen is applied at open water without any lateral restrictions, this process will definitely take place.
- The authors attribute the high reduction of flow velocity at mid-depth to the existence of a near-bed jet flow and a recirculation zone above. However, the measurement location is situated at about 6 times the water depth downstream. This will probably be in the zone

of flow recovery, where mid-depth flow velocities should at least equal the upstream values and might even be slightly higher. Instead, the reduced flow velocity can be explained very well by the presence of horizontal diversion, which leads to a decrease of specific discharge by about 50%.

- The increase of depth-averaged SSC from upstream to downstream can be caused by a number of different processes. First of all, a continuous upstream supply of suspended sediment gives rise to turbulent diffusion into the recirculation zone, leading to an increase of SSC in the upper part of the water column. However, it was mentioned before that the profiles are obtained downstream of the recirculation zone. Second, screen-induced erosion might be a source of suspended sediment downstream of the silt screen. Sediment samples indicate that the bed contains significant silt and clay fractions. Finally, it might be possible that measurements are conducted when the main part of a dredging spill has already passed by. Persistent turbidity in the recirculation zone might give rise to high downstream SSC. Again it should be noted that measurements are conducted downstream of the recirculation zone.

- The 55% decrease of SSC flux at mid-depth is explained by the authors as a local phenomenon. They expect depth-integrated fluxes to be equal on both sides of the screen. This would only hold when the situation can be schematised with a 2DV approach. Due to horizontal diversion this is not the case. Additional sediment fluxes around the screen's side edges will probably account for the remaining percentage.

The last case study was investigated by Vu et al. (2010). Again, the silt screen was deployed at open water. The water depth, flow velocity and screen dimensions are well outside the allowable ranges commonly encountered in literature. Suspended sediment is released by grab dredgers, operating at an unspecified distance from the silt screen. The tidal current is directed perpendicular to the screen.

At both sides, SSC and flow velocities are measured at 10, 20 and 30 m from the screen. When the current is directed from the dredging area towards the screen, significant reductions of SSC and especially sediment flux are found at the downstream side, see figure I.3. The authors admit that knowledge on the hydrodynamic processes and sediment behaviour in the vicinity of the silt screen is lacking. Hence they draw no conclusions regarding silt screen effectiveness for this case study. Nevertheless, a number of interesting remarks is made here:

- The observed reduction of SSC corresponds fairly well with results obtained in this research for inflow profile U1 (uniform over the entire water column). For discontinuous plumes with a relatively long inflow duration, a reduction of 18% near the free surface is plausible. Nevertheless, instantaneous SSC values alone do not represent the full story regarding silt screen effectiveness. Both the conversion to environmental impact potential and integration over time (for discontinuous plumes) should be carried out to provide a more complete picture.

- The reduction of SSC fluxes is open to various interpretations. The flux is computed as the product of flow velocity, SSC and vertical bin height. It is corrected to account for the angle between the incoming flow and the silt screen. A lower value downstream with respect to upstream can be explained by a couple of different reasons, including horizontal diversion and extensive settling. The latter is certainly not expected within 10 m upstream and downstream of the silt screen. Although it is questionable as well whether high lateral fluxes of sediment still occur within 10 m upstream of the screen, the data give reason to believe that this is the case. If the flow would be highly two-dimensional (2DV), 0 to 20% near-bed reduction of SSC fluxes would not occur. SSC values only decrease by 0 to 5% (see upper panel of figure I.3) and flow velocities will show a strong increase due to

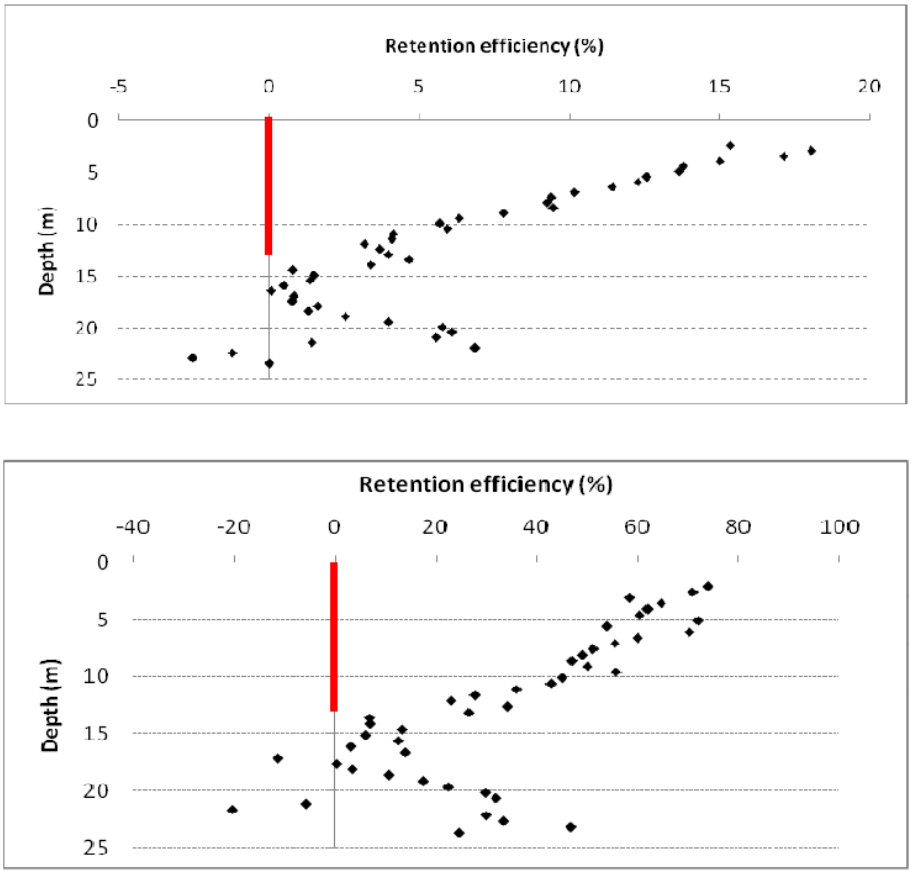

Figure I.3: Percentual reduction of SSC (upper panel) and SSC flux (lower panel) over depth at 10 m downstream with respect to 10 m upstream as found by Vu et al. (2010).

flow contraction. As the bin height and upstream current direction do not change, lateral sediment fluxes should be present at the upstream side. The only alternative explanation would be a change in upstream conditions due to the time gap between upstream and downstream profile measurements.